DISSERTATION

# CHARACTERIZING THE DIFFUSIONAL BEHAVIOR AND TRAFFICKING PATHWAYS OF KV2.1 USING SINGLE PARTICLE TRACKING IN LIVE CELLS

Submitted by

Aubrey Weigel

Graduate Degree Program in Bioengineering

In partial fulfillment of the requirements

For the Degree of Doctor of Philosophy

Colorado State University

Fort Collins, Colorado

Spring 2013

Doctoral Committee:

Advisor: Diego Krapf

Michael Tamkun
James Bamburg
Randy Bartels

# ABSTRACT

## CHARACTERIZING THE DIFFUSIONAL BEHAVIOR AND TRAFFICKING PATHWAYS OF KV2.1 USING SINGLE PARTICLE TRACKING IN LIVE CELLS

Studying the diffusion pattern of membrane components yields valuable information regarding membrane structure, organization, and dynamics. Single particle tracking serves as an excellent tool to probe these events. We are investigating of the dynamics of the voltage gated potassium channel, Kv2.1. Kv2.1 uniquely localizes to stable, micro-domains on the cell surface where it plays a non-conducting role. The work reported here examines the diffusion pattern of Kv2.1 and determines alternate functional roles of surface clusters by investigating recycling pathways using single particle tracking in live cells.

The movement of Kv2.1 on the cell surface is found to be best modeled by the combination of a stationary and non-stationary process, namely a continuous time random walk in a fractal geometry. Kv2.1 surface structures are shown to be specialized platforms involved in trafficking of Kv channels to and from the cell surface in hippocampal neurons and transfected HEK cells. Both Kv2.1 and Kv1.4, a non-clustering membrane protein, are inserted and retrieved from the plasma membrane at the perimeter of Kv2.1 clusters. From the distribution of cluster sizes, using a Fokker-Planck formalism, we find there is no evidence of a feedback mechanism controlling Kv2.1 domain size on the cell surface. Interestingly, the sizes of Kv2.1 clusters are rather governed by fluctuations in the endocytic and exocytic machinery. Lastly, we pinpoint the mechanism responsible for inducing Kv2.1 non-ergodic dynamics: the capture of Kv2.1 into growing clathrin-coated pits via transient binding to pit proteins.

# ACKNOWLEDGEMENTS

There are many people I would like to thank. Without the support from friends, family and colleagues I wouldn't be where I am today. I owe a great deal of gratitude to my graduate committee. I thank you all very much for the time and effort you have invested. Your encouragment and mentorship is truely appreciated.

*Diego*, when I started the lab was brand new, and my how it has changed since then! We were both younger then, and experiencing a lot of things for the first time. It was a bit of a bumpy road at times but in the end a great time. It was an experience for the both of us growing and building the lab to what it is today. An experience for which I will forever be grateful. I have learned *so* much working with you. I have witnessed what it truly means to be passionate about science, how to juggle this passion and life with a bit of grace, and how to slam a 'clinker' on unsuspecting foosball competitors. Thank you for all of your guidance and your patience.

*Mike*, you have been an amazing mentor. While you'd like to have the world see you as a grumpy, ruthless pessimist, I feel priveledged to have known your truer side: a wise, merciful pessimist. You have an amazing talent of looking at the larger picture and answering the bigger questions. An attribute that is very admirable. Not only has it been very fortunate to collaborate with you and your lab but it has been truly instrumental and foundational to the body of work that I have been able to put together for my PhD. (You should also be commended for your ability to consistently brew excellent beer)

To my lab-mates past and present, you guys rock! Much of what I have learned has come from interactions with everyone. *Kristen*, you reminded me there is more to life than just science. *Jenny*, you have been an amazing officemate - I wouldn't trade our time together for anything, I think that we have learned so much from eachother. *Sanaz*, you are just starting to get your feet wet in this lab and already you have done so much! I know that you are going to great things! *Bryce*, you have great experiments ahead of you, and all the best to you in the future. A huge deal of thanks goes to *Kari Ecklund* as well. So much time doing tedious data analysis was saved with your efforts! The work in Chapter 4 determing the size of Kv2.1 clusters was made possible with your efforts. Also, thank you *Mike Reid* for taking the time to help our lab with your help in analyzing the seemingly infinite arrays of data that we put together in Chapter 4. To *Edwin Chong*

and *Shankar Ragi,* I also owe a great deal of thanks. Your contribution of simlutions and analytical expertise helped us form a beautiful story in Chapter 4. To everyone, thank you for all of your support, patience, and friendship.

Tamkunites, where do I even begin. Every ounce of cellular and molecular biology I know, I owe to you. I can not thank each and every one of you enough for taking the time to 'show me the ropes'. I know it had to be painful at first - a physicist doing molecular biology! We have grown so far beyond just being collaborators and I thank you all for your endeared friendship. *Liz*, I can not send you enough gratitude for taking the time to work with me and teach me the ins and outs of plasmid cloning and mutagenesis. *Phil*, it has been a great privelege to get to know you. To the both of you, it has been awesome working with you! I have learned a great deal from our improntu brain storm sessions, throwing our edeas at eachother, though vague, often not well thought through, usually not to the point, they have been extremly instructional and have shaped the thinking of us all. Bears, beers, and science should be combined in a frequent fashion. I would specifically like to acknowledge the work that is presented in Chapter 4 which was largely done by the hands of *Emily Deutsch*, *Liz Akin*, *Phil Fox*, *Rob Loftus* and *Chris Haberkorn*. All of the experiments in neurons, mirroring what we observed in HEK cells was performed by this group, as well as the elegant experiments showing the insertion of nascent Kv2.1 channels.

I am so fortunate to be surrounded by such a grand support group of friends and family. Thank you, for your love, your support, your guidance, and your patience.

# DEDICATION

Dedicated to the loving memory of my father, Michael Rankin,
1961–2010

TABLE OF CONTENTS

# LIST OF FIGURES

# LIST OF TABLES

# ACRONYMS

AIC ..... Akaike information criterion

AIS..... axon initial segment

ATOF..... acousto-optic tunable filter

BAD..... biotin acceptor domain

BIC..... Bayesian information criterion

BSA..... bovine serum albumin

CCD..... charged-coupled device

CCP ..... clathrin-coated pit

CDF ..... cumulative distribution function

CFP ..... cyan fluorescent protein

CHO ..... Chinese hamster ovary

CLC ..... clathrin light chain

CME ..... clathrin-mediated endocytosis

CTRW..... continuous-time random walk

DMEM ..... Dulbecco's modified eagle medium

EMCCD ..... electron-multiplied charge-coupled device

FBM ..... fractional Brownian motion

FBS..... fetal bovine serum

FCS ..... fluorescence correlation spectroscopy

FRAP ..... fluorescence recovery after photobleaching

FRET..... fluorescence resonance energy transfer

FRSK..... fetal rat skin keratinocyte

FWHM ..... full width at half maximum

GFP..... green fluorescent protein

HEK..... human embryonic kidney

HEPA-OVA..... mouse hepatoma

MDCK..... Madin-Darby canine kidney epithelial

MSD ..... mean square displacement

MTT..... multiple-target tracing

NA ..... numerical aperature

NaN..... not-a-number

NRK..... normal rat kidney

PBS..... phosphate buffered saline

PDF..... probability density function

PSF..... point spread function

PtK2..... rat kangaroo

QD ..... quantum dot

RFP ..... red fluorescent protein

ROI ..... region of interest

sem ..... standard error of the mean

SNR ..... signal to noise ratio

SPT ..... single particle tracking

TEA-MSD ..... time-ensemble averaged MSD

TIR..... total internal reflection

TIRF..... total internal reflection fluorescence

YFP ..... yellow fluorescent protein

# CHAPTER 1: INTRODUCTION

This chapter begins by introducing the complexity of the cell membrane. Then experimental and analytical techniques that were used in this dissertation to these particular cellular processes and components is provided. These include total internal fluorescence microscopy and single particle tracking. The topic of diffusion is discussed next and three popular models for anomalous subdiffusion, namely fractional Brownian motion, continuous time random walk and diffusion on a percolation cluster, are given. We next introduce the particular protein studied in this dissertation, the Kv2.1 channel, and the motivation for this research. Lastly, an overview of this thesis is given.

## 1.1 the cell membrane

The cell membrane att he simplest level is a barrier that separates the interior of the cell from its external environment [1]. It encloses the cell, maintains fundamental differences between the cytosol and extracellular space, and defines the boundaries of the cell. It is composed of a double layer ofl ipids and is less than 10 nm in thickness. The most abundant membrane lipids are phospholipids. The plasma membrane is also embedded with a wide variety of proteins some of which can perform as channels and pumps to move different molecules in and out of the cell across the cell membrane.

In 1972, Singer and Nicholson proposed a model for the plasma membrane; the fluid mosaic model [2]. Within this model proteins and lipids are allowed to move laterally throughoutt he membrane, making the membrane more like a fluid than a solid. The assortment of proteins and lipids, i.e. integral proteins, peripheral proteins, glycoproteins, cholesterol and lipoproteins, portray a mosaic made up of many different parts. Since then, our view of the cell membrane has drastically shifted [3, 4, 5]. We know now thatt here are high degrees of complexity and compartmentalization [6, 7, 8]. Experimental work has provided detailed information on protein and lipid dynamics in the cell membrane that has made it apparentt hat it is far from a homogenous mixture ofl ipids and proteins [9, 10, 11].

Over the years the picture of the cell membrane has evolved from a uniform mixture of composites to an entity with a high degree of order and organization. We know that the proteins embedded within the membrane do not simply serve as holes in the plasma membrane but have a multitude of functions. The plasma membrane is a system with a high degree of heterogeneity and active organization across several length and time scales. And it is precisely this dynamic organization that is essential to maintain many cellular functions including, but not limited to: cell-cell communication [12], signal reception and transduction [13, 14, 15], trafficking [16, 17], and receptor recognition [10].

## 1.2 MICROSCOPY TOOLS

The development and improvement of microscopy techniques has given rise to major advances in cell biology. Live cell imaging is important in unraveling dynamic processes such as membrane trafficking, cell signaling and remodeling of the cytoskeleton. Often times there are states within a process that are missed when analyzing the ensemble population. These transient intermediate states are revealed only when probing at the single molecule level. This requires highly sensitive microscopy equipment with a high degree of spatiotemporal resolution. There are various experimental techniques that have been implemented to study the dynamics of particles diffusing in the cell membrane [18]. These optical techniques include but are not limited to fluorescence correlation spectroscopy (FCS) [19], fluorescence resonance energy transfer (FRET) [20, 21], fluorescence recovery after photobleaching (FRAP) [22], and single particle tracking (SPT) [23].

*Ensemble measurements: FRAP and FCS*

Two widely used ensemble fluorescence microscopy techniques to study the diffusion of membrane proteins are FRAP and FCS. FRAP takes use of particles' diffusion and yields information about the behavior of an ensemble of molecules. A small area of fluorescently labeled molecules on the membrane is photobleached using a brief and intense excitation source [22]. Then, the time required for unbleached molecules to diffuse into the bleached area is measured. The diffusion coefficient can be directly calculated from this time. While this technique is excellent at

measuring the bulk diffusion coefficient of an ensemble of membrane molecules, it falls short in differentiating between multiple subpopulations within the ensemble.

FCS is a time-averaging fluctuation analysis developed by Elson and Webb in 1972 [24]. It can measure the diffusion coefficients and binding kinetics of small molecular ensembles, and combines high sensitivity with statistical confidence [25]. Typically an FCS setup consists of a confocal microscope and a photon detector, such as an avalanche photodiode. Fluorescence is collected from labeled molecules in a small well defined volume near the focus of a laser beam. The fluorescent fluctuations arise from particles diffusing in and out of the detection volume and is proportional to the number of fluorescent molecules in the volume. A requirement of FCS however, is that the magnitude and frequency of the fluctuations reside above the total intensity of the fluorescence signal. An advantage of FCS is the high temporal resolution, it is able to achieve a resolution in the microsecond timescale. However, the spatial resolution is more limited. In a conventional FCS microscope a resolution on the order of 100 nm is expected. Upon the development of microscopy techniques such as **STED!** (STED!), the focal volume of FCS can be reduced to nanoscopic scales, enabling single particles to diffuse in and out of the detection volume and increasing the spatial resolution by an order of magnitude or more.

### 1.2.1 *Single particle tracking*

The point spread function (PSF) of a point source of light can be closely approximated by a two-dimensional Gaussian. In Fig. 1.1 a single quantum dot (QD) point source (A) is shown along with its two-dimensional Gaussian fit (B). The accuracy of the system is determined by the standard error of the mean (sem) of the PSF. Thompson et al [26] derived a theoretical calculation for the sem taking into account several noise factors such as photon noise or shot noise, camera readout, pixelation effects and fluorescent background, Eq. 1.1.

$$\sigma^2 = \frac{s^2}{N} + \frac{a^2/12}{N} + \frac{8\pi s^4 b^2}{a^2 N^2} \tag{1.1}$$

where $s$ is standard deviation of the PSF, $a$ is the pixel size, $b$ is background and $N$ the number of photons collected. The shot noise of the system is represented by the first term $s^2/N$, the second

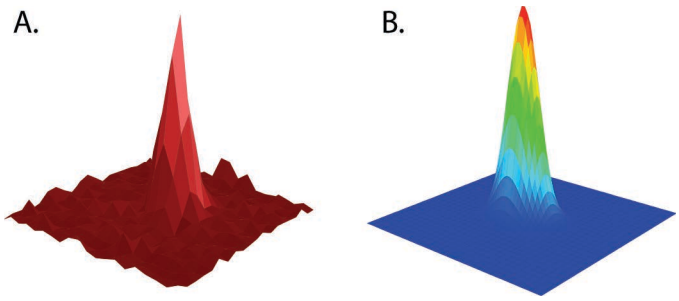


Figure 1.1: *Point source PSF and 2D Gaussian approximation* (A) PSF of a QD point source of light imaged in a fluorescence microscope. (B) Two-dimensional Gaussian fit to the QD PSF.

term is a result of the pixel size of the detector, and the last term the background fluorescence. All of these factors can be minimized by increasing the collection of photons.

In a single molecule imaging experiment the pixel size, $a$, is determined by the detection method and magnification (charged couple device). The width of the PSF is a characteristic of the imaging system. Thus, overall, the PSF width can not be decreased to enhance the accuracy, and the pixel size can only finitely be improved upon. This leaves us with minimizing the the background fluorescence $b$, or rather increasing the signal to noise ratio (SNR). While this appears simple enough in practice, reducing the background can be challenging, especially with live cell imaging. For instance biological structures such as lysosomes and mitochondria have auto-fluorescent properties [27], which increase background fluorescence rather than reducing it.

To achieve nm resolution it is necessary to have a high SNR. This can prove to be a difficult task in live cell imaging because of their auto-fluorescent qualities mentioned above. As a work around, confocal microscopes optically section the cell, by use of a pinhole, to reduce background noise and improve SNR. Another approach, total internal reflection fluorescence (TIRF) microscopy, selectively excites only the fluorophores within a very thin section [28]. The basis of TIRF microscopy stems from the behavior of the light at the interface between to mediums with different refractive indexes. Snell's law, Eq. 1.2, tells us that a ray of light will bend away from normal, or refract, as it passes through the interface of a medium of higher refractive index, $n_{glass} = n_1 \sim 1.5$, to medium of lower refractive index, $n_{water} = n_2 = 1.33$.

$$n_1 \sin\theta_1 = n_2 \sin\theta_2 \tag{1.2}$$

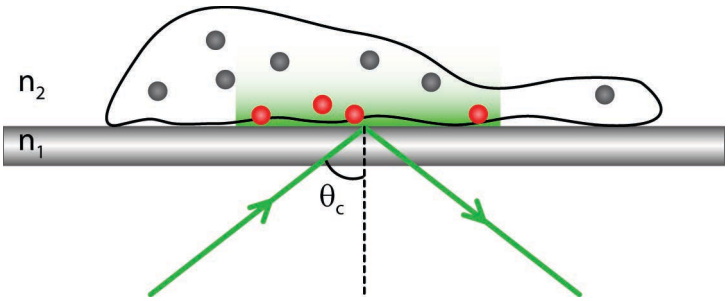


Figure 1.2: *TIRF* An incident ray of light strikes the glass-water interface at the critical critical angle and it total internally reflected. An evanescent wave is generated and propagates into the cell, illuminating a thin section of fluorophores. As a result background fluorescence is reduced.

As the angle of incidence increases to a critical angle, $\theta_c$, the light is no longer refracted into the lower refractive index medium but instead travels parallel to it. Here $\sin\theta_2 = 1$ simplifying Snell's law to Eq. 1.3:

$$\theta_c = \sin^{-1}\left(\frac{n_1}{n_2}\right) \tag{1.3}$$

Once the critical angle is surpassed the light is totally internally reflected back into the higher refractive index medium, i.e. the glass. This reflection within the higher refractive index medium is highly efficient. In fact fiber-optic lines use total internal reflection to bounce light along hundreds of thousands of kilometers. The key principle though, for the use of single molecule imaging, is that even though the ray of light is totally internally reflected a thin (typically ~ 100 nm), exponentially decaying electromagnetic field is generated and propagates into the medium of lower refractive index, i.e the water/sample. The intensity of the evanescent wave, $I_e$, can be expressed by Eqs. 1.4 and 1.5.

$$I_e(z) = I(0)\, e^{-z/d} \tag{1.4}$$

$$d = \frac{\lambda_0}{4\pi\sqrt{n_1^2 \sin^2\theta_1 - n_2^2}} \tag{1.5}$$

where,

$I$ : intensity of evanescent wave

$z$ : distance from glass coverslip

$d$ : penetration depth, decay of $I_e(z)$

$\lambda_0$ : wavelength of light

A shallow evanescent wave is therefore generated by having a large difference in refractive index between the two mediums, high angle of incident light, and short wavelength. Most of these parameters, however, are experimentally constrained. The wavelength of light is set by the fluorophore that needs to be excited and the refractive indexes of the sample and glass coverslips are fixed. The angle of incidence is determine by the numerical aperature (NA) of the objective in objective-type TIRF microscopy, Eq. 1.6.

$$NA = n_3 \sin\theta_1 \tag{1.6}$$

Here $n_3$ is the refractive index of the immersion media. For high NA (1.45) oil-objective this is usually ~ 1.51. This is one of the reasons why high numerical aperture objectives are important for high-sensitivity, high-accuracy TIRF microscopes.

*Probes*

Sir George G. Stokes was one of the first scientists to describe fluorescence in 1852 [29]. He observed that the mineral fluorspar emitted red light when illuminated with ultraviolet light. Further observations led to the discovery that fluorescence emission always occurred at a longer wavelength than the excitation wavelength. This difference between excitation and emission wavelengths is the Stokes shift. Fluorescent molecules absorb photons, gain energy and enter an excited state. The most probable process following absorption starts with relaxation to the lowest vibrational energy level, this process is known as vibrational relaxation or internal conversion. Fluorescence occurs when relaxation from this state back down to the ground state is accompanied by the emission of a photon. Most fluorophores can repeat this process thousands of

times before the molecule photobleaches. Photobleaching is the loss of the molecule's ability to fluoresce due to photon-induced chemical damage.

It was not until the 1930s that the use of fluorescent molecules was initiated in biological studies. The true jumpstart however was in the 1990s when the first fluorescent protein, green fluorescent protein (GFP) was purified and expressed in live cells[1] [30]. Over the last couple decades the collection of genetically encoded fluorescent proteins from jellyfish has ignited a revolution for live cell imaging. Since the development of GFP, many color variants have been designed, including yellow fluorescent protein (YFP), red fluorescent protein (RFP), and cyan fluorescent protein (CFP). There a now hundreds of different fluorescent probes, each with their own spectral properties and size variations [31]. There are even fluorophores that have color-switching ability. An advantage to fluorescent proteins is that they can be genetically encoded and linked to a cDNA for expressing a specific protein as a chimera with a fluorescent protein.

Organic fluorophores do have some disadvantages. They are only excited by a precise wavelength of light and they photobleach fairly rapidly when continuously illuminated. However, recently more stable inorganic fluorophores have been developed to overcome these disadvantages. One example of these fluorochromes are nanocrystals made of semiconductor material called QDs [32]. QDs are excited with a broad spectrum of wavelengths but emit at a very specific peak. The emission wavelength of the QD depends on the size of the nanocrystal itself. The smaller the QD the lower the wavelength. Usually QD's are 2-10 nm in diameter. For use in biological systems the QDs are conjugated with useful substrates such as antibodies or streptavidin, to enable specific labeling of molecules of interest. The combination of long-lived fluorophores such as QDs and fluorescent probes such as GFP has enabled elaborate and elegant investigations of live cells at the single molecule level that were before impossible.

Colloidal gold nano-particles and latex beads.

1 The first description of green fluorescent substance in the jellyfish Aequorea victoria was in 1955. However it wasn't until 40 years later that the protein responsible for the jellyfish's fluorescence was purified, constructed into an expression vector and expressed in E. coli and C. elegans. Martin Chalfie, Osamu Shimomura, and Roger Y. Tsien together were awarded the 2008 Nobel Prize in Chemistry for their discovery and development of the green fluorescent protein.

## 1.3 DIFFUSION: THEORETICAL MODELS

The first recorded observations of diffusion extend as far back as 60 BC. The Roman poet and philosopher Lucretius described the motion of dust particles in his scientific poem, De rerum natura (On the Nature of Things). "...their dancing is an actual indication of underlying movements of matter that are hidden from our sight..."[33]

In 1828 Robert Brown, a botanist, observed pollen grains suspended in water, visible with his microscope, perform a sort of dance [34]. At first Brown suspected that this movement was some sort of life process. However, with more careful observations he found that the motion of the pollen never stopped. If in fact this motion were a life process, eventually the small pollen grains would run out of food and movement would cease. Taking these observations one step further he looked at soot in the same manner. He even went as far as to look at ground-up bits of the Sphinx [35]! For all of these similar-sized particles in water at the same temperature the motion was always the same . In the end, the motion of these particles had nothing to do with life. The dance-like movement that Brown observed was the result of constant collision between the grains of pollen and water molecules being agitated by their thermal motion. This random motion of particles suspended in a liquid or gas due to thermal energy has thusly been coined Brownian motion, or rather normal diffusion. Diffusion is very important in cells. It is how many molecules find each other to complete certain tasks and even how bacteria finds its food [36].

### 1.3.1 *The random walk*

We will start with a simple example of a one-dimensional random walk. Consider a particle (the random walker) starting at a site, $x = 0$, Fig. 1.3. We can describe the movement of our particle as jumps of distance, $l$ either to the right or left with equal probability. The jumps are i.i.d. After one jump the walker will be located at $\pm l$. Where will the walker end up after several jumps, potentially it could end up very far from its origin at $x = 0$? We can calculate this easily

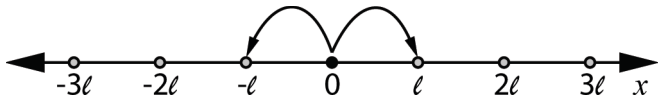


Figure 1.3: *One dimensional random walk* The random walker starts at $x = 0$ and moves either to the left or to the right with equal probability such that after one step its new location is $\pm l$.

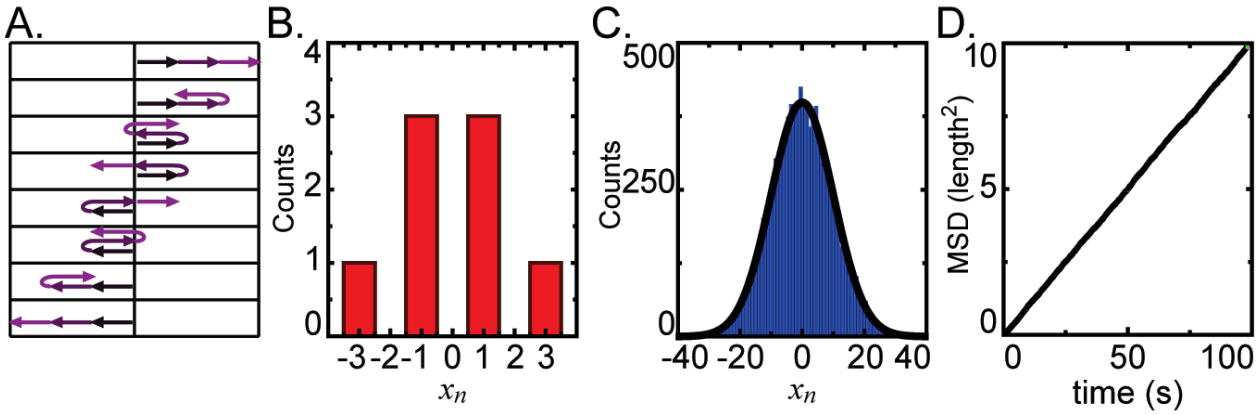


Figure 1.4: *The random walker* (A) For a walker allowed to take $n = 3$ steps these are the $2^n = 8$ possible outcomes. Each row depicts a possible trajectory of the walker. (B) Histogram plot of the distance traveled by the walker in each scenario in (A). (C) Repeat of the histogram plot in (B) only now the walker is allowed $n = 40$ steps and 10,000 possible outcomes. The average distance moved by the walker is zero, $\langle x_n \rangle = 0$. (D) MSD, ($\langle x_n^2 \rangle$) of the same walker described in (C).

enough by summing the contributions to the particle's overall trajectory made with each jump, $j_i = \pm l$,

$$x_n = \sum_{i=1}^{n} j_i. \tag{1.7}$$

Fig. 1.4A shows all the possible walks for $n = 3$. Each example in Fig. 1.4A can be regarded as a trajectory. Lets consider all $2^n$ possible trajectories, and find $\langle x_n \rangle$,

$$\langle x_n \rangle = \left\langle \sum_{i=1}^{n} j_i \right\rangle = \sum_{i=1}^{n} \langle j_i \rangle = \sum_{i=1}^{n} 0 = 0. \tag{1.8}$$

So the $\langle x_n \rangle = 0$, which is made apparent in Fig. 1.4B and C. Fig. 1.4B shows the count of our walker for $n = 3$ and $2^n = 8$ trials, while Fig. 1.4C shows the displacement of the walker for $n$ =40 and 10,000 trajectories. But we know, as seen in Fig. 1.4A that the walker does indeed move! What this example shows us is that the probability of the walker ending up where it started is small for large $n$. However we can still gather information from the displacement of the walker.

Lets now consider a more useful average. Instead of the mean displacement we'll calculate the mean squared displacement (MSD), $\langle x_n^2 \rangle$.

$$\begin{aligned}\left\langle x_n^2 \right\rangle &= \left\langle \left( \sum_{i=1}^{n} j_i \right)^2 \right\rangle && (1.9)\\ &= \left\langle \sum_{i=1}^{n} \sum_{k=1}^{n} j_i j_k \right\rangle \\ &= \sum_{i=1}^{n} \left\langle j_i^2 \right\rangle \\ &= nl^2 && (1.10)\end{aligned}$$

Because, given that the jumps are i.i.d., $\langle j_i j_k \rangle = \langle j_i^2 \rangle \delta_{i,k}$. If each jump were to occur at a regularly spaced time interval $\Delta t$, then the particle will make $n = {}^{t}/_{\Delta t}$ random jumps. We define the diffusion constant to be $D = {}^{l^2}/_{(2\Delta t)}$. The generalized MSD then becomes:

$$\left\langle r^2 \right\rangle = 2dDt \tag{1.11}$$

where $r$ is the displacement of the particle and $d$ is the lattice dimension. We can see from Eq. 1.11 that the MSD grows linearly with time, Fig. 1.4D.

The MSD can also be calculated from the probability density of displacements, $P(\boldsymbol{r}, t)$, that is the probability that the walker is displaced to $\boldsymbol{r}$ after time $t$ (i.e. the propagator)

$$\left\langle r^2(n) \right\rangle = \int r^2 P(\boldsymbol{r}, t)\, d^d \boldsymbol{r}. \tag{1.12}$$

For our one-dimensional random walker $P(x, t)$ is straightforward to calculate. Jumps to the right occur with probability $p$ and jumps to the left $1 - p$. The walker's displacement if it moved $m$ steps to the right and $t - m$ steps to the left is then $x = m - (t - m) = 2m - t$. This probability is given by a binomial distribution:

$$p(m, t) = \begin{pmatrix} t \\ m \end{pmatrix} p^m (1 - p)^{t-m}. \tag{1.13}$$

The probability of jumping to the left or right is equal, $p = 1/2$. Substituting this into Eq. 1.13, using the Sterling approximation[2] $t! \cong (2\pi t)^{1/2} (t/e)^t$, and $x \ll t$,

$$P(x,t)\,dx \cong \frac{1}{(2\pi t)^{1/2}} e^{-x^2/(2t)} dx, \tag{1.14}$$

a Gaussian distribution, shown in Fig. 1.4B and C.

The case may be however, that we are interested in a more general derivation of the probability of $\boldsymbol{r}$ after $n$ steps, $P_n(\boldsymbol{r})$. To do this we will use the method of characteristic functions. Consider a walk that starts at the origin in a continuous space (so that the particle's positions are not confined to the lattice space), $R^d$, whose steps come from the probability density $p(\boldsymbol{r}')$. The characteristic function of the probability density is

$$P(\boldsymbol{k}) = \int P_n(\boldsymbol{r})\, e^{i\boldsymbol{k}\cdot\boldsymbol{r}} d^d\boldsymbol{r}, \tag{1.15}$$

the Fourier transform of $P_n(\boldsymbol{r})$. In the same manner the characteristic function of the probability density of steps is

$$\lambda(\boldsymbol{k}) = \int p(\boldsymbol{r\prime})\, e^{i\boldsymbol{k}\cdot\boldsymbol{r}'} d^d\boldsymbol{r}'. \tag{1.16}$$

Note that

$$\lambda(0) = \int_{-\infty}^{\infty} p(\boldsymbol{r})\, d\boldsymbol{r} = 1, \tag{1.17}$$

following from the definition and normalization of $p(\boldsymbol{r})$. Recall that the steps are independent. Thus thee process obeys the Markov property

$$P_{n+1}(\boldsymbol{r}) = \int P_n(\boldsymbol{r}')\, p(\boldsymbol{r} - \boldsymbol{r}')\, d^d\boldsymbol{r}', \tag{1.18}$$

making it a Markov process. The Fourier transform of Eq. 1.18 is

$$P_{n+1}(\boldsymbol{k}) = P_n(\boldsymbol{k})\, \lambda(\boldsymbol{k}). \tag{1.19}$$

2 Sterling's Approximation: $n! = \sqrt{2\pi n} n^n \exp(-n)$

It can be seen that Eq. 1.19 is a recursive relation yielding,

$$P_n(\boldsymbol{k}) = \lambda(\boldsymbol{k})^n. \tag{1.20}$$

We can obtain the probability density, $P_n(\boldsymbol{r})$ from the inverse transform of $P_n(\boldsymbol{k})$

$$P_n(\boldsymbol{r}) = \frac{1}{(2\pi)^d} \int P_n(\boldsymbol{k}) e^{-i\boldsymbol{k}\cdot\boldsymbol{r}} d^d\boldsymbol{k}. \tag{1.21}$$

Because the characteristic function of a distribution stands as a generating function of its moments we can easily find the MSD (the second moment) from here.

Lets take the example of a Gaussian step probability density in one-dimension with zero mean and finite variance,

$$p(x) = \frac{1}{\sqrt{2\pi\sigma^2}} e^{-x^2/2\sigma^2}, \tag{1.22}$$

with

$$\int xp(x)\,dx = 0 \quad \text{and} \quad \int x^2 p(x)\,dx = \sigma^2 < \infty\ . \tag{1.23}$$

The step characteristic function, $\lambda(k)$ , using Eq. 1.16 is then

$$\lambda(k) = e^{-\sigma^2 k^2/2}, \tag{1.24}$$

so that, from Eq. 1.20, $P_n(k) = e^{-n\sigma^2 k^2/2}$. Taking the inverse Fourier transform of $P_n(k)$ we obtain the propagator (Eq. 1.21),

$$P_n(x) = \frac{1}{\sqrt{2\pi n\sigma^2}} e^{-x^2/2n\sigma^2}. \tag{1.25}$$

We can write Eq. 1.25 in terms of time,

$$t = n\tau,$$

where $\tau$ is the step time unit,

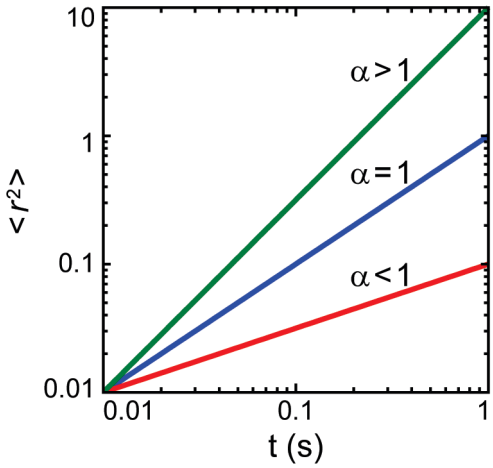


Figure 1.5: *Deviation from normal diffusion* The MSD as a function of time for super diffusion, $\alpha > 1$ (green), normal diffusion $\alpha = 1$ (blue) and subdiffusion $\alpha < 1$ (red).

$$P(x,t) = \frac{1}{\sqrt{4\pi D t}} e^{-x^2/4Dt}, \tag{1.26}$$

where $D = \sigma^2/2\tau$ is the diffusion constant. This result is essentially the same probability density we found in Eq. 1.14, apart from the normalization factor of $(4\pi D t)^{-1/2}$.

### 1.3.2 *Deviations from normal diffusion*

There are often many instances where a particle's motion is hindered. Diffusion processes that deviate from Brownian motion are considered anomalous. Anomalous diffusion has been experimentally observed in the cell membrane of a variety of different cell lines by an assortment of techniques, including single-particle tracking described in Section 1.2.1. With anomalous subdiffusion the MSD is non-linear with time, Eq. 1.27.

$$\left\langle r^2 \right\rangle \sim \Gamma t^{\alpha} \tag{1.27}$$

where $\alpha$ is the anomaly exponent. These deviations from Brownian motion can be due to a number of combinations of events such as active transport, transient binding, confinement, tethering, and/or the partitioning of membrane domains; the first event resulting in super-diffusion ($\alpha > 1$)

and the latter four events leading to anomalous subdiffusion ($\alpha < 1$). Note that $\alpha = 1$ is normal diffusion, Fig. 1.5.

Anomalous subdiffusion is not limited to cells and plasma membranes. Occurrences of anomalous subdiffusion have been observed in a variety of different systems, both organic and inorganic. Charge carrier transport in amorphous semiconductors [37, 38, 39, 40, 41, 42, 43] and controlled dynamics of bulk-surface exchange in porous glasses [44, 45, 46] are a couple of examples of inorganic subdiffusion. Anomalous subdiffusion is also observed in one, two and even three dimensional spaces. For instance, in 1D the dynamics of a polymer through a pore in a membrane [47, 48], the 2D motion of a transmembrane protein in the plasma membrane [49, 50, 51, 52], and the 3D diffusion of a molecule in the cell cytoplasm [53] and in Cajal bodies [54].

Three popular models for anomalous subdiffusion are provided in this section. First the continuous time random walk (CTRW) is presented. This model describes the effect of transient immobilization due to temporary binding. Next diffusion on a percolation cluster is discussed. This model effectively describes diffusion through a crowded, obstructed area. Lastly fractional Brownian motion is described.

*Continuous time random walk*

The CTRW model describes a non-stationary process. It was originally formulated by Montroll and Weiss [55] in 1964 and more recently described and summarized nicely by Klafter and Sokolov [35] and ben-Avraham and Shlomo Havlin [56]. Examples drawn from these two sources are reproduced here to describe the CTRW model.

In brief: The random walker moves from one site to another the same as our Brownian walker. However the walker has a modified time scale. Before each new jump the walker waits a certain time, $t$ that follows a probability density function (PDF) of waiting times, $\psi(t)$. Fig. 1.6 gives a schematic representation of this sort of walk on a square lattice. Here the walker moves from lattice point to lattice point randomly. However, at each step it waits a certain amount of time, represented by the circle (i.e. the larger the circle the longer the walker waits before taking the next step). If we were to plot the sizes of all of these circles the distribution of sizes is analogous

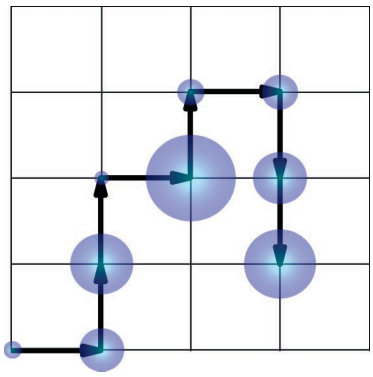

Figure 1.6: *CTRW schematic* Schematic representation of a CTRW on a square lattice. At each site the walker has equal probability of moving to the left, right, up or down, just as in a two-dimensional random walk. However, at each site the walker has to way a certain amount of time (represented by the size of the circles) before it can move on to the next site. The smaller the circle, the less time the walker waits before moving, the larger the circle, the longer it waits. The distribution of circle sizes would be the waiting-time distribution for that particular walk.

to the waiting time distribution. It can be seen then that the main parameter defining the walk is the distribution of waiting times.

We begin with a random walk on a lattice that starts at the origin, *but* the steps are taken at random times given by the probability density of waiting times, $\psi(t)$. We define the waiting times for different jumps as statistically independent and to be characterized by $\psi(t)$. The probability that the waiting time between steps is greater than $t$ is

$$\Psi(t) = \int_t^\infty \psi(t')\, dt' \tag{1.28}$$

We define $\psi_n(t)$ as the probability density that the $n^{\text{th}}$ jump occurs at time $t$. Similarly to Eq. 1.18, because the waiting times between steps are independent

$$\psi_{n+1}(t) = \int_0^t \psi_n(t')\, \psi(t-t')\, dt'. \tag{1.29}$$

Also, $\psi_1(t) = \psi(t)$. Note that the waiting times are all non-negative values allowing us to make use of the Laplace transform

$$\hat{\psi}(s) = \int_0^\infty \psi(t)\, e^{-st} dt. \tag{1.30}$$

Taking the Laplace transform of Eq. 1.29

$$\hat{\psi}_n(s) = \hat{\psi}(s)^n, \tag{1.31}$$

and similarly for Eq. 1.28,

$$\hat{\Psi}(s) = \frac{1 - \hat{\psi}(s)}{s}. \tag{1.32}$$

From the probability density of the position of a walker at time $t$ we can translate from steps into time,

$$P(x,t) = \sum_{n=0}^{\infty} P_n(x)\,\chi_n(t). \tag{1.33}$$

Here, $\chi_n(t)$ is the probability of the walker taking $n$ steps up to time $t$. Taking the Laplace transform, followed by the Fourier transform we obtain

$$P(k,s) = \sum_{n=0}^{\infty} P_n(k)\,\chi(s) = \frac{1-\psi(s)}{s} \sum_{n=0}^{\infty} \lambda^n(k)\,\psi^n(s). \tag{1.34}$$

The geometric series can be summed resulting in:

$$P(\boldsymbol{k},s) = \frac{1-\psi(s)}{s} \frac{1}{1-\lambda(\boldsymbol{k})\,\psi(s)}, \tag{1.35}$$

the Fourier-Laplace transform of the probability density of finding the walker at position $\boldsymbol{r}$ at time $t$.

If we were to first suppose that all the waiting times are equal $\psi(t) = \delta(t-\tau)$ ($\tau$ is a constant) each step will wait the same amount of time before the next step. With this distribution of waiting times we obtain a random walk as described in Section 1.3.1. In the case of diffusion in the plasma membrane (a key interest in this dissertation) this is a rare situation. Upon the introduction of any disorder, seen with the waiting time PDF, the walk becomes a much more complicated process.

Let's next consider an exponential distribution of waiting times, $\psi(\tau) = \frac{1}{\tau}\exp^{-t/\tau}$. As time passes for the walker in this case the probability of becoming stuck for a long time does not grow. Using this transform lets us more easily compute the MSD in the Laplace domain for this case. The Laplace transform of this waiting-time PDF is

$$\psi(s) = \frac{1}{1+s\tau} \tag{1.36}$$

The second moment of the characteristic function is the MSD. In general the $n$th moment in the Fourier domain is given as:

$$M_n(t) = (-i)^n \left.\frac{d^n P(k,t)}{dk^n}\right|_{k=0},$$

and in the Laplace domain

$$\begin{aligned} M_n(s) &= \int_0^\infty M_n(t)\, e^{-st} dt = (-i)^n \left.\frac{d^n P(k,s)}{dk^n}\right|_{k=0} \\ M_2(s) &= -\left.\frac{d^2 P(k,s)}{dk^2}\right|_{k=0} = -\left.\frac{1-\psi(s)}{s}\frac{d^2}{dk^2}\frac{1}{1-\lambda(k)\,\psi(s)}\right|_{k=0} \\ &= \frac{\psi(s)}{s\left[1-\psi(s)\right]}\left\langle l^2\right\rangle + \frac{2\psi^2(s)}{s\left[1-\psi(s)\right]^2}\left\langle l\right\rangle^2. \end{aligned} \tag{1.37}$$

We use the Fourier-Laplace transform PDF in Eq. 1.35 and the fact that $\lambda(0) = 1$. We also define $\left\langle l\right\rangle = \int_{-\infty}^{\infty} x p(x)\, dx$ and $\left\langle l^2\right\rangle = \int_{-\infty}^{\infty} x^2 p(x)\, dx$. These are the first and second moments of the displacement of one step. In the case of a symmetric CTRW the second term in Eq. 1.37 vanishes,

$$\begin{aligned} M_2(s) = \left\langle x^2(s)\right\rangle &= \frac{\psi(s)}{s\left[1-\psi(s)\right]}\left\langle l^2\right\rangle \\ &= \left\langle l^2\right\rangle \frac{\frac{1}{1+s\tau}}{s\left[1-\frac{1}{1+s\tau}\right]} \\ &= \left\langle l^2\right\rangle \frac{1}{s^2\tau} \end{aligned} \tag{1.38}$$

Applying an inverse Laplace transform we get,

$$\left\langle x^2(t)\right\rangle = \frac{\left\langle l^2\right\rangle t}{\tau} \tag{1.39}$$

It is important to notice the linear dependence the MSD has on time. So long as the first and second moment of the waiting time PDF exist this will always be the case.

What is the case then when the first moment does not exist for the waiting-time distributions? One such example is a power law distribution of waiting times, $\psi(t) \sim t^{-1-\alpha}$. Consider a heavy-tailed waiting-time distribution,

$$\psi(t) = \frac{\alpha}{\Gamma(1-\alpha)} \frac{\tau^{\alpha}}{t^{1+\alpha}}, 0 < \alpha < 1 \tag{1.40}$$

With this distribution of waiting times the probability of getting trapped for a long time increases as time passes. This is an important difference from the exponential waiting-time distribution and is what makes distributions with no first moment (such as the power-law distribution) so special. The MSD for the power law distribution of waiting times does *not* grow linearly with time as with the exponential distributed waiting times. Instead the MSD grows as

$$\left\langle x^2(t) \right\rangle \propto t^{\alpha} \tag{1.41}$$

Immobilization due to temporary binding can give rise to the sort of heavy-tailed waiting time distributions described above leading to anomalous subdiffusion [42]. This has been observed experimentally by several groups in live cells [49, 57, 58].

*Diffusion on percolation clusters*

Fractals are everywhere in nature. In fact, natural objects are more likely than not to be fractals[3]. One of the most well understood and important phenomena that gives rise to natural fractals is percolation. Percolation is important due to is ability to model phase transitions and yet be understood and formulated with simple geometrical concepts [56]. The examples provided here in order to explain diffusion on percolation clusters are derived from the work of ben-Avraham and Havlin [56].

Let's begin by considering a square lattice (i.e. Fig. 1.7A). Each bond of the lattice has a probability of being present $p$ or absent $1-p$. When the probability of the bonds being present $p$ is small one can imagine that there is a small number of clusters with connected bonds, Fig. 1.7B. However, as we increase $p$ the size of these clusters grows. This will continue until we reach a

3 "Clouds are not spheres, mountains are not cones, coastlines are not circles, and bark is not smooth, nor does lightning travel in a straight line."[59]

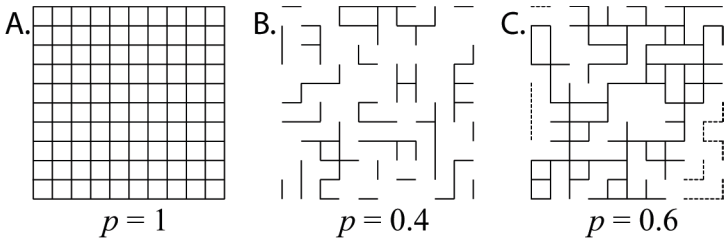


Figure 1.7: *Percolation* (A) Lattice with probability of bonds being present $p = 1$. (B) Lattice with probability of bonds being present $p = 0.4$ and (C) $p = 0.6$. Notice how the clusters of connected bonds grows as $p$ increases. The lattice in (C) has a concentration that is equal to the critical concentration for percolation. Here a cluster spanning from one edge to the other is shown in bold and the non-spanning clusters with dotted lines.

point that a cluster of connected bonds exists that spans from one edge of the lattice to the other edge, Fig. 1.7C. When the size of our lattice is infinite the concentration of connected bonds that creates this condition is called the critical threshold. Namely,

$$p = p_c \tag{1.42}$$

Below the critical threshold the clusters are finite and have a fractal dimension of

$$d_f = d - \beta/\nu \tag{1.43}$$

When the concentration reaches criticality, Eq. 1.42, a developing infinite percolation cluster forms along with other finite clusters. The infinite cluster can be described as a random fractal. The dimension of the fractal is given by Eq. 1.43. Once the concentration is pushed above criticality, $p > p_c$ the system still contains the infinite cluster and finite clusters with the same fractal dimension $d_f$ described above. However, the infinite cluster changes when the concentration is pushed beyond the critical threshold. At distances shorter than the correlation length $\xi(p)$, where $\xi \sim |p - p_c|^{-\nu}$, the cluster resembles a fractal. When the distances are larger than $\xi(p)$ the cluster acts as a regular space.

With these characteristics we can explain diffusion in percolation clusters as diffusion in fractals [56]. This type of diffusion can be envisioned as a 'blind ant' wandering through a maze, with each connected bond being a wall the ant cannot pass through. When $p > p_c$ the infinite cluster is homogenous at long length scales therefore diffusion is normal[4]. When the system reaches the critical threshold, Eq. 1.42, diffusion is anomalous due to the self-similarity of the infinite

4 This applies in the long-time asymptotic limit with the fractal dimension of the walk, $d_w = 2$.

cluster at all length scales (again with the fractal dimension of the walk, $d_w = 2$). Below criticality the walker is limited by the finite size of the clusters. Therefore the MSD is dependent on the correlation length, $\left\langle x^2(t) \right\rangle \sim \xi(p)^2$ in the limit $t \to \infty$. Generally speaking, so long as the mean displacement of the walk is smaller than the span of the cluster the MSD is

$$\left\langle r^2(t) \right\rangle \sim t^{2/d_w} \tag{1.44}$$

The relation of this model to diffusion in the cell membrane is quite direct. When there are no obstacles[5] to hinder the walker diffusion is normal. As the concentration of obstacles increases diffusion transitions from anomalous at short time scales to normal at long time scales. As the concentration is pushed to the percolation threshold this crossover from anomalous to normal diffusion is also pushed to longer and longer times, making the walk more anomalous. When the concentration is equal to the percolation threshold the crossover time becomes infinite [60]. This means that diffusion on a percolation cluster ($p = p_c$) is anomalous at all time scales. Going back the our "blind ant" wandering through a maze, one can perceive that the ant will run into many dead-ends causing it to turn back on its path and re-walk a certain area several times before being able to escape. In the case of proteins on the cell surface this is a very important aspect. In order for many cellular events to take place two different molecules must find each other, sometimes even more than once. The retracing of steps enforced by diffusion on a percolation cluster induces the molecules to search an area more thoroughly allowing molecules within a close vicinity to find each other much more quickly [61].

*Fractional Brownian motion*

Crowding is often a reality in cellular environments. Some work has proposed that crowding leads to viscoelastic properties that result in long-time correlations in the trajectory of a particle. This scenario can be modeled by fractional Brownian motion (FBM) [62, 60]. However, the physical mechanism regarding crowding is not fully understood in terms of the FBM model. FBM is a generalization of Brownian motion. With FBM the noise is correlated. This correlation is described by the Hurst exponent $H$, $0 < H < 1$, where $H = 1/2$ is normal diffusion.

5 Obstacles include immobile objects, both in the sense of things not moving at all and things moving much more slowly than the walker. Both cases appear immobile and present themselves as obstacles to the walker.

Let $B(t)$ be ordinary Brownian motion. Following the definition of Mandelbrot and Van Ness [62] the definition of FBM is

$$\begin{aligned} B_H(t) &= \frac{1}{\Gamma(H+1/2)}\left[\int_{-\infty}^{0}\left(|t-s|^{H-1/2}-|s|^{H-1/2}\right)dB(s)\right. \\ &\quad \left.+\int_0^t |t-s|^{H-1/2}\,dB(s)\right] \end{aligned} \tag{1.45}$$

An importantly unique property of FBM is that it is $H$-self similar. While FBM is not stationary itself, its increments are stationary [63]. The sequence of increments of FBM are very strongly correlated:

$$b_H(j) = B_H(j+1) - B_H(j) \tag{1.46}$$

The autocovariance of the increments, $b_H(\cdot)$, satisfies

$$\begin{aligned} r(j) &= E\left(b_H(j)\,b_H(0)\right) \\ &\sim \sigma^2 H(2H-1)\,j^{2H-2} \end{aligned}$$

as $j \to \infty$ [64]. The MSD for FBM is also sublinear in time [65],

$$\left\langle x^2(t)\right\rangle \propto t^{2H} \tag{1.47}$$

thus for $H < 1/2$ subdiffusive dynamics are observed.

## 1.4 REVIEW OF EXPERIMENTAL OBSERVATIONS IN LIVE CELLS

While advances in microscopy have provided tools for studying individual molecules *in vivo*, the difficulties of these measurements still remain. There are many uncontrollable variables in live cell experiments that can not be avoided, such as: variability from cell to cell due to different states within the cell cycle, the size of cells places a threshold on the accessible length scale, mutant or artificial probes may cause an altered artifactual cellular response. Additionally to these inherent traits of living cells, it is very difficult, if not almost impossible to probe a single event

or protein. The movement of proteins and transport of cargo within a cell is a concerted effort with many different players. For example, current research suggests that kinesin an anterograde specific motor, and dynein a retrograde specific motor team together to move cargo bidirectionally within the cell, either through concerted efforts or in a 'tug-of-war' fashion [66, 67, 68]. It has also been shown, experimentally and theoretically, that a mixture of passive and active diffusion often occurs with cargo [69, 70] where motor proteins facilitate active transport [71] and cytoplasmic flows induced by cytoskeletal networks generate passive transport [72, 73]. Also, DNA/RNA binding proteins such as transcription factors [74, 75], experience a mixture of sliding and hopping in order to more quickly find target sequences along the nucleic acids [76, 77, 78, 79]. It can quickly be seen that simple classification of anomalous or normal diffusion is often times not enough, as there is most oft a mixture of several different systems resulting in a complexity that must be carefully sorted through. While this may seem a logical conclusion, often times only one model for anomalous diffusion is chosen to explain experimental results. Not until recently has the combination of theoretical models been used to describe the motion of cellular components accurately [49], this is described in more detail in Chapter 4.

An important feature to consider when attempting to classifying diffusion is the spatio-temporal scale. For instance, a particle may be undergoing normal diffusion on one scale and anomalous diffusion on another scale. One example is the instance of caged diffusion where a particle is retained within compartments such as the cytoskeletal network. On the short time scale (or small length scale) the particle displays normal diffusion. Within this length of time the particle does not reach the boundaries of the compartment and thereby does not appear to be confined. However as the time scale is lengthened the particle interacts with the boundaries of the compartment and consequently anomalous subdiffusion is observed. The particle is not indefinitely confined within a compartment, and can escape from one compartment to be caught into another compartment. If the time scale (or length scale) is long enough, this hopping from one compartment to the next will appear as normal diffusion, at a much slower rate than before. The crossover from one diffusion regime to another may be observed through the MSD,

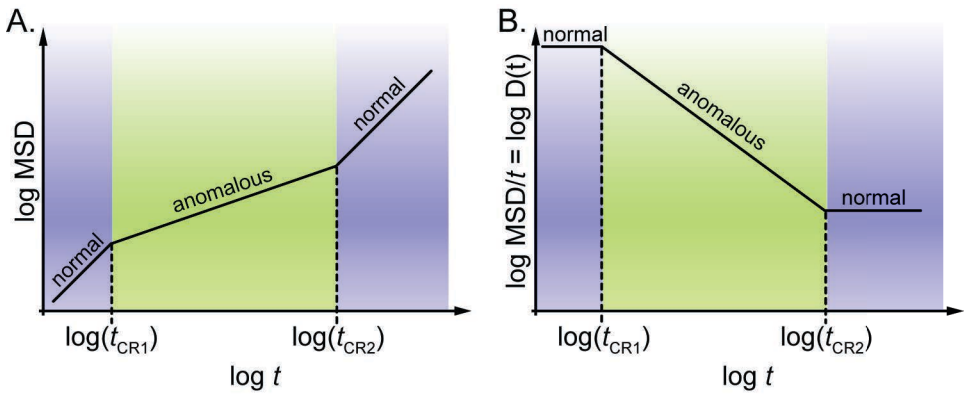


Figure 1.8: *Crossover diffusion* (A) Schematic MSD displaying the crossover from normal to anomalous and then back to normal diffusion. As in Eq. 1.48 the normal diffusion regimes go as $t$ and the anomalous regimes as $t^{\alpha}$. (B) Schematic of the time dependent diffusion coefficient, $D(t) = \langle r^2(t) \rangle / t$.

$$\langle r^2 \rangle \propto \begin{cases} t & \text{for } t \ll t_{CR1} \\ t^{\alpha} & \text{for } t_{CR1} < t < t_{CR2} \\ t & \text{for } t \gg t_{CR2} \end{cases} . \tag{1.48}$$

This crossover from normal to anomalous and back to normal diffusion has been described thoroughly by Saxton [80, 81] and others [82, 83] and is schematically shown via the MSD in Fig. 1.8A and the time-dependent diffusion coefficient, $\langle r^2(t) \rangle / t = D(t)$, in Fig. 1.8B. It has also been observed experimentally by Kusumi [84] as well as in our lab. The diffusion of cargo transport also sees a crossover from passive to active transport in a similar manner. In short distances the movement of the cargo is slow and diffuses normally. However on a larger length scale the motion of the cargo is directed and superdiffusive ($\alpha > 1$), as it is driven by molecular motors [85, 86].

Next a compilation of experimental results will be covered along with the characterization of the diffusion within that system. First research in the cytoplasm and nucleoplasm will be presented, followed by investigations in cellular membranes. An extensive amount of work studying lipid granules in fission yeast, *Schizosaccharomyces pombe* (*S. pombe*), has been carried out by Tolić-Nørrelykke, Oddershede and Metzler *et al* [87, 88, 89, 90]. Lipid granules are fat storages inside cells and provide a very nice, inert probe to investigate the diffusion properties in the cytoplasm of living cells. Extensive work was performed over a decade using both optical tweezers and video microscopy by this group to measure the motion of lipid granules in *S. pombe* across sev-

eral orders of magnitude in time (from the μs regime to minutes). The authors are able to show that at short times (in the ms range) the data is best described by a CTRW with a truncated power-law waiting time distribution, displaying weak ergodicity breaking. However, contrastingly at the longer times the motion of these lipid granules is found to be best modeled by FBM. The authors have not been able to resolve a model that is consistent with the data at all time scales.

Other groups have investigated the motion of fluorescently labelled mRNA macromolecules [61], GFP-labelled chromosomal loci in *E. coli* and *Caulobacter crescentus* [91] and telomeres in the nucleus of mammalian cells [57, 92] in order to probe the motion of molecules within the cytoplasm of living cells. All of these groups found the motion of these macromolecules to be subdiffusive. The work of Golding and Cox revealed that the motion of mRNA is subdiffusive with an exponent of $\alpha = 0.77 \pm 0.03$ over three orders of magnitude in time [61]. In nice agreement with Golding and Cox, Weber *et al*. showed that RNA proteins also exhibit subdiffusive behavior with a similar exponent, also over three orders of magnitude in time. The authors were also able to dismiss a CTRW scheme due to the coinciding time and ensemble averaged data. Instead they found their observations are most consistent with fractional Langevin motion [91]. Garini *et al*. have put together a nice body of work concerning the motion of fluorescently labeled individual telomeres in the nucleus of mammalian cells. They were able to acquire data over six decades in time by combining different acquisition methods, namely the combination of a charged coupled device (CCD) camera (fast 2D measurements) and a confocal setup (quicker 3D measurements) on the same microscope. The motion of the telomeres is seen to be anomalous up to 100 s and then crosses over to normal diffusion with the MSD exponent moving from $\alpha = 0.03$ to 1. Two different models are compared to interpret the data, a CTRW and various models of polymer dynamics. The authors find that the dynamics of the telomeres is consistent with a reptation model for a Rouse chain, a model describing the thermal motion of long, entangled ideal chain [57]. Later, using p-variation, displacement correlation, and ergodicity convergence the authors were able to eliminate CTRW as a possible model for the telomere mode of motion, suggesting that the data instead obeyed a fractional process [92].

As described in Section 1.1 the plasma membrane of cells is a highly complex and heterogenous landscape. There has been extensive, comprehensive work done with a multitude of membrane components including membrane proteins and lipid varieties in the plasma membrane. A thor-

ough review by Hölfling and Franosch [93] does a commendable job of summarizing the history of these experiments and their results. Many groups have used SPT to probe the dynamics of membrane components [84, 94, 95, 96] including work from our lab presented in succeeding chapters [49, 50]. Another popular technique to study the motion of membrane components is FCS and numerous groups have used this setup [97, 98, 99, 100]. In the work of Franosch *et al*. [101] FCS was used to measure the displacements of diffusing proteins over long times. A model membrane system was used with a lipid bilayer of SPOC and immobilized DPPE. The protein avidin irreversibly

binds to the DPPE lipid anchors and was fluorescently labeled. The immobilization fraction is controlled by the concentration of lipid anchors, thusly also controlling the surface coverage of avidin. The authors observe subdiffusive behavior with a crossover from normal to anomalous transport depending on the surface coverage (i.e. amount of crowding). Both a CTRW scenario and FBM are excluded based on the experimental results, and instead the anomalous diffusion is owed to motion in a percolating system. The main drawback to this system is also its biggest advantage, and that is the simplicity and control that a model lipid bilayer provides in comparison to the plasma membrane of live cells.

Espinoza *et al*. investigated the movement of the high affinity IgE receptor, FcεRI, labeled with QDs in mast cells using SPT [102]. They analyze the probability distribution of jump lengths and demonstrate the presence of corals ranging in size from a tens of nanometers to hundreds of nanometers. They show that the movement of IgE-FcεRI is restricted, as in diffusion on a fractal with a dimension $d < 2$. Investigations of the integral membrane protein aquaporin-1 revealed that this membrane protein displays normal diffusion across several microns, and on the scale of minutes [103]. QD-labeled aquaporin channels were imaged at frame rates up to 91 Hz for up to 6 minutes. In COS-7 fibroblast cells and Madin-Darby canine kidney epithelial (MDCK) cells Crane and Verkman found that > 75% and ~ 60% of the integral membrane protein aquaporins respectively diffused freely over 7 μm in 5 minutes. Upon cytoskeletal disruption with latrunculin B no effect was seen, however in protein de-enriched blebs the diffusion was increased by fourfold. In cholesterol depleted MDCK cells aquaporin-1 diffusion was significantly restricted arguing against the accumulation of aquaporin-1 in lipid raft domains. The authors conclude that

aquaporin-1 is a non-interacting protein displaying mostly Brownian motion, dependent on the concentration of obstructions.

Overall, there is an extremely large body of work that aims to elucidate the motion of molecules within the cell. These investigations encompass both three-dimensional studies within the cytoplasm and nucleoplasm of cells as well as two-dimensional research in the plasma membrane. A re-occurring theme among these results is deviations from normal diffusion within some spatio-temporal scale. While the topic of anomalous subdiffusion is extensively studied, understanding the underlying mechanism responsible for observed diffusional behavior has proved a difficult task due to the complexity and intricacy of intertwined cellular processes.

## 1.5 THE VOLTAGE-GATED POTASSIUM CHANNEL, KV2.1

We now shift to the main protein of interest in this dissertation, Kv2.1. Experimental techniques described in Section 1.2 combined with analysis described in Section 1.3 were used to study this protein channel.

The voltage-gated potassium channel is widely expressed in a number of tissues in mammals including: hippocampal neurons, pulmonary smooth muscle cells, cerebral artery smooth muscle, myocardium and pancreatic $\beta$-cells. In these cells Kv2.1 plays a prominent role in the regulation of excitability. These channels are also uniquely known to target to stable, micron sized cell surface puncta. The physiological importance of Kv2.1 is almost an exhaustive list and only a handful of examples are presented here. It encodes a slowly inactivating delayed rectifier current in the mouse heart and reduction of the current is responsible for long QT syndrome [104, 105, 106]. Kv2.1 regulates the membrane potential of pancreatic beta cells which thereby regulates insulin release [107, 108]. In cortical neurons Kv2.1 plays a role in apoptosis [109, 110] and in hippocampal pyramidal neurons it helps regulate somato-dendritic excitability [111]. Kv2.1 is also important in pulmonary artery vascular smooth muscle where it is responsible for the hypoxia-sensitive delayed rectifier current [112, 113, 114] and in cerebral circulation as well.

The Kv2.1 channel is tightly regulated, primarily by phosphorylation on the C-terminus. There are at least 15 different sites of phosphorylation on the C-terminus [115, 116]. We know that the C-terminus is necessary for cluster formation. Upon the removal of the last 318 amino acids of

the C-terminus the channel no longer forms cell surface puncta [117]. These clusters are regulated by several different stimuli resulting in declustering. This includes: glutamate treatment, $K^+$-induced depolarization [115], ionomycin treatment, muscarinic stimulation via treatment of carbachol, and chemically induced ischemia. All of these physiological stimuli increase cytoplasmic concentrations of $Ca^{2+}$and induce dephosphorylation. A shift in the membrane activation curve is also seen upon declustering. Together these collective observations suggest Kv2.1 clusters might serve as a neuro-protective order in hippocampal neurons [118, 119, 115].

Remarkably, although 97% of Kv2.1 channels on the cell surface reside within these microdomains, only the 3% of non-clustered channels are responsible for generating the high-threshold delayed rectifier currents indicative of Kv2.1 [120]. This suggests that perhaps Kv2.1 clusters have a non-traditional function, beyond the scope of membrane excitability.

## 1.6 OVERVIEW OF THIS DISSERTATION

The work presented in this thesis is focused on characterizing the movement of plasma membrane components, specifically the Kv2.1 channel. By trying to understand the underlying mechanisms of organization at the single molecule level, important information can be gained about the intricate network of cellular processes. Following this logic, studying the diffusion pattern of membrane components yields valuable information regarding membrane structure, organization, and dynamics. Single particle tracking is an excellent tool to probe these dynamics and is used to study membrane proteins and lipids and interactions with their surroundings. While it is often observed that the diffusion pattern of components in the membrane of live cells is anomalous, the underlying mechanisms that give rise to this diffusion pattern remain highly controversial.

We are investigating the dynamics of the voltage gated potassium channel, Kv2.1. Despite the clear physiological importance of Kv2.1 channels and exposed location dependence of channel function, the mechanisms underlying cluster formation and maintenance are still largely unknown. The work presented in this dissertation characterizes the diffusion pattern of Kv2.1 and determines alternate functional roles of surface clusters by investigating recycling pathways using single particle tracking in live cells. By understanding the physical mechanisms responsible

# CHAPTER 2: ERGODIC AND NONERGODIC PROCESSES COEXIST IN THE PLASMA MEMBRANE

Diffusion in the plasma membrane ofl iving cells is often found to display anomalous dynamics. However, the mechanism underlying this diffusion pattern remains highly controversial. In this chapter, we study the physical mechanism underlying Kv2.1 potassium channel anomalous dynamics using single molecule tracking. Our analysis includes both time series averages ofi ndividual trajectories and ensemble averages. We show that an ergodic and a nonergodic process coexist in the plasma membrane. The ergodic process resembles a fractal structure with its origin in macromolecular crowding in the cell membrane. The nonergodic process is found to be regulated by transient binding to the actin cytoskeleton and can be accurately modeled by a continuous-time random walk. When the cell is treated with drugs that inhibit actin polymerization, the diffusion pattern of Kv2.1 channels recovers ergodicity. However, the fractal structure that induces anomalous diffusion remains unaltered. These results have direct implications on the regulation of membrane receptor trafficking and signaling.

## 2.1 introduction

The plasma membrane is a highly complex system with a dynamic organization required to maintain many fundamental processes that include signal transduction, receptor recognition, endocytic transport and cell-cell adhesion. The study of the diffusion pattern of transmembrane proteins and lipids grants biophysical information on membrane organization, structure and dynamics. In particular, single molecule tracking provides insight into the interaction of membrane proteins with their surroundings. Stochastic molecular transport is described by the probability distribution of displacements and how it evolves over time. This distribution is called a propagator, and in the case of Brownian motion it is Gaussian. Diffusion processes that deviate from Brownian motion are considered anomalous and they involve propagators that may or may not be Gaussian. For example, diffusion in a fractal has a stretched Gaussian propagator [121].

Experimental and theoretical work suggests there is a correlation between macromolecular crowding and anomalous diffusion [122, 123, 101]. However, the mechanism behind hindered diffusion in living cells remains controversial. Several models have been proposed, including mem-

brane compartmentalization, receptor and cytoskeleton binding, and membrane heterogeneity (lipid rafts). Particle trajectories are frequently characterized by their MSD [124]. A Brownian particle in a two-dimensional space yields an MSD of $\left\langle \Delta r^2 \left( t \right) \right\rangle = 4Dt$. However, in many systems the MSD scales as a sublinear power law, indicating anomalous diffusion. In general $\left\langle \Delta r^2 \left( t \right) \right\rangle \propto t^{\gamma}$, where $\gamma$ is the anomaly exponent. Anomalous subdiffusion is manifested by a characteristic exponent $\gamma < 1$, and anomalous superdiffusion by $\gamma > 1$.

Two biologically relevant processes are recognized to induce anomalous subdiffusion in the plasma membrane: i) transient immobilization and ii) geometrical inhomogeneities. The former can be modeled by a CTRW with a heavy tailed waiting-time probability distribution function [125]. Besides giving rise to anomalous diffusion, a CTRW is nonergodic, in other words the temporal average of a long trajectory differs from the ensemble average [126, 127, 128]. Molecular crowding and fence-like structures are responsible for space inhomogeneities that can give rise to a hierarchy of cul-de-sacs in the molecule path. One well-known model of such a scenario is given by the percolation cluster, which may be regarded as a random fractal [56]. Diffusion on a fractal is a stationary process and thus ergodic. Both a CTRW and diffusion on a fractal have non-Gaussian propagators. A third anomalous diffusion model is FBM [62, 129, 89], characterized by long-time correlations. Contrary to the previously discussed models, FBM has a Gaussian propagator with a time-dependent diffusion coefficient. Different methods such as p variation tests for categorizing diffusion are emerging [130**?** ]. Currently these tests are still too simple to handle cases like the one presented here, where more than a single mechanism may be involved. Analysis of the propagator $P\left( r \right)$ can provide information on the anomalous behavior, but elucidating the underlying mechanism from the MSD or the propagator alone is an insurmountable task.

It is common to use the cumulative distribution function (CDF), ($CDF\left( r^2, t_{lag} \right) = \int_0^r P\left( r' \right) 2\pi r' dr'$ in two dimensions) to distinguish between normal and anomalous diffusion [131, 132]. Within this formalism, Brownian motion yields a single-exponential curve

$$CDF\left( r^2, t_{lag} \right) = 1 - \exp\left( -r^2 / r_0^2 \right) \tag{2.1}$$

where $r_0^2$ is the MSD in a time $t_{lag}$. On the other hand, assuming a two-component mobility leads to a double-exponential curve

$$CDF\left(r^2, t_{lag}\right) = 1 - \left[w \exp\left(-r^2/r_1^2\right) + (1-w)\exp\left(-r^2/r_2^2\right)\right] \tag{2.2}$$

where $r_1$ and $r_2$ are defined by the diffusion constants of the fast and slow mobility component respectively, $r_i^2 = 4D_i t_{lag}$, with fractions $w$ and $(1-w)$ [131]. This method gives minimal information about the diffusion process but it provides enough information to identify whether the diffusion pattern is normal or anomalous. Normal diffusion yields $w$ values close to 1 (or zero) in the biexponential fit, but when diffusion becomes anomalous, $w$ approaches 0.5.

Here we report studies on the membrane diffusion of the voltage-gated potassium channel Kv2.1 analyzed by single particle tracking. Our previous work suggests that clusters are formed by an actin-based mechanism that corrals mobile channels behind a diffusion barrier [133, 117]. We dually label the channels with GFP and QDs and track their position with nanometer accuracy using TIRF microscopy. We acquired 1,015 trajectories, many of them longer than 10 minutes, to allow the analysis and comparison of both time and ensemble averages. We studied the underlying mechanisms for the observed anomalous diffusion focusing our attention on the CTRW, diffusion on a fractal and a combination of both. Our findings show that Kv2.1 trajectories are best modeled by a CTRW in a fractal geometry. The implications of these processes are discussed. The CTRW is regulated by the actin cytoskeleton while the geometric inhomogeneities are consistent with macromolecular crowding.

## 2.2 METHODS

### 2.2.1 *Cell culture and transfection*

human embryonic kidney (HEK) 293 cells (American Type Culture Collection, passage 38-45) were cultured in Dulbecco's modified eagle medium (DMEM), supplemented with 10% fetal bovine serum (FBS), at 37˚C in a 5% $CO_2$ atmosphere. HEK cells were transfected with 0.5 µg/µL GFP-Kv2.1-BAD and 1.5 µg/µL BirA vectors 8.3 as described previously [117, 134] to express Kv2.1 channels labeled with GFP on the N-terminal domain. A biotin acceptor domain (BAD) for biotin ligase BirA was added to the extracellular region between S1 and S2 in order to tag channels with QDs. After electroporation, cells were plated on cover-glass-bottom culture dishes

(Bioptechs, Butler, PA) precoated with Matrigel (BD Biosciences, San Jose, CA). All cells were used for measurements within 24 hours of transfection.

### 2.2.2 *Total internal reflection microscope*

All images were acquired using an objective-type TIRF microscope. The microscope was home-built around an Olympus IX71 body. A 473 nm laser line with 2.5 mW of power after the objective (Olympus PlanApo 100x/1.45) was used as excitation source. A back-illuminated electron-multiplied charge coupled device (EMCCD) camera (Andor iXon DU-888) operated at -85˚C, with an electronic gain of 300 was used. Simultaneous two color imaging was achieved by optically splitting the image onto two halves of the camera, each corresponding to a separate color. Both the stage (Bioptechs, Butler, PA) and the objective were maintained at 37˚C. Movies (>5000 frames) were acquired using Andor IQ software at an average frame rate of 8 frames per second.

### 2.2.3 *Imaging conditions*

GFP-tagged Kv2.1 channels were labeled with QDs through a biotin-streptavidin biochemistry. Prior to imaging, the cells were rinsed six times with a dye-free imaging saline 8.6 to remove the media. The cells were incubated for 5 minutes in a 0.1 nM solution of streptavidin conjugated QDs (Qdot 655, Invitrogen, Carlsbad, CA) and 150 μM bovine serum albumin (BSA) (IgG- fatty-acid-free, Sigma-Aldrich) in imaging saline 8.4. Following incubation the cells were rinsed again 6 times with imaging saline to ensure the removal of any unbound QDs. During imaging, cells were maintained at 37˚C.

### 2.2.4 *Actin cytoskeleton disruption*

Actin depolymerizing drugs were used to disrupt the cytoskeletal network. Swinholide A (Sigma-Aldrich, St Louis, MO) was dissolved in DMSO and added during imaging experiments to the cells at a final concentration of 70 nM [133]. Cytochalasin D (Sigma-Aldrich, St Louis, MO) was dissolved in DMSO and added to the cells while imaging, at a final concentration of 20 nM. Cells were imaged up to 20 min after drug application. DMSO-only controls showed no evident effect on Kv2.1 clusters.

### 2.2.5 *Models for anomalous diffusion*

*Continuous time random walk*

A CTRW represents energetic disorder that may stem from transient binding [124**?** , 135]. In this model, a particle jumps between lattice sites, having a random waiting time at each site with a probability density that scales as $t^{-(\alpha+1)}$. The energy landscape of this process is distinguished by wells with a broad depth distribution that transiently trap the particle. This landscape yields an infinite characteristic waiting-time mean and a finite jump-length mean. Many different physical systems are described by CTRWs [136, 137, 138, 139, 140]. This behavior is nonergodic and it can only exist away from thermodynamic equilibrium. Despite the complexity of CTRWs, the cause for ergodicity breaking is fairly simple. Generally, a system exhibits ergodicity when the measurement time is long in relation to the characteristic time scale [126]. In the CTRW, the experimental time can never reach the characteristic time of the process because the mean waiting time is infinite. Therefore, time averages never approach the ensemble averages, independent of the experimental time. The ensemble-averaged MSD follows a power law $t^{\alpha}$, but the time-averaged MSD is linear, resembling Fickian diffusion [126, 127, 128]. However, the time-ensemble averaged MSD (TEA-MSD) (i.e. averaging over both time and ensemble) exhibits aging behavior [127, 128, 141].

*Diffusion on a fractal.*

Diffusion on a fractal resembles a random walk in an entangled labyrinth with the walker encountering dead ends on all length scales. Fractal geometries are found in a broad range of structures in nature, and thus the implications of diffusion in fractals are extensive [56, 142]. In the cell membrane a fractal structure may appear, for example, when macromolecular crowding reaches the percolation threshold [132, 143]. Fractals are characterized by a non-integer dimension $d_f$ and diffusion in a fractal is found to be subdiffusive with a critical exponent $\beta < 1$. This parameter is related to the fractal dimension of the walk $d_w$ by $\beta = {}^{2}/_{d_w}$ [56, 132, 144]. Intuitively, the dimension of a random walk in a plane is two dimensional. However, if $d_w > d_f$ then each site in the fractal is visited by the walker several times before moving on to explore a different

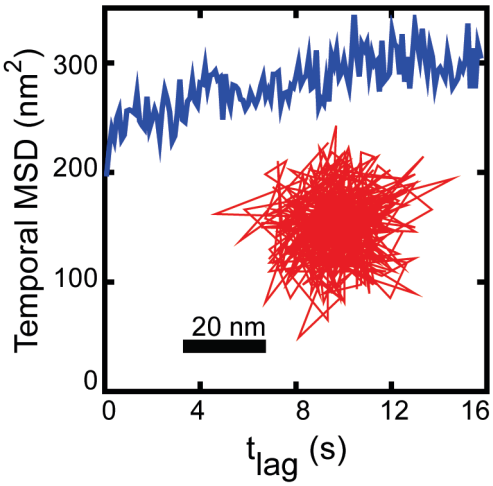


Figure 2.1: *MSD of bound QD on glass*MSD (blue) of a single QD bound to glass. The inset (red) shows the trajectory of the same dot.

region. As in the labyrinth analogy, the walker returns through the same path every time it hits a dead end.

## 2.3 RESULTS

### 2.3.1 *Kv2.1 diffusion pattern is non-Gaussian and nonergodic*

*Single Particle Tracking*

QDs enabled us to track individual channels, while GFP fluorescence provided characteristics of the clusters as an ensemble. QD labeling was carefully controlled so that QDs remained at low density to allow for individual particle tracking. QDs present advantages over fluorescent proteins both in signal to noise ratio and in the total time an individual tracer can be followed. We track single particles and analyze their trajectories using custom-written LabView codes, 5. For tracking, we manually select the position of the particles in the first frame and a 10x10 pixel region of interest (ROI) is created around each selected particle. The software fits a 2-dimensional Gaussian function to the particle [145, 23] using a Levenberg-Marquardt least squares algorithm. The image of individual QDs is set by the point spread function of our imaging system, in our case it has a standard deviation $s$ =150 nm. Subsequently, the code analyzes the following frame and the ROI surrounding each particle is automatically adjusted to follow the particle. We analyzed the absolute error in our system using QDs bound to glass. The position of the bound QD has a

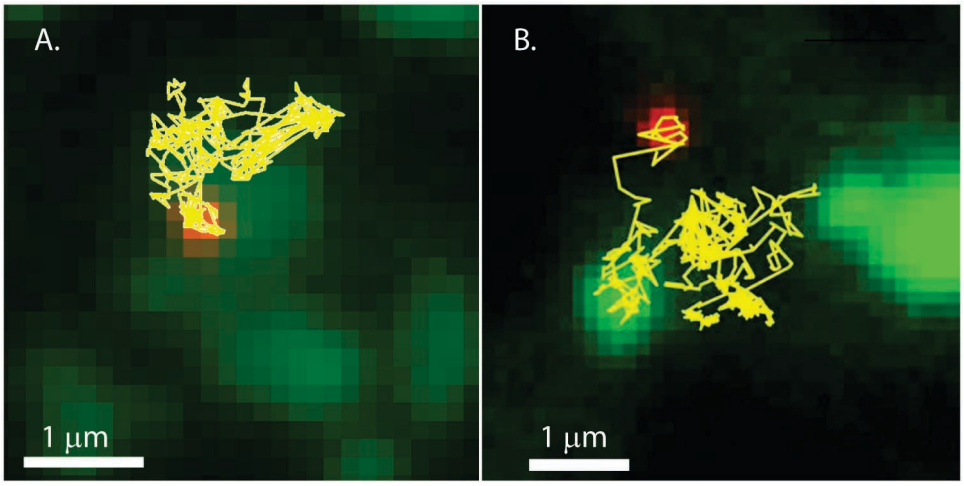


Figure 2.2: *Clustered and non-clustered Kv2.1 trajectory* Overlay image of GFP-tagged Kv2.1 clusters and individual QDs. Kv2.1 clusters are shown in green and QD-tagged channels in red. The trajectories of (A) a clustered and (B) a nonclustered (free) Kv2.1 channel are shown. Interestingly, the nonclustered channel ignores the compartment perimeters and the channel travels freely into and out of a cluster. Scale bars: 1 μm.

distribution with a standard deviation of $\sigma$ = 8 nm (Fig. 2.1) which corresponded to an average 350 photons collected within 80 ms exposure time [23]. To account for blinking behavior, only QDs with intensity above a predetermined threshold were used in the analysis, all other frames were discarded.

In order to optimize the algorithm, we have checked its reliability dependence on ROI size. As we reduce ROI size, the algorithm becomes faster but the accuracy starts to decrease when the ROI becomes smaller than 10 pixels. We have also compared the accuracy of Gaussian non-linear fittings vs. center of mass algorithms using a similar moving ROI strategy. Our center of mass algorithms were found to have worse accuracy than Gaussian fits with an additional 1 nm sem.

The MSD of each trajectory was calculated in LabView, 9.4.1, by averaging over all point pairs because it was previously found to yield more accurate results than averaging independent pairs [146].

Fig 2.2 shows two-color TIRF images of HEK cells expressing GFP-Kv2.1 channels, labeled with QDs. Representative QD trajectories are superimposed on the images. All Kv2.1 channels expressed in the cell are conjugated to GFP to provide information on cluster size and location. From GFP photobleaching step analysis [147] we find that Kv2.1 density is 15-70 molecules/$\mu m^2$ inside clusters. On the other hand, only one QD is present every 10 clusters. Two distinct channel

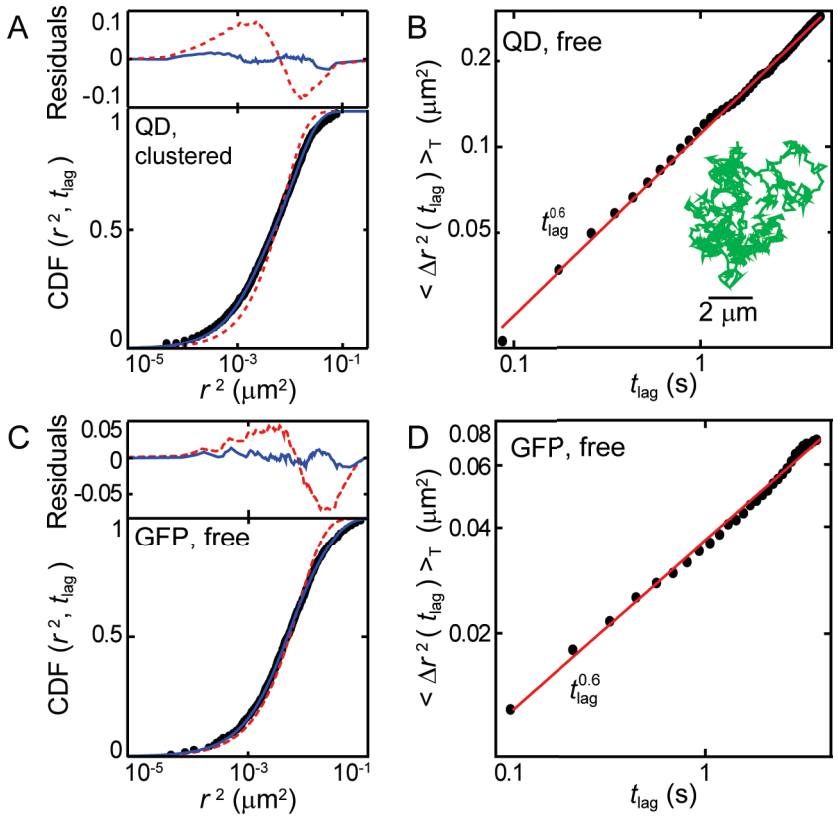


Figure 2.3: *Statistical analysis of both QD- and GFP-labeled channels* (A) Square displacement CDF of QD-tagged clustered channel. CDF data are fit to both a single- (dashed red line) and a double- (solid blue line) exponential curve, Eq. 2.1 and 2.2 respectively. (B) MSD of QD-tagged non-clustered channel. The inset shows the corresponding trajectory. (C) Square displacement CDF of GFP-tagged non-clustered channel (D) MSD of GFP-tagged non-clustered channel.

populations are observed, clustering and freely diffusing channels [133]. About 97% of the QDs remain confined to one cluster for the entire experimental time.

As control experiments we checked that non-clustered channels tracked through their QD or their GFP tags yield the same results as those obtained by tracking clustered QD-labeled channels. Fig. 2.3 shows temporal MSD and CDF data of representative trajectories of both GFP- and QD-tagged channels. Clearly the same behavior is observed for QD and GFP channels. Namely, the temporal MSD of non-clustered channels follows anomalous diffusion, which scales as $t^{\gamma}$, and the CDF fits to a double exponential curve.

*Distribution of square displacements.*

In order to determine whether channel diffusion is normal or anomalous, we constructed the CDFs of all trajectories at numerous time lags and fit the data to monoexponential or biexponential functions using an automated least squares algorithm in MATLAB [131, 94]. The starting point

of the MSD, CDF, and waiting time analysis is finding the square displacements. We have written automated software in LabView 9.4.1 to perform this task on each individual trajectory. First, we identify all intensity values below a threshold and discard those frames by replacing the X and Y coordinates with not-a-number (NaN) values. This addresses the problem of QD blinking and frames with low SNR. Then the square displacements $R^2$ for all $t_{lag} = mt_1$ are found:

$$R^2_{m,i,j} = \left(X_{i+m,j} - X_{i,j}\right)^2 + \left(Y_{i+m,j} - Y_{i,j}\right)^2 \tag{2.3}$$

where $i$ is the frame number of trajectory $j$.

The temporal MSD is found for each trajectory $j$,

$$\left\langle \Delta r^2 \left(t_{lag} = mt_1\right)\right\rangle_T = \frac{1}{M}\sum_i^{T/t_1} R^2_{m,i,j} \tag{2.4}$$

where $M$ is the total number of square displacements different from NaN and $T$ is the total averaging time.

The ensemble MSD is found at each frame $i$,

$$\left\langle \Delta r^2 \left(t_{lag} = mt_1\right)\right\rangle_T = \frac{1}{N}\sum_i^{N} R^2_{m,i,j} \tag{2.5}$$

where $N$ is the number of available trajectories (not NaN) at frame $i$.

The time-ensemble square displacement average in a total time $T$ at $t_{lag} = mt_1$ is

$$\left\langle \left\langle \Delta r^2 \right\rangle_T \right\rangle_{ens} = \left\langle \left\langle \Delta r^2 \right\rangle_{ens} \right\rangle_T = \frac{t_1}{NT}\sum_i^{T/t_1}\sum_j^{N} R^2_{m,i,j} \tag{2.6}$$

The CDF is computed in LabView, 9.4.1. Given that $r_k^2$ is the displacement square value greater than the corresponding $p_k$ percent of the data values in the $R_{m,1<i<m,j}$ array, then $CDF_{m,j}\left(r_k^2\right)$.

We have performed measurements on a non-clustering potassium channel, Kv1.4, as an additional control on our analysis. Even though larger square displacements are seen in Kv1.4, this channel yields anomalous diffusion characteristics similar to Kv2.1 (Fig. 2.8, Fig. 2.9 and Table 2.1). In the case of Kv1.4, the temporal MSD distribution is also observed to be broader that the ensemble MSD (Fig. 2.1), but not as broad as in Kv2.1 (Fig. 2.4). This indicates that this channel is also subjected to a CTRW, but the effect of the CTRW is less dominant than in Kv2.1.

Table 2.1: *MSD and CDF Parameters* Statistical results (mean and standard deviation) as obtained from the MSD and CDF

| | | MSD | | CDF | |
|---|---|---|---|---|---|
| | Drug | mean $\gamma$ | s.d. $\gamma$ | mean $w$ | s.d. $w$ |
| Kv2.1 | none (normal cells) | 0.65 | 0.22 | 0.52 | 0.14 |
| Kv2.1 | Cytochalasin D | 0.70 | 0.16 | 0.51 | 0.17 |
| Kv2.1 | Swinholide A | 0.78 | 0.18 | 0.54 | 0.13 |
| Kv1.4 | none (normal cells) | 0.77 | 0.22 | 0.56 | 0.19 |
| Simulation | | 0.92 | 0.03 | 0.85 | 0.21 |

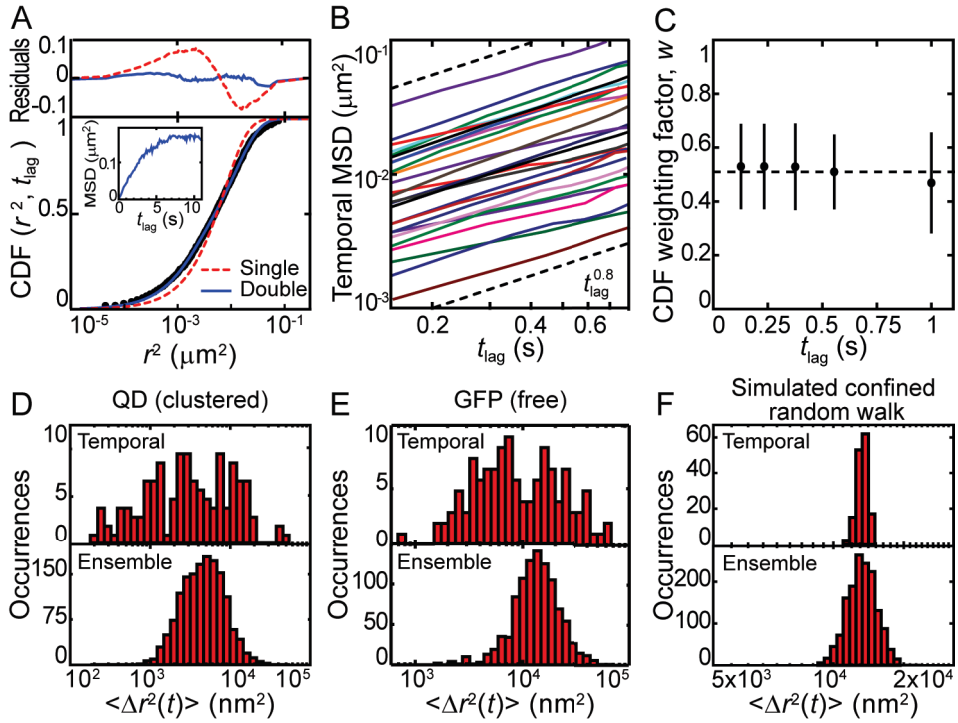


Figure 2.4: *Statistical analysis of Kv2.1 channel trajectories* (A) Square displacement CDF of a representative clustered channel at $t_{lag}$ = 0.1 s. Fits to both single-exponential using Eq. 2.1, dash red, and biexponential using Eq. 2.2, solid blue, are shown together with their respective residuals. The inset is the MSD of this trajectory. (B) Log-log plot of the temporal MSD of 26 representative trajectories of clustered channels. The dashed lines scale as t 0.8 in order to show that the trajectories are sublinear with an exponent equal to or smaller than 0.8. The MSD data for a longer time range is presented in Fig. 2.5. (C) Weighting value of the slow mobility component ($w$) in Eq. 2.2 vs. lag time. (D) Distribution of MSD values calculated from individual trajectories and ensembles in clustered channels for $t_{lag}$ = 0.1 s. (E) Control measurements of MSD distribution in GFP-tagged channels without QDs. In order to track individual GFP we analyzed non-clustered channels, which exhibit a 5-time higher median effective diffusion constant. (F) Distribution of MSD values calculated from simulated confined random walkers.

### *Probability density functions*

Given that walker is at the origin $r_0 = 0$ at $t_0 = 0$, the propagator $P(r)$ is the probability density of finding the walker at a distance $r$ at time $t > 0$. We experimentally found $P$ for a trajectory $j$ from the square displacements. First we compute the histogram of displacements

$R_i = \sqrt{R^2_{m=1,i,j}}$. Then we normalize each histogram element $h_q$ to the total counts and to the corresponding volume $2\pi R_q d$, where d is the bin size and $R_q$ is the bin center, to obtain the probability density function

$$P\left(R_q\right) = {}^{h_q}/_{\left(2\pi R_q d \sum_u h_u\right)} \tag{2.7}$$

The analysis of residuals reveals strong systematic deviations from the monoexponential functions. All analyzed CDFs, belonging to both free and clustered channels, fit well to a biexponential form indicating the diffusion pattern is not Gaussian (Fig. 2.4A and Fig. 2.3). The temporal MSD agrees with these results (Fig. 2.4B). The diffusion parameter is very broadly distributed but in almost all free and clustered (at short times) channels the MSD scales as a sublinear power law. The details of the CDF and MSD statistical results are shown in Fig. 2.8 and Table 2.1. Besides the fact that a biexponential fit yields better results than a monoexponential one, we use the parameter $w$ in Eq. 2.2 as an indicator of diffusion anomaly. This parameter is found to be independent of time lag (Fig. 2.4C) and it is 0.5, suggesting all trajectories are anomalous. Normal diffusion would yield $w$ close to zero or one. The clustered channels are analyzed at short times so that the cluster perimeter does not influence our results.

*MSD and CDF Analysis of Anomalous Diffusion*

Individual trajectory analysis (Figs. 2.4A and 2.4B) is an excellent starting point to characterize anomalous diffusion even though it gives limited information. The MSD curves are fit to $MSD = \Gamma t^{\gamma}_{lag}$. The MSD of clustered channels is not expected to scale linearly with time indefinitely, even in the case of normal diffusion, due to the lack of space availability for the displacement to keep growing. At short times the cluster perimeter should not interfere with the particle trajectory but at long times the MSD asymptotically approaches a limiting value. If confined diffusion were following Fick's law, the MSD could be modeled by approximation to a series solution [148], in which its first terms are equivalent to extrapolating a linear growth for short times with a constant (saturation) at long times.

$$\left\langle \Delta r^2\left(t\right)\right\rangle \cong r_c^2\left[1-\exp\left(-{}^{rDt}/_{r_c^2}\right)\right] \tag{2.8}$$

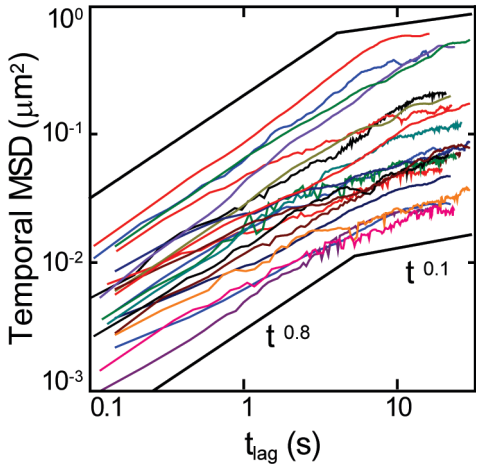


Figure 2.5: *Time-averaged MSDs for different trajectories of cluster-confined channels* As can be seen from this plot, the MSDs do not reach a plateau but instead they continue to increase across all times. The solid black lines serve as a guide, exemplifying the continuous growth of the MSDs over time.

For a circular cluster, $r_c^2$ is the cluster area. Hence, the crossover time at which the behavior changes from exponential to constant is $\tau_c = r_c^2/4D$. Following the same path, we can approximate the trajectory of a confined particle diffusing on a fractal to the equation

$$\left\langle \Delta r^2 \left(t\right)\right\rangle \cong r_c^2 \left[1 - \exp\left(-\Gamma t^\beta / r_c^2\right)\right] \tag{2.9}$$

which yields a crossover time $\tau_c = \left(r_c^2/\Gamma\right)^{1/\beta}$.

The MSD of a CTRW with the walker confined to a finite volume was recently examined by Neusius et al [149]. In contrast to stationary diffusion processes and against intuitive thinking, the temporal MSD is sublinear in lag time for long times. It was found that at long times the temporal MSD scales as $\left\langle \Delta r^2 \right\rangle_T \sim t^{1-\alpha}$ and the crossover time $\tau_c = \left(r_c^2/2\Gamma\right)^{1/\alpha}$. For short times, as expected, the walker is not affected by the confinement and the time-ensemble average scales as $T^{1-\alpha} t_{lag}$.

Fig. 2.4D displays distributions of time- and ensemble-averaged MSDs. Temporal MSD distributions are constructed from the individual trajectories. The ensemble MSD distribution is measured by averaging the square displacements of all trajectories occurring at a specific time, e.g. the displacements occurring between 100.0 s and 100.1 s. If the diffusion process were ergodic, both distributions would be similar. However, the temporal MSD is significantly broader than the ensemble MSD for both free and clustered channels. We confirmed that these results are not due to

interactions between the QD and the extracellular matrix or the cover slip surface by analyzing the trajectories of GFP-Kv2.1 channels. Because 3% of the Kv2.1 channels do not cluster, we can find individual non-QD-tagged, GFP-Kv2.1 channels freely diffusing outside the clusters. The signal to noise ratio and thus the tracking accuracy are poorer than those of QDs but we are able to track and analyze these channels, following only the GFP signal, as control measurements. Single GFP-Kv2.1 yielded the same CDF, MSD and distributions of square displacements as the ones found using QDs (Fig. 2.4E and Fig. 2.3). The median of the effective diffusion constant, i.e. $\langle \Delta r^2 \rangle / 4t_{lag}$, is five-fold higher in free channels than in clustered channels; but the temporal MSD distribution remains significantly broader than the ensemble MSD. This effect is seen in both GFP and QD tracking of non-clustered channels. As a control of our averaging algorithms, Fig. 2.4F shows the time and ensemble averages for the simulated confined random walkers. The two distributions are very similar and, as expected from the central limit theorem applied to a Gaussian process, the width of the distribution for the simulated data is $\sigma \propto 1/\sqrt{N}$ , where $N$ is the number of independent variables.

The effects of the cluster perimeter are apparent in the temporal MSD of individual trajectories. Fig. 2.5 shows a set of temporal MSDs. Due to the CTRW effect the magnitude of the MSD scatters over a broad range. However, most trajectories show similar critical exponent. For times shorter than the crossover time the MSD scales as $t^{\beta}$. For longer times the combined effect of the CTRW and the confinement are clear. Instead of observing a MSD saturation at $r_c^2$, the trajectories display a sublinear growth in $t_{lag}$. Fig. 2.5 also shows lines indicating different power laws at short and long times. At short times, the lines scale as $t^{\beta}$, with $\beta$ coming from the fractal structure. At long times, they scale as $t^{1-\alpha}$, with $\alpha$ set by the CTRW. Good agreement between the data and these lines is seen. The $\alpha$ and $\beta$ parameters used for drawing them are taken directly from the aforementioned analysis without any fitting to the data.

In order to compare the diffusion pattern to the CTRW model predictions, we examined the TEA-MSD for all data at different lag times. The TEA-MSD was obtained by applying an additional ensemble average to the temporal MSD. Fig. 2.6A shows the MSD vs. the length of the trajectory, which was measured by truncating the experimental data at a time $T$ and performing a temporal average (i.e. a moving average). The TEA-MSD fluctuated for short times (due to small number statistics) but it scaled as a power law $\left\langle \left\langle \Delta r^2 \right\rangle_T \right\rangle_{ens} \sim T^{\alpha-1}$ beyond 3 s (30 points) with $\alpha$ = 0.90

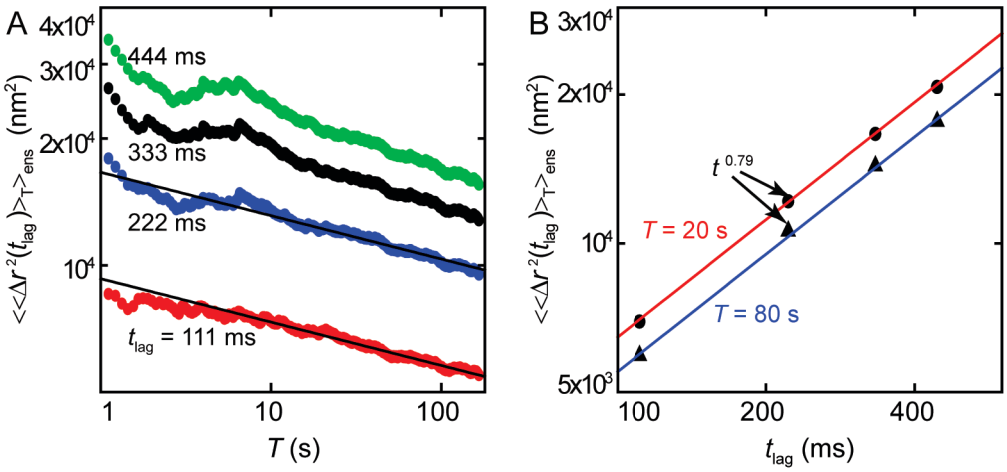


Figure 2.6: *Time-ensemble averaged MSD of clustered Kv2.1 channels* (A) The MSD is plotted against total time, i.e. the time used in the moving average. The straight lines show a power law fit $MSD \sim T^{\alpha-1}$, with a slope $\alpha - 1 = -0.10$. (B) The MSDs for total times 20 s and 80 s are plotted against lag time. At both total times the MSDs exhibit the same subdiffusion critical exponent.

± 0.01 for all lag times. The TEA-MSD was found to scale as $\left\langle \left\langle \Delta r^2 \right\rangle_T \right\rangle_{ens} \sim t_{lag}^{\gamma}$ with $\gamma = 0.79 \pm 0.02$ (Fig. 2.6B). Only lag times up to 0.5 s were included in these data to avoid boundary effects (these are appreciated in the inset of Fig. 2.4A). All the previously discussed anomalous diffusion models predict the ensemble average scales as $\left\langle \Delta r^2 \right\rangle_{ens} \sim t_{lag}^{\eta}$. The analysis presented in Fig. 2.6 confirms this behavior, with the exponent determined to be 0.8 ± 0.1.

*Propagator results*

We have fit the propagators of normal diffusion, two-component mobility, geometrical fractal [121], and percolation cluster (i.e. random fractal) [142] to the CDF of Kv2.1 trajectories. FBM has a Gaussian propagator so at a fixed time it cannot be distinguished from normal diffusion. Fig. 2.7 shows representative fits with the corresponding residuals and the plots of the different fits with the probability distribution function. The propagator of the CTRW as given by [124] was fit directly to the probability distribution. In contrast to FCS [132, 97], our single particle tracking data do not fit equally well the different models. The propagator fits better to an approximate double Gaussian than to fractal equations. We propose that the reason for this is that single particle tracking captures the spatial inhomogeneities of the cell membrane to a larger extent than FCS. The propagators for two realistic anomalous components, such as the combination of a

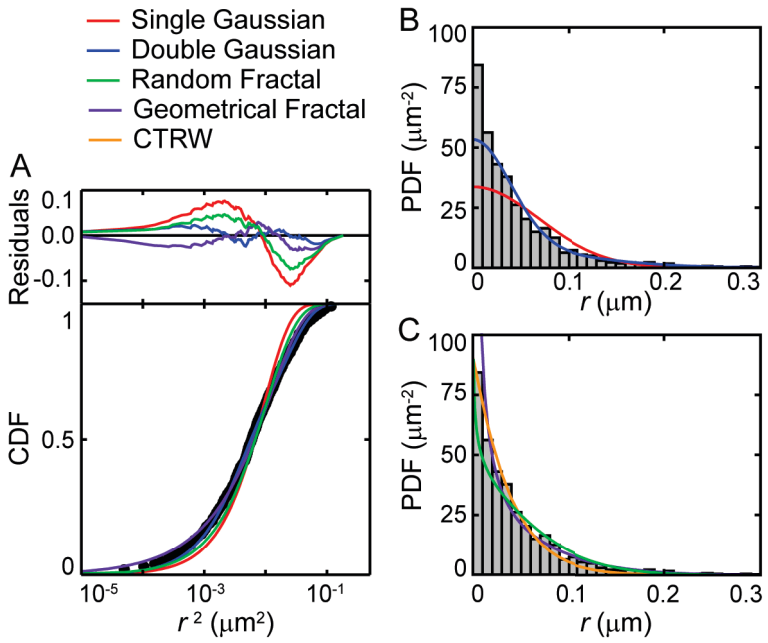


Figure 2.7: *Fits to the propagators arising from the different anomalous diffusion models* We have included the Gaussian (normal and fractional Brownian motion), double Gaussian (2-component mobility), random fractal (e.g. percolation cluster), geometrical fractal and CTRW propagators. (A) fits to CDF and corresponding residual. (B) Plot of the single and double Gaussian fits on the probability distribution function (PDF). (C) Plot of the random fractal, geometrical fractal and CTRW fits on the PDF. The CTRW was fit directly to the PDF.

CTRW and a fractal or the combination of two fractal structures, have too many free parameters to provide any useful information.

*Monte Carlo simulation of a confined random walker*

In order to provide an unequivocal test of our analysis and averaging programs we simulated normal diffusion in a confined environment. Then we analyzed the simulated trajectories using our home-written algorithms. The resulting histograms are shown in Fig. 2.8B, F and Fig. 2.9A.

The random walk implementation was written in LabView. A walker is placed at the origin of a square lattice and it randomly jumps to one of its four nearest neighbors' lattice locations. The walker remains confined to a 40 pixel radius by applying reflecting boundary conditions at

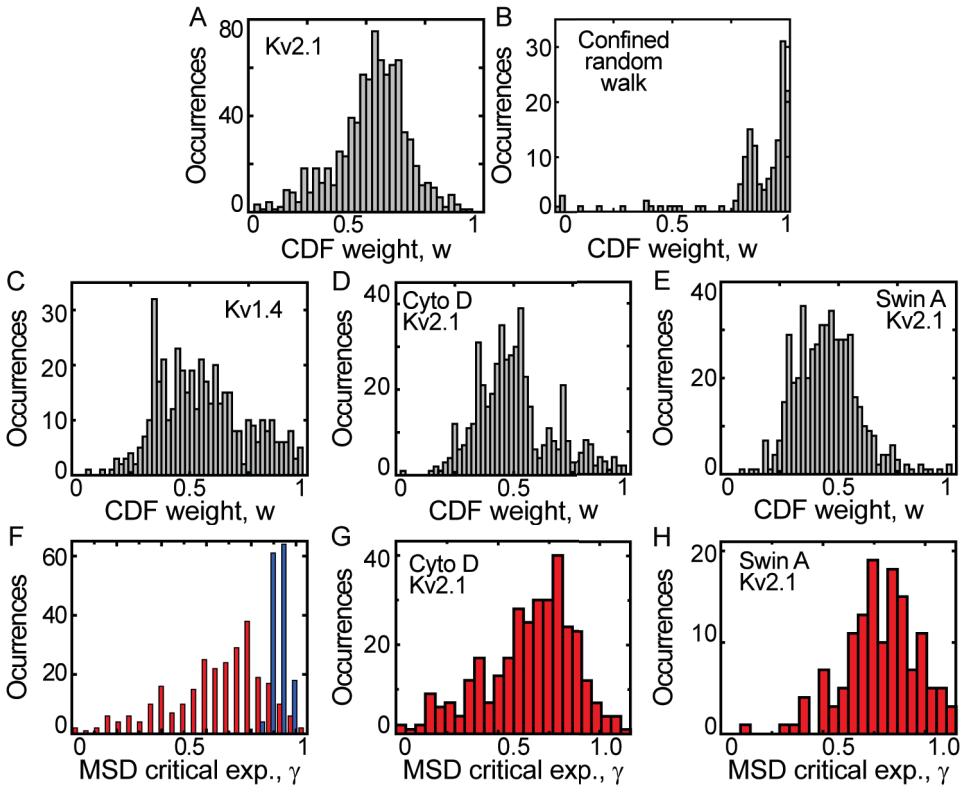


Figure 2.8: *Statistical result from the analysis MSD and CDF* (A-E) Histograms of the parameter w in Eq. 2.2 as follows: (A) Kv2.1 in normal cells, (B) Monte Carlo simulation control, (C) Kv1.4 non-clustering channels control, (D) Kv2.1 in cells treated with Cytochalasin D, (E) Kv2.1 in cells treated with Swinholide A. (F-H) Histograms of the sublinear exponent $\gamma$ in the MSD, i.e. MSD ~ $t_{lag}^{\gamma}$. Each plot is: (F) Kv2.1 and simulation control, (G) Kv2.1 in cells treated with Cytochalasin D, (H) Kv2.1 in cells treated with Swinholide A.

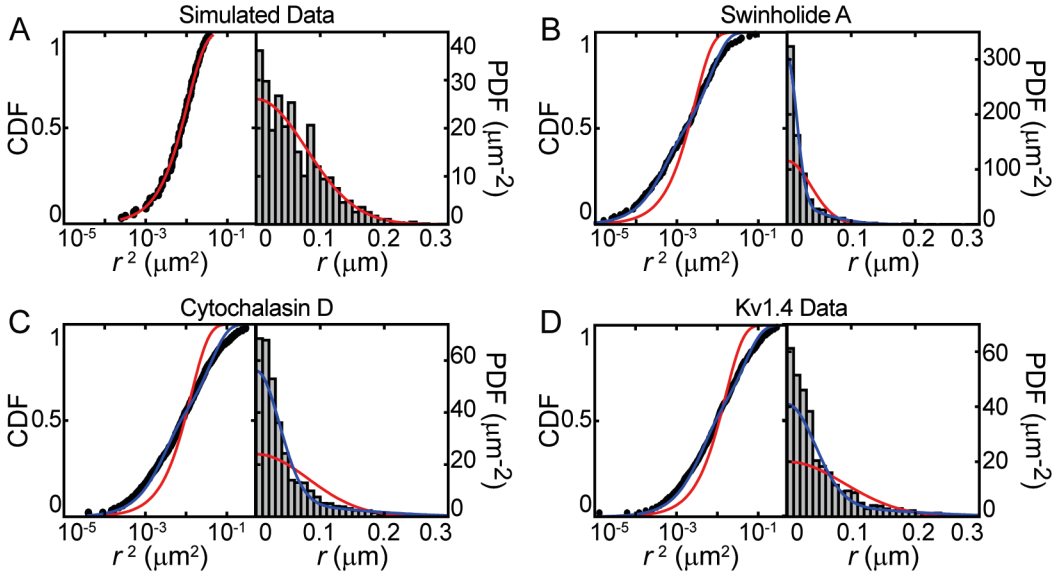


Figure 2.9: *Fitting to monoexponential and biexponential CDFs* The plots on the right show the corresponding probability distribution function. (A) Simulated confined random walker. This control yields a good fit to a monoexponential CDF. (B) Cells treated with Swinholide A. (C) Cells treated with Cytochalasin D. (D) Non-clustering Kv1.4 channel.

$x^2 + y^2 \geq 40$. A single step consists of 100 jumps. 1500 steps are recorded and analyzed as an individual walker trajectory.

*Experimental waiting time distribution of a 2D random walker*

The probability of finding a random walker confined within a radius $R$ during a time $\tau$is the probability $P_w(\tau, R)$ that it remains within a given region of radius $R$ for all time $< \tau$. This was derived in 2D by Saxton [81]. In brief, the probability density of finding a walker at a distance $r$ from the origin, at time $t$, in a cylindrical region of radius $R$ with absorbing boundaries is

$$P(r,t) = \frac{1}{\pi R^2} \sum_{n=1}^{\infty} \frac{J_0(r\alpha_n)}{J_1^2(R\alpha_n)} \exp\left(-\alpha_n^2 Dt\right) \tag{2.10}$$

where $J_0$and $J_1$ are Bessel functions of zeroth and first order, respectively, and $R\alpha_n$ are zeros of $J_0$: i.e., $J_0(R\alpha_n) = 0$. Then, the probability that the random walk remains within the region until time $\tau$ is

$$P_w(\tau, R) = \int_0^R P(r,t)\, 2\pi dr = 2\sum_{n=1}^{\infty} \frac{1}{R\alpha_n J_1(R\alpha_n)} \exp\left(-\alpha_n^2 Dt\right) \tag{2.11}$$

In order to simplify this notation, we have named the threshold radius $R$ in this derivation. However, this variable appears as $R_{TH}$ everywhere else in the text.

*Analysis of waiting time distributions*

Heavy-tailed CTRWs display waiting times in all scales, enabling the observation of transient channel immobilization. We identified the events in which the channel remained confined within a radius $R_{TH}^2 \ll$MSD and constructed the distribution of waiting times from these events. The waiting time distribution is computed for the channel trajectories using an algorithm implemented in MATLAB. For a specific radial threshold $R_{TH}$, the displacement squares $R_{m=1,i,j}^2 < R_{TH}^2$ are identified. Then for each identified $i,j$ matrix element we count the number of frames where the channel does not cross the threshold. This is accomplished by evaluating displacement squares at higher $m$ values - i.e. $\mu = \max m$ with . The waiting time distribution is found from the occurrences of $\tau = \mu t_1$. Fig. 2.10 shows the distributions for three different thresholds, $R_{TH}^2$ = 500, 1000, and 2000 nm², which correspond to radii 3, 4, and 6 times the standard error of the mean

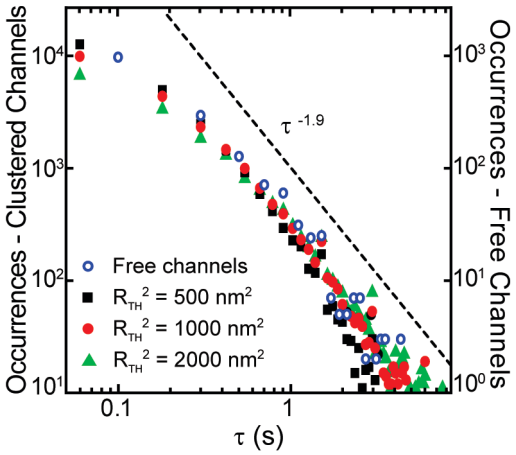


Figure 2.10: *Distribution of waiting times as measured using different radial thresholds* The solid symbols are from clustered channels (left axis) and the open circles from free channels (right axis). The threshold value indicates that the particle was measured to remain within that circle for the specific time. The dashed line indicates a power law $P_w(\tau) \sim \tau^{-(1+\alpha)}$ with $\alpha = 0.9$. This value corresponds to the measured MSD. At long times ($\tau > 3$ s) the distribution appears to drop faster than $\tau - 1.9$, suggesting a breakdown in the heavy tail of the CTRW. However, this is an artifact in our measurement, which derives from QD blinking because QDs are not in the "bright" state for that long. To verify this, we determined the probability distribution of QD "bright" times and found it to have a median of 10 s. For comparison, the figure shows a line that scales as $\tau^{-1.9}$, as expected from a CTRW with $\alpha = 0.9$. The distribution for clustered channels is identical to that of the free channels (o).

localization accuracy (22, 32, 45 nm respectively). Remarkably, the distribution of immobile times does not change with the threshold radius, which is consistent with a binding model. The same distribution is found for non-clustering channels.

### 2.3.2 *Kv2.1 anomalous diffusion is modeled by a CTRW on a fractal*

The distributions of temporal and ensemble MSDs are consistent with the nonergodic CTRW model where the temporal averages become random quantities different from the ensemble averages [128]. Noticeably, the time-ensemble averaged MSDs exhibit aging, which can be modeled by a CTRW with a waiting time distribution that scales as $1/\tau^{1+\alpha}$ [124, 135]. The agreement between our results and the CTRW is very convincing, but both the temporal MSDs and the time-ensemble MSDs are sublinear in lag time. This is expected from diffusion on a fractal but not from a CTRW [127]. In theory, the two processes can coexist, and thus we investigated the combination of a CTRW and a fractal [150, 151]. Meroz et al. recently simulated a CTRW on a fractal structure [151]. The ensemble-averaged MSD was found to follow a power law

$$\left\langle \Delta r^2 \left( t_{lag} \right) \right\rangle_{ens} = \Gamma t_{lag}^{\alpha \cdot \beta} \tag{2.12}$$

where $\alpha$ and $\beta$ are the critical exponents of the CTRW and the fractal, respectively. Due to the fractal structure, the temporal MSD exhibited anomalous subdiffusion . An additional ensemble average yielded aging and sublinearity in lag time

$$\left\langle \left\langle \Delta r^2 \left(t\right) \right\rangle_T \right\rangle_{ens} \sim T^{\alpha-1} t_{lag}^{1-\alpha+\alpha\beta} \tag{2.13}$$

These theoretical predictions agree with all our data (time MSD, ensemble MSD and time-ensemble averages) yielding $\alpha$ = 0.90 ± 0.01 and $\beta$ = 0.77 ± 0.04. For comparison, the theoretical value of $\beta$ of a walker on a percolation cluster is 0.70 and on a Sierpinski gasket is 0.86 [56].

What physical mechanisms induce a CTRW? This process can be caused by either transient binding or membrane compartmentalization. In the former model the waiting times correspond to the dissociation constant while in the latter they are related to the probability of hopping to the next compartment. The data in Fig. 2.10 indicate that if the CTRW corresponded to hop diffusion, the compartments would have radii smaller than 22 nm. While this is theoretically possible, such dense compartmentalization is highly improbable. Several studies have reported membrane compartmentalization in the range 140-350 nm [131, 6, 152]. Lipid raft microdomains with radii as small as 20 nm have been reported [153, 154, 155], but in these cases the compartments are produced by self-association of lipids with saturated chains. Kv2.1 channels have been shown to target lipid rafts [156] and thus it is possible that the transient localization occurs within raft domains tethered to the cytoskeleton. The evidence presented here shows that the channels are either transiently immobile or localized within very small compartments because the waiting time distribution does not change upon measuring the probability that the molecule stays within radii of 22, 32 or 45 nm. Furthermore, we found the time distribution scaled close to $1/\tau^{1.9}$, corresponding to $\alpha$= 0.9 as found from the MSDs. The same distribution is found in the single GFP trajectories showing once more that this effect is not induced by the QDs.

### 2.3.3 *Effect of actin cytoskeleton on Kv2.1 diffusion pattern*

We hypothesized actin plays a dominant role in Kv2.1 dynamics and investigated its effect by treating the cells with Swinholide A, a toxin that disrupts actin fibers [157]. After Swinholide A application, clusters are rapidly dissolved and Kv2.1 channels become free. Strikingly, the

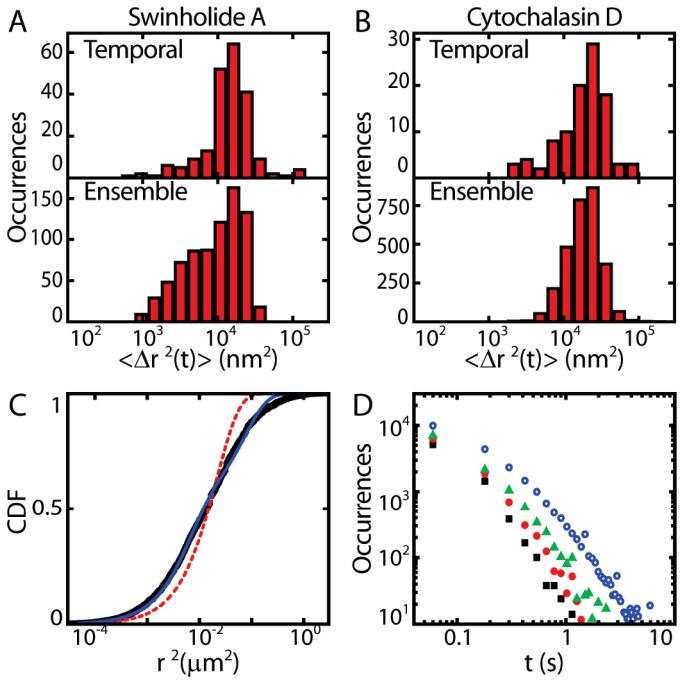


Figure 2.11: *Kv2.1 analysis after treatment with actin inhibitors* Channels were originally cluster-confined. After Cytochalasin D the channels remain inside clusters, but after Swinholide A, the channels become free. (A-B) Distribution of time averaged (top) and ensemble averaged (bottom) MSDs in cells treated with (A) Swinholide A and (B) Cytochalasin D. The distribution of temporal MSDs is no longer broader than the ensemble distribution. (C) CDF of representative trajectory after treatment with Swinholide A. (D) Distribution of waiting times as measured using different radial thresholds of 500 $nm^2$, 1000 $nm^2$, and 2000 $nm^2$ in Swinholide A treated cells. For comparison the distribution in untreated cells is also shown.

Kv2.1 diffusion process becomes ergodic (Fig. 2.11A) but anomalous diffusion is still found (Fig. 2.11C, Fig. 2.8E, H, Fig. 2.9B). Individual trajectories analysis shows the CDF is anomalous and MSD is sublinear in $t_{lag}$. Therefore, the mechanism underlying stationary anomalous diffusion is independent of actin filaments suggesting it is governed by interactions with macromolecular obstacles not dependent on the cytoskeleton. Similar results to those with Swinholide A were obtained with a different actin inhibitor, namely Cytochalasin D (Fig. 2.11B, Fig. 2.8D, G, Fig. 2.9C).

Motivated by the recovery of ergodicity, we measured the new distribution of waiting times. This distribution strongly depended on the radial threshold indicating that stationary anomalous diffusion was not related to transient binding (Fig. 2.11D). Why are there immobile episodes without transient binding? Even a Brownian walker has a finite probability of remaining within a very small radius. The qualitative difference between a Brownian walker and a walker in a CTRW is the dependence on $R_{TH}$.

The implications of our findings are clear. The actin cytoskeleton sets in action a non-stationary CTRW mechanism through a network of anchoring points. As experiments progress, Kv2.1 channels find more stable binding sites and remain on those locations for longer times. Each channel moves toward an equilibrium state and, eventually, it will find a location where it would pause for an extremely long time, such as the lifetime of the cell. In practice, this never happens. As in many physical processes in living cells, the diffusion pattern of potassium channels is actively maintained out of equilibrium. The cell constantly recycles transmembane proteins by absorbing them and sending new ones into the membrane [158]. If the system were left alone, i.e. no energy was being spent on the plasma membrane, it would eventually reach a quasi-equilibrium state where all Kv2.1 potassium channels would be immobile

## 2.4 DISCUSSION

We found that the diffusion pattern of Kv2.1 channels is governed by a CTRW on a fractal. Naturally, these mechanisms have biological implications. Previously, it was suggested that telomere's anomalous diffusion leads to spatial chromosome organization in eukaryotes [57] and that anomalous diffusion in the bacterial cytoplasm helps transcription factors find their DNA target [61]. Many transmembrane proteins are involved in cell signaling and cell-to-cell communication. For these pathways to be accurate, it is important that receptors are found rapidly. The fractal structure of the plasma membrane may be a crucial part in receptor recognition. A fractal structure increases the dimension of the random walk and hence the same site is visited several times before the protein leaves to explore a new region. Therefore, the search for receptors is performed more carefully by a walker, minimizing the chances of missing a target in the close vicinity. On the other hand, the actin role in the CTRW suggests two different benefits for the cell. As in the case of telomeres, it favors membrane compartmentalization and organization into segregated domains. A second process that may benefit from a CTRW is endocytosis, actually the same process that keeps the CTRW running. Channels run from one anchoring point to another, but some of these may be endocytic sites from where the channel will be engulfed. Many transmembrane proteins have an intracellular domain that recognizes specific adaptor molecules and bind to them with high specificity but low affinity [159]. Some of these adaptors are transiently immobile

[160]. Thus, the CTRW may be involved in maintaining the channel at an endocytic site so that the interaction between protein and adaptor is enhanced. Furthermore, it is observed that endocytic sites enrich specific protein concentrations [161] as expected from a CTRW-based membrane organization. In conclusion, we have shown that the potassium channel Kv2.1 displays anomalous diffusion with a nonergodic underlying physical mechanism. A comprehensive analysis of the diffusion pattern that goes beyond MSD analysis and also includes time series analysis of individual trajectories and ensemble averages was performed. In general, single-molecule experiments provide information on particle fluctuations that average out in ensemble measurements. However, when the population is homogeneous, this information can in theory be obtained from the ensemble measurements using the fluctuation-dissipation relation. Our findings show that due to the ergodicity breaking, single-particle trajectories contain information not attainable by ensemble experiments, emphasizing the relevance of single-molecule studies. Two processes are found to coexist in the complex environment of the living cell membrane, one of them non-stationary, namely a CTRW. The actin cytoskeleton network is found to regulate the CTRW. We propose biological implications for both mechanisms underlying anomalous diffusion. Importantly, we showed that the availability of both temporal and ensemble statistics provide enough evidence to elucidate the mechanisms associated with anomalous diffusion. A very recent report by Jeong et. al. [90], showing ergodicity breaking of lipid granules in the cytoplasm of fission yeast cells, suggests that our findings may also be relevant to three dimensional diffusion processes.

## 2.5 ACKNOWLEDGEMENTS AND CONTRIBUTIONS

Michael M. Tamkun and Diego Krapf designed the research. Blair Simon and Diego Krapf contributed analytical tools. Aubrey Weigel performed the research and together Aubrey Weigel and Diego Krapf analysed the data.

# CHAPTER 3: OBSTRUCTED DIFFUSION PROPAGATOR ANALYSIS FOR SINGLE PARTICLE TRACKING

We describe a method for the analysis of the distribution of displacements, i.e., the propagators, of single-particle tracking measurements for the case of obstructed subdiffusion in two dimensional membranes within this chapter. The propagator for the percolation cluster is compared with a two-component mobility model against Monte Carlo simulations. To account for diffusion in the presence of obstacle concentrations below the percolation threshold, a propagator that includes the transient motion in finite percolation clusters and hopping between obstacle-induced compartments is derived. Finally, these models are shown to be effective in the analysis of Kv2.1 channel diffusive measurements in the membrane ofl iving mammalian cells.

## 3.1 introduction

Membrane proteins exhibit complex dynamics, often accompanied by anomalous diffusion. The complexity in protein motion lies in the factt hatt he plasma membrane is a heterogeneous environmentt hat exhibits microdomain organization, is densely packed with proteins, and is tethered to the cytoskeleton through different proteins and lipids [3]. The diffusion of membrane molecules is studied by a variety of methods that include FRAP [22], FCS [162, 163, 164], and SPT [96, 165, 148]. In particular, SPT enables the localization of an individual molecule with nanometer precision in real time, yielding detailed information on its molecular motion and the interactions between a protein or lipid with its environment. The diffusive transport of membrane proteins has vital biological implications related to many cellular processes. However, the analysis of anomalous diffusion in live cells is challenging because it can originate via different mechanisms: (a) Membrane proteins and lipids tethered to the cytoskeleton behave as immobile obstacles, hindering the free diffusive transport [166, 167, 168? , 169, 132, 122, 170, 101]. The resulting motion is termed obstructed diffusion. (b) Macromolecular crowding has been experimentally shown to induce anomalous subdiffusion in some systems [171, 129, 172], butt he link between anomalous diffusion and crowding is still controversial [53]. It was proposed that crowding gives rise to viscoelastic effects leading to long-time correlations in a particle trajectory [172, 173], which may be modeled by FBM [62, 60]. Nevertheless, the physical mechanism by which crowding can be mod-

eled by FBM is not fully understood. (c) Transient immobilization achieved by temporary binding with a heavy tailed distribution of waiting times lead to subdiffusion and ergodicity breaking [95, 174, 175]. This process is modeled by a CTRW [42]. In general, more than one single physical mechanism may be simultaneously responsible for anomalous diffusion in living cells. In the previous chapter, chapter 4, we demonstrated that the subdiffusion of Kv2.1 potassium channels in the plasma membrane of mammalian cells is best characterized as a CTRW coexisting with a fractional ergodic mechanism such as obstructed diffusion or FBM [49]. Interestingly, the dynamics of lipid granules in the cytoplasm of yeast have also recently been shown to be influenced by similar mechanisms [90].

Even though obstructed diffusion is not the sole cause for anomalous diffusion in the plasma membrane, it has long been recognized to be an important factor in the diffusion pattern of proteins and lipids. Comparison of diffusion in the axon initial segment (AIS) and blebs shows the relevance of obstruction. AIS: An unusually high local density of ankyrin-G and actin forms a region with a large number of immobile obstacles. This obstruction pattern hinders diffusion to such a point that long range motion is not observed and it effectively functions as a diffusion barrier, a phenomenon that is vital to neuronal polarization [176]. Blebs: These spherical protrusions that occur at the periphery of eukaryotic cells [177] lack cytoskeletal anchoring points and are, thus, practically free from immobile obstacles. The diffusion coefficient of proteins in blebs is observed to be dramatically higher than in the rest of the membrane linking the diffusion pattern to cytoskeleton-bound molecules [178].

Several reports show via the use of actin depolymerization drugs that the cytoskeleton is implicated in restricting the diffusion of membrane proteins [167, 178]. Truncation of the cytoplasmic domain of membrane proteins was also shown to increase the diffusion coefficient [166, 179]. Recently, Andrews et al. provided evidence that actin forms a dynamic meshwork involved in forming barriers to free diffusion [180]. In contrast, the ectodomain of some proteins is the key determinant of their lateral diffusion suggesting that anomalous subdiffusion in the plasma membrane can be also induced by interactions with the extracellular matrix or the ectodomains of neighboring membrane proteins [179]. Kusumi's lab has shown that lipids and proteins in the plasma membrane appear to be temporarily confined to microdomains 30 to 800 nm in size. Temporal confinement seems to be widespread and it was observed in many different cell types

including chinese hamster ovary (CHO), mouse hepatoma (HEPA-OVA), rat kangaroo (PtK2), fetal rat skin keratinocyte (FRSK), HEK, HeLa, T24, and normal rat kidney (NRK) cells [168]. Edidin and co-workers showed that vesicle trafficking to and from the plasma membrane in combination with barriers to lateral diffusion can maintain microdomains in the cell surface with characteristic lifetimes in the tens of seconds [17, 181]. These observations can be explained by the existence of clusters of immobile proteins that behave as discontinued fences in the plasma membrane. In order for a walker to hop between compartments it needs to find a gap in the fence. Alternatively, this is achieved by fluctuations in the position of quasi-immobile obstacles. This mechanism has been referred to as the anchored-protein picket model [167]. Obstructions to diffusion in the cell membrane were also observed with optical tweezers. It was shown that as a molecule is dragged along the plasma membrane it encounters frequent obstacles in its path [182, 183]. Both elastic and inelastic barriers were found to be present in the cell membrane with the elastic ones being actin-cytoskeleton dependent [184].

As highlighted in previous chapters 44, in SPT analysis, the MSD measures the apparent diffusion coefficient and provides the simplest type of classification of the diffusion pattern. Brownian motion yields a linear MSD, $\left\langle r^2\left(t\right)\right\rangle = 2dDt$ where $D$ is the diffusion coefficient and $d$ is the substrate dimension ($d = 2$ for a membrane). In contrast, anomalous subdiffusion is characterized by a sublinear MSD, $\left\langle r^2\left(t\right)\right\rangle \sim t^{\alpha}$ with $\alpha < 1$ being the subdiffusive exponent [148]. When $\alpha > 1$, the motion is termed superdiffusion. Experimental observations of anomalous diffusion with values of $\alpha$ between 0.1 and 0.9 have been reported by different groups [96, 185, 131]. Unfortunately, the information obtained from MSD analysis is very limited and, in practice, many anomalous subdiffusion models yield the same MSD power law. The problem is that the MSD analysis does not take advantage of the full probability of displacements $P\left(r,t\right)$, viz., the propagator, which is naturally available in SPT measurements [131]. $P\left(r,t\right)dV$ gives the probability that a particle at the origin at time zero is found in an element of volume $dV$ at $r$, at time $t$. The distribution of displacements for Brownian motion is Gaussian,

$$P\left(r,t\right) = \frac{1}{4\pi Dt}e^{-r^2/4Dt} \tag{3.1}$$

In order to take advantage of the probability of displacements analysis, without the need to impose bin sizes, the CDF is used [132, 175, 131, 94]. The CDF $F\left(r^2,t\right)$ can be interpreted as the probability that a particle at the origin at time zero is found within a circle of radius $r$ at time $t$. In a two-dimensional (2D) space, $dV = 2\pi r dr$, and thus, $F\left(r^2,t\right) = 2\pi \int_0^r P\left(r',t\right) r' dr'$. This yields a monoexponential function, $F\left(r^2,t\right) = 1 - e^{-r^2/4Dt}$ , for Brownian motion. A two-component mobility model is often used to distinguish between normal and anomalous diffusion by comparing the residuals from a monoexponential CDF fit and a biexponential fit [168, 132, 49, 103, 186, 187]. The two-component cumulative distribution becomes

$$F\left(r^2,t\right) = 1 - we^{-r^2/\sigma_1^2} - (1-w)\, e^{-r^2/\sigma_2^2} \tag{3.2}$$

where $\sigma_1^2$ and $\sigma_2^2$ are the slow- and fast-mobility mean square displacements, respectively, i.e., $\sigma_i^2 = 4D_i t$, with weighting factor $w$.

The propagators for a CTRW and FBM are well documented. The particle displacement of a CTRW is given by a Fox function [188, 189, 190, 124] and that of FBM is a Gaussian distribution with a time-dependent diffusion coefficient [191]. However there is a great deal of confusion in the literature about the propagators for obstructed diffusion. Obstructed diffusion can be modeled as a percolation problem. Under the influence of constant thermal agitation, the motion of randomly wandering molecules is closely related to a random walk. Monte Carlo calculations are particularly suitable to simulate the effect of obstruction in the cell membrane because a random set of lattice sites can be directly blocked. Diffusion in a percolation cluster has been extensively studied near criticality [56, 192] and, in a series of seminal papers, Saxton has simulated diffusion in the presence of both mobile and immobile obstacles with a wide range of obstacle concentrations, elucidating many of the obstructed diffusion and crowding theoretical predictions [122, 193]. The work presented here builds on these reports.

In this chapter, we report Monte Carlo simulations to characterize the motion of particles in the presence of immobile objects. We describe a method to analyze the particle trajectory based on the distribution of displacements taking into consideration the fractal dimension of the matrix and the fractal dimension of the walk. The dimension of the walk is found from the simulated trajectory. The dimension of the matrix describes the fractal on which the tracer performs a

random walk. This matrix is naturally embedded in a 2D space. Because of the self-similarity properties of percolation clusters, obstructed diffusion bears a vast resemblance to FBM. We apply a recently developed method based on p-variation [64] to evaluate the underlying mechanism of anomalous diffusion and show that both FBM and obstructed diffusion give the same results. Finally, we compare simulation results to recently reported single-particle tracking measurements of Kv2.1 potassium channels in the membrane of living cells [49].

## 3.2 MATERIALS AND METHODS

### 3.2.1 *Obstructed diffusion simulations*

We implemented random walk simulations on a 2D square lattice to model obstructed diffusion. Obstacles were randomly distributed on the lattice at a concentration $c$. Obstructed diffusion simulations were implemented in MATLAB using a "blind ant" algorithm. First, we generated a lattice where each site was assigned a random number between 0 and 1. All sites with a number smaller than c are considered obstacles. A walker is placed in the center of the lattice and it is only allowed to move into vacancies, which are sites with assigned numbers bigger than $c$. The walker attempts to move to one of the four nearest-neighbor sites with equal probability. If the chosen site is blocked, the walker remains at the original position. The clock ticks independent of the outcome of the attempted jump and the protocol is looped $N$ times. The MATLAB built-in algorithm used for random number generation is based on the Mersenne twister algorithm [194]. The results returned are pseudorandom values drawn from a standard uniform distribution.

All lattice generated were 2000 × 2000 sites and periodic boundary conditions were implemented on the random walks. We created three different lattices for each obstacle concentration and obtained three random walks of $2 \times 10^6$ steps, per lattice. Each of these nine random walks was then fit independently according to the text. All results presented here show the mean ± standard deviation of the distribution of fitting results.

### 3.2.2 *Single particle tracking in living cells*

Chapter 4 describes these single particle tracking measurements in live cells in more detail[49]. In brief, HEK293 cells were transfected with Kv2.1 channels containing an extracellular biotin

acceptor domain that is the substrate for BirA biotin ligase 8.3. The transfected cells were incubated with streptavidin-conjugated QDs (Qdot 655, Invitrogen, Carlsbad, CA), which bound to the biotinylated Kv2.1 channels 8.4. QDs enabled us to track individual channels with nanometer accuracy. The basal membrane of the labeled cells was imaged using a home-built objective-type TIRF microscopy. QDs were excited with a 473 nm laser line and the fluorescence was collected in a back-illuminated EMCCD camera (Andor iXon DU-888). Both the stage (Bioptechs, Butler, PA) and the objective were maintained at 37°C. Individual particles were localized and tracked by fitting the intensity image of an appropriate region of interest to a two dimensional Gaussian function [49, 145].

## 3.3 RESULTS

### 3.3.1 *Diffusion in an infinite percolation cluster*

When the concentration of obstacles is low, small clusters of connected occupied sites, i.e., fences, are formed. Below a critical concentration threshold, the cluster size remains finite but as the concentration increases, so does the mean cluster size. At criticality, an infinite cluster of obstacles develops and the system undergoes a percolation transition. Havlin *et al*. [192, 195] have shown that the propagator for an infinite percolation cluster can be described by $P(r,t) \sim r^{d_f-d} f\left(r/t^{1/d_w}\right)$, where $d_w$ is the fractal dimension of the walk, $d_f$ the fractal dimension of the cluster, $d$ the underlying dimension, and $f(u) = \exp\left(-K_0 u^{1.65}\right)$. A percolation cluster in a membrane is characterized by a fractal dimension $d_f$ =1.896, $d$ = 2, and the subdiffusive exponent is given by $d_w$: MSD $\sim t^{2/d_w}$. In a percolation cluster, the propagator gives the probability density that a particle is found in an element of volume $dV$ within a random fractal with dimension $d_f$, given by [195]

$$dV = \frac{2\pi^{d_f/2}}{\Gamma\left(d_f/2\right)} r^{d_f-1} dr \tag{3.3}$$

where $\Gamma$ is the Gamma function, $\Gamma(x) = \int_0^\infty e^{-t} t^{x-1} dt$. Eq 3.3 yields

$$P(r,t) = B r^{d_f-d} \exp\left[-K(t)\, r^{1.65}\right] \tag{3.4}$$

$$B = \frac{1.65\Gamma\left(d_f/2\right)}{2\pi^{d_f/2}\Gamma\left[\left(2d\_\{f\}-d\right)/1.65\right]} K\left(t\right)^{\left(2d_f-d\right)/1.65} \tag{3.5}$$

where $K\left(t\right) = a/t^{1.65/d_w}$, $d_f - d = -0.104$, and $B$ is the normalization factor. Integrating over the fractal volume, the cumulative distribution is

$$F\left(r^2,t\right) = \frac{\gamma\left[\left(2d_f-d\right)/1.65, K\left(t\right)r^{1.65}\right]}{\Gamma\left[\left(2d_f-d\right)/1.65\right]} \tag{3.6}$$

where $\gamma\left(a,x\right)$ is the incomplete gamma function defined by $\gamma\left(a,x\right) = \int_0^x e^{-t}t^{a-1}dt$. Because $d_f$ and $d$ are known, the CDF is defined by a single parameter $K\left(t\right)$.

The critical obstacle concentration threshold in a square lattice is 40.7255 ± 0.0002% [196]. Fig. 3.1a shows a CDF of a simulated trajectory for a walker in a square lattice at criticality. The fit to the percolation model (Eq. 3.6) is shown together with the fits to simple diffusion (Gaussian propagator) and to a two-component mobility model (Eq. 3.2). While both simple diffusion and an infinite percolation cluster model are characterized by a single parameter, the two-component mobility model is fit to three parameters. Both the two-component and the percolation cluster fits are of good quality, with the two-component model being slightly better. As discussed below, the percolation cluster fitting parameter reproduces well the predicted power law $K\left(t\right) = a/t^{1.65/d_w}$, with $d_w$ = 2.8. The same value is found from the MSD subdiffusive exponent.

The cumulative distribution eliminates the dependence on bin size and it integrates out noise but the displacement probability is more informative from a qualitative perspective. In order to compute the displacement distribution $P\left(r,t\right)$, the number of displacements, i.e., root of square displacements, between $r - \Delta r/2$ and $r + \Delta r/2$ is counted and the occurrences are normalized by the bin volume, $\Delta V = 2\pi r\Delta r$. However, this procedure introduces a large degree of error at small $r$ values. This method also assumes a 2D underlying space, which is incorrect for diffusion on a fractal structure. A more suitable procedure involves computing the number of displacements and renormalizing the propagator in order to show $P\left(r,t\right)\Delta V$. Fig. 3.1B shows the propagators using the results from the CDF fits. For diffusion in a percolation cluster, the normalization volume, as given by Eq. 3.3, is $\Delta V_{d_f} = 2\pi^{d_f/2}r^{d_f-1}\Delta r/\Gamma(d_f/2)$. Fig. 3.1C shows the distribution of displacements normalized to a 2D space. The comparison shows that the raw-displacement occurrences (as shown in Fig. 3.1B) provide better visual results.

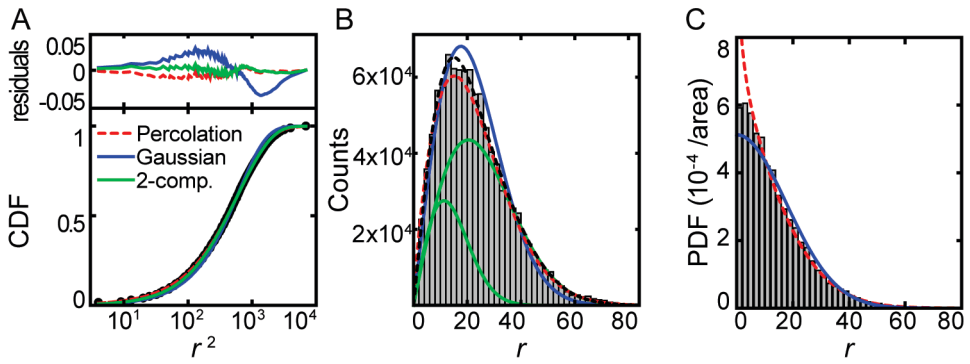


Figure 3.1: *Propagator analysis of diffusion of a representative trajectory in a percolation cluster close to criticality* The data were generated from the random walk simulations on a square lattice with an obstacle concentration of 41%, i.e. (a) CDF at $t$ = 10,000 with fits to percolation cluster as a dashed red line (Eq. 3.6), normal-diffusion as a solid blue line (Gaussian), and two-component mobility as a green line (light grey, Eq. 3.2). (b) Histogram of displacements. The continuous lines show the renormalized propagators , obtained from the fit to the CDF. Each Gaussian of the two-component mobility model is shown as a green line (light grey) independently for clarity and the sum of the two components is shown as a black dashed line. (c) Probability density function obtained by normalizing the distribution of displacements for $t$ = 10,000. The distribution is normalized by the volume , where $\Delta r$ is the bin size. The propagators of percolation-like- and normal-diffusion, as obtained from the fits to the CDF, are shown. Because the propagator of diffusion in a percolation cluster operates in $d_f$ dimensions, the curve shown is $P(r,t)^{\Delta V_{d_f}/\Delta V_{2D}}$, where $\Delta V_{d_f}$is the volume corresponding to a fractal dimension $d_f$, as in the text.

### 3.3.2 *Diffusion in a deterministic fractal*

The percolation cluster at criticality can be described by a random fractal with dimension $d_f$. Thus, it is interesting to compare this motion with the propagator for diffusion in a deterministic fractal, which was derived by O'Shaugnessy and Procaccia [144],

$$P(r,t) = \frac{d_w \Gamma\left(d_f/2\right)}{2\pi^{d_f/2}\Gamma\left(d_f/d_w\right)} \left(\frac{1}{4D_F t}\right)^{d_f/d_2} \exp\left(-\frac{r^{d_w}}{rD_f t}\right) \tag{3.7}$$

Integrating over the fractal volume [132] given by Eq. 3.2 yields

$$F\left(r^2,t\right) = \gamma\left(d_f/d_w, r^{d_w}/rD_F t\right)/\Gamma\left(d_f/d_w\right) \tag{3.8}$$

which includes three independent parameters, $d_f$, $d_w$, and $D_F$, that are constrained by the fractal structure: $1 < d_f \leq 2$ and $d_w \geq 2$. This model has been successfully applied to obstructed diffusion experimental measurements in supported lipid bilayers [132]. We have modeled our simulations using this equation and found a best non-linear fit when $d_w$ = 2.05 ± 0.05. This value disagrees with the value found from the MSD subdiffusive exponent ($d_w$ = 2.8). For comparison, the residuals for the deterministic fractal model with $d_w$ = 2 and $d_w$ = 2.8 are shown together with

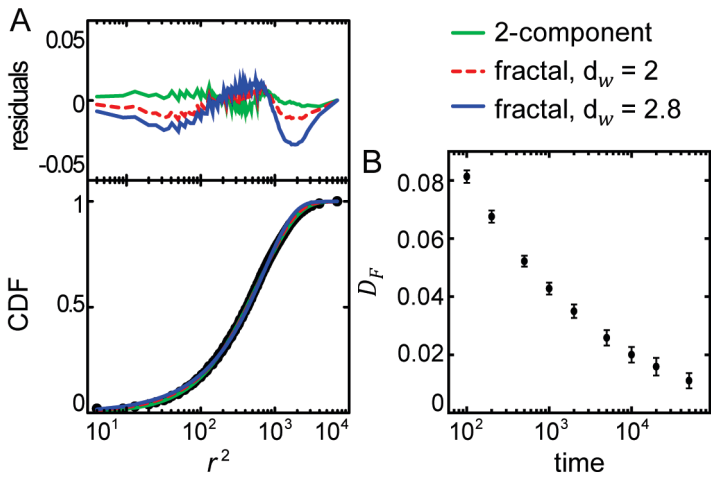


Figure 3.2: *CDF of simulated obstructed diffusion with obstacle concentration at lag time t = 10,000*. (a) The CDF of a representative trajectory is modeled by a deterministic fractal as given by Eq. 3.6. The best non-linear fit is found for $d_w = 2$ and $d_f = 1.6$ (dashed red line). Note that the fit is constrained by $d_w \geq 2$. For comparison the biexponential fit (Eq. 3.2) and the fit using $d_w = 2.8$ are also shown. (b) The diffusion coefficient $D_F$ is shown as found from fitting to the CDF at different lag times to a deterministic fractal model (Eq. 3.8). All the CDFs are described by $d_w = 2$.

the two-component model in Fig. 3.2a. Fitting Eq. 3.8 to the CDF of our simulation also yields a time-dependent coefficient $D_F$ (Fig. 3.2B), which is not consistent with a deterministic fractal, indicating the failure of this model to describe obstructed diffusion.

### 3.3.3 *Obstructed diffusion below the percolation threshold*

For the analysis of obstructed diffusion in cellular environments, it is necessary to consider a wider obstacle concentration range than that close to the percolation threshold. At criticality, an infinite percolation cluster is formed and diffusion is anomalous on all time scales [56]. At concentrations below the percolation threshold, Saxton [122] has shown that diffusion is anomalous at short times and becomes normal at long times. The crossover time increases as the concentration of obstacles approaches the threshold. The transition from anomalous to normal diffusion can be observed in plots of $\log\left[\langle r^2\rangle/t\right]$ as a function of $\log t$. Normal diffusion yields a constant while subdiffusion yields a power law with an exponent $(2/d_w) - 1$ [122]. This can be observed for concentrations below and at the percolation threshold in Fig. 3.3. It has been shown [122] that when the data are presented as a function of $c/c_P$, where $c$ is the obstacle concentration and $c_P$ the percolation threshold, the results do not depend on the lattice geometry or obstacle size.

Recently, a method to distinguish between FBM and a CTRW [64] has been reported. This test is based on the p-variation method and has been applied to experimental data describing the

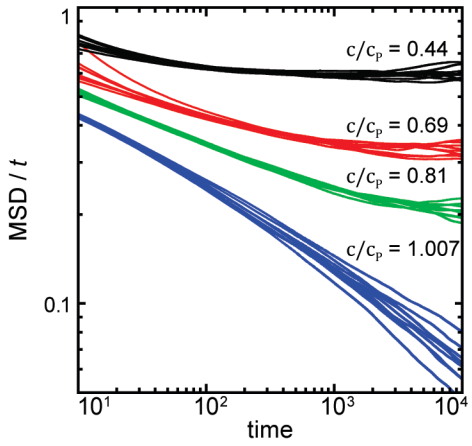


Figure 3.3: $\langle r^2 \rangle / t$ *as a function of* $t$ *in a log-log scale for a tracer in the presence of immobile obstacles at different concentrations.* $\langle r^2 \rangle$ is the mean square displacement and $t$ the lag time. All nine simulated trajectories are shown together for each obstacle concentration.

motion of mRNA in bacteria [130] and the dynamics of telomeres in the nucleus of mammalian cells [92]. The p-variation is defined as the limit of the partial sums of a random process $X(t)$, in a time interval $[0, T]$, raised to the power of $p$.

$$V_n^{(p)}(t) = \sum_{j=0}^{2^n-1} \left| X\left[\min(j+1)\frac{T}{2^n}, t\right] - X\left[\min j\frac{T}{2^n}, t\right] \right|^p \tag{3.9}$$

with

$$V^{(p)}(t) = \lim_{n\to\infty} V_n^{(p)}(t) \tag{3.10}$$

The total time is $T$, and the minimum value yields partial sums up to times shorter than $t$. In the case of FBM, the p-variation satisfies [64]

$$V^{(p)} = \begin{cases} +\infty & \text{if } p < \frac{1}{H} \\ t\alpha & \text{if } p = \frac{1}{H} \\ 0 & \text{if } p > \frac{1}{H} \end{cases} \tag{3.11}$$

$$\alpha = \frac{2^{1/2H}}{\sqrt{\pi}}\Gamma\left(\frac{1}{2H} + \frac{1}{2}\right) \tag{3.12}$$

where $H$ is the Hurst exponent and is related to the MSD subdiffusive exponent $\left\langle X(t)^2 \right\rangle \sim t^{2H}$.

For a CTRW results are different and the p-variation yields

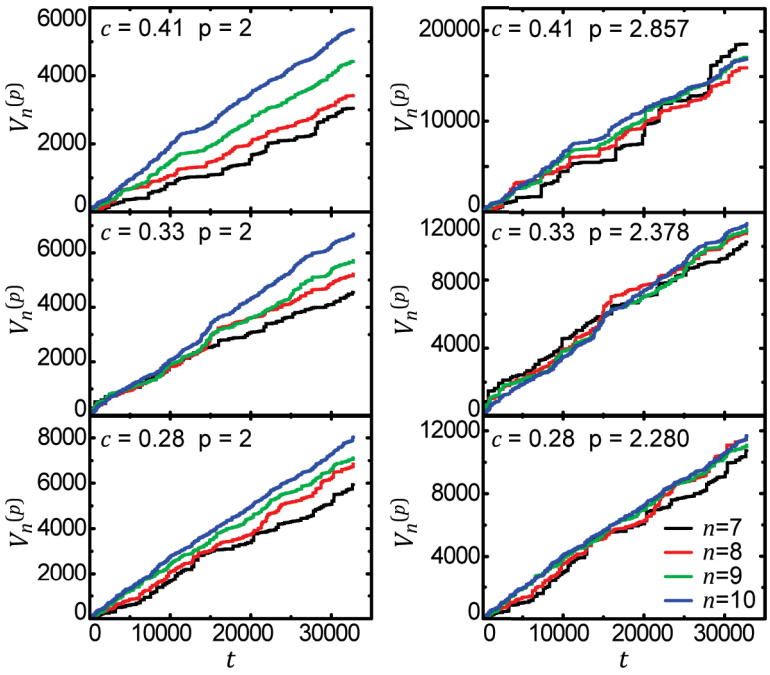


Figure 3.4: *p-variation analysis* $V_n^{(2)}(t)$ and $V_n^{(1/H)}$ obtained from the obstructed diffusion simulations at three different obstacle concentrations. $c = 0.41$ is at the percolation threshold. Four values of $n$ are presented, namely 7, 8, 9, and 10.

$$V^{(p)} = \begin{cases} +\infty & \text{if } p < \frac{1}{H} \\ S_\alpha(t) & \text{if } p = \frac{1}{H} \\ 0 & \text{if } p > \frac{1}{H} \end{cases} \tag{3.13}$$

where $S_\alpha(t)$ is the inverse $\alpha$-stable subordinator [64, 197].

We applied the p-variation test to our obstructed diffusion simulations. Following previous works [64, 130, 92] we implemented the p-variation test by computing the partial sums with p = 2 and p = $1/H$. $H$ was extracted from the previous analysis, $H = 1/d_w$. Results for $n$ = 7, 8, 9, and 10, at relative concentrations $c/c_P$ = 0.63, 0.80, and 1 are presented in Fig. 3.9. The p-variation applied to either the $x$ displacements or the $y$ displacements yields similar results, so only one of the two dimensions is shown.

Fig. 3.4 shows that for p = 2 the slope of $V_n^{(p)}$ increases as $n$ increases from 7 to 10, suggesting that the p-variation grows to infinity. However, for p = $1/H$, it appears that the slope of $V_n^{(p)}$

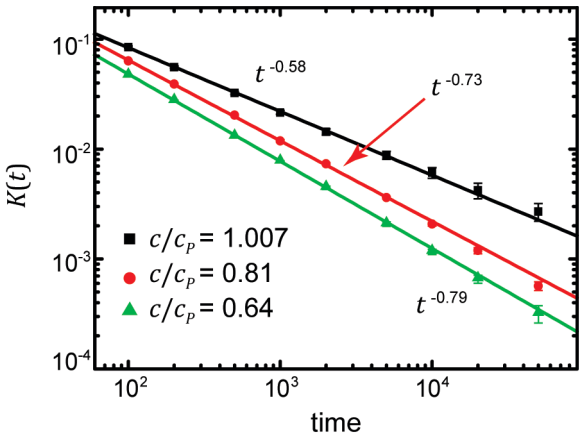


Figure 3.5: *Percolation fit parameter* $K(t)$ in Eq. 3.6 as a function of lag time at two moderate obstacle concentrations and close to criticality. The parameter exhibits a power law $K(t) = \alpha/t^{1.65/d_w}$.

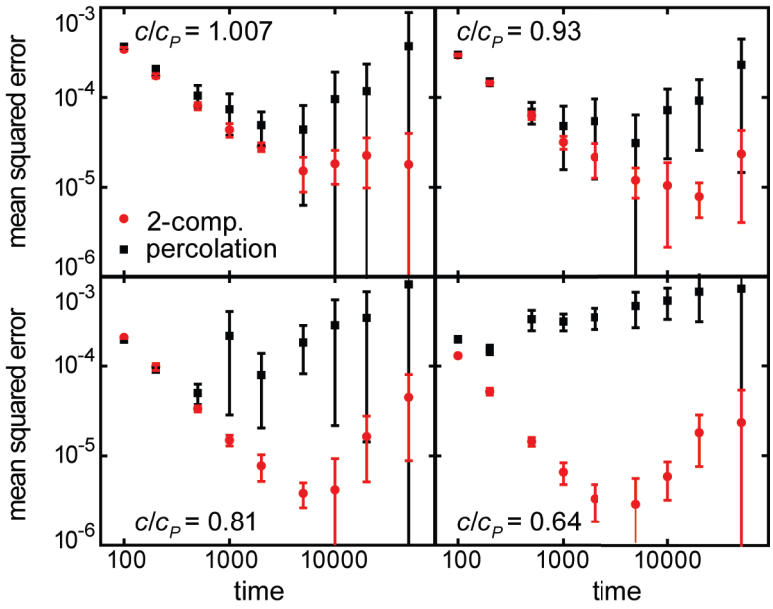


Figure 3.6: *Mean squared errors* Mean squared errors of the fits to the obstructed diffusion simulations with different obstacle concentrations using the 2-component mobility and the percolation cluster models.

fluctuates within a finite range without any clear dependence on $n$. These results are the same as that expected from a FBM process.

When the p-variation test was applied to the obstructed diffusion simulations the same results were obtained as those of FBM. The two diffusion processes are clearly different, which is most evident when examining the propagators. Obstructed diffusion has a non-Gaussian propagator for all obstacle concentrations and it approaches Eq. 3.4 as the obstacle concentration grows towards the percolation threshold. On the other hand FBM is characterized by a Gaussian propagator [198] with a time-dependent diffusion coefficient $D \sim t^{2H-1}$. Nevertheless, obstructed

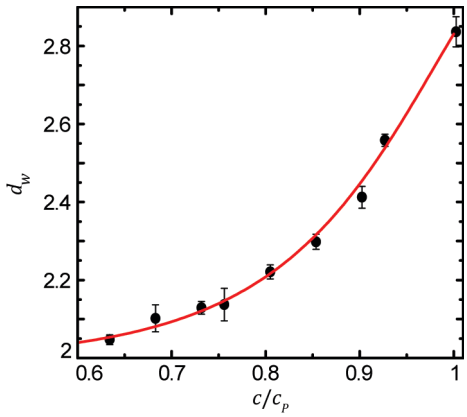


Figure 3.7: *Fractal dimension of the walk $d_w$ as a function of relative obstacle concentration.* $d_w$ is obtained from the fit to the percolation model as shown in Fig. 3.5. The red line is a least square fit to $d_w$ as performed in Ref.[122]: $d_w = (2-3.630x+1.758x^2)/(1-1.806x+0.850x^2)$, $x = c/c_P$, $c$ is the obstacle concentration and $c_P$ the concentration at criticality.

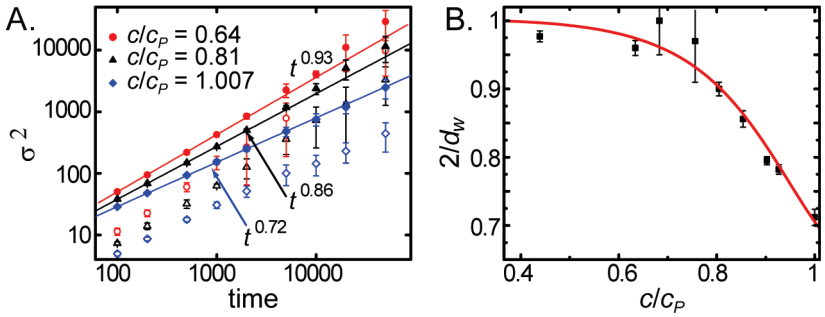


Figure 3.8: *Two-component mobility model*. A. MSD of each of the two mobilities. Full symbols: fast component. Hollow symbols: slow component. B. Subdiffusion exponent as a function of relative obstacle concentration. The red line is the function found from the least square fit in Fig. 3.7.

diffusion and FBM share similarities regarding long-time correlations and scaling laws. Therefore the p-variation test of percolation clusters shows similar results to those of FBM.

The main result obtained from the percolation propagator is the parameter $K(t)$ from Eqs. 3.4 and 3.6. Results are presented as a function of lag time in Fig. 3.5. $K(t)$ clearly follows a power law $K(t) = \alpha/t^{1.65/d_w}$. Note that while $d_w$ depends on the cluster size, $d_f$ is universal [56] thus $d_w$ is the only parameter that varies with obstacle concentration. To obtain a single scalar statistic for the goodness of fit, it is reasonable to use an aggregate or mean squared residual. This statistic is common in several standard goodness-of-fit tests, including the chi-square [199] and Cramér–von Mises [200] tests. Comparing the mean squared errors of the percolation model to that of the two-component mobility fit (Fig. 3.6), it is observed that at concentrations close to the

percolation threshold, both models give similar results. However, for lower obstacle concentrations, the results from the two-component mobility are significantly better.

The slope of $\log[K(t)]$ vs. $\log(t)$ in Fig. 3.5 is $-1.65/d_w$, thus, by means of the percolation cluster model, the fractal dimension of the walk $d_w$ is obtained for each obstacle concentration. Fig. 3.7 shows $d_w$ obtained in this manner for a wide range of obstacle concentrations. It is seen that $d_w$ increases smoothly from 2 to 2.8, reaching this value when the obstacle concentration equals the percolation threshold, i.e., $c = c_P$. This result is not surprising and it is the same that is obtained by fitting the MSD [122]. However, when the form of the propagator is known, fitting the propagator bears the advantage that the whole distribution of displacements is used instead of only the second moment. Because the whole distribution is used and the fit has a single unknown parameter, the accuracy of the obtained $d_w$ values is fairly high as seen by the small error in $d_w$ at each concentration. This reduces the need for averaging over many trajectories and also allows the study of shorter paths.

As expected, the MSD of the fast mobility in the two-component mobility model follows a similar trend as the percolation model with $\sigma_2^2 \sim t^{2/d_w}$. Results of $\sigma_i^2$ versus lag time are presented in Fig. 3.8A showing that $\sigma_2^2$ follows a power law. The time dependence of $\sigma_2^2$ yields $2/d_w$ (shown in Fig. 3.8B). At concentrations close to criticality this empirical model gives robust results but it becomes very unreliable for lower concentrations. Thus for lower concentrations the error bars in $2/d_w$ cover a large range from subdiffusion to superdiffusion rendering this model useless unless a very large amount of data is available.

### 3.3.4 *Derivation of a propagator for obstructed diffusion below the percolation threshold*

The exact propagator of this problem combines percolation-like diffusion at short distances and normal diffusion at long distances. The difficulty in this model is that the two parts operate on different dimensions. Percolation-like short-distance diffusion acts on $d_f$ dimensions but long-range normal diffusion is performed in two dimensions. Thus, we cannot integrate this function in a straightforward way because both parts have different Jacobians, i.e., different differential volumes. If we allow a percolation part $P_1 dV_1$ according to Eq. 3.3 and Eq. 3.4, and a normal diffusion part $P_2 dV_2$ according to Eq. 3.1, we obtain $P(r,t)\,dV = \omega P_1 dV_1 + (1-\omega)\,P_2 dV_2$. Then,

$$
\begin{aligned}
P(r,t)\,dV &= \left[\frac{1.65\omega}{\Gamma\left(\frac{2d_f-d}{1.65}\right)}K(t)^{\left(2d_f-d\right)/1.65}\,r^{2d_f-d-1}\right. \\
&\times \exp\left(-K(t)\,r^{1.65}\right) \\
&+ \left.(1-\omega)\,\frac{2r}{\sigma_1^2}\exp\left(-\frac{r^2}{\sigma_1^2}\right)\right]dr
\end{aligned}
\tag{3.14}
$$

where $\omega$, $K(t)$, and $\sigma_1$ are defined previously. All three parameters are time dependent. The cumulative distribution function is

$$
\begin{aligned}
F\left(r^2,t\right) &= \omega\frac{\gamma\left[\left(2d_f-d\right)/1.65, K(t)\,r^{1.65}\right]}{\Gamma\left[\left(2d_f-d\right)/1.65\right]} \\
&+ (1-\omega)\left(1-e^{-r^2/\sigma_1^2}\right)
\end{aligned}
\tag{3.15}
$$

These equations give the accurate distribution of displacements for obstructed diffusion with any obstacle concentration below the percolation threshold. However, as in the two-mobility model they involve three different fitting parameters, which means that more data is needed to fit this function than the simple percolation approximation.

### 3.3.5 *Comparison to experimental data*

It is possible to use the percolation model to obtain information on the obstacle concentration for diffusion in an obstructed environment. Kv2.1 potassium channels are best modeled by a non-ergodic CTRW on a percolation cluster [49]. However, when cells are treated with actin polymerization inhibitors, such as swinholide A, the CTRW is eliminated and ergodicity is recovered. After treatment with swinholide A, the diffusion is still anomalous over lag times of more than two decades (Fig. 3.9A). We have previously proposed [30] that the reason for this anomaly is the presence of immobile obstacles in the plasma membrane which obstruct the path of the Kv2.1 channels. While in three dimensions a particle easily finds a path to escape from obstacle-induced

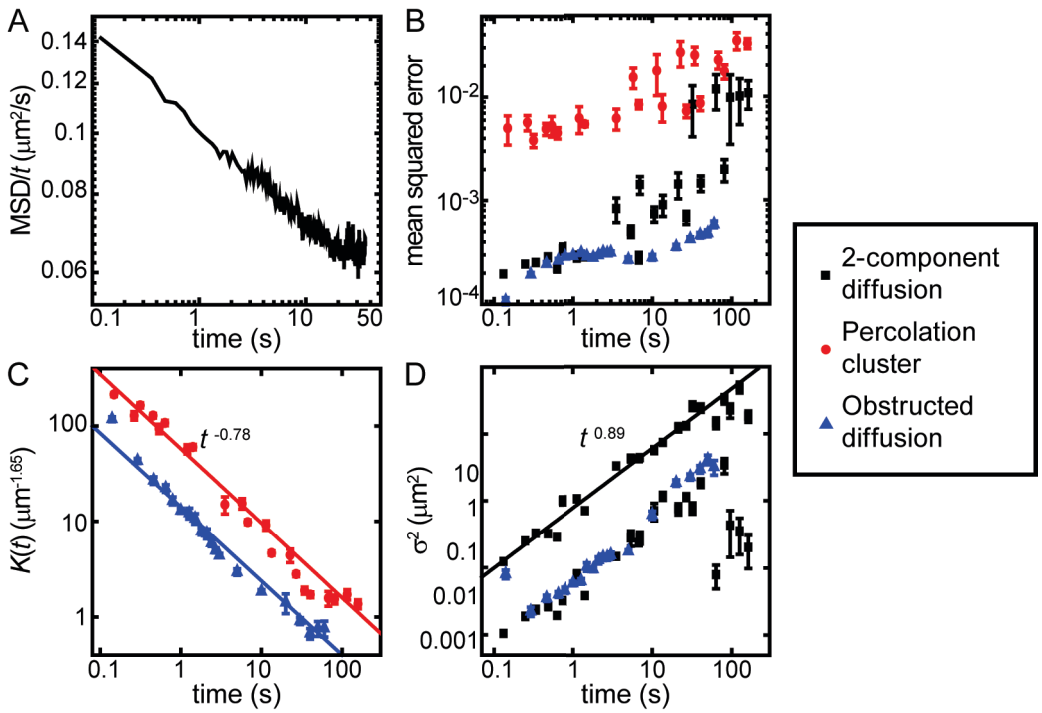


Figure 3.9: *Analysis of experimental Kv2.1 single-particle tracking in the plasma membrane of living HEK cells*. All error bars indicate standard error of the mean. (a) $\langle r^2 \rangle / t$ as a function of $t$ in a log-log scale. A negative slope between 0.1 and 20 s is evident indicating anomalous subdiffusion across this time scale. (b) Mean squared errors from fitting the CDF at different lag times to three different models as described in the text: 2-component mobility, percolation cluster, and obstructed diffusion. (c) $K(t)$-values as a function of $t$, obtained from fitting the experimental data to the percolation cluster and obstructed diffusion. A power law dependence is obtained from which $d_w$ is found. (d) Mean square displacements obtained by modeling the experimental data with 2-component mobility [$\sigma_1^2$ and $\sigma_2^2$ in Eq. 3.2], and with obstructed diffusion [$\sigma_1^2$ in Eq. 3.15. The slow-mobility component MSDs from the two different models coincide.

compartments, in 2D the confinement within finite percolation-like compartments is enhanced because there are fewer escape paths [143].

Fig. 3.9B shows the mean squared errors obtained from fitting the CDF of Kv2.1 channels in cells treated with swinholide A to a percolation cluster (Eq. 3.6), to a two-component mobility model (Eq. 3.2), and to the subcritical obstructed diffusion propagator derived in Eq. 3.15. The obstructed diffusion propagator gives the smallest mean squared errors over all lag times. These results correspond to the mean from 158 trajectories. A mixed propagator result is shown in Fig. 3.10 together with the plots for $\omega = 0$ and$\omega = 1$. The percolation cluster and the obstructed diffusion models yield values of $K(t)$ that scale as a power law in the same fashion as the obstructed diffusion simulations (Fig. 3.9C). From these fits, the fractal dimension of the walk is obtained, $d_w = 2.12 \pm 0.08$. It is also observed in Fig. 3.9C that both models yield very similar values for $d_w$. Using the empirical fit in Fig. 3.7, $d_w = \left(2-3.630x+1.758X^2\right)/\left(1-1.806x+0.850x^2\right)$ , where $x = c/c_p$, we can calculate the relative obstacle concentration. A range between 0.62 and 0.79 is

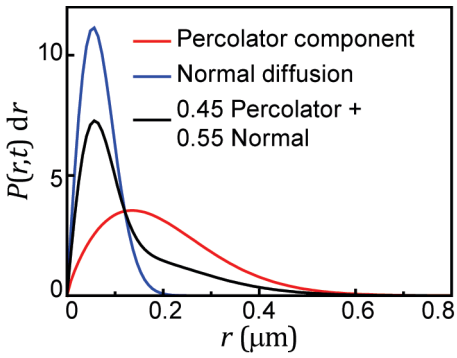


Figure 3.10: *Mixed propagator* Mixed propagator with $\omega = 0.45$ as defined in Eq. 3.14 for $t = 1$ s. For comparison the components obtained with $\omega = 0$ and $\omega = 1$ are also shown.

obtained for $c/c_P$. Fig. 3.9D shows the results of the fast- and slow-mobility MSDs from the two-component model and the slow mobility (long-range) MSD from the obstructed diffusion model. The long-range MSDs for the two models match satisfactorily but the values obtained with the obstructed diffusion propagator are less prone to errors, particularly at large lag times.

## 3.4 DISCUSSION

Analysis of the CDF at different lag times provides important information. The simulations presented here show that, independent of the obstacle concentration, the CDF can be approximated to either a two-component mobility model or a percolation cluster. One could always argue that the two-component mobility model introduces two additional fitting parameters and thus the model fits better to the simulation in the trivial way, regardless of the actual process. However, the two-component model actually approaches the propagator of obstructed diffusion because the obstacles form fences which in turn compartmentalize the cell membrane. Thus, for short distances, the particle moves according to a fast mobility within a single compartment. For long distances, the particle traverses several compartments and it resembles to be diffusing with a slow mobility. The reason this model is not exact is that at short distances the motion is performed within a finite percolation cluster, thus the substrate is a random fractal of dimension df, but at long distances the motion is normal according to a substrate with dimension $d = 2$.

The percolation propagator gives excellent results close to the percolation threshold. At small obstacle concentrations, this model fits worse than the two-component mobility. The cause for the

deterioration of the fit quality is that the percolation model does not account for the transition to normal diffusion. In spite of this shortcoming, the percolation model can be used to obtain information on the membrane structure without the need for extensive data. We observe that this model is more robust than the two component model.

The analysis presented here suggests Kv2.1 channels in cells treated with swinholide A undergo anomalous diffusion due to an intermediate concentration of immobile obstacles leading to transient percolation-like motion. The presence of anchored proteins has been proposed by Kusumi and co-workers to be partially responsible for the diffusion anomaly seen in the plasma membrane [9]. Complexity in cell membranes is also enhanced by the presence of slow and fast moving obstacles. Experimental evidence shows that the diffusion of streptavidin in solutions crowded with bovine serum albumin (BSA) is anomalous [171]. Diffusion of proteins in solutions of random-coil polymers at high concentrations is significantly more anomalous than in BSA solutions [171, 129]. It was proposed that subdiffusion induced by rapidly moving obstacles may be grounded in a FBM process [129]. Whether anomalous diffusion in the nucleus and cytoplasm is percolation-like or FBM is still under debate [92]. Scaling similarities between the two models further complicates the discrimination. In the plasma membrane of a living cell, it is likely that both mobile (fast- and slow-moving) and immobile obstacles are present and maybe both FBM and percolation are responsible for the diffusion anomaly. This problem may be addressed in the future by studying supported lipid bilayers under controlled conditions in order to discriminate between these two processes. Equations 3.14 and 3.15 derived here provide a good platform for the analysis of the obstructed diffusion component.

## 3.5 CONCLUSIONS

In conclusion, we have provided a method for the analysis of propagators of obstructed subdiffusion in single-particle tracking data. The propagator for the percolation cluster at criticality is explicitly given and is shown against Monte Carlo simulations, in order to eliminate confusion and disagreement commonly found in the literature. We have also derived the propagator for obstructed diffusion at obstacle concentrations below the percolation threshold by combining a percolation model with hop diffusion between obstacle-induced compartments. By analyzing the

time dependence of the propagator, it is possible to obtain information on the concentration of immobile obstacles. Experimental data from Kv2.1 channels in live mammalian cells treated with an actin polymerization inhibitor were analyzed using the derived obstructed diffusion propagator. The obstructed diffusion propagator provided good agreement with the experimental data. The discrimination between percolation and fractional Brownian motion is shown to be highly complex, even with the use of advanced tests such as the p-variation method. The propagators of the two models are qualitatively different, but a non-Gaussian propagator as seen here is not enough to exclude the combination of both obstructed diffusion and FBM.

## 3.6 ACKNOWLEDGEMENTS AND CONTRIBUTIONS

Michael Tamkun and Diego Krapf designed the research. Shankarachary, Diego Krapf, and Edwin Chong contributed analytical tools. Aubrey Weigel performed the research. Aubrey Weigel, Diego Krapf and Michael Reid analysed the data.

# CHAPTER 4: KV2.1 CELL SURFACE CLUSTERS ARE INSERTION PLATFORMS FOR ION CHANNEL DELIVERY TO THE PLASMA MEMBRANE

Voltage-gated $K^+$ (Kv) channels regulate membrane potential in many cell types. While the channel surface density and location must be well-controlled, little is known about Kv channel delivery and retrieval on the cell surface. The Kv2.1 channel localizes to micron-sized clusters in neurons and transfected HEK cells where it is non-conducting. Since Kv2.1 is postulated to be involved in SNARE-mediated membrane fusion, we examined the hypothesis thatt hese surface clusters are specialized platforms involved in membrane protein trafficking. total internal reflection (TIR)-based FRAP studies and quantum dot imaging of single Kv2.1 channels revealed that Kv2.1-containing vesicles deliver cargo att he Kv2.1 surface clusters in both transfected HEK cells and hippocampal neurons. Greater than 85% of cytoplasmic and recycling Kv2.1 channels were delivered to the cell surface att he cluster perimeter in both cell types. At least 85% of recycling Kv1.4, which unlike Kv2.1 has a homogenous surface distribution, is also delivered here. Actin depolymerization resulted in Kv2.1 exocytosis at cluster-free surface membrane. These results indicate that one non-conducting function of Kv2.1 is to form microdomains involved in membrane protein trafficking. This study is the firstt o identify stable cell surface platforms involved in ion channel trafficking.

## 4.1 introduction

As described in the Introduction, chapter 4, the Kv2.1 channel holds clear physiological importance and its stable cell surface clusters are highly unique. Our previous work using cell-attached patch clamp indicates thatt he Kv2.1 channel within the clusters is non-conducting, with whole cell Kv2.1 current likely derived from a sub-population of non-clustered channels [120]. However, the clustered channels produce gating currents and are therefore capable of sensing membrane potential, potentially linking plasma membrane electrical activity to intracellular events similar to the function of L-type Ca2+ channels att he skeletal muscle T-tubule/SR junction [ 201]. One intriguing possibility given the SNARE protein interactions [202, 203, 204] is thatt he Kv2.1 clus-

ters couple membrane potential to secretion and/or the delivery of membrane cargo to the cell surface.

In this chapter we use QD labeling and TIRF imaging approaches to test the hypothesis that the Kv2.1 plasma membrane clusters are specialized platforms involved in the trafficking of membrane proteins to and from the cell surface. Hundreds of observations detail the location of Kv2.1 plasma membrane insertion for both nascent and recycling Kv2.1 channels as well as the location of endocytosis from the surface. The data indicate that Kv2.1 clusters represent platforms for the insertion and endocytosis of not only Kv2.1 but also the unrelated $K^+$ channel, Kv1.4. This study is the first to define stable cell surface sites for Kv channel delivery in mammalian cells.

## 4.2 MATERIALS AND METHODS

### 4.2.1 *Plasmid constructs, cell culture and transfections*

Fluorescent protein tagged caveolins 1 and 3 have been previously used by other investigators [205]. Human clathrin light chain (CLC) A sub-cloned into the mRFP-C1 and eGFP-C1 expression vectors was kindly provided by Dr. Santiago Di Pietro (Department of Biochemistry and Molecular Biology, Colorado State University). HEK 293 cells (American Type Culture Collection, passage 38-45) cells were transfected with 1-3 μg of Kv2.1 expressing DNA and 1μg of pSec BirA using a BioRad Genepulser Xcell (BioRad Laboratories, Hercules, CA) with a 0.2 cm gap cuvette and a single 110 V 25 ms pulse. Transfected cells were plated on glass-bottom 35 mm dishes (Matek, Ashland, MA and Bioptech that had been previously Matrigel-coated and covered in DMEM + 10% fetal bovine serum. HEK cells were imaged within 24 h of electroporation in HEK physiological imaging saline 8.6. Neurons from cryo-preserved E18 rat hippocampal dissociations were plated at a density of ~ 15,000 - 30,000 cells/cm² on poly-D-lysine coated glass-bottom dishes (Matek) and cultured in glial-cell conditioned neurobasal medium containing B27 supplement (Invitrogen) as previously described [117]. Animals were deeply anesthetized with isoflurane and euthanized by decapitation according to a protocol approved by the Institutional Animal Care and Use Committee (IACUC) of Colorado State University. Transfections were performed after 6 - 8 days in culture with 2.0 μl of Lipofectamine 2000 (Invitrogen) and 0.75 μg of Kv2.1-expressing plasmid DNA in 100 μl OptiMem (Invitrogen) according to the manufacturer's directions. When

necessary 0.5 μg of pSec BirA expressing DNA was co-transfected. Two-hours after transfection, the culture medium was replaced with fresh Neurobasal/B27 media. Neurons were imaged 24 - 48 hours post-transfection in neuronal imaging saline consisting of (in mM) 126 NaCl, 4.7 KCl, 2.5 $CaCl_2$, 0.6 $MgSO_4$, 0.15 $NaH_2PO_4$, 0.1 ascorbic acid, 8 glucose, and 20 HEPES, pH 7.4.

### 4.2.2 *Antibody and quantum dot labeling*

Neurons expressing GFP-Kv2.1 were fixed in 4% formaldehyde, 4% sucrose in phosphate buffered saline (PBS) for 15 min, incubated in 0.5% 3-[(3-Cholamidopropyl) dimethylammonio]-1-propanesulfonate (CHAPS) in PBS for 5 min, blocked in 5% non-fat milk and 1% goat serum in PBS for 1 h, and labeled with the indicated antibody diluted in PBS containing 1% BSA. A mouse monoclonal anti-MAP-2 antibody (Sigma, 1:2000 dilution) was used in conjunction with a goat anti-mouse secondary antibody conjugated to Alexa 594 (Molecular Probes) diluted 1:1000 in 1% BSA PBS. Live HEK cells expressing GFP-Kv2.1-HA were labeled with Alexa 594-conjugated anti-HA antibody (1:1000 dilution in 1% BSA containing HEK imaging saline) in order to detect and monitor internalization of surface GFP-Kv2.1-HA. HEK cells were labeled for 5 to 10 minutes at 37˚C before being rinsed and imaged at 37˚C. For QD labeling cells expressing either BAD-containing Kv1.4 or Kv2.1 constructs were first incubated in 1% BSA (Sigma, IgG/fatty acid-free) in imaging saline for 5 min and then incubated for 5 min with 0.1 nM streptavidin-conjugated QDs (QD605 or QD655 from Invitrogen) in imaging saline containing 1% BSA 8.4. The BSA was essential to minimize nonspecific QD absorption to the cell surface and coverslip. The QD concentration and incubation time were empirically determined to minimize both nonspecific and specific QD binding, for it is increasingly difficult to track individual QDs as the cell surface QD number increases. The cells were then rinsed extensively with imaging saline and either returned to the tissue culture incubator or placed on a heated microscope stage. All incubations were performed at 37˚C. Controls for nonspecific QD binding included imaging cells expressing GFP-Kv2.1-HA that had been carried through the entire QD labeling protocol or using cells expressing GFP-Kv2.1-loopBAD that were not co-transfected with the BirA biotin ligase.

### 4.2.3 *Confocal and TIRF microscopy*

HEK cells and neurons expressing fluorescent protein tagged constructs were imaged with one of five microscope systems depending on the experiment performed. Standard 3D imaging, 0.3 μm z steps, was performed with an Olympus FV1000 confocal microscope equipped with spectral detectors and the SIM scanner. GFP was excited using the 488 nm line of an argon laser and emission was collected using the variable bandpass filter set at 500-530 nm. Alexa 594 fluorophores were detected using a 543 nm HeNe laser with the variable bandpass filter set at 600-630 nm. A 60X, 1.4NA oil immersion objective was used for imaging and the pinhole diameter set for the appropriate Airy unit when using one laser. An intermediate pinhole diameter was used when two fluorophores were being detected simultaneously. For each image, the detector voltage was adjusted as necessary to utilize the full 12-bit range.

Experiments examining the insertion sites of intracellular, as opposed to recycling, channels were performed on one of two Olympus microscope systems, each equipped with a Yokogawa CSU-22 spinning disk head. The confocal nature of these systems combined with the CCD camera sensitivity was required to image cells bathed in the 1 nM QD solution required by the insertion site assay described below. The first system is built around an Olympus IX81 stand using a 100X, 1.4 NA Plan Apo objective and a 1024x1024 Cascade EMCCD camera operated at -80˚C, 2x2 binning and maximum electronic gain. Temperature control was via a forced air incubation chamber surrounding the stage and objectives. The second spinning disk confocal scope is built around an Olympus IX71 stand equipped with an Olympus 100x, 1.45 NA, TIRFM Plan Apo objective and an Andor 512x512 iXon DU-897 EMCCD camera operated at -85˚C and an electronic gain of 300. Temperature control here was via a Zeiss/Pecon stage heating insert and objective heater. Both systems use acousto-optic tunable filter (ATOF) controlled lasers and standard dichroic mirror and filter sets for detecting fluorescent proteins and QDs. Exposure times varied between 20-100 ms using frame rates of 0.5-20 Hz.

Two different TIRF imaging systems were used to detect QDs bound to Kv2.1 and Kv1.4 channels. The first is described in Chapters 4 and 4. Simultaneous two color imaging was achieved by optically splitting the image into two halves, each corresponding to a separate color, using an Optosplit (Cairn, Ireland). Both the tissue culture dish and the objective were maintained at 37°C

using heating elements from Bioptechs (Butler, PA). Videos (>5000 frames) were acquired using Andor IQ software at an average frame rate of 8 frames per second. The second TIRF system is a Nikon Eclipse Ti Perfect-Focus equipped TIRF/widefield fluorescence microscope equipped with AOTF controlled 405, 488, 543 nm diode lasers, 100 mW each, and an Intensilight wide-field light source. A 100X PlanApo TIRF, 1.49 NA, objective was used for image acquisition. Emission was collected through a Sutter Lambda 10-3 filter wheel containing the appropriate band pass filters. The stage and objective are temperature controlled via a Zeiss/Pecon stage heating insert and objective heater at 37°C. This microscope is equipped with the Andor iXon EMCCD DU-897 camera, 512x512. For all imaging experiments, the cells were imaged for less than one hour. However, no changes in the Kv2.1 surface expression were observed after up to 3 h in imaging saline at 37°C.

In order to view the activity of sub-membranous Kv2.1-containing trafficking vesicles, a TIR-based photobleach approach was employed with the Nikon TIRF system. GFP-Kv2.1 or YFP-Kv2.1 expressing HEK cells or hippocampal neurons in close contact with the bottom of the dish were bleached in TIRF to decrease the intensity of the cell surface Kv2.1-containing clusters. A one min bleach at 100% 488 nm laser power was performed in triplicate with a one min delay between each bleach. These three steps reduced the intensity of both the immobile Kv2.1 clusters and the free, non-clustered Kv2.1 diffusing into the basal surface from the top of the cell. The bleached cells were imaged at 1-3% 488 laser power for up to 45 minutes to capture vesicular activity. Since intracellular vesicles are mobile and thus not consistently within the TIRF field they are less susceptible to bleach than the cell surface clusters. Image sequences were analyzed in Volocity 6.0 and ROI specific fluorescence intensity changes over time were quantitated and background subtracted. Cytoplasmic vesicles were defined by their size, fluorescence intensity, and trafficking motility (see Figure 4.3).

### 4.2.4 *Detection of intracellular channel insertion into the plasma membrane*

The QD-based assay to detect the location of Kv2.1 cell surface insertion with single molecule sensitivity involved first incubating cells expressing biotinylated GFP-Kv2.1-loop BAD with 1 μM neutravidin for 5 min in imaging saline containing 1% BSA. Neutravidin was used to saturate the biotinylated Kv2.1 channels on the surface because it has less nonspecific binding activity than

streptavidin and thus the excess neutravidin is easier to remove in the following washes. After 4 to 5 washes in imaging saline containing 1% BSA, the cells were imaged in the presence of 1 nM 605 QDs using a spinning disk confocal. This QD concentration was required to minimize nonspecific binding during the relatively long imaging periods.

### 4.2.5 *Detection of channel recycling*

The dissociation rate of biotin-streptavidin binding is relatively slow, with 4 and 25% dissociation over 1 h at 37˚C for biotin-conjugates or biotin, respectively [206, 207]. HEK cells and neurons expressing biotinylated channels were labeled with QDs at low efficiency as described above and then returned to the tissue culture incubator for 1-2 h to allow endocytosis and recycling to the cell surface to approach steady-state. The cells were then removed from the incubator and imaged using one of the TIRF systems described above. Spontaneous QD appearance represents a cytoplasmic channel previously on the cell surface now entering the 100 nm TIRF field, i.e. approaching or inserting into the membrane. Spontaneous loss of a cell surface QD represents a channel undergoing endocytosis.

### 4.2.6 *Quantitation of QD blinking behavior*

Since many of the experiments presented here rely on QD appearance or disappearance as an indication of exocytosis or endocytosis, the possibly of QDs entering or exiting such a dark state was a serious concern. To address this issue we examined the distribution of dark state life-times under our imaging conditions and with the QD reagents used in this study. Since QD blinking behavior is sensitive to the environment [208] we chose to immobilize QDs on the HEK cell surface as opposed to glass. HEK cells where incubated with a 1 nM HEK imaging saline solution for 5 min at 37˚C. This solution lacked the 1% BSA used to inhibit nonspecific binding as described above. Therefore, the cells had immobile QDs adhered non-specifically to the cell surface and imaging these over time provided a quantitative measurement of BSA blinking behavior and dark state lifetimes under the imaging conditions used. The nonspecifically bound QDs were imaged for 30 min at 2-10 Hz using laser intensities typical for the experiments presented here. The distribution of dark state durations is presented in Fig. 4.9 in addition to three examples of blinking and/or

dark state behavior. Dark states lasting longer than 60 s were rare, representing only 3% (14 of 460) of total blinking events > 3 sec ( 22,458 s of total QD imaging).

### 4.2.7 *Actin disruption*

Actin depolymerizing agents, cytochalasin D and swinholide A, were used to disturb the cytoskeletal network. Both actin inhibitors were dissolved in DMSO (Sigma-Aldrich) and added while imaging to a final concentration of 125 nM, 5 μM for swinholide A and cytochalasin D, respectively. Cells were imaged up to 20 min after drug application.

### 4.2.8 *Image presentation and data analysis*

Images were imported into Volocity 6.0 software for contrast enhancement, 3D reconstruction, object detection/tracking and quantitative analysis. Numerical data were exported into Origin Pro 8.5 for further analysis and curve fitting. Image sequences were analyzed for the location of QD appearance, i.e. membrane insertion, or disappearance, i.e. endocytosis, by both manual inspection and an automated analysis. In the case of the manual analysis, QDs that appeared or disappeared within 2 μm of the cell perimeter were not counted due to concerns that they may be just entering or leaving the basal cell surface. QDs were classified as entering or leaving the surface at a Kv2.1 cluster if the appearance or disappearance occurred within 0.5 μm of the cluster perimeter. Potential dark states less than 60 s were deemed most problematic and were dealt with as follows. Only QD appearances that occurred more than 60 s following the disappearance of a QD within a 1 μm radius where counted as indicating surface insertion, as opposed to representing detection of the same QD emerging from a dark state. The same logic applied to QDs that disappeared only to be followed by reappearance in less than 60 s less than 1 μm away, i.e. these QDs were not counted as being internalized by the cell. For the automated detection and tracking of QD labeled Kv2.1 and Kv1.4 channels we used a multiple-target tracing (MTT) approach based on the algorithm developed by Serge et al [209, 210], see Appendix 5 for more details, 9.3.2. This analysis provides the positions and intensities for each frame of targets throughout the entire video duration, allowing for determination of the time and location of newly arriving channels to the cell surface. Using the results of the MTT algorithm, QD tagged Kv1.4 and Kv2.1 channels that arrived to the cell surface after a delay relative to the start of the image sequence (to allow

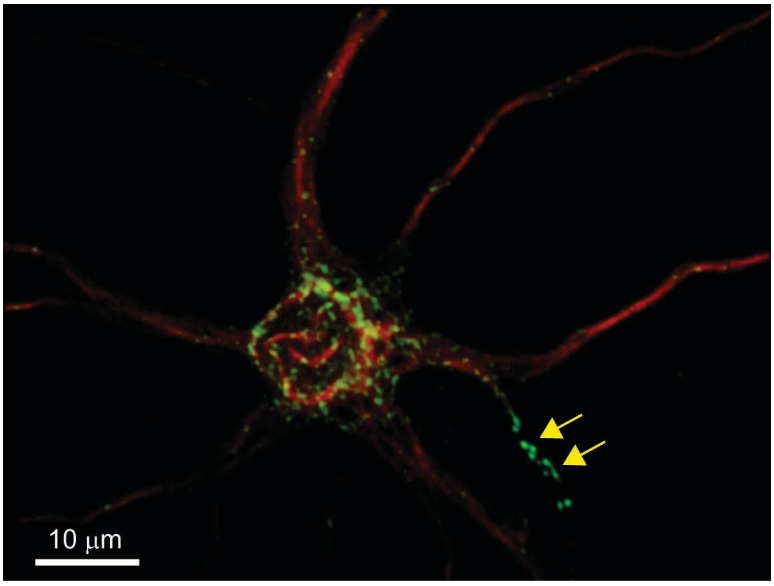


Figure 4.1: *Kv2.1 localizes to clusters on the neuronal cell surface.* 3D reconstruction of confocal sections of an 8 DIV rat hippocampal neuron expressing GFP-Kv2.1 (green). The cell was fixed and labeled with Alexa 594-conjugated anti-MAP2 antibodies (red) to identify the soma and dendrites. The arrows indicate Kv2.1 clusters within the MAP2-negative axon initial segment.

for potential QD dark states) were categorized as arriving to a cluster or not. This classification was determined by overlaying the individual QD tagged channel signal with the ensemble GFP channel signal along with the MTT algorithm trajectories. If the channel arrived within one pixel of cluster perimeter (1 pixel = 130 nm) it was categorized as arriving to a cluster, and similarly for channels not arriving to a cluster. Channels that appeared to diffuse from the side of the cell to the basal surface were discarded. The percentages of recycling Kv2.1 channels inserting at a Kv2.1 cluster perimeter were 75 and 76 for the 25 and 60 s delays, respectively. Since these numbers are similar, QD dark states are unlikely to contribute significantly to this automated insertion site detection.

## 4.3 RESULTS

### 4.3.1 *Kv2.1 localizes to clusters on the neuronal cell surface*

The 3D reconstruction presented in Fig. 4.1 illustrates the surface distribution of GFP-Kv2.1 following expression in cultured hippocampal neurons. The clusters are distributed evenly over the soma, concentrated at the MAP2 negative axon initial segment and present to a limited extend within the MAP2 positive proximal dendrites as previously described [211]. This expression

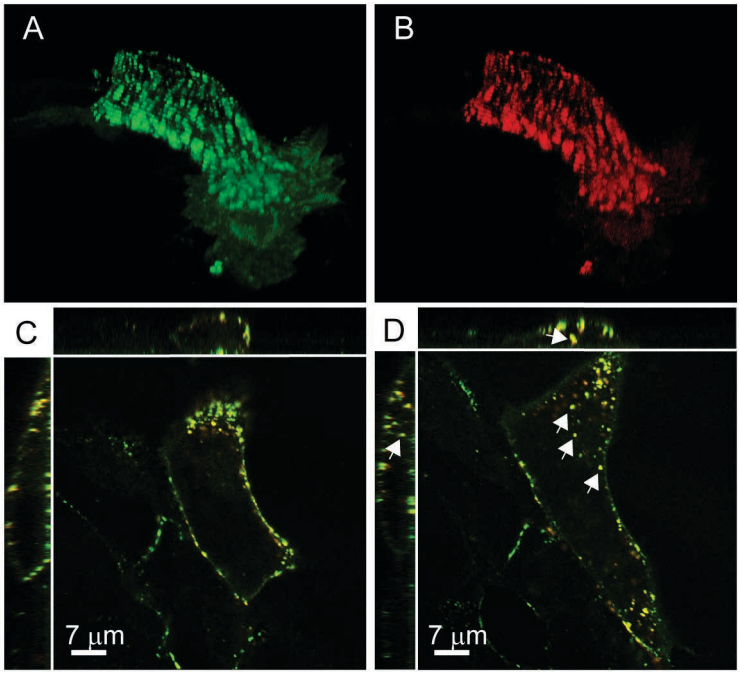


Figure 4.2: *Kv2.1 traffics efficiently to the cell surface in transfected HEK cells and is rapidly internalized.* (A) GFP-Kv2.1-HA expression pattern 16 h post-transfection. The GFP fluorescence in this 3D reconstruction of confocal sections is illustrated in green. (B) Detection of cell surface GFP-Kv2.1-HA in the same cell. The red indicates the binding of Alexa 594-conjugated anti-HA antibody to the external HA epitope. Image shown was taken immediately after antibody binding to live cells. (C) XYZ view of the GFP and anti-HA antibody localization patterns in the same cell as in A and B. (D) Same cell as in C after 10 additional min at 37oC. Note the internalization of the anti-HA antibody that appears as yellow puncta due to the overlay of the GFP and AlexaFluor594 fluorescence (arrows).

pattern also exists in the intact brain [119] and in acutely isolated brain slices [212, 213]. Our previous work indicates that the localization mechanism involves the trapping of mobile channels behind a cytoskeletal-based diffusion barrier as opposed to individual channels being statically tethered to sub-membrane anchors [133, 49].

### 4.3.2 *Kv2.1 exists primarily on the cell surface but rapidly recycles between membrane and intracellular compartments*

Kv2.1 localizes to micron-sized clusters in transfected HEK cells that are similar to those present in cultured and native hippocampal neurons [119, 214, 117]. We chose to initially examine Kv2.1 trafficking in transfected HEK cells since these cells lack endogenous Kv2.1 [117, 120]. Therefore, all the Kv2.1 in transfected cells is readily detectable using the attached fluorescent proteins and epitope tags. HEK cells were transfected with a modified Kv2.1 carrying GFP on its N-terminus and an anti-hemagglutinin antibody epitope on the extracellular surface (GFP-Kv2.1-HA) between the first two transmembrane domains [117]. Fig. 4.2A shows a 3D reconstruction of the

GFP fluorescence. Note that Kv2.1 also exists outside the clusters on the cell surface. This construct, and all others used in our work, demonstrate wild-type channel trafficking and function [120]. Panel B illustrates the binding of an AlexaFluor 594-conjugated anti-HA antibody to the same live, non-permeabilized cell confirming that the Kv2.1 channel is on the cell surface. Fig. 4.2C shows the same cell in a XYZ format immediately after AlexaFluor 594 anti-HA antibody labeling. The lack of readily detectable GFP fluorescence within the cytoplasm demonstrates that in transfected HEK cells the trafficking of Kv2.1 to the surface is highly efficient as compared to other Kv channels [215, 216, 217]. Fig. 4.2D shows the same antibody-labeled cell 10 min later. Intracellular AlexaFluor 594 is now detected (arrows), demonstrating that Kv2.1 is internalized over this time frame. The goal the following experiments was to test the hypothesis that the Kv2.1 clusters act as cell surface platforms involved in the transport of Kv2.1, and other membrane proteins, to and from the cell surface.

### 4.3.3 *Intracellular Kv2.1-containing trafficking vesicles dock at the Kv2.1 cell surface clusters*

If Kv2.1 recycles between cell surface and intracellular compartments we should be able to detect an intracellular Kv2.1 channel vesicular population using appropriate techniques. We applied a TIR photobleaching approach to remove the cell surface cluster fluorescence and allow detection of a weak vesicular intracellular signal normally masked by the high intensity surface clusters. Putative trafficking vesicles were detected following photobleach of the surface YFP-Kv2.1 in transfected HEK cells. Vesicular movement was often directed and occurred with rates of 1.4 ± 0.5 $\mu$m/s, n = 13, consistent with motor based transport as opposed to random diffusion. We next determined the number of Kv2.1 channels present in each cytoplasmic vesicle. HEK cells were transfected with GFP-Kv2.1 and following TIR-photobleach single GFP molecule fluorescence intensity was determined by quantitating the bleach step magnitude of single GFP-Kv2.1 channels observed on the cell surface. This single step intensity was then compared to that of individual trafficking vesicles fusing with the cell surface to estimate the number of Kv2.1 channels contained within each vesicle, assuming four GFP molecules per channel tetramer. As summarized

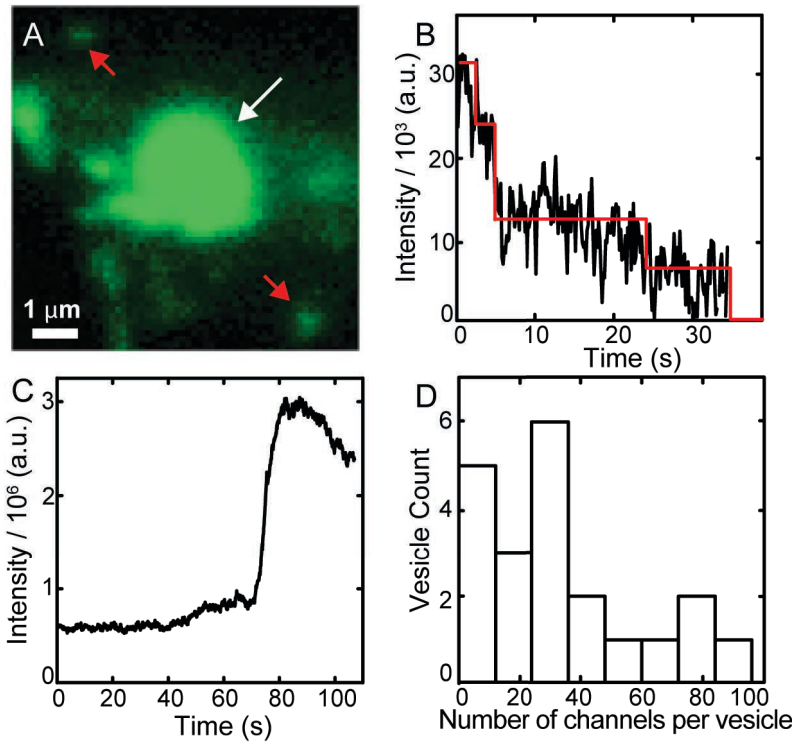


Figure 4.3: *Quantitation of Kv2.1 channel number in intracellular vesicles* (A) Imaging of trafficking vesicles and single GFP-Kv2.1 channels. The red arrows indicate puncta defined as single Kv2.1 channels based on the number of photobleach states while the white arrow indicates a trafficking vesicle based on its rapid movement. (B) Representative four-step bleach within a single GFP-Kv2.1 channel during imaging at 8 Hz. The bleach step magnitude, illustrated by the red line, corresponds to the intensity of a single GFP. (C) Vesicle fluorescence reaches a maximum as it approaches the membrane. Fluorescence intensity is critically dependent on Z position in the TIR field. To relate vesicle fluorescence to that of single Kv2.1 channels in the plasma membrane peak vesicle intensity was obtained immediately prior to fusion and subsequent GFP-Kv2.1 delivery to the membrane as illustrated. (D) Number of GFP-Kv2.1 channels per trafficking vesicle. These values were determined from vesicle GFP intensity and single channel bleach step magnitude, assuming four GFP molecules per channel was assumed. The indicated error was derived from variability in the single GFP bleach steps. Single GFP was determined from 190 bleach steps in 10 cells.

in Fig. 4.3, the mean channel number per vesicle was 34 ± 4, with a range of 5-90 molecules, n = 21.

If the Kv2.1 surface clusters are platforms for Kv2.1 delivery and retrieval at the plasma membrane, it should be possible to detect both the tethering of mobile vesicles and cargo delivery to the plasma membrane. We performed a partial TIR-based photobleach experiment such that cluster bleach was incomplete. This approach allowed the cluster itself and adjacent trafficking vesicles to be visualized simultaneously in TIRF since the vesicles are partially or totally outside of the TIR illumination and thus not significantly bleached. Fig. 4.4 shows representative results of one such experiment. Panels A and B show the clusters on the basal membrane of a GFP-Kv2.1 transfected HEK cell imaged in TIRF prior to, and immediately after, partial photobleaching. Panel C is an enlargement of the region indicated by the larger white square in panel B and shows

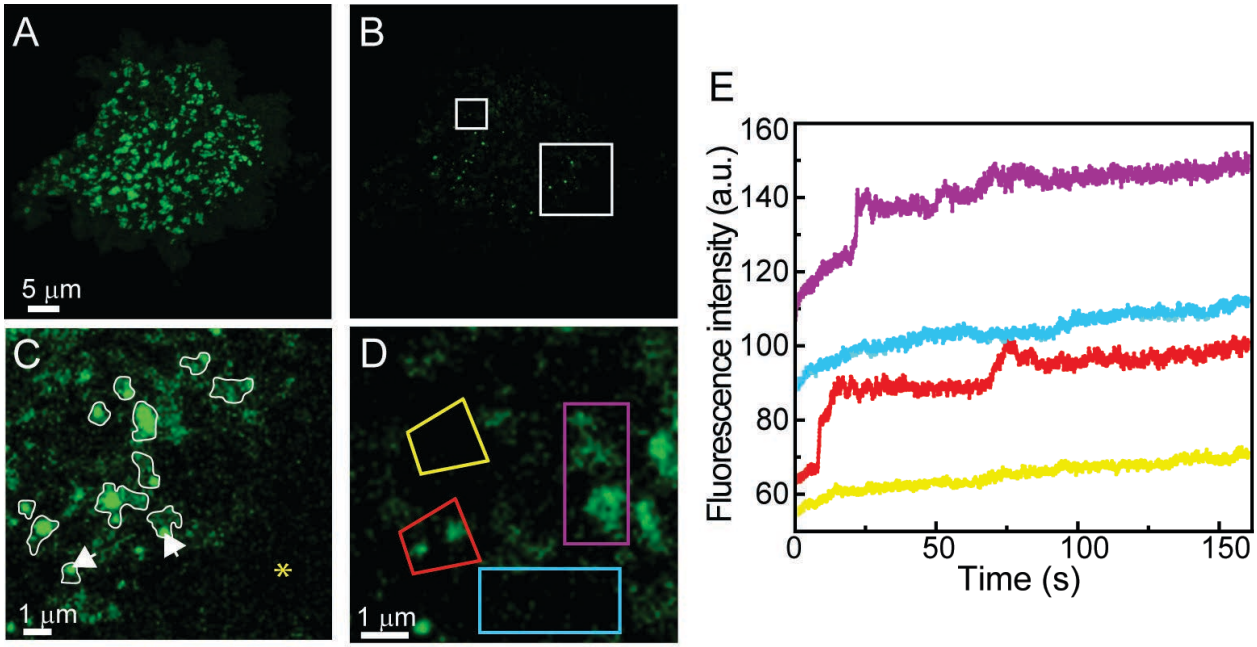


Figure 4.4: *TIR-based FRAP analysis illustrates vesicle tethering and fusion to Kv2.1 surface clusters in transfected HEK cells.* (A) Surface clusters containing GFP-Kv2.1 imaged using TIRF microscopy prior to photobleach. (B) TIRF image immediately after TIR-based photobleach. (C) Higher magnification of the area enclosed by the larger white box in panel B. The original cluster positions are outlined in white and the white arrows point to two adhered vesicles. The ∗ denotes a Kv2.1 cluster-free membrane region also devoid of adhered trafficking vesicles. (D) Higher magnification of the area enclosed by the smaller white box in panel B. Time here is immediately post bleach. (E) Time course of fluorescence recovery within the four regions indicated in D.

bright puncta that we interpret as trafficking vesicles tethered to the partially bleached clusters which are outlined in white. The asterisk indicates an area with neither bleached clusters nor tethered vesicles. In this particular cell 49 of 50 tethered vesicles were located at the edge of the surface clusters immediately after bleaching, suggesting the clusters and vesicles have a specific interaction, especially since only 24% of the surface area was occupied by the Kv2.1 clusters in this cell but approximately half of the clusters had associated vesicles. Of the 50 vesicles observed at the beginning of the FRAP period, 17 remained statically tethered after 4 min. Additional vesicles appear and deliver Kv2.1 to the cell surface clusters as illustrated in Panels D and E of Fig. 4.4. Panel D is an enlargement of partially bleached surface clusters within the smaller white square indicated in Panel B. Quantitation of postbleach fluorescence recovery within the four ROIs indicated in Panel D is shown in Panel E. The two ROIs that originally contained clusters (red and purple) show greater rates of fluorescence recovery as compared to the two ROIs drawn over cluster-free membrane (blue and yellow). The acquisition of new GFP-Kv2.1 in a step-wise fashion, as seen between 10-30 s for the ROIs drawn around bleached Kv2.1 clusters, is predicted

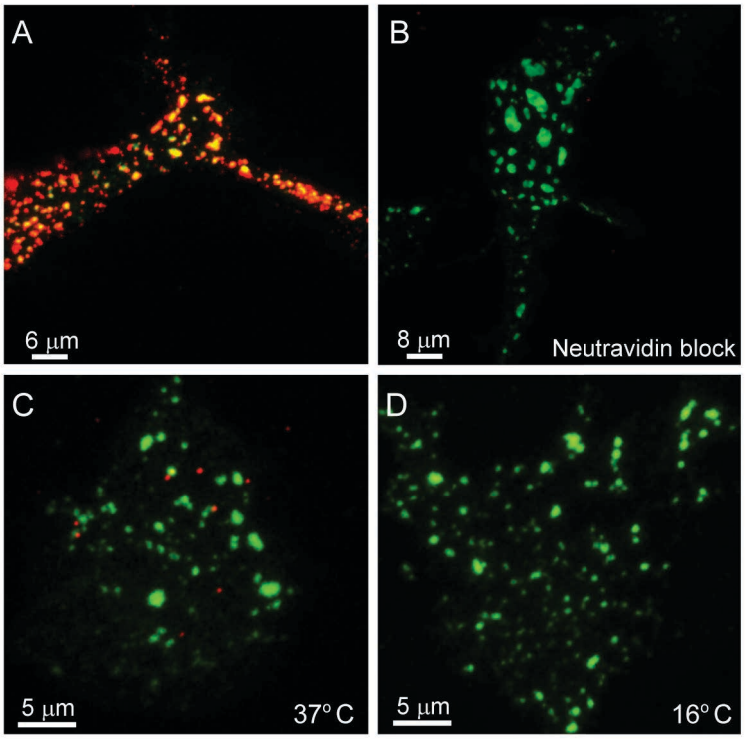


Figure 4.5: *Specificity of QD binding.* (A) QD binding to HEK cells expressing biotinylated GFP-Kv2.1-loopBAD without neutravidin block. (B) QD binding following neutravidin block. Following neutravidin removal the cell were QD labeled as in A. (C and D) Surface delivery of Kv2.1 at 37 and 16˚C, respectively. Following the 37˚C incubation 7 of 9 bound QDs were cluster associated. Overall, 89 ± 9% of QDs (n = 211 from 14 cells) in this type of assay were cluster associated. The lack of any bound QDs in panel D is expected since no insertion of Kv2.1 channel should occur at the 16˚C temperature.

if individual vesicles arrive over time and dock or deliver cargo within the ROI. The ROIs that are over cluster-free membrane show a slow, but steady, increase in fluorescence as non-clustered, freely diffusing channels from the unbleached top of the cell diffuse to the basal surface. Overall, 87 ± 12% of vesicles were cluster associated after the TIR-based photobleach even though clusters occupied only 21 ± 4% of the basal surface in the 5 cells examined. In addition, 75 ± 9% of the clusters gaining GFP-Kv2.1 after photobleach showed step-wise increases in fluorescence during recovery as illustrated in Fig. 4.4E. In summary, these whole cell photobleach experiments confirm our previous [117], but limited observations, that the Kv2.1 clusters are involved in channel delivery to the cell surface.

### 4.3.4 *Detection of single Kv2.1 channels being delivered directly to the surface clusters*

Since we relied on fluorescent protein imaging to observe multiple Kv2.1 channels being delivered to the cell surface clusters as illustrated in Fig. 4.4 it remained possible that single Kv2.1

channels arrived at the cell surface via delivery to Kv2.1 cluster-free plasma membrane. In addition, the TIRF imaging of Fig. 4.4 does not confirm true cell surface insertion, showing instead that the GFP-Kv2.1 is within the TIR field. To address these issues we expanded our previous QD-based detection of single Kv2.1 channels [117, 133, 49]. QD labeling is extremely specific since streptavidin-conjugated QDs are attached to the extracellular surface of Kv2.1 via channel-specific biotinylation. In addition, QD do not photobleach so channels can be tracked for hours. Our QD-based insertion site assay to detect the location of Kv2.1 cell surface insertion with single molecule sensitivity involved first incubating live cells expressing biotinylated GFP-Kv2.1-loopBAD with 1 μM neutravidin for 5 min to saturate biotinylated surface channels and hence prevent streptavidin-conjugated QD labeling. Following extensive washes to remove unbound neutravidin, the cells immediately were imaged in the presence of 1 nM 605QDs using a spinning disk confocal. Freely diffusing QDs move too rapidly to be effectively detected under our imaging conditions. As Kv2.1 channels that were synthesized de novo or were intracellular during neutravidin binding insert into the cell surface they become QD labeled. Thus, spontaneous QD appearance during the continuous imaging represents QD binding to a recently inserted channel. Fig. 4.5 shows that the neutravidin block is highly effective and that QD binding after this block requires temperatures allowing intracellular trafficking. Fig. 4.6 indicates QDs bind cell surface Kv2.1 soon after being added to the culture dish, with 75 s required to reach 50% binding. QD binding during the insertion site assay is likely to occur much faster since the cells are continuously bathed in a QD solution (as opposed to the dots being added to dish as in Fig. 4.6 where diffusion is delayed). Since the median distance covered by a non-clustered Kv2.1 channel in 40 s is 375 nm [49], the inserted Kv2.1 channels are unlikely to diffuse far from their site of membrane insertion before being bound by a QD. If single channels were inserted at locations outside of the GFP-Kv2.1 clusters, more QDs should first appear off cluster. In contrast, if the clusters are the predominant insertion sites, even for single molecules, then QD appearance should favor the clusters themselves. QDs appearing within 0.5 μm of the cluster perimeter were defined as appearing at that cluster.

Fig. 4.7 shows the results of a representative experiment where QD binding to newly inserted Kv2.1 channels was used to determine the location of channel insertion. As outlined in Fig. 4.7A, HEK cells expressing GFP-Kv2.1-loopBAD that was biotinylated intracellularly via co-

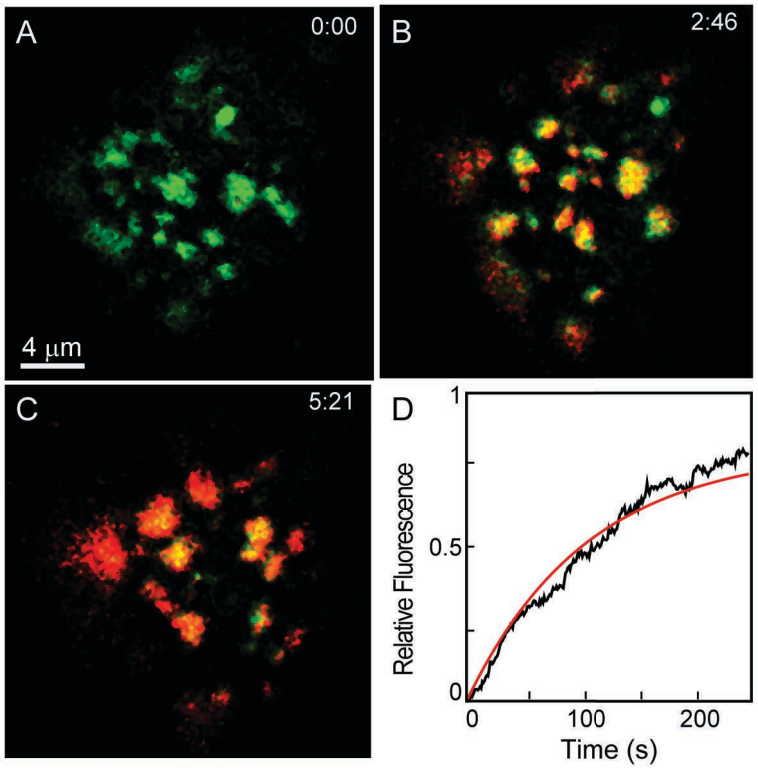


Figure 4.6: *Time course of QD binding to GFP-Kv2.1-loopBAD channels.* (A-C) QD binding observed at the indicated times following the addition of a 1 nM QD solution. (D) Quantitation of QD fluorescence over time. The data from three binding time courses were normalized, averaged and fitted to. Here = 108 sec. Since , the fitted curve indicates binding reached 50% at 75 s.

Table 4.1: *QD based detection of cytoplasmic Kv2.1 insertion into the plasma membrane of transfected HEK cells*. Location of QD appearance based on manual detection.

| Cell # | QDs appearing within 0.5 μm of a cluster border | QDs appearing at cluster-free membrane | % appearances associated with a cluster | % basal surface area in clusters |
|---|---|---|---|---|
| 1 | 36 | 11 | 76.7 | 7.2 |
| 2 | 3 | 1 | 75 | 36.8 |
| 3 | 29 | 8 | 78.4 | 9.7 |
| 4 | 30 | 0 | 100 | 24 |
| 5 | 31 | 4 | 88.6 | 10.1 |
| 6 | 25 | 4 | 87.1 | 18.5 |
| 7 | 13 | 4 | 81 | 16.5 |
| 8 | 22 | 2 | 91 | 15.1 |
| Total | 189 | 34 | 84.7 ± 8.4 | 17.2 ± 9.5 |

transfection with biotin ligase (BirA) were neutravidin blocked and then imaged in the presence of QDs as described above. Fig. 4.7B shows the lack of detectable QDs at the beginning of the time

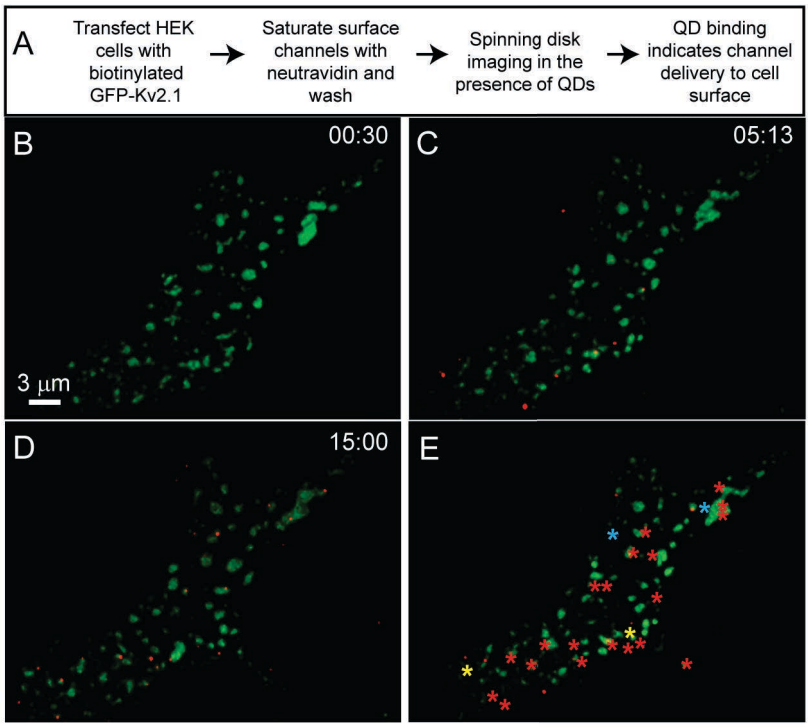


Figure 4.7: *Detection of single channel insertion sites in transfected HEK cells.* Basal membrane GFP-Kv2.1-loopBAD clusters are shown in green and 605 QDs in red. (A) Outline of the QD-based insertion site protocol. (B) QD labeling immediately following neutravidin block of surface GFP-Kv2.1-loopBAD. (C and D) QD labeling observed at the indicated times. (E) Summary of sites at which QDs were first detected. The 20 red asterisks indicate the appearance at a cluster perimeter and subsequent trapping within the cluster. The two yellow asterisks indicate channels arriving at a cluster border that were not retained within the cluster but diffused away to be confined to different clusters 3 and 4 min later. The cyan asterisks represent QDs first observed off cluster that then become confined within a Kv2.1 cluster.

series. Fig. 4.7C shows that by 5 min 8 QDs are observed, 6 within, and confined to, the Kv2.1 clusters as visualized via their GFP fluorescence, and 2 freely diffusing outside of the clusters. By 15 min, 19 cluster associated QDs are seen along with 6 off cluster dots, Fig. 4.7D. Fig. 4.7E summarizes the locations at which QDs appear over the entire 18 min time series. Twenty QDs appeared at a cluster perimeter with subsequent trapping within the cluster. Two QDs appeared at a cluster border but were not retained within the cluster, instead diffusing away to be trapped in a cluster 3 and 4 min later. These events explain how channel insertion at the clusters can still contribute to freely diffusing QDs. In addition, we have observed single Kv2.1 channels leaving one cluster only to be trapped in an adjacent one within a few minutes (data not shown). Thus, single Kv2.1 molecules are continuously exchanging between the cluster and non-cluster membrane compartments even though the clusters are preferred insertion sites and individual Kv2.1 channels can reside within the cluster for over an hour. In summary, this QD binding-based insertion assay supports the hypothesis that the Kv2.1 surface clusters are the preferred sites for

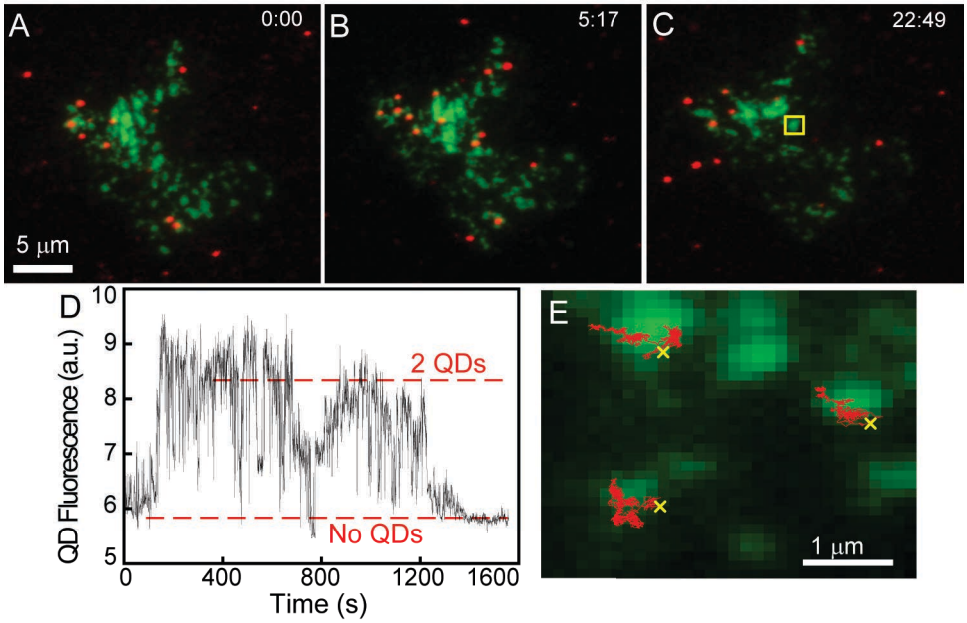


Figure 4.8: *Recycling GFP-Kv2.1-loopBAD channels are targeted to surface clusters.* HEK cells expressing biotinylated GFP-Kv2.1-loopBAD were labeled with streptavidin-conjugated 605QDs, unbound QDs were removed, and the tissue culture dish then returned to the tissue culture incubator for 1 h to allow QD-bound channel recycling to reach steady-state. The basal membrane was then continuously imaged in TIRF at 2 Hz and 37˚C for 30 min. (A) QDs (red) bound to GFP-Kv2.1-loopBAD channels (green) at the beginning of the imaging period. (B and C) QD localization at the indicated times. (D) QD fluorescence intensity over time within the white ROI of panel C. The increase in intensity represents the delivery of two QD-labeled channels to the cluster which is followed by endocytosis. (E) Algorithm-based detection of QD bound Kv2.1 appearance and subsequent single molecule diffusion. Sites of QD appearance, i.e. Kv2.1 exocytosis, are indicated by the yellow crosses. Note that the subsequent single particle tracks shown in red are confined to the Kv2.1 clusters.

Kv2.1 insertion into the cell surface in HEK cells. Additional experiments are summarized on a per cell basis in Table 4.1. Analyzing eight cells indicated that 84.7 ± 8.4%, n = 223, of the QDs spontaneously appearing on the cell surface, were cluster associated, appearing within 0.5 μm of the GFP-defined cluster border. In these cells the cluster surface area represented 17.2 ± 9.5% of the basal surface, indicating Kv2.1 insertion does not occur at random sites.

### 4.3.5 *Recycling Kv2.1 channels arrive to, and depart from, the plasma membrane at the cell surface clusters*

During our previous work examining Kv2.1 diffusion where a low number of QDs were tracked over 15-45 min we often observed fluctuations in the number of QDs on the cell surface suggesting Kv2.1 is constantly being internalized and recycled to the cell surface [49, 133]. Therefore, we examined whether Kv2.1 endocytosis and reinsertion into the plasma membrane occurs at the surface clusters. HEK cells expressing biotinylated GFP-Kv2.1-loopBAD were labeled with QDs at low efficiency, unbound QDs removed and the cells returned to the incubator for 1-2 h to allow

QD recycling to begin. TIRF imaging was then used to detect QD removal and appearance, i.e. endocytosis and reinsertion into the plasma membrane, respectively. Cytoplasmic Kv2.1 vesicles with a single QD were transported at the same rate as QD-free vesicles (1.3 ± 0.6 vs. 1.4 ± 0.5 μm/s, respectively, data not shown), suggesting that QD bound Kv2.1 channels traffic normally. In addition, Petrini et al [218] found that QD labeled AMPA receptors undergo normal clathrin-based endocytosis and Zhang et al have followed the exocytosis of QDs confined within synaptic vesicles to demonstrate complete vesicle fusion with the plasma membrane without the QD mass altering vesicle delivery or fusion [219]. Thus, limited QD labeling is unlikely to alter membrane protein internalization and subsequent trafficking. Representative results for recycling Kv2.1 channels are shown in Fig. 4.8. Panels A-C show the surface distribution of QD labeled Kv2.1 channels at the indicated times after a one hour incubation to allow recycling to begin. Note the changing QD-GFP relationship in the three selected time points. Dots both appear and disappear during this 30 min period, reflective of exocytosis and endocytosis, respectively, while total QD number remains relatively constant at 16 in this particular cell. Over 30 min of TIRF imaging there were 4 QDs appearing at cluster perimeters and 6 instances of QDs disappearing at cluster perimeters. In two cases, when the QDs disappeared GFP fluorescence intensity was also lost suggesting that multiple channels were endocytosed (data not shown). During most of this sequence there were on average 14 cluster-confined QDs and two freely diffusing QDs not associated with a cell surface cluster. Panel D shows the QD fluorescence over time within the ROI indicated in Panel C. Note the sudden increase in the QD signal, representing two QDs approaching the membrane and being inserted into the GFP-Kv2.1 cluster. The intensity decrease is consistent with the sequential endocytosis of the two recently inserted QD labeled channels.

Overall, 96%, n = 146, of QD bound Kv2.1 channels appeared on the surface at the cluster perimeter while 97%, n = 42, of the QDs were internalized at this location. While QDs can enter a stable, long-lived dark state lasting up to 500 s [208], the frequency of such a long-lived state is very low as indicated in Fig. 4.9. Only 14 of 460 long-lived dark events exceeded 60 s in a total observation time of 22,000 s. Therefore, long-lived dark states greater than 60 s should not interfere with our data analysis and QD blinking behavior is not responsible for the observed endo and exocytosis activity. Manual inspection of our image files to determine where QDs appear at the cell surface is both labor-intensive and prone to investigator bias. Therefore, we also used

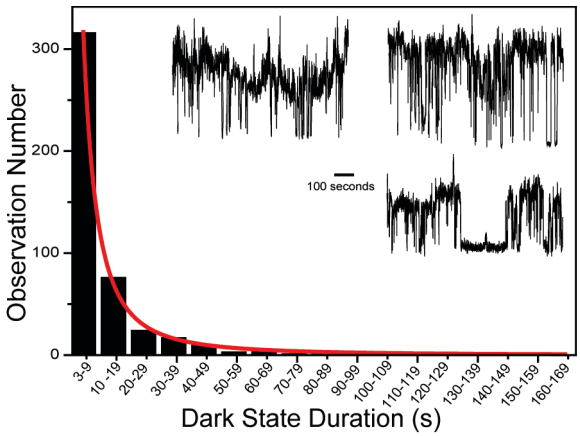


Figure 4.9: *QD blinking behavior under the imaging conditions used.* Nontransfected HEK cells where incubated with 0.1 nM 605 QDs in imaging saline without BSA for 10 min at 37˚C, washed and the non-specifically bound, immobile QDs imaged at 2-10 Hz in TIRF to quantitate the duration of any long-lived dark states. The three traces shown illustrate the typical blinking behavior observed and the histogram summarizes data collected from 26 QDs. Only 14 of 460 long-lived dark states exceeded 60 s during > 22,000 sec of imaging. The histogram was fit with a power law, $N = 27021t^{-2}$.

a MTT [209, 210] to detect the appearance of QDs and track them until they were endocytosed. Fig. 4.8E presents an example of this analysis where the sites of membrane delivery of three QDs bound to Kv2.1 are indicated by the yellow crosses. The single particle tracks starting at the insertion points show the QDs remain confined within the cluster over the next 876 frames (126 s). Note that each Kv2.1 channel was confined to the cluster at which perimeter it is first observed. Using this algorithm we found that 78%, n = 130, of recycling QD-labeled Kv2.1 channels appear at a cluster perimeter and 87% of these remained trapped in the cluster for the duration of imaging or until endocytosis. Estimation bias can be present in both an automated algorithm and a human-based approach, but the bias in the two methods is very different (for a discussion of this topic see [220]). Therefore, the use of both tools further substantiates the validity of the results. Manual and algorithm-based detection and tracking of recycling Kv2.1 channels independently support our hypothesis that the Kv2.1 surface clusters are sites for membrane insertion of Kv2.1 channels.

### 4.3.6 *Kv2.1 insertion requires an intact actin cytoskeleton.*

We previously demonstrated a role for the actin cytoskeleton in Kv2.1 surface cluster maintenance [133]. To examine the role of cortical actin in Kv2.1 delivery to the cell surface, the recycling experiments illustrated in Fig. 4.8 were repeated in the presence of either 5 μM cytochalasin D or 125 nM Swinholide A, 20 min each (data not shown). Only 5% of QD labeled Kv2.1 channels were

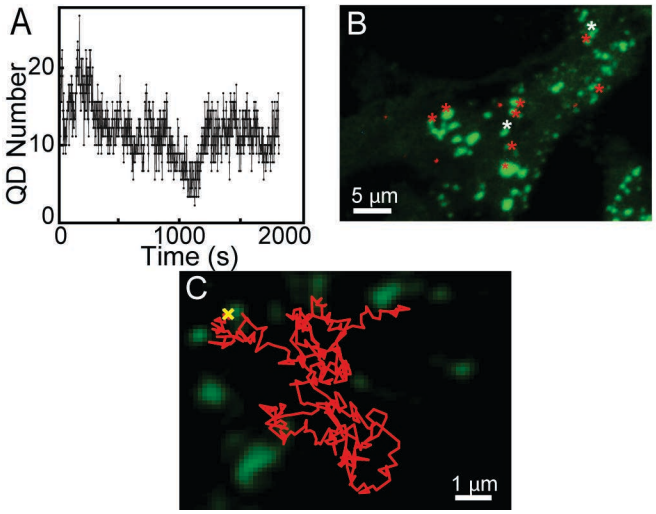


Figure 4.10: *Trafficking of Kv1.4 channels.* (A) QD number over time. Note that QD number slowly cycles as expected if there is continuous insertion and retrieval at the cell surface. The high frequency fluctuations are derived from the QD blinking while the low frequency fluctuations are from the insertion-retrieval events since the surface residence is greater than 100 s. (B) Locations of QD arrival and removal at the surface. The red asterisks indicate points of Kv1.4 insertion near a Kv2.1 cluster perimeter and the white asterisks indicate where Kv1.4 internalization occurred. (C) Algorithm-based detection of membrane insertion site for Kv1.4 (yellow cross) and subsequent single molecule diffusion track (red). Unlike the Kv2.1 channels that usually are retained within the cluster, Kv1.4 rapidly diffuses away.

delivered to clusters following Swinholide A and 0%, following cytochalasin D treatments, n = 57 and 18, respectively. In both cases the QDs showed non-confined diffusion immediately after appearance at the cell surface and were not trapped into a cluster. These experiments with actin inhibitors indicate that the trafficking machinery associated with Kv2.1 clusters is dependent on an intact actin cytoskeleton. The role of actin in exocytosis, while studied extensively, is not completely clear. In neuroendocrine cells the cortical actin appears to interfere with or restrict chromaffin granule fusion [221, 222]. In contrast, in PC12 cells actin polymerization enhances stimulated secretion [223]. Future experiments are required to determine whether f-actin has a direct role in Kv channel exocytosis or whether the actin serves simply as a scaffold assembling the exocyst machinery. More importantly, these actin disruption experiments indicate that randomly occurring, long-lived QD dark states do not simply create the impression of delivery at a Kv2.1 surface cluster.

### 4.3.7 *Kv1.4 also traffics to and from the Kv2.1 surface clusters.*

We next examined whether other membrane proteins also traffic to and from the cell surface at the Kv2.1 surface clusters. We studied membrane insertion and retrieval of Kv1.4 since this

K+ channel can also be specifically biotinylated on the extracellular surface and labeled with a streptavidin-conjugated QD [49]. In contrast to Kv2.1, Kv1.4 has a homogenous cell surface expression pattern with no apparent localization [133]. When Kv1.4 is co-expressed with Kv2.1 it ignores the Kv2.1 surface clusters, being found at equal densities inside and outside these domains and freely diffusing across the Kv2.1 cluster perimeter [133]. Thus, a priori, there is no reason to expect Kv1.4 to have any trafficking association with the Kv2.1 clusters.

HEK cells were transfected with GFP-Kv2.1, GFP-Kv1.4-loopBAD and BirA biotin ligase, labeled with QDs, returned to the incubator for one h after unbound QD removal, and then continually imaged with TIRF microscopy. As illustrated in Fig. 4.10A the GFP-Kv2.1 clusters are seen against a background of the homogeneous GFP-Kv1.4 fluorescence. The appearance and disappearance of Kv1.4 bound-QDs in one cell is summarized in Fig. 4.10A. The red asterisks in Fig. 4.10A indicate points of Kv1.4 insertion at a Kv2.1 cluster perimeter and the white asterisks indicates where Kv1.4 internalization occurred. Panel B summarizes QD number over time. Note that QD number slowly cycles as expected if there is continuous insertion and retrieval at the cell surface. In this particular cell eight QDs appeared and two QDs disappeared at the cluster perimeter. Unlike the Kv2.1 channels, which usually become trapped within the cluster, Kv1.4 rapidly diffuses away as is expected given its homogenous cell surface pattern. Manual analysis of Kv1.4 bound QD recycling in 11 cells indicated 91 ± 12% of Kv1.4 bound QDs appeared at a cluster perimeter (n = 44) while 90 ± 14% of Kv1.4 QDs were lost from the cell surface at the cluster perimeter (n = 11). Among this group of cells, only 20 ± 9.3% of the basal cell surface was occupied by the Kv2.1 clusters, again indicating Kv1.4 delivery to the surface at the Kv2.1 clusters cannot be attributed to chance.

We again applied the MTT algorithm-based approach to insertion site detection and subsequent single particle tracking as illustrated in Fig. 4.10C. As expected, Kv1.4 bound QDs appeared on the cell surface at the Kv2.1 cluster boundary. In contrast to the Kv2.1 mobility illustrated in Fig. 4.8E, the post delivery Kv1.4 diffusion track indicates free diffusion as opposed to trapping within the adjacent Kv2.1 cluster. 78%, n = 170, of the Kv1.4 channels appeared on the cell surface at the Kv2.1 cluster perimeter even though these two channels have no common localization pattern on the cell surface. Taken together, these data show that Kv1.4 is delivered to the same cell surface sites as Kv2.1 but lacks cluster retention. When QD labeled Kv1.4 disappeared from the surface

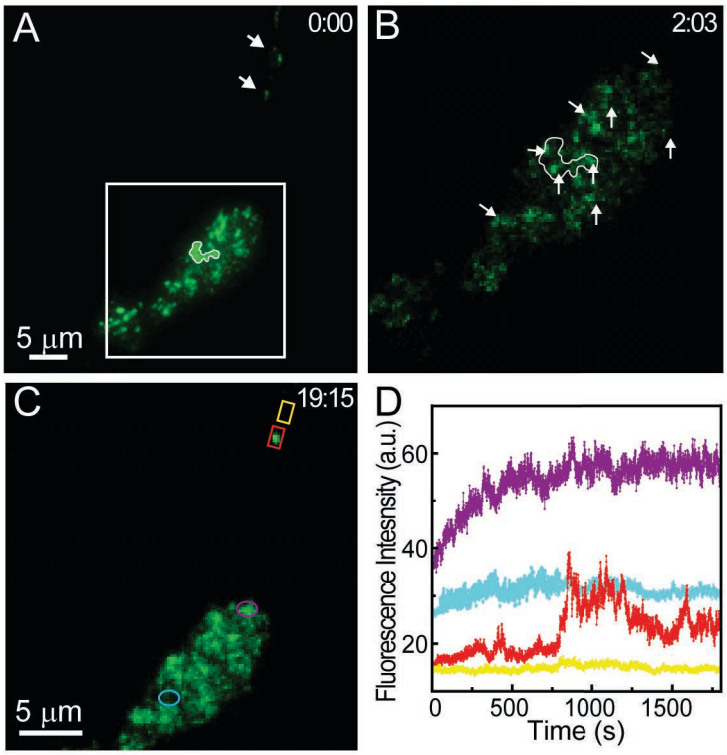


Figure 4.11: *TIR-based FRAP analysis detects vesicular tethering and Kv2.1 delivery to Kv2.1 surface clusters in cultured hippocampal neurons.* (A) Surface clusters prior to photobleach. The arrows highlight Kv2.1 clusters potentially in the axon initial segment. (B) Tethered vesicles (arrows) detected at the end of incomplete cluster photobleach within the white box shown in A. Note the three vesicles within the white outline of the large cluster present before bleach. (C) Fluorescence pattern after 19 min, 15 s of recovery. (D) Time course of fluorescence recovery within the regions indicated in C.

endocytosis also occurred at the cluster perimeter just as described for Kv2.1. Thus, two distinct Kv channels are trafficked to and from the cell surface at the same locations, suggesting the Kv2.1 surface clusters represent general sites for membrane insertion and retrieval in HEK cells.

### 4.3.8 *Trafficking vesicles associate with, and deliver Kv2.1 cargo, to Kv2.1 surface clusters in hippocampal neurons.*

While Kv2.1 expression and regulation is similar between HEK cells, cultured hippocampal neurons and brain slice preparations (compare Figs. 4.1 and 4.2 and see refs. [115, 119, 212, 214]), we confirmed that our findings in HEK cells were applicable to neurons. We detected numerous intracellular vesicles within neuronal soma and neurites. To determine whether these vesicles associated with the cell surface Kv2.1 clusters, we performed a TIR-based FRAP experiment with GFP-Kv2.1 transfected hippocampal neurons as illustrated in Fig. 4.11. Panel A shows soma- and neurite (arrow) localized Kv2.1 clusters before the TIR-based partial photobleach. The boxed area

within Panel A is enlarged in Panel B and shows tethered vesicles at the surface clusters following the partial photobleach (arrows). Note the large cluster on the soma outlined in white that has three bound trafficking vesicles. Time-lapse imaging was then performed and the recovery after 19 min is illustrated in Panel C. Quantitation of the fluorescence within the ROIs indicated in Panel C showed that delivery to cluster-containing regions occurred more rapidly, and in a step-wise pattern, as compared to fluorescence recovery within cluster-free soma or neurite membrane (see Panel D). As with HEK cells, this off-cluster recovery likely represents the unrestricted diffusion of non-clustered Kv2.1 from the top, and thus unbleached, region of the cell. The recovery occurring within what is likely the axon initial segment [211] illustrates both transient vesicle tethering at 450 s and delivery of GFP-Kv2.1 to the bleached cluster at 800 s. Taken together, these data suggest that the Kv2.1 surface clusters on the neuronal soma and axon initial segment are preferred vesicle docking and membrane fusion sites for cytoplasmic vesicles containing Kv2.1 and that Kv2.1 remains within these domains following delivery to the surface.

#### 4.3.9 *Detection of single channel insertion sites in hippocampal neurons*

The neutravidin block approach with the GFP-Kv2.1-loopBAD construct to detect single channel insertion sites was repeated in neurons as illustrated Fig. 4.12. Fig. 4.12A shows the lack of detectable QDs at the beginning of the time series, indicative of little to no channel insertion at this time. One and a half minutes later one bound QD was detected as shown in Fig. 4.12B. Fig. 4.12C shows that by 11 min 44 s seven QDs were observed, six within, and confined to, the Kv2.1 clusters visualized via the GFP fluorescence, and one freely diffusing off clusters. Fig. 4.12D summarizes the location of QD appearance over this time series. The red asterisks indicate QD appearances at cluster perimeters where the QD was immediately trapped within the Kv2.1 cluster. The yellow asterisks indicate appearances at a cluster perimeter where the QD was not retained within the cluster. Examination of 59 QD appearances in 7 neurons indicated that 90 ± 11% of insertion events per cell occurred at the Kv2.1 cluster perimeter.

#### 4.3.10 *Recycled Kv2.1 channels also insert at the surface clusters in hippocampal neurons*

Neurons expressing biotinylated GFP-Kv2.1-loopBAD were labeled with a sub-saturating concentration of QDs, washed and returned to the tissue culture incubator for 1-2 h to allow recycling

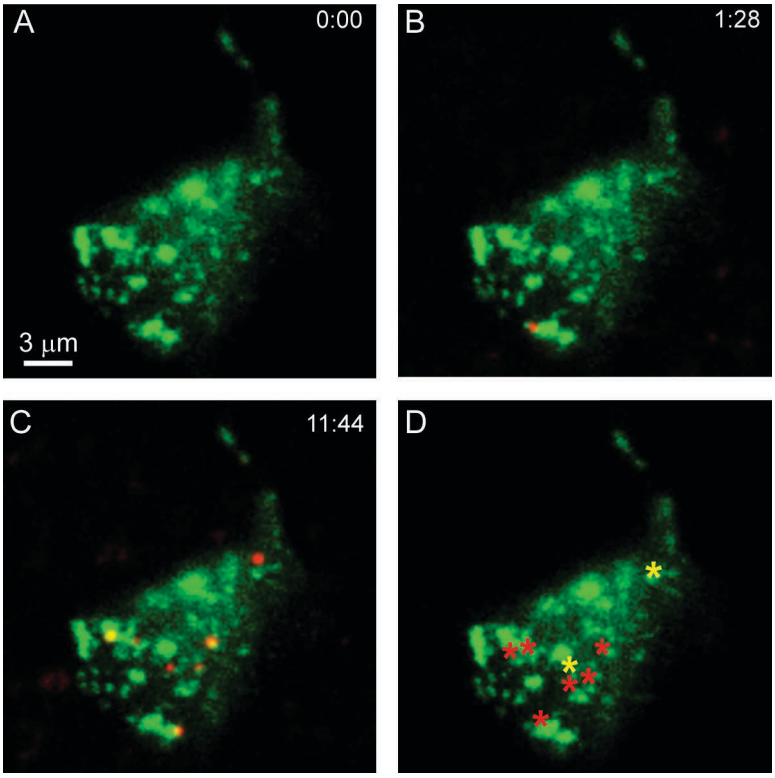


Figure 4.12: *Detection of single channel insertion sites in hippocampal neurons.* (A) QD labeling immediately following neutravidin block of surface GFP-Kv2.1-loopBAD. (B and C) QD labeling observed at the indicated times during continuous spinning disk imaging at 37˚C and 1 Hz in the presence of a 1 nM QD solution. (D) Summary of sites at which QDs first bound. The red asterisks indicate QD appearance at a cluster border and immediate confinement within the cluster. The yellow asterisks indicate channels arriving at cluster borders where they were not retained but diffused away to be trapped later.

to progress. The neurons were then continuously imaged in TIRF for up to 1 hr. Representative results are shown in Fig. 4.13. Panels A-D show the surface distribution of QD labeled Kv2.1 channels at the indicated imaging times after QD labeling and the following one hour incubation during which internalization occurs. Many of these internalized QDs reappeared on the cell surface during the illustrated time series. Note that some Kv2.1 clusters accumulated multiple QDs while others are QD-free, suggesting that Kv2.1 recycling back to the surface may prefer specific clusters. Analysis of Kv2.1 recycling in seven neurons indicated that 45 of 53 QD labeled Kv2.1 channels (85%) arrived back at the cell surface at a cluster perimeter. Three of these 45 QDs were not retained within the cluster at which they arrived. In addition, there were 8 QDs observed undergoing endocytosis at the Kv2.1 surface cluster perimeter.

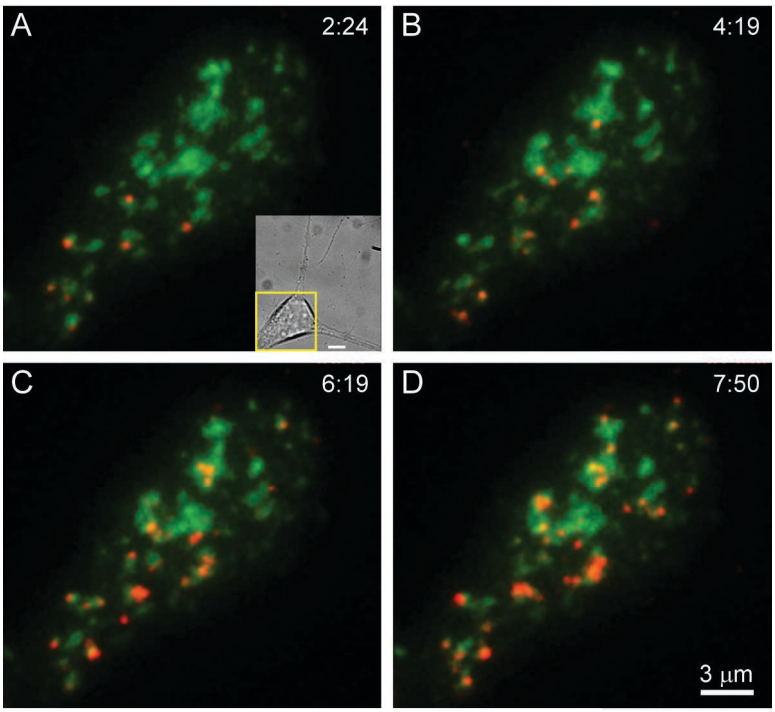


Figure 4.13: *Recycling GFP-Kv2.1-loopBAD channels are targeted to surface clusters in the soma of cultured hippocampal neurons.* Neurons expressing biotinylated GFP-Kv2.1-loopBAD (green) were labeled at low density with 605 QDs (red), 1 nM for 5 min at 370C, rinsed and returned to the tissue culture incubator for 1 h to allow QD-bound channel recycling to reach a steady state. The basal membrane was then continuously imaged in TIRF at 2 Hz and 37˚C for 30 min. QDs that were internalized during the first h are now likely recycling back to the cell surface. (A) GFP-Kv2.1-loopBAD channel clusters partially labeled with QDs at the beginning of the imaging series. The inset shows a DIC image of this neuron with the yellow box indicating the area imaged in TIRF. Bar, 5 µm. (B-D) QD localization at the indicated times. Note that by almost 8 min some Kv2.1 clusters have accumulated multiple QDs while others remain QD-free, indicating that Kv2.1 recycling back to the surface does not occur equally at all clusters.

## 4.4 DISCUSSION

Even though it is critical that ion channel surface densities and location be well-controlled, little is known concerning the location of Kv channel delivery and retrieval on the cell surface. The Kv2.1 delayed rectifier channel regulates electrical activity in nerve and muscle [224] and is unusual among voltage-gated $K^+$ channels in that it localizes to micron-sized clusters on the cell surface of neurons and transfected HEK cells [225]. Surprisingly, within these surface microdomains Kv2.1 is non-conducting at depolarized potentials. Since in neuroendocrine cells Kv2.1 is postulated to play a non-conducting role in SNARE-mediated membrane fusion, we tested the hypothesis that the surface clusters are specialized platforms involved in membrane trafficking to and from the cell surface. The TIR-based FRAP studies indicated that GFP-Kv2.1 containing cyto-

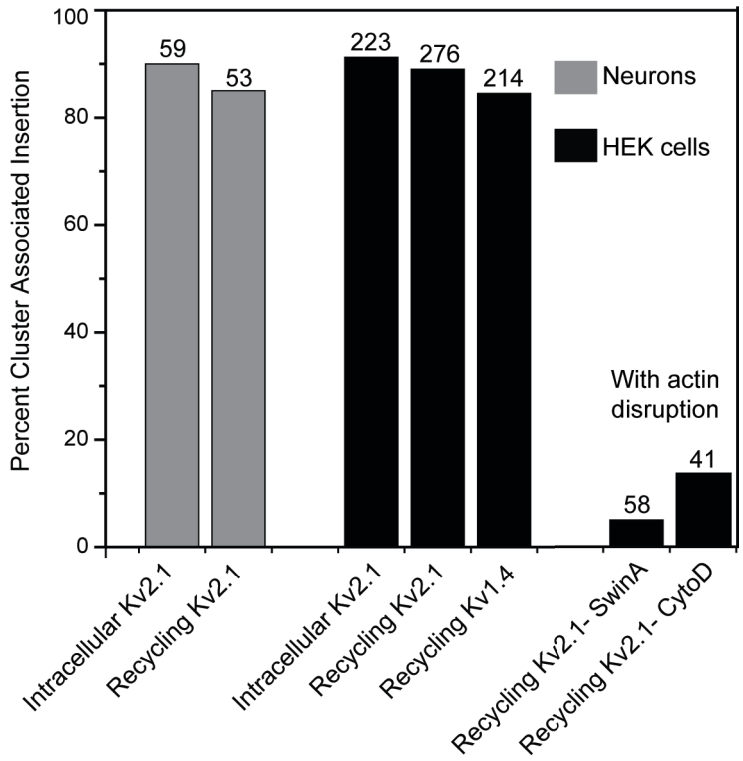


Figure 4.14: *Summary of Kv channel membrane insertion.* The percent of total insertions that occurred at a Kv2.1 cluster are indicated. The grey bars represent neuronal insertions while the black bars summarize the data from HEK cells. The insertion percentages determined by manual and automated detection were averaged. The numbers above each bar refer to the total number of surface insertions observed for the indicted condition.

plasmic vesicles tether to, and deliver cargo in a discrete fashion at the Kv2.1 surface clusters in both transfected HEK cells and cultured hippocampal neurons. QD-based single molecule imaging indicated that the delivery and surface retrieval of Kv2.1 occurs at the perimeter of the surface clusters. Overall, the majority of nascent and continuously recycling Kv2.1 channels in HEK cells and hippocampal neurons arrive at the cell surface within 0.5 μm of the cluster perimeter and are immediately confined within the cluster. The majority of Kv2.1 channel endocytosis in HEK cells occurred within this same region even though the clusters represented less than 20% of the cell surface. The non-clustering Kv1.4 channel also traffics to and from the plasma membrane at the Kv2.1 cluster perimeter, demonstrating that the Kv2.1 clusters represent cell surface platforms for the insertion and retrieval of other Kv channels. Together, these results, which are summarized in Fig. 4.14, indicate that Kv2.1 clusters function as specialized cell surface microdomains involved in membrane protein trafficking.

Why use Kv2.1 clusters as cell surface trafficking platforms for Kv channels? We previously showed that while the Kv2.1 channels within the clusters are non-conducting, they are capable of sensing membrane voltage in that the clustered channels produce gating currents in response to depolarization [120]. Thus the Kv2.1 clusters could serve as voltage-sensing domains that link membrane fusion and/or endocytosis to neuronal electrical activity. Alternatively, the cluster-based trafficking could be influenced by extracellular events. For example, in α-motoneurons Kv2.1 clusters on the soma colocalize with large cholinergic synaptic inputs suggesting that muscarinic receptor activation could modulate trafficking at these sites [226]. Most recently, a Kv2.1 beta subunit has been proposed that has the characteristics of a cell surface adhesion molecule [227]. Since this adhesion protein is concentrated within the Kv2.1 clusters on the neuronal surface, extracellular matrix interactions could also potentially modulate membrane protein delivery and retrieval. And as noted earlier, the Kv2.1 clusters are regulated by ischemia in the intact brain, where ischemia blocks glutamate uptake by adjacent astrocytes thereby activating extrasynaptic NMDA receptors with the resulting $Ca^{2+}$ influx inducing Kv2.1 declustering [212, 213]. Altered neuronal membrane trafficking after an ischemic insult could be either damaging or neuro-protective.

The use of stable, reusable sites for exocytosis is not a commonly accepted idea. Notable exceptions are neuronal and immunological synapses, budding yeast and polarized epithelium [16]. However, exocyst localization has obvious advantages:

1. Static localization avoids the energy and time required to constantly reassemble the exocyst protein complex.
2. Trafficking vesicles can be delivered to stable sites along relatively static microtubules and then handed off to the cortical actin network.
3. Such localization should also provide for enhanced regulation since GTPases, kinases, etc can be stably incorporated into the exocyst complex.

In adrenal chromaffin cells exocytic release does occur at specific reusable sites [228, 229, 230]. Interestingly, Kv2.1 has been implicated in SNARE-mediated exocytosis in these neuroendocrine

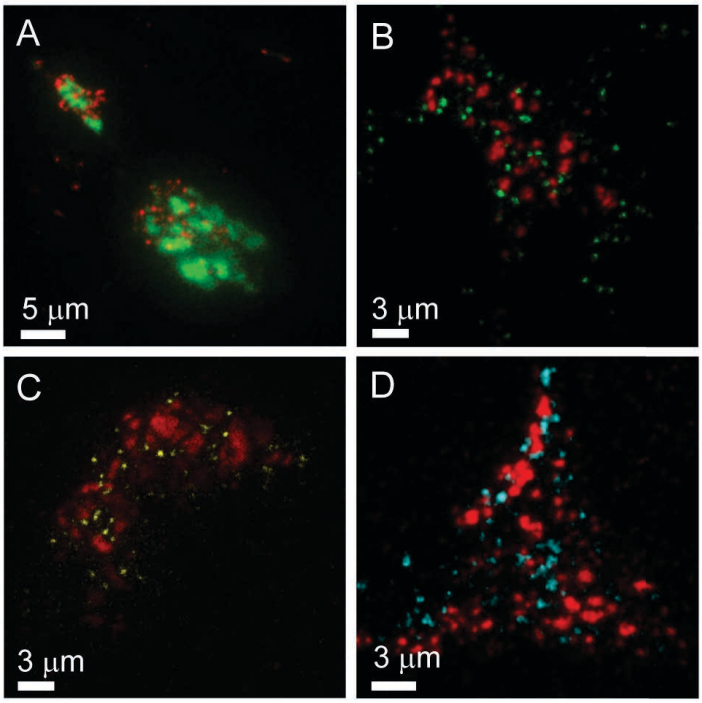


Figure 4.15: *Clathrin and caveolins prefer the Kv2.1 cluster perimeter.* (A) Relationship between RFP-clathrin light chain and GFP-Kv2.1 surface clusters in transfected 7DIV hippocampal neurons. In the 11 neurons examined, 76 ± 15% of the clathrin puncta were within 0.5 μm of the cluster perimeter while the perimeter occupied only 8 ± 2% of the basal cell surface. (B) Relationship between GFP-clathrin light chain and Kv2.1-HA surface clusters in transfected HEK cells. Kv2.1-HA was visualized using AlexaFluor594-conjugated anti-HA antibody. 60 ± 9% (9 cells) of the puncta were cluster-associated while the cluster perimeter occupied only 14 ± 6% of the basal cell surface. (C and D) Relationship between YFP-caveolin 1 or CFP-caveolin 3, respectively, and Kv2.1-HA surface clusters in transfected HEK cells. 66 ± 10% (9 cells) of the YFP-caveolin 1 puncta were within 0.5 μm of the Kv2.1 cluster perimeter while the perimeter occupied 16 ± 5% of the basal cell surface. 64±14% (6 cells) of the CFP-caveolin 3 puncta were adjacent to the cluster while the perimeter occupied only 17 ± 5% of the basal cell surface.

cells [202]. Recent studies of Glut 4 trafficking suggest specialized plasma membrane domains in adipose cells are used for Glut 4 delivery to the cell surface [231]. Under control conditions the majority of vesicular Glut 4 is delivered to Glut 4 clusters on the cell surface where it remains confined. The surface delivery that does occur at cluster-free membrane has the delivered Glut 4 being rapidly dispersed. Similar to what we describe here for Kv2.1, endocytosis of Glut 4 occurs primarily at the surface Glut4 clusters. While in the past it was often assumed that endocytosis outside presynaptic membranes was randomly distributed over most cell surfaces [232], the existence of stable "hot spots" for clathrin mediated endocytosis is now accepted for many cell types [16, 4, 233, 234]. In agreement with this idea clathrin puncta localize adjacent to the Kv2.1 clusters in transfected hippocampal neurons and HEK cells as shown in Fig 4.15A and 4.15B. This association is especially strong in the neurons where 76 ± 15% of the clathrin puncta were within

0.5 μm of the cluster perimeter while the perimeter occupied only 8 ± 2% of the basal cell surface. Caveolae are involved in certain types of endocytic trafficking [235], and caveolin 1 and 3 puncta also prefer the cluster perimeter as illustrated in Fig. 4.15C and 4.15D. In summary, localized sites for membrane protein insertion and retrieval may be much more common than previously thought, especially in neuronal cells.

## 4.5 CONCLUSION

Kv2.1 clusters represent approximately 20% of the soma cell surface in hippocampal neurons where their existence is regulated by neuronal activity and insult even though the clustered channels are non-conducting [115, 119, 212, 120]. In alpha motor neurons these microdomains exist at synaptic inputs where they colocalize with muscarinic acetylcholine receptors and other proteins involved in cholinergic transmission [226]. Our present work indicates that in transfected HEK cells and hippocampal neurons these structures are trafficking platforms involved in Kv channel movement to and from the cell surface. Whether a non-conducting function of Kv2.1 is to actually form these specialized cell surface microdomains involved in membrane protein trafficking is an area requiring further study. Nonetheless, the present work is the first to define stable cell surface sites for ion channel delivery and retrieval at the cell surface.

## 4.6 ACKNOWLEDGEMENTS AND CONTRIBUTIONS

Michael M. Tamkun and Diego Krapf designed the research. Aubrey Weigel and Diego Krapf contributed analytical tools. Emily Deutsch, Elizabeth Akin, Phil Fox, Gentry Hansen, Christopher Haberkorn, Rob Loftus and Aubrey Weigel performed the research and analyzed the data.

# CHAPTER 5: SIZE OF CELL-SURFACE KV2.1 DOMAINS IS GOVERNED BY GROWTH FLUCTUATIONS

The Kv2.1 voltage gated potassium channel forms stable clusters on the surface of different mammalian cells. Even though these cell-surface structures have been observed for almost a decade, little is known aboutt he mechanism by which cells maintain them. We measure the distribution of domain sizes to study the kinetics of their growth. Using a Fokker-Planck formalism, we find no evidence for a feedback mechanism presentt o maintain specific domain radii. Instead, the size of Kv2.1 clusters is consistent with a model where domain size is established by fluctuations in the trafficking machinery. These results are further validated using likelihood and Akaike weights to selectt he best model for the kinetics of domain growth consistent with our experimental data.

## 5.1 introduction

Membrane compartments or domains appear in many different cell types. These domains are varied in their composition and in the residence time that an individual molecule remains confined within the specific domain. The mechanisms by which a cell forms and maintains these specific structures in the plasma membrane can be very diverse, depending on the length and timescales involved. To name a few examples, MHC-I forms dynamic clusters with typical lifetimes of tens of seconds that are governed by the concerted action of exocytosis and the existence of cytoskeleton-based diffusion barriers [236, 181]. Both cadherin [237] and transferrin receptors [183] undergo transient confinement as they diffuse over the cell surface presumably due to transientt rapping within various cytoskeletal domains. IgE receptors diffuse within micron-sized membrane domains defined by actin bundles, over time-scales of seconds [180].

Hemagglutinin molecules form dynamic irregular clusters on length scales from 40 nm up to micrometers [238]. In sharp contrastt o these examples of membrane domains, the voltage gated K+ channel Kv2.1 forms micron-sized clusters that are stable over the course ofh ours. These surface domains appear in hippocampal neurons in vitro and in vivo [211, 239, 240], in spinal cord motor neurons [226], and in transfected HEK cells [119, 214, 134, 133, 49]. Kv2.1 clusters are proposed to have a neuroprotective role in the mammalian brain [119]. However, as mentioned

in previous chapters, the physical mechanism behind cluster formation and maintenance is still unknown.

As shown in Chapter 4, the insertion of channels into the plasma membrane occurs solely at the perimeter of clusters via a vesicle docking and delivery mechanism. Similarly, internalization of Kv2.1 channels occurs from the cluster perimeter. However, the question of how the cell regulates Kv2.1 domain size remains unanswered. Given that delivery and internalization of potassium channels takes place at the cluster perimeter [241], the cellular trafficking machinery has some "knowledge" of the cluster location. Therefore, it is tempting to hypothesize that cluster sizes are actively regulated by balancing internalization and exocytosis events via a feedback mechanism. Alternatively, cluster sizes may be left to the fate of fluctuations in the exocytic/endocytic machinery. Even though this latter pathway lacks some degree of control it has the advantage of being favorable from an energy budget perspective.

In this chapter, we study the Kv2.1 domain size distribution on the surface of HEK cells to shed light into the mechanism by which Kv2.1 clusters are regulated. We use a simple growth model to investigate the distribution of domain sizes in a similar fashion to Gov's model for the size distribution of focal adhesions [242]. The size distribution is directly linked to the maintenance and regulation of domains. For example, if a feedback mechanism maintained a specific domain size by locally balancing endocytosis and exocytosis, this preferred size would have the highest probability. Thus the probability density of domain radii would peak at this specific value. In general, the evolution of cluster size distribution can be modeled, in the continuum approximation, by a Fokker-Planck equation, which makes a direct connection between the kinetic model of growth and the size distribution [243]. The Fokker-Planck equation in one variable is derived from the stochastic differential equation

$$\frac{dx}{dt} = v_c\left(x\right) + v_f\left(t\right)$$

where $v_c$ is a deterministic velocity and $v_f$ is a stochastic quantity. We have ignored any inertial terms that are not relevant to growth models. The fluctuations in the velocity are often assumed to be $\delta$-correlated

$$\left\langle v_f(t)\, v_f\left(t'\right)\right\rangle = 2D\delta\left(t - t'\right), \tag{5.1}$$

and the corresponding Fokker-Planck equation for the distribution function $P(x,t)$ is[244]

$$\frac{dP}{dt} = -\frac{\partial}{\partial x}\left[v_c(x)\, P\right] + D\frac{\partial^2 P}{\partial x^2}. \tag{5.2}$$

Using this formalism, we find that the size distribution of Kv2.1 domains is governed by fluctuations in the trafficking pathways and that no local feedback exists between endocytosis and exocytosis

## 5.2 MATERIAL AND METHODS

### 5.2.1 *Cell culture and transfection*

Kv2.1 channels labeled with an intracellular GFP at the N-terminus have been used previously and are also described in more detail in Chapter 4 [GFP-Kv2.1, [134, 133, 49]]. HEK 293 cells (American Type Culture Collection, passage 38-45) were kept in DMEM (Gibco, Life Technologies, Carlsbad, CA) supplemented with 10% fetal bovine serum (FBS, Gibco) at 37˚C and 5% CO2. Cells were transfected by electroporation using a BioRad Genepulser Xcell (BioRad Laboratories, Hercules, CA) with a 0.2 cm gap cuvette and a single 110-V 25-ms pulse with 3 µg of GFP-Kv2.1 expressing DNA, Appendix 5 (8.3). Following electroporation cells were plated on cover-glass-bottom culture dishes that had been previously Matrigel-coated (BD Biosciences, San Jose, CA) and covered in DMEM without phenol red (Life Technologies) and 10% FBS. Cells were used for live cell imaging within 24 hours of transfection.

### 5.2.2 *Live cell imaging*

Prior to imaging, cells were always rinsed twice with a HEK physiological imaging saline, 8.6. Cells expressing fluorescent protein-tagged constructs were imaged in imaging saline at 37˚C in a home-built, objective-type TIRF microscope built around an Olympus IX71 [49]. GFP was excited using a 473 nm diode pumped solid-state laser (Shanghai Dream Lasers, Shanghai, China). The beam was expanded, re-collimated, attenuated with a neutral density filter to yield 2.5 mW after

the objective, and focused at the back focal plane of a 100x objective (Olympus PlanApo N.A. 1.45) using an antireflection-coated achromatic doublet with a focal length of 400 mm (Thorlabs, Newton, NJ). The GFP fluorescence was collected in an electron-multiplied charge coupled device (iXon DU-888, Andor, Belfast, Ireland). Both the dish and the objective were maintained at 37˚C using a temperature control system (Bioptechs, Butler, PA).

### 5.2.3 *Image and data analysis*

Images were acquired using Andor IQ 2.3 software and saved as 16-bit tiff files. The images were analyzed with a custom-written algorithm in LabView, see Appendix 5 (5). We manually selected the center of each cluster and, then, the intensity of the pixels in the horizontal and vertical cross sections of the clusters was generated. These line profiles were fit to Gaussian functions using the Levenberg-Marquardt least-square method. The LabView codes used to perform this analysis are available upon request. The obtained data were imported into Origin 8.1 for further processing.

### 5.2.4 *Cytoskeleton disruption reagents*

Latrunculin A (LatA, Sigma) was used in order to disrupt the cortical actin. In these experiments, LatA was dissolved in dimethyl sulfoxide (DMSO, Sigma-Aldrich) and directly added to the imaging dish to a final concentration of 100 nM [117].

### 5.2.5 *Models*

In general, the three different types of domain growth without any feedback mechanism are:

1. channels exchange with a reservoir, i.e., the membrane outside the domains, by permeating through the domain perimeter;
2. channels are directly inserted from the cytosol into the interior of the domain and are retrieved from the interior of the domain to the cytosol; and
3. a constant inward/outward flux is directly maintained independent of domain size.

The first two models of growth were given by Gov [242] and are also reproduced here for convenience. A fourth model is also given below for a feedback mechanism between growth rate and cluster size.

*Model 1*

The mass balance equation for a domain with area A, allowed to grow only by permeation through its perimeter is

$$\frac{\partial A}{\partial t} = -k_{off} r + k_{on} n r, \tag{5.3}$$

where $k_{on}$ and $k_{off}$ are the on- and off-rates, $n$ is the surrounding mean protein density, and $r$ is the radius of the domain, such that $A = \pi r^2$. Replacing variables in Eq. 5.3, we get the equation of motion for the radius $r$,

$$\frac{\partial r}{\partial t} = -\frac{k_{off}}{2\pi} + \frac{k_{on} n}{2\pi}. \tag{5.4}$$

From Eqs. 5.2 and 5.4 we can write the corresponding Fokker-Planck equation for the radius PDF,

$$\frac{\partial P}{\partial t} = -\frac{1}{2\pi}\left(k_{on} n - k_{off}\right)\frac{\partial P}{\partial r} + D\frac{\partial^2 P}{\partial r^2}. \tag{5.5}$$

The noise term $D$ accounts for temporal fluctuations in the insertion and retrieval of molecules into and out of a cluster (given by Eq. 5.1) and results in an effective broadening of the distribution. Sources of fluctuations include ATP and GTP availability (for the action of motors and GTPases), obstruction by intracellular compartments, anomalous Brownian motion of channels to arrive to endocytic pits, dynamic distribution of microtubules, etc. Fluctuations in the trafficking machinery are assumed to be intrinsic to the endocytic and exocytic machinery and to have $\delta$-function correlations [245, 246]. The resulting steady-state solution to Eq. 5.5 is an exponential in $r$,

$$P_1(r) = R_n e^{-r\left(k_{off} - k_{on} n\right)/2\pi D}, \tag{5.6}$$

where $R_n$ is a normalization constant. The normalization constant in Eq. 5.6 is found from

$$\int_a^\infty P_1(r)\,dr = 1,$$

where $a$ is the minimum radius that can be assigned to a domain. Then,

$$R_n = \lambda \exp(\lambda a), \tag{5.7}$$

where

$$\lambda = \frac{(k_{off} - k_{on} n)}{2\pi D}.$$

Then, the log-likelihood function is

$$\ln[L_1(\lambda \mid r)] = n \ln n + n\lambda a - \lambda \sum_i^n r_i, \tag{5.8}$$

where $r = r_1, r_2, \ldots, r_n$ is our data set and $L_1$ is the likelihood of the parameter $\lambda$, given the data set.

*Model 2*

When we consider a domain that can grow at any point in its interior,

$$\frac{\partial A}{\partial t} = -k_{off} A + k_{on} n A \tag{5.9}$$

the corresponding Fokker-Planck equation is

$$\frac{\partial P}{\partial t} = -\left(k_{on} n - k_{off}\right) \frac{\partial (AP)}{\partial A} + D \frac{\partial^2 P}{\partial A^2} \tag{5.10}$$

The resulting PDF is a Gaussian in $A$,

$$P_2(A) = R_n e^{-A^2\left(k_{off} - k_{on} n\right)/2D} \tag{5.11}$$

Or, by changing variables

$$P_2(r) = R_n r e^{-\left(-\pi^2 r^4 \left(k_{off} - k_{on} n\right)\right)/2D} \tag{5.12}$$

The normalization constant in Eq. 5.12 is

$$R_n = r\sqrt{\frac{\lambda}{\pi}}\left[\text{erfc}\left(a^2\sqrt{\lambda}\right)\right]^{-1}, \tag{5.13}$$

where

$$\lambda = \pi^2 \frac{\left(k_{off} - k_{on} n\right)}{2D},$$

and *erfc* is the complimentary error function defined as

$$\text{erfc}(x) = \left(\frac{2}{\sqrt{\pi}}\right)\int_x^\infty \exp\left(-r^2\right) dt.$$

The log-likelihood function is

$$\begin{aligned} \ln\left[L_2(\lambda \mid r)\right] &= \frac{n}{2}\ln\left(\frac{16\lambda}{\pi}\right) - n\ln\left[\text{erfc}\left(a^2\sqrt{\lambda}\right)\right] \\ &+ \sum_j^n \ln r_j - \lambda\sum_i^n r_i^4. \end{aligned} \tag{5.14}$$

*Model 3*

In the last case, when there is a constant source and sink, we have the mass balance equation

$$\frac{\partial A}{\partial t} = -k_{off} + k_{on} n, \tag{5.15}$$

with the corresponding Fokker-Planck equation

$$\frac{\partial P}{\partial t} = -\left(k_{on} n - k_{off}\right)\frac{\partial P}{\partial A} + D\frac{\partial^2 P}{\partial A^2}. \tag{5.16}$$

The resulting PDF is an exponential in $A$,

$$P_3(A) = R_n e^{-A\left(k_{off}-k_{on}n\right)/D} \tag{5.17}$$

and

$$P_3(r) = R_n r e^{-\pi r^2\left(k_{off}-k_{on}n\right)/D}. \tag{5.18}$$

The normalization constant in Eq. 5.18 is

$$R_n = 2\lambda \exp\left(a^2\lambda\right), \tag{5.19}$$

where

$$\lambda = \pi\frac{\left(k_{off}-k_{on}n\right)}{D}.$$

The log-likelihood function is

$$\ln\left[L_3(\lambda \mid r)\right] = n\ln(2\lambda) + na^2\lambda + \sum_j^n \ln r_j - \lambda\sum_i^n r_i^4. \tag{5.20}$$

*Model 4*

A different model of growth takes place when there exists feedback between on- and off-rates, in order to maintain a given domain size. The coupling of growth rates to the size of the domain can be modeled in different ways. A simple approach to this problem is to have an insertion term that is dependent on cluster size so that $k_{on}n = k_{off}$ when $r = R_0$, $k_{on}n$ decreases when and $k_{on}n$ increases when $r < R_0$. In a proportional negative feedback control (linear approximation),

$$k_{on}n = k_{off} + \alpha\left(R_0 - r\right) \tag{5.21}$$

where $\alpha$ is a coupling constant with units of $s^{-1}$, i.e., the proportional gain. Then, assuming the domain grows by permeation through its perimeter,

$$\frac{\partial A}{\partial t} = -k_{off} r + k_{on} n r = \alpha \left( R_0 - r \right),$$

$$\frac{\partial r}{\partial t} = \frac{\alpha}{2\pi} \left( R_0 - r \right), \tag{5.22}$$

$$\frac{\partial P}{\partial t} = -\frac{\alpha}{2\pi} \frac{\partial}{\partial r} \left[ \left( R_0 - r \right) P \right] + D \frac{\partial^2 P}{\partial r^2}. \tag{5.23}$$

This Fokker-Planck equation has the steady-state solution

$$P_4 \left( r \right) = R_n e^{\alpha \left( 2 R_0 r - r^2 \right) / 4 \pi D}, \tag{5.24}$$

which grows exponentially for values $r \ll R_0$, is a Gaussian tail for large radii, and peaks at $r = R_0$. In Models 1-3, the off rate must be larger than the on rate for the distributions to be normalizable [242]. This constraint is naturally taken care of within the feedback model. Other types of feedback mechanisms can be formulated but little is gained by studying them in the context of Kv2.1 domain radii. As an example, a different formalism is presented in Model 5. The normalization constant in Eq. 5.24 is

$$R_n = \frac{2 \sqrt{\lambda / \pi \exp \left( -\lambda R_0^2 \right)}}{\operatorname{erfc} \left[ \left( a - R_0 \right) \sqrt{\lambda} \right]}, \tag{5.25}$$

where $\lambda = \alpha / 4 \pi D$.

The log-likelihood function is

$$\begin{aligned} \ln \left[ L_4 \left( \lambda, R_0 \mid r \right) \right] &= \frac{n}{2} \ln \left( \frac{4 \lambda}{\pi} \right) + n R_0^2 \lambda \\ &- n \ln \left[ \operatorname{erfc} \left[ \left( a - R_0 \right) \sqrt{\lambda} \right] \right] \\ &+ 2 \lambda R_0 \sum_j^n r_j - \lambda \sum_i^n r_i^2. \end{aligned} \tag{5.26}$$

*Model 5 (alternate to Model 4)*

We also considered a different feedback mechanism as an alternative to Model 4. In Model 4 we maintain a radius-dependent on-rate with molecules being incorporated at the domain perimeter. However, in a similar fashion to Model 3, we consider a model where the growth is radius-dependent but the incorporation of new molecules is independent of domain size. Thus,

$$\frac{\partial A}{\partial t} = \alpha \left( R_0 - r \right). \tag{5.27}$$

The corresponding Fokker-Planck equation is

$$\frac{\partial P}{\partial t} = -\frac{\alpha}{\sqrt{\pi}} \frac{\partial}{\partial A} \left[ \left( \sqrt{\pi} R_0 - \sqrt{A} \right) P \right] + D \frac{\partial^2 P}{\partial A^2}. \tag{5.28}$$

In steady state we obtain,

$$P_5 \left( A \right) = R_n e^{Z_1 A - Z_2 A^{3/2}}, \tag{5.29}$$

where

$$Z_1 = \frac{\alpha R_0}{D} \text{ and } Z_2 = \frac{2\alpha}{\left( 3\sqrt{\pi} D \right)}.$$

Then,

$$P \left( r \right) = R_n r e^{\alpha \pi \left( e R_0 r^2 - 2 r^3 \right) / 3D}. \tag{5.30}$$

## 5.3 RESULTS AND DISCUSSION

### 5.3.1 *Characterization of the distribution of domain radii*

Fig. 5.1A shows a TIRF image of the basal surface of a cell expressing Kv2.1 channels tagged with GFP. Kv2.1 domains are visible as spots with high intensity levels. The size of the apparent domains is measured by fitting the intensity cross-section profile of each spot to a Gaussian

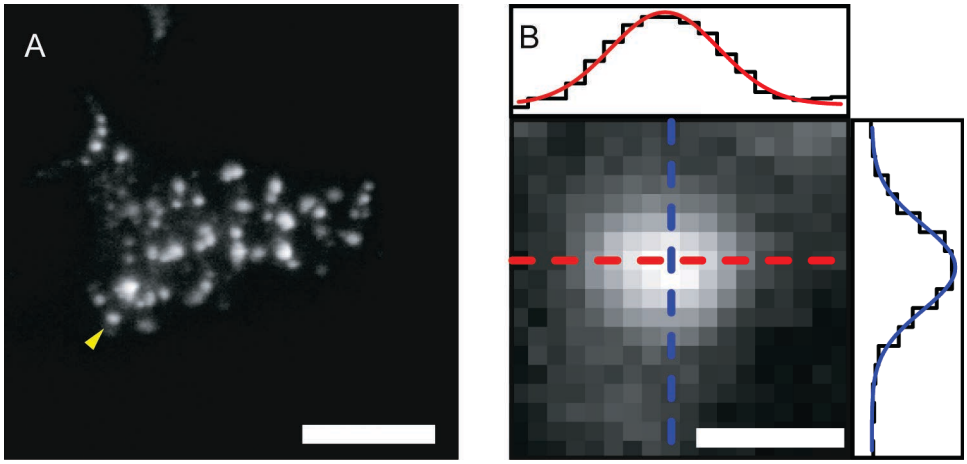


Figure 5.1: *GFP-Kv2.1 clusters in the basal membrane of transfected HEK293 cells.* (A) TIRF image showing clusters in a cell. Scale bar is 10 μm. (B) Zoom of the cluster marked with the yellow arrow. The two cross-section intensity profiles are fit to a Gaussian curve. Scale bar is 1 μm. Pixel size is 0.13 μm.

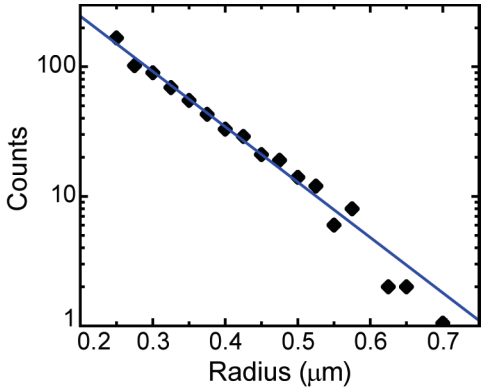


Figure 5.2: *Distribution of cluster radii* Distribution of cluster radii obtained from fitting Gaussian functions to the intensity profile of the cross-sections of each cluster. The line shows a fit to $R_n \exp(-\lambda r)$.

curve as shown, for a typical domain, in Fig. 5.1B. The full width at half maximum (FWHM) of the Gaussian curve provides a good estimate of the diameter of the domain. We have included in our analysis clusters that are either circular or elliptical. Irregularly-shaped domains, accounting for only 5% of the total clusters, are discarded to avoid including two domains into a single fit. The probability distribution of cluster radii built from the measurement of 674 radii in 16 different cells is shown in Fig. 5.2. For each cluster, two radii are obtained: the first one from the vertical cross section and the second one from the horizontal cross section, as indicated in Fig. 5.1B. Both radii are included in the distribution. As is apparent in Fig. 5.2, the obtained distribution is an exponential decay.

Two correlated effects limit the sensitivity of our size measurements. On one hand, when a domain is too small, the intensity profile width is dictated by the PSF independent of domain size.

In general, the image is given by the convolution of the PSF and the observed structure. In our setup, the PSF can be roughly approximated by a 2D-Gaussian with a FWHM of 350 nm. Thus, the smallest spots will appear to have an effective diameter of 350 nm. On the other hand, when the number of channels is small, the definition of a cluster as a circular domain with a well-defined perimeter is not applicable. Namely, the perimeter of the area occupied by structures containing two or three channels is poorly defined. In order to deal with this problem, we obtained the number of channels in each spot and consider only domains that contain at least five channels. Channel number quantification was performed by measuring discrete photobleaching steps of individual GFP tags.

In order to obtain the density of Kv2.1 channels inside clusters, we measured both the cluster area and the number of channels. The intensity of an individual GFP was measured from the bleaching steps of single fluorophores [147]. Individual channels located away from clusters were manually identified and they were then tracked with a custom-written center-of-mass algorithm. A 10x10 ROI was centered around the selected channels and the image was thresholded to reduce bias due to background fluorescence [145]. The XY centroid of the thresholded image was obtained and the ROI was moved to the new location to account for channel motion. The center of mass in the next frame was then found and the algorithm was looped until the particle was lost. Particles are lost by the tracking algorithm either because they are photobleached or because they collide with a Kv2.1 cluster or with another individual channel. The tracking algorithm was implemented in LabView.

The photobleaching of an individual fluorophore occurs in a discrete manner and a step can be observed for each bleaching molecule. Because Kv2.1 is tetrameric, each channel is labeled with four GFP fluorophores and several steps are seen before the channel trajectory is lost. In order to characterize the intensity of a bleaching step the intensity of all the pixels in the threshold image is summed. Figure 5.3A shows characteristic bleaching steps. After a number of steps were collected from different trajectories in a cell the average step intensity is obtained. Fig. 5.3B shows a histogram of the measured intensity change during 39 steps in a single cell. The mean of the step intensity is 10418, measured in arbitrary units and the standard deviation 2374. Due to the tetrameric character of Kv2.1 channels, we obtain the channel number inside each cluster

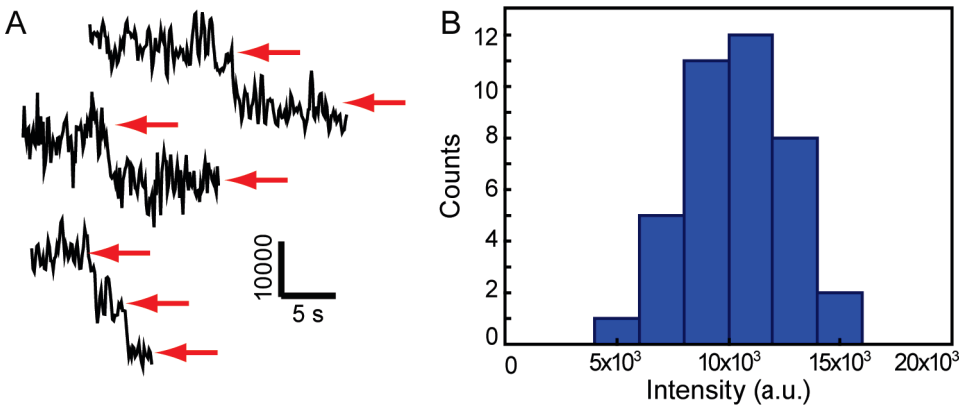


Figure 5.3: *Bleaching steps of individual GFP.* (A) Time-course of the fluorescence emission of three characteristic channels obtained by thresholding and summing the intensities in a 10x10 pixel region of interest. The scale bars show an intensity of 10000 in arbitrary units and a time course equivalent to 5 s. (B) Distribution of the step intensities from the collection of 39 steps in a single cell.

by dividing the sum of the intensities of the pixels in a cluster by 4 times the intensity of a fluorophore.

We found that the density of channels in the clusters was 27.8 ± 8.7 channels per $\mu m^2$ (mean ± standard deviation, $n$ = 53, Fig. 5.4). Then, a domain with five channels has a diameter of 0.5 μm. Therefore, these structures do not suffer from limitations in the resolution imposed by the system's PSF described above.

The probability density function of domain radii fits well to an exponential distribution. This is consistent with a mode of growth where channels are inserted into and extracted from the clusters by exchange with a channel reservoir crossing the domain boundaries, i.e., Model 1 as described in the materials and methods. At first sight, this hypothesis appears to contradict measurements showing that the main pathway of channel trafficking to and from the Kv2.1 clusters is via endocytic and exocytic mechanisms [241]. In Deutsch et al[241] and Chapter 4, we used QD labeling and TIRF imaging approaches to show that Kv2.1 clusters are specialized platforms involved in the trafficking of membrane proteins to and from the cell surface. This approach enabled us to track individual channels and to directly detect the location of plasma membrane insertion of Kv2.1 channels as well as the location of endocytosis from the surface. We observed that Kv2.1 clusters represent platforms for the insertion and retrieval of not only Kv2.1 but also the unrelated $K^+$ channel, Kv1.4.

A different explanation to the apparent growth mode, which is consistent with our previous observations, is that the number of endocytic/exocytic spots is proportional to the domain

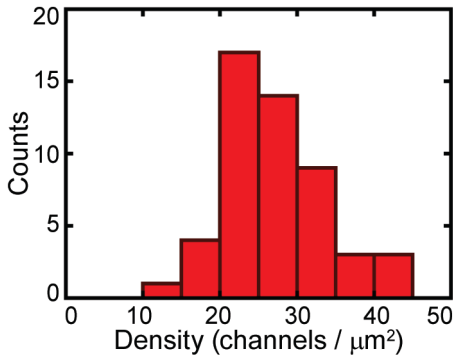


Figure 5.4: *Density of Kv2.1 channels inside clusters*. The number of channels is recorded as described in the text and the area is computed as $\pi d_1 d_2/4$, where $d_1$ and $d_2$ are the diameters found from the cross sections of the cluster intensity profiles.

perimeter. The measured domain size distribution implies that the rate of channel trafficking to and from the cluster is proportional to the domain circumference length. Thus, these results are in agreement with the hypothesis that the larger the cluster, the higher the probability of introducing a trafficking spot and, therefore, the number of these spots grows linearly with domain radius.

The type of growth described by Eq. 5.3 assumes no explicit correlation between cluster size and on-off rates. If the growth rates were controlled by a feedback mechanism that actively maintained a constant domain size, the probability density function of radii would peak at some given value. This can be achieved via an on-rate that increases above the off-rate when the domain shrinks, as modeled by Eq. 5.21. However, the distribution of radii monotonically decreases (see Fig. 5.2), which suggests that no feedback exists between the growth rates and the domain size. The selection of the exponential distribution over the other potential models is rigorously confirmed in the next section through the Akaike information criterion.

Model 1 implies that removal is more predominant than delivery, $k_{off} > k_{on}$. Otherwise, the domains would grow indefinitely. In the limiting case that fluctuations in the endocytic/exocytic machinery were negligible, the steady state solution to this model would be non-zero only for $r = 0$. In other words, because endocytosis dominates over exocytosis, all domains would disappear. However, temporal fluctuations in the on/off rates lead to a finite broadening of the distribution of domain sizes. The strength of these fluctuations is characterized by the parameter $D$. From the distribution of radii we find the relative magnitude of the fluctuations in the on/off rate is .

### 5.3.2 *Model selection*

The semi-log histogram depicted in Fig. 5.2 is indicative of a population of Kv2.1 surface domains that are merely controlled by fluctuations in the endocytosis and exocytosis machinery. However, it is desirable to quantify the likeliness of the proposed model by considering alternative distributions and performing goodness-of-fit tests. The simple and widely used approach of fitting histograms to a model distribution can be problematic due to binning artifacts and the lack of consideration of bins with zero counts. In order to avoid these drawbacks, alternative competing hypotheses can be considered. Then, biological inferences can be drawn by model selection grounded in likelihood theory [247]. Model selection is generally used to select the model that is best supported by the experimental data.

We performed a test based on the statistical theory of likelihood that circumvents the problems described above. Techniques of model selection use negative log-likelihood as a metric for lack-of-fit. Several criteria for model selection exist. The Akaike information criterion (AIC) is the approach of choice in most cases [247, 248]. AIC estimates the Kullback-Leibler information lost by approximating the experimental data to the fitting model [249]. A drawback of AIC is that it is biased towards more complex models. On the other hand, the Bayesian information criterion favors the simpler model. Nevertheless, we see that in the analysis of domain size distribution the model selection using AIC yields the simplest model and, thus, complexity bias is not a concern.

Our approach is based on the Akaike information criterion to determine whether our measured set of domain radii provides evidence for one of the proposed hypotheses. AIC quantifies the relative support for each competing model. Given the measured radii r, we can obtain the log-likelihood function for model $i$ ($i = 1, 2, 3, 4$),

$$\ln\left[L_i\left(\lambda \mid \text{data } r\right)\right],$$

where $\lambda$ is the set of unknown parameters. Details of the methods used to obtain the log-likelihood functions and sets of parameters $\lambda$ of each model are given in the *Methods*. The AIC for each model is given by

Table 5.1: *Analysis of the Kv2.1 sizes from control cells.* AIC applied to the four distributions described in the *Materials and Methods* section over the interval $r \geq 0.25$ μm. $\Delta_i$ are the AIC differences and wi the Akaike weights. The maximum likelihood estimates are $\lambda_1 = \pi(k_{off} - k_{on}n)/2\pi D$, $\lambda_2 = \pi^2(k_{off} - k_{on}n)/2D$, $\lambda_3 = \pi(k_{off} - k_{on}n)/D$, and $\lambda_4 = \alpha/4\pi D$. Note that the definitions and the units of $k_{on}$ and $k_{off}$ are model-dependent according to Eqs. 2.1, 3.5, 3.14, and 5.17. For Model 4, two different values of $R_0$ are reported to indicate the fast decay of the likelihood with $R_0$.

| Model | Maximum likelihood estimates | $\Delta_i$ | $w_i$ |
|---|---|---|---|
| 1: Perimeter-dependent growth | $\lambda_1 = 10.7$ μm$^{-1}$ | 0 | 0.94 |
| 2: Bulk-dependent growth | $\lambda_2 = 45.3$ μm$^{-4}$ | 98.9 | $10^{-20}$ |
| 3: Size-independent growth | $\lambda_3 = 16.6$ μm$^{-2}$ | 5.4 | 0.06 |
| 4: Feedback regulation | $\lambda_4 = 35.6$ μm$^{-2}$ | 22.5 | $10^{-5}$ |
| | $R_0 = 0.25$ μm | | |
| | $\lambda_1 = 44.6$ μm$^{-2}$ | 56.2 | $10^{-15}$ |
| | $R_0 = 0.30$ μm | | |

$$\mathrm{AIC}_i = -2\ln\left[L_i\left(\hat{\lambda}_i \mid \text{data } r\right)\right] + 2p_i, \tag{5.31}$$

where $p_i$ is the number of free parameters and $\hat{\lambda}_i$ is the maximum likelihood estimate of parameters and $\lambda_i$, for model $i$. Then, the AIC differences are $\Delta_i = \mathrm{AIC}_i - \mathrm{AIC}_{min}$. The relative weight of evidence for each model is known as the Akaike weight and is given by

$$w_i = \frac{\exp\left(-\Delta_i/2\right)}{\sum_j \exp\left(-\Delta_j/2\right)}. \tag{5.32}$$

The Akaike weights are values between 0 and 1 that can be interpreted as the probability that a given model is the best approximating model for the measured data. Table 5.1 shows the weights of each of the models described in the *Methods* section. In good agreement with the semi-log plot of the histogram (Fig. 5.2), the model by which the on and off rates are linearly proportional to the perimeter of the domain, i.e., Model 1, is strongly supported by the data. This model has a relative likelihood of 94% as compared to the other hypotheses.

The model that describes growth rates involving the insertion of molecules directly into the domains, not involving the perimeter, has the lowest likelihood. The ratio of its likelihood to the likelihood of the perimeter-dependent hypothesis is $10^{-20}$. This is in agreement with our experimental observations that insertion and retrieval of Kv2.1 channels occurs primarily at the cluster perimeter, emphasizing the accuracy of the used statistical criteria.

The feedback mechanism described by Model 4 was tested for values of $R_0 \geq 0.25$ μm. This is the minimum value of well-defined clusters and, thus, the proposed feedback mechanism aimed at stabilizing clusters to $R_0$ is not relevant for smaller values of $R_0$. The highest likelihood of this model was obtained for $R_0 = 0.25$ μm, but it was several orders of magnitude smaller than the models not involving any feedback control. The likelihood decreased very fast for larger values of $R_0$ indicating the lack of evidence for this model. The likelihood of Model 5 is found to be smaller than that of Model 4. Even though, the models discussed here are not necessarily exhaustive, the goodness-of-fit of the exponential distribution is remarkable.

### 5.3.3 *Changes in the kinetics of growth affect domain size distribution*

As a control experiment of our distribution analysis, we sought to introduce changes in the growth kinetics of Kv2.1 microdomains. One way to drastically alter Kv2.1 clusters is to disrupt the cortical actin cytoskeleton [241, 49]. The effect of cortical actin disruption on Kv2.1 is complex as treatment with different pharmacological inhibitors of actin can cause clusters to dissolve or fuse depending on the concentration applied. We used the G-actin sequestering agent LatA [250] to inhibit the polymerization of actin and induce coalescence of Kv2.1 clusters. Upon treatment with 100 nM LatA, Kv2.1 clusters become more dynamic and merge. We then examined whether there is a measurable change in the cluster size distribution induced by the disruption of cortical actin. If the distribution of radii were sensitive to the physical mechanism of cluster maintenance, pharmacological treatment with an actin polymerization inhibitor should induce an observable change in this distribution.

The radii of Kv2.1 domains in seven different cells were measured both immediately before and 10 minutes after LatA application. We observed that, after treatment, not only did the total number of clusters decrease from 767 to 248 but also their average size increased as expected from the aggregation of clusters. This is can seen in the images of a cell before (Fig. 5.5A) and 10 minutes after (Fig. 5.5B) LatA application. Additionally Fig. 5.5C shows the mean area of the clusters. After a lag phase of 300 s, a dramatic 5 fold increase in size is seen as LatA takes effect. A complementary analysis of the effect of actin on domain dynamics is presented in the next section. As shown in Fig. 5.5D, the distribution of radii 10 min after Lat A addition is no longer

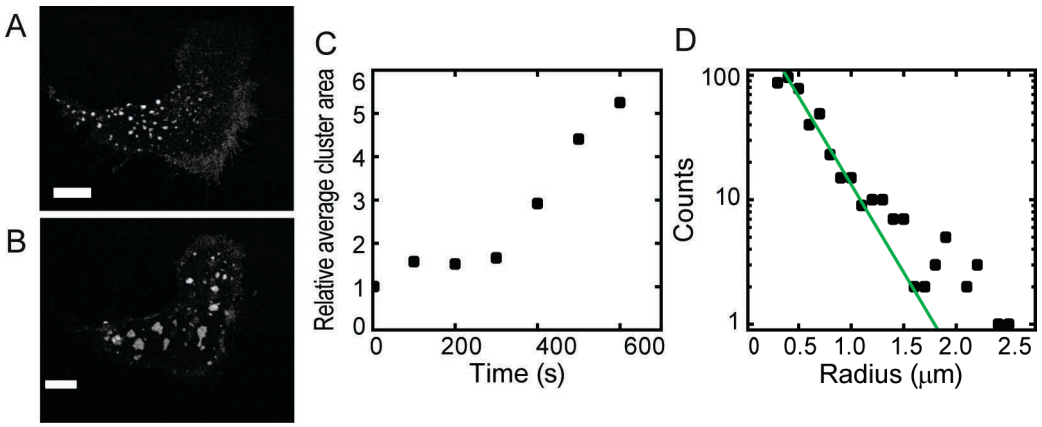


Figure 5.5: *Cells treated with LatA.* (A) TIRF image showing Kv2.1 clusters immediately before LatA application. The scale bar is 10 μm. (B) Same cell, 10 minutes after addition of LatA. The number of Kv2.1 clusters has decreased and their area clearly increased. (C) Time-course of the average cluster size in a single cell after application of LatA. The cluster area was normalized to the average area of the clusters immediately before LatA application. The addition of LatA occurs at time zero. LatA appears to take effect 300 s after application. Until this time the cluster size distribution remains in steady state. (D) Distribution of cluster radii in cells treated with the actin inhibitor LatA. The straight line shows a distribution $R_n \exp(-\lambda r)$.

an exponential for the probed range. Instead, a slower decay is observed with larger domains being prominent.

Our simple measurement of the distribution of domain sizes shows that the growth model is affected by inhibition of cortical actin and, in turn, the distribution of cluster sizes changes. Unfortunately the information theory analysis used in control cells cannot be applied to the LatA-treated cells because, as seen in Fig. 5.5C, in this case the domain size distribution is not in steady state. Nevertheless, a change is directly seen in the dynamic cluster size distribution, which provides further evidence for the link between the distribution of domain sizes and the membrane compartmentalization mechanism.

### 5.3.4 *Effect of latrunculin A on Kv2.1 cluster dynamics*

We assessed the dynamics of individual clusters by tracking their center of mass. The trajectories from 31 clusters were obtained in control cells and 39 clusters in cells treated with LatA. The obtained trajectories were then characterized through their MSD. The MSD provides a simple characterization of the mode of random motion. Unrestricted Brownian motion yields a MSD linear with time: in two dimensions, MSD $\sim 4Dt$, where $D$ is the diffusion coefficient that depends on domain size. However, restricted diffusion results in a subdiffusive type of motion where the MSD becomes sublinear in time, MSD $= K_\alpha t^\alpha$, with $0 < \alpha < 1$ [124]. Figures 5.6A and 5.6B show

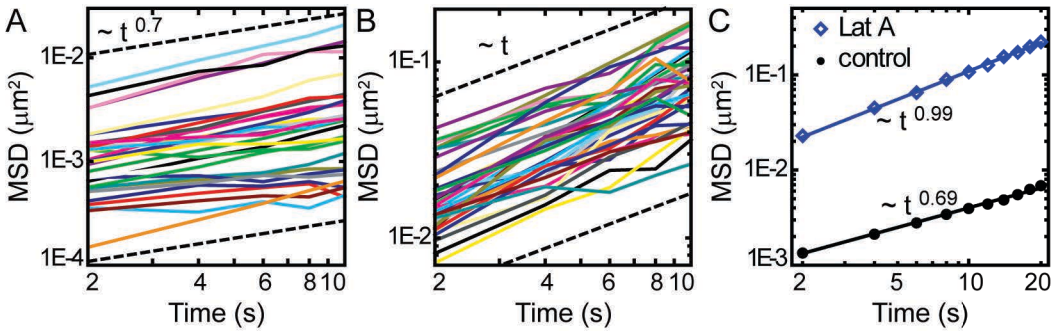


Figure 5.6: *Mean square displacement analysis of the motion of Kv2.1 domains on the cell surface.* Log-log plot of the MSDs of domain trajectories from (A) control and (B) latrunculin A treated cells. In order to show sublinearity with control cells and normal diffusion in latrunculin A cells, dashed lines that scale as to.7 and t are shown (C) Ensemble averaged MSD of 31 control cell clusters (solid circles) and 39 clusters from cells treated with 5 μM latrunculin A (open diamonds). MSDs are fit to a power law, MSD$\sim t^{\alpha}$ to determine diffusion anomaly. Domains in control cells diffuse with an anomalous subdiffusive exponent of 0.69 ± 0.01. Domains in cells treated with latrunculin A are more mobile and display normal diffusion, ($\alpha$ = 0.99 ± 0.01).

log-log plots of the temporal MSD of trajectories in controls and LatA-treated cells, respectively. Dashed lines corresponding to MSD ~ t and MSD ~ $t^{0.7}$ are shown as a visual guide to the eye. Domains in control cells are seen to display anomalous subdiffusion while the domains in treated cells obey normal Brownian motion. Furthermore, the characteristic square displacement, or the diffusion coefficient, in treated cells is more than an order of magnitude higher than the values in control cells. Figure 5.6C shows the MSD in both cases after ensemble averaging the MSD of all the trajectories. Fitting to a power law yields an exponent $\alpha$ = 0.69 for control cells. In LatA-treated cells, the diffusion becomes normal with an exponent of 0.99.

LatA experiments show that the actin cytoskeleton plays a crucial role in the anomalous subdiffusive motion of Kv2.1 domains. These experiments, as well as previous observations [133], also suggest that cortical actin hinders aggregation by forming physical barriers between domains.

## 5.4 CONCLUSIONS

The distribution of domain sizes provides a straightforward method for obtaining kinetic information on the formation and maintenance of membrane domains. The strength of this method lies in its simple application. The distribution of Kv2.1 domain sizes implies that cluster growth is proportional to the cluster perimeter length. Additionally we do not find evidence for local feedback between endocytic and exocytic events at the individual cluster level. The model scenarios analyzed in this work are not exhaustive, and other kinetic models can be proposed, in particular

at longer length scales. The likelihood of the proposed model was rigorously established through the Akaike information criterion. The distribution analysis is consistent with a model where the cluster size is simply governed by the fluctuations of the endocytic and exocytic processes.

## 5.5 ACKNOWLEDGEMENTS AND CONTRIBUTIONS

Michael M. Tamkun and Diego Krapf designed the research. Aubrey Weigel and Diego Krapf contributed analytical tools. Aubrey Weigel performed the research in control cells and together Phil Fox and Elizabeth Akin performed the research in LatA treated cells. Aubrey Weigel and Kari Ecklund analysed the data.

# CHAPTER 6: CCP TRAPPING ENERGIES

Clathrin mediated endocytosis is the major route of cargo internalization in mammalian cells. The assembly of CCPs is a multistep process that includes nucleation of a clathrin coat and growth by recruitment of clathrin molecules, adaptors and cargo. This process is terminated either non-productively (the pit breaks up) or productively (a vesicle forms and is internalized). Even though the association of cargo to CCPs is crucial in the regulation of endocytosis, the study of this interaction in vivo remains challenging. In this chapter we study the recruitment of cargo by characterizing the interactions of clathrin coated pits with Kv2.1. As shown in Chapter 4 Kv2.1 displays a confined subdiffusion type of motion on the cell surface and it undergoes frequent stalls. Multicolor imaging indicates thatt hese stalls are caused by stable CCPs that capture Kv2.1 channels. By monitoring the residence time of Kv2.1 within a CCP, we are able to study the binding strength as a function of the age of a pit, e.g., the time since coat initiation. Due to the dynamic growth of CCPs, the interaction between the pit and cargo is not Poissonian. A kinetic model thatt akes into accountt he coat assembly via the recruitment of adaptor proteins leads to nonstationary and nonergodic Kv2.1 dynamics. This model accurately predicts the statistics of transient binding between pit and cargo.

## 6.1 introduction

clathrin-mediated endocytosis (CME) is the dominant route of cargo internalization in mammalian cells [251, 252, 253, 254]. This process occurs through the nucleation, maturation, invagination, and pinching offof clathrin-coated pits. Clathrin is linked to the membrane via adaptor proteins such as AP-2. Adaptor proteins serve to both link clathrin to the membrane and also select and recruit cargo to the CCP [255, 256, 257, 258]. As the pit grows the membrane is mechanically deformed and a vesicular bud is formed [256, 258, 257]. The pit continues to grow and mature until a narrow neck is the only bit joining itt o the membrane. It is then pinched offfrom the membrane by the GTPase dynamin and becomes a clathrin-coated vesicle.

Fluorescent microscopy has enabled the direct visualization of CCPs and their dynamics. Cells expressing fluorescently labeled clathrin contain CCPs that appear as diffraction limited fluores-

cent spots on the cell surface. One of the leading assays to detect these fluorescent spots is TIRF microscopy [259, 260, 261, 262]. This imaging technique allows the lifetime of the CCPs to be directly observed, an important parameter for analyzing CCP dynamics[253]. The lifetime of a CCP starts with the assembly of clathrin, seen as the appearance of fluorescence within the TIRF illumination. The extinguishing of fluorescence indicates the end of the CCP lifetime either through abortive or productive pathways, where a productive pit results in a clathrin-coated vesicle. Abortive pits begin the initial stages of coat assembly but break apart prematurely, possibly due to the lack of cargo[252, 232]. The relationship between cargo capture and successful clathrin-coated vesicle formation is indeed important. In this chapter we investigate this relationship with fluorescently labeled clathrin-light chain and the voltage-gated potassium channel Kv2.1.

In Chapter 4 we reported on the dynamics of the Kv2.1 channel on the cell surface. We found that the channel's motion displays anomalous subdiffusion, and that the combination of a stationary and non-stationary processes, a CTRW in a percolation cluster, best models the underlying mechanisms for the observed anomalous subdiffusion[49]. Geometric inhomoegenities giving rise to a percolation cluster are consistent with macromolecular crowding, often observed on the cell membrane[263, 122, 170, 143, 95]. We predict that transient binding events, best modeled by a CTRW [124, 42, 135], may be involved in maintaining the Kv2.1 channel at endocytic sites to allow interactions between the channel and adaptor proteins.

Here we use multi-color TIRF microscopy to simultaneously image individual Kv2.1 channels and fluorescently labeled CCPs. We establish that Kv2.1 is endocytosed via CME pathways. Localization of Kv2.1 stalls lasting longer than 0.5 s, indicative of binding events, also occurs within CCPs. We derive a kinetic model for cargo capture within a CCP, taking into account the coat assembly through the recruitment of adaptor proteins. This model leads to nonstationary and nonergodic cargo dynamics. Direct comparison of model predictions reveals that the broad distribution of stalling times observed by Kv2.1 channels (modeled by a CTRW) is due to Kv2.1 capture within a CCP. Furthermore, we show that upon deletion of the C-terminal tail the Kv2.1 channel no longer stalls and ergodicity is recovered.

## 6.2 MATERIALS AND METHODS

### 6.2.1 *Cell culture and transfection*

Three different combinations of plasmids were used for experiments with clathrin and Kv2.1:

1. GFP-Kv2.1-loop BAD with RFP-CLC
2. Kv2.1-loop BAD with GFP-CLC
3. ΔC-Kv2.1-loop BAD with GFP-CLC

The same human CLC A sub-cloned into the mRFP-C1 and eGFP-C1 expression vectors used in Chapter 4, were kindly provided by Dr. Santiago Di Pietro (Department of Biochemistry and Molecular Biology, Colorado State University). Kv2.1 channels have been described previously[134, 133, 49]. We found three binding motifs for AP2 in the cytoplasmic domains of Kv2.1, D675 [DPTPLL], E704 [ECASLL], and D757 [DEGQLL]. Standard PCR mutagenesis techniques were used to construct ΔAP2-Kv2.1-GFP. We used a single point mutation LL761\2AA to alter the dileucine binding site in the furthest motif from the transmembrane domain of the rat Kv2.1 primary sequence. As in previous chapters, HEK 293 cells (American Type Culture Collection, passage 38-45) were cultured in DMEM (Gibco, Life Technologies, Carlsbad, CA) supplemented with 10% fetal bovine serum (FBS, Gibco) at 37˚C and 5% $CO_2$. Following Protocol 8.3, cells were transfected by electroporation using a BioRad Genepulser Xcell (BioRad Laboratories, Hercules, CA) in a 0.2 cm gap cuvette with a single 110-V 25-ms pulse with a combination of 3 μg of GFP-Kv2.1-loop BAD, 3 μg Kv2.1-loop BAD, 3μg ΔC-Kv2.1-loopBAD, 1 μg pSec BirA, and 200 ng fluorescently labeled CLC (either GFP or RFP) expressing DNA depending on the experiment (see list above for experimental combinations used). Following electroporation cells were plated on cover-glass-bottom culture dishes that were previously Matrigel-coated (BD Biosciences, San Jose, CA) and supplemented with DMEM without phenol red (Life Technologies) and 10% FBS. Cells were used for live cell imaging within 24 hours of transfection.

### 6.2.2 *Live cell imaging*

Prior to imaging, cells were rinsed three times with a HEK physiological imaging saline (8.6). Biotinylated Kv2.1 channels were then incubated with 0.1 nM solution of streptavidin conjugated QDs (Qdot 655 or Qdot 705, Invitrogen) and 150 μM BSA (IgG- fatty-acid-free, Sigma-Aldrich) in imagine saline for 5 minutes then rinsed two more times with HEK imaging saline to remove any unbound QDs (8.4). For three-color imaging of RFP-CLC and GFP-Kv2.1-QD, 705 nm QDs were used. For two-color imaging of GFP-CLC and Kv2.1-QD 655 QD were used. Transfected cells were imaged in imaging saline at 37˚C.

Imaging took place on the same microscope described in previous chapters [49]. For two-color TIRF imaging (2 and 3) the 473 nm laser was used to excite both GFP-CLC and 655QD-Kv2.1. The fluorescent emissions were then optically split (Optosplit, Cairn) onto the two halves of an electron-multiplied charge coupled device (iXon DU-888, Andor) . For three-color TIRF imaging experiments (1) the RFP-CLC was excited with the 532 nm laser, GFP-Kv2.1with the 473 nm laser, and the 705QDs excited by both lasers. The emissions were separated both spectrally and temporally. Alternate shuttering (Uniblitz vmm-d3) of the 473 and 532 nm laser allowed separation between GFP and RFP fluorescence. The 705QD fluorescence was then separated optically from the GFP/RFP signal similar to the two-color TIRF imaging experiments. Both the dish and the objective were maintained at 37˚C using a temperature control system (Bioptechs).

### 6.2.3 *Endocytosis disruption reagents*

Dynasore and Pitstop2 were used to disrupt CME. Dynasore works by inhibiting the GTPase dynamin[264, 265]. Dynamin is principally responsible in the scission of vesicular buds from the plasma membrane. It has been suggested that dynamin is also involved in the early stages of CCP formation, serving as both a regulator and integrity monitor [253, 266, 267]. Pitstop2 (Pitstop2, abcam) is a small molecule inhibitor of CME and works by blocking endocytic ligand association, such as amphiphysin, with the clathrin terminal domain[268]. In these experiments, Dynasore and Pitstop2 were all dissolved in dimethyl sulfoxide (DMSO, Sigma-Aldrich) and directly added to the imaging dish to a final concentration of 80 μM[264, 265] and 30 μM[268] respectively.

### 6.2.4 *Image and data analysis*

*Image processing and single-particle tracking*

Images were acquired using Andor IQ 2.3 software and saved as 16-bit tiff files. The images were overlaid using the Cairn-Optosplit plugin available in ImageJ. The images were frame averaged using a custom-written algorithm in LabView that averages the intensities of every pair of images, reducing the number of frames to half. Then the 2x-frame averaged images were filtered using a Gaussian kernel with a standard deviation of 1.0 pixel in ImageJ. Both GFP-CLC and QD-Kv2.1 were tracked. Single-particle tracking of GFP-CLC was done using the Danuser lab u-track (9.3.3) [269]. Single-particle tracking of QD-Kv2.1 was performed with a modified version of this algorithm. The modifications include alterations to the cost functions within the code to account for the inherent blinking behavior of QDs. To determine if Kv2.1 are endocytosed via CME the disappearance of individual QD-Kv2.1 channels were manually counted. The endocytic event was marked as clathrin-mediated when the disappearance of the channel coincided with the disappearance of a GFP-labeled CCP.

*Displacement square analysis*

The square displacements of QD-Kv2.1 trajectories were found using automated software written in LabView (5) [49]. As shown in Chapter 4 (4) , we identified events in which the channel remained confined within a radius of $R^2_{TH} = 500$ nm². All displacement squares less than $R^2_{TH}$ were identified and the number of frames where the channel does not cross the radial threshold, $R^2_{TH} = 500$ nm². The time and location of each stall lasting longer than 0.5 s were recorded. This information was used to determine where stalls occurred with respect to clathrin. Stalls that occurred within 1 pixel (130 nm) from the edge of a CCP were considered colocalized to clathrin.

*Lifetime analysis*

Clathrin coated pits were analyzed in terms of their lifetimes following the work of Loerke et al[253]. To account for trajectories that are not seen in their entirety due to the movie start and/or end point the histogram counts were corrected[253]:

$$C(t_i) = \frac{F(t_i)\,T}{T - t_i} \tag{6.1}$$

where $C(t_i)$ are the corrected counts, $F(t_i)$ are the original counts, $T$ is the movie length, and $t_i$ the length of the trajectory (i.e. the lifetime of the pit). The CDF is then

$$CDF(t_i) = \sum_i \frac{C(t_i)}{\sum_i C(t_i)} \tag{6.2}$$

The models were fit to the CDF to avoid any bias due to bin size. Exponential distributions with one, two, three, and four populations were fit along with the combination of Rayleigh distributions with Exponential distributions. Equations for a single exponential PDF, the combination of an exponential and Rayleigh distribution PDF, and the combination of two exponential distributions and one Rayleigh distribution PDF are provided below.

$$PDF_{exp1}(t) = \frac{1}{\tau}\exp\left(-t/\tau\right) \tag{6.3}$$

$$PDF_{exp1ray1}(t) = \frac{At}{\tau_1^2}\exp\left(-t^2/2\tau_1^2\right) + \frac{(1-A)}{\tau_2}\exp\left(-t/\tau_2\right) \tag{6.4}$$

$$PDF_{exp2ray1}(t) = \frac{A_1 t}{\tau_1^2}\exp\left(-t^2/2\tau_1^2\right) + \frac{A_2}{\tau_2}\exp\left(-t/\tau_2\right) + \frac{(1-A_1-A_2)}{\tau_3}\exp\left(-t/\tau_3\right) \tag{6.5}$$

Here $A_n$ is the weight of each distribution and $\tau_n$ is the characteristic time of each distribution.

*Model selection*

The BIC is a model selection criterion for a finite set of models. The BIC presents a measure of fit between the data and models and penalizes for over-parameterization. The penalty for over-parameterization is higher in BIC than in AIC, especially for larger $n$. In accordance to Loerke et al's work, BIC model comparison of fits to the CDF with corrected counts was used to determine the best model for the given data,

$$\text{BIC} = \left(n \cdot \log\left(RSS/n\right)\right) + p \cdot \log(n) \tag{6.6}$$

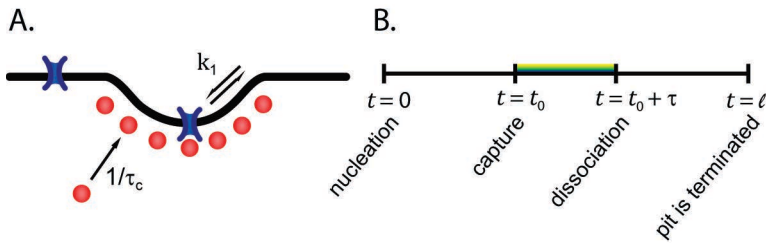


Figure 6.1: *CCP trapping of Kv2.1 Model* (A) Cargo (blue) diffuses laterally across the membrane and binds to adaptor molecules in a forming pit (red) with a dissociation rate of $k_1$. Adaptor proteins arrive to the growing pit at a rate of $1/\tau_c$. (B) The lifetime of a CCP begins at time $t = 0$ with nucleation. At some time, $t = t_0$ cargo is captured within the pit due to binding to adaptor molecules. The cargo remains captured for a time $\tau$. The lifetime of the pit is terminated either abortively or productively at $t = l$.

where $n$ is the sample size, $RSS$ the residual sum of squares of the fit, and $p$ the number of free parameters[270]. The model that minimizes the $BIC$ implies that the residuals and the number of parameters is also minimized.

### 6.2.5 *Clathrin coated pit trapping of Kv2.1 model*

Here we derive a kinetic model for the interactions between CCPs and cargo. with In this model the channel, Fig. 6.1A (blue) diffuses laterally across the membrane and binds to adaptor molecules (red) in a forming pit with a dissociation rate of, $k_1$. Experimentally, binding to adaptor molecules is seen as Kv2.1 stalls, $\tau$. The pit lifetime begins at time $t = 0$, grows with the addition of pit proteins at a rate of $1/\tau_c$, and terminates either abortively or productively at time $t = l$. The mean time of arrival of an extra adaptor to the pit is $\tau_c$. At time $t = t_0$ the channel is captured in the pit (Fig. 6.1B) and remains there for a time $\tau$ (colored box in Fig. 6.1B) until it unbinds and is able to escape at time $t = t_0 + \tau$. The number of adaptors in the pit can be expressed in terms of time as $n = t/\tau_c$. The rate at which the channel escapes from the pit depends on the number of adaptors in the pit and the rate of unbinding, $k_{off} = k_1/n = k_1\tau_c/t$. In this model we assume the pit grows linearly with time.

We first derive the survival probability of the channel still being captured within the pit at a time larger than $\tau$. Then the conditional PDF of binding times is then found. From here we find the three PDFs used to compare our model to experimental data:

1. The conditional PDF of binding times given the channel binds at time $t_0$: $\psi(\tau \mid t_0)$
2. The PDF of channel capture times: $P(t_0 \mid \text{bind})$

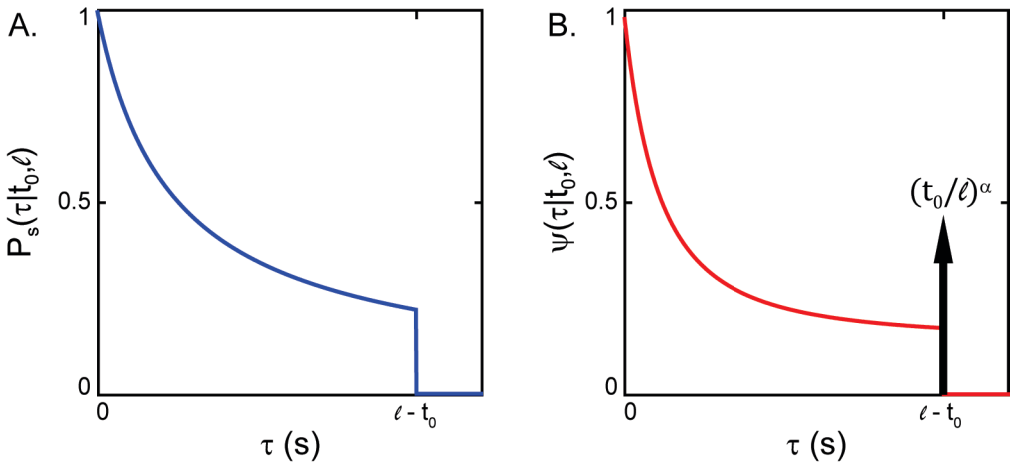


Figure 6.2: *Schematic Representation of* $\Psi(\tau \mid t_o,l)$ *and* $\psi(\tau \mid t_o,l)$ (A) $\Psi(\tau \mid t_0,l)$ from Eq. 6.7. (B) $\psi(\tau \mid t_0,l)$ from Eq. 6.8

3. The PDF of stalling times: $P(\tau)$

The probability of the channel still being bound at a time larger than $\tau$ given it binds at $t_0$ in a pit with lifetime $l$ is non-Poissonian due to the time dependence of $k_{off}$.

$$\frac{d\Psi}{d\tau} = -k_{off}\Psi$$

$$\Psi(\tau \mid t_0,l) = \begin{cases} \left(\frac{t_0}{t_0+\tau}\right)^{\alpha} & , \quad 0 < \tau \leq l - t_0 \\ 0 & , \quad \tau > l - t_0 \end{cases} \tag{6.7}$$

where $\alpha = k_1\tau_c$. The conditional PDF of stalling times is then

$$\psi(\tau \mid t_0,l) \;=\; \tfrac{d}{d\tau}\left(1 - P_s(\tau \mid t_0,l)\right) \;=\; -\tfrac{dP_s(\tau|t_0,l)}{d\tau}$$

$$\psi(\tau \mid t_0,l) = \begin{cases} \frac{\alpha t_0^{\alpha}}{(t_0+\tau)^{1+\alpha}} + \frac{t_0^{\alpha}}{(l)^{\alpha}}\delta(\tau - l + t_0) & , \quad 0 < \tau \leq l - t_0 \\ 0 & , \quad \text{otherwise} \end{cases} \tag{6.8}$$

We next formulate the PDF of stalling times given the channel is captured in the pit at time $t_0$. This conditional PDF is given that the channel becomes bound within the CCP:

$$\begin{aligned}\psi(\tau \mid t_0) &= \psi(\tau \mid t_0, \text{bind}) \\ &= \int_0^\infty \psi(\tau \mid t_0, l, \text{bind})\, P(l \mid \text{bind})\, dl \\ &= \int_0^\infty \psi(\tau \mid t_0, l)\, P(l \mid \text{bind})\, dl \end{aligned} \tag{6.9}$$

We have $\psi(\tau \mid t_0, l)$ from Eq. 6.8 and thus only need to obtain $P(l \mid \text{bind})$. We can use Bayes' theorem to retrieve $P(l \mid \text{bind})$:

$$P(l \mid \text{bind}) = \frac{P(\text{bind} \mid l)\, P(l)}{P(\text{bind})} \tag{6.10}$$

To obtain $P(\text{bind} \mid l)$ we integrate the probability of capture time $t_0$, given the lifetime of the pit $l$ over all possible capture times. This probability is proportional to the perimeter of the pit and we assume the pit grows linearly with time, such that $n \propto t_0$:

$$\begin{aligned} P(t_0, \text{bind} \mid l) &= c_1 r \\ &= c_2 \sqrt{n} \\ &= c_3 \sqrt{t_0} \end{aligned}$$

for $0 < t_0 < l$. In complete form:

$$P(t_0, \text{bind} \mid l) = \begin{cases} c_3 \sqrt{t_0} & , \quad 0 < t_0 < l \\ 0 & , \quad \text{otherwise} \end{cases} \tag{6.11}$$

where $c_3$ is a constant. Integrating over all possible capture times we find the probability of binding given the lifetime of the pit,

$$P(\text{bind} \mid l) = \int_0^l P(t_0, \text{bind} \mid l)\, dt_0 = c_3 \int_0^l \sqrt{t_0} dt_0 = c_4 l^{3/2} \tag{6.12}$$

where $c_4$ is a constant of integration. And now Eq. 6.10 becomes

$$P\left(l \mid \text{bind}\right) = \frac{P\left(\text{bind} \mid l\right) P\left(l\right)}{P\left(\text{bind}\right)} = \frac{c_2 l^{3/2} P\left(l\right)}{c_B} = C l^{3/2} P\left(l\right)$$

where

$$\begin{aligned} P\left(\text{bind}\right) &= c_B & (6.13)\\ P\left(\text{not bind}\right) &= 1 - c_B & (6.14) \end{aligned}$$

and $c_B$ is a constant that depends on channel density. $C = {}^{c_2}/_{c_B}$, which can directly be found from the normalization of $P\left(l \mid \text{bind}\right)$ ,

$$C = \frac{1}{\int_0^\infty l^{3/2} P\left(l\right) dl} \tag{6.15}$$

We can now find $\psi\left(\tau \mid t_0\right)$, the probability density function of stalling times given the channel is captured within the pit at time $t_0$, from Eq. 6.9.

$$\begin{aligned} \psi\left(\tau \mid t_0\right) &= \int_0^\infty \psi\left(\tau \mid t_0, l\right) P\left(l \mid \text{bind}\right) dl \\ &= C \int_{t_0+\tau}^\infty \left[ \frac{\alpha t_0^\alpha}{\left(t_0+\tau\right)^{1+\alpha}} + \left(\frac{t_0}{l}\right)^{alpha} \delta\left(\tau - l - t_0\right) \right] l^{3/2} P\left(l\right) dl \\ \psi\left(\tau \mid t_0\right) &= \frac{t_0^\alpha}{\left(t_0+\tau\right)^{1+\alpha}} \frac{1}{\int_{t_0}^\infty P\left(l\right) dl} \left[ \alpha \int_{t_0+\tau}^\infty P\left(l\right) dl + \left(t_0+\tau\right) P\left(l = t_0+\tau\right) \right] \end{aligned} \tag{6.16}$$

We will now find the final two PDFs for capture times and stalling times. The probability of binding times given the lifetime of the pit and given the channel binds is,

$$P\left(t_0 \mid l, \text{bind}\right) = \begin{cases} c_5 \sqrt{t_0} & , \quad 0 < t_0 < l \\ 0 & , \quad \text{otherwise} \end{cases} \tag{6.17}$$

where $c_5$ is a normalization constant, so that $\int_0^l P\left(t_0 \mid l, \text{bind}\right) dt_0 = 1$,

$$c_5 = \frac{3}{2} l^{-3/2} \tag{6.18}$$

From this we can directly extract the probability of stalling times given that the channel binds:

$$\begin{aligned} P(t_0 \mid \text{bind}) &= \int_{t_0}^{l} P(t_0 \mid l, \text{bind})\, P(l \mid \text{bind})\, dl \\ &= \frac{3\sqrt{t_0}}{2\int_0^{\infty} P(l)\, l^{3/2} dl} \int_{t_0}^{\infty} P(l)\, dl \end{aligned} \tag{6.19}$$

Lastly, the probability density of channel stalls is,

$$\begin{aligned} P(\tau) &= \int_0^{\infty} \psi(\tau \mid t_0)\, P(t_0)\, dt_0 \\ &= \frac{3}{2} C \int_0^{\infty} \left[ \sqrt{t_0} \left( \frac{t_0^{\alpha}}{(t_0+\tau)^{1+\alpha}} \right) \right. \\ &\quad \left. \left( \alpha \int_{t_0+\tau}^{\infty} P(l)\, dl + (t_0+\tau)\, P(l = t_0+\tau) \right) \right] dt_0 \end{aligned} \tag{6.20}$$

The models were computed using Matlab and directly compared to experimental data.

The interactions between Kv2.1 channels and CCPs was analyzed by first matching QD-Kv2.1 stalls with GFP-CLC trajectories. An automated program written in Labview was used to match the stalls and trajectories according to their temporal and spatial location (Chapter 5, 9.4.3). For each Kv2.1 stall, the frame and the location (i.e. XY coordinates) where the stall occurred was noted. Then each CCP trajectory was searched at that specific frame for a matching location, within 3 pixels or rather 390 nm (to account for error in the overlay of images), of the Kv2.1 stall location. Once matched, each stall ($\tau$) of the matched Kv2.1 channels were associated with the lifetime of the corresponding pit ($l$) and the time (from the beginning of the pit lifetime) at which the stall occurred ($t_0$).

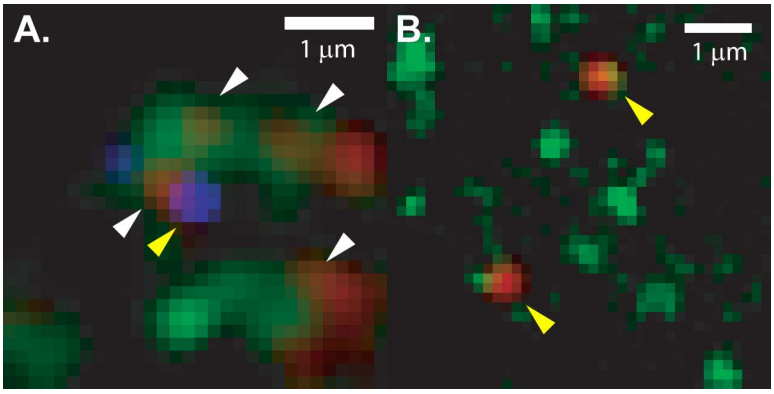


Figure 6.3: *Kv2.1 colocalizes to clathrin* (A) GFP-Kv2.1 (green) labeled with 705-QDs (blue) and RFP-CLC (red) were simultaneously imaged in HEK 293 cells. The yellow arrow indicates the colocalization of a QD-labeled, cluster confined Kv2.1 channel with a clathrin coated pit. White arrows indicate that clathrin coated pits (red diffraction limited spots) are localized to the perimeter of GFP-Kv2.1 clusters (in green) as predicted in Chapter 04, [MBoC]. (B).

## 6.3 RESULTS

### 6.3.1 *Kv2.1 is endocytosed via clathrin mediated endocytosis*

Fig. 6.3A shows a three-color TIRF image of HEK cells co-expressing GFP-Kv2.1 channels labeled with 705QDs and RFP-CLC. All Kv2.1 channels in the cell are fused to a GFP molecule to provide information on the cluster. Individual Kv2.1 channels are extracellularly labeled with QDs to allow for single-particle tracking. White arrows indicate CCPs, denoted by the red fluorescence of RFP-CLC, that localize to the perimeter of Kv2.1 clusters as predicted in Chapter 4 and 4[1] [241, 271]. The yellow arrow in Fig. 6.3B shows colocalization of a cluster confined, QD labeled Kv2.1 channel with a CCP consisting of GFP-CLC.

To provide further evidence that Kv2.1 channels are recycled via CME, endocytic events of Kv2.1 channels were tallied as 'on' and 'off' clathrin. When the extinction of QD-Kv2.1 fluorescence coincided with the loss of GFP-CLC from the TIRF illumination the event was marked as being endocytosed on clathrin and visa versa. Fig. 6.4 summarizes these results. 87 ± 3% (n = 97, mean ± s.d.) of Kv2.1 channels were endocytosed via CME in control cells, Fig. 6.4A. Furthermore 13 ± 4% (n = 729, mean ± s.d.) of Kv2.1 channels were endocytosed within a 10 minute time frame, Fig. 6.4B. We next inhibited endocytosis with 30 μM Pitstop2[268]. The rate of endocytosis decreased slightly 20 minutes after application of Pitstop2 shown in Fig. 6.4B. The percentage of channels

1 In Chapters 04 and 05 we show that recycling occurs at the cluster perimeter both through experimental observations[241] and modeling of cluster the cluster size distribution using a Fokker-Planck formalism[271].

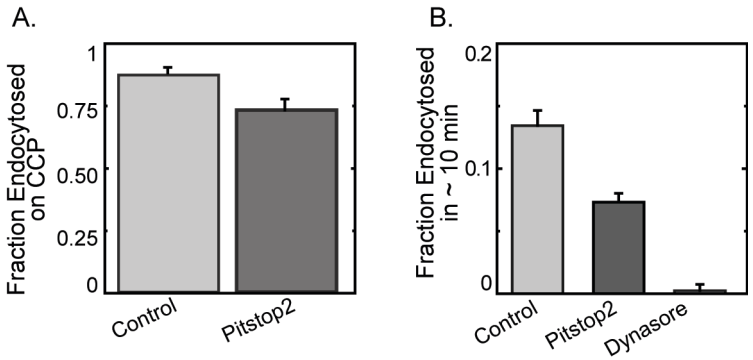


Figure 6.4: *Kv2.1 is endocytosed via CME* (A) Out of 97 endocytic events 87 ± 3% (n = 97, mean ± s.d.) were via clathrin mediated pathways in control cells and 73 ± 5% (n = 65, mean ± s.d.) in cells treated with Pitstop2. (B) In a 10 minute time frame 13 ± 4% (n = 729, mean ± s.d.) of Kv2.1 channels were endocytosed in control cells and 7 ± 3% (n = 888, mean ± s.d.) in cells treated with Pitstop2 and only one endocytic event out of 421 trajectories observed with Dynasore, 0.2 ± 0.2% (n = 421, mean ± s.d.).

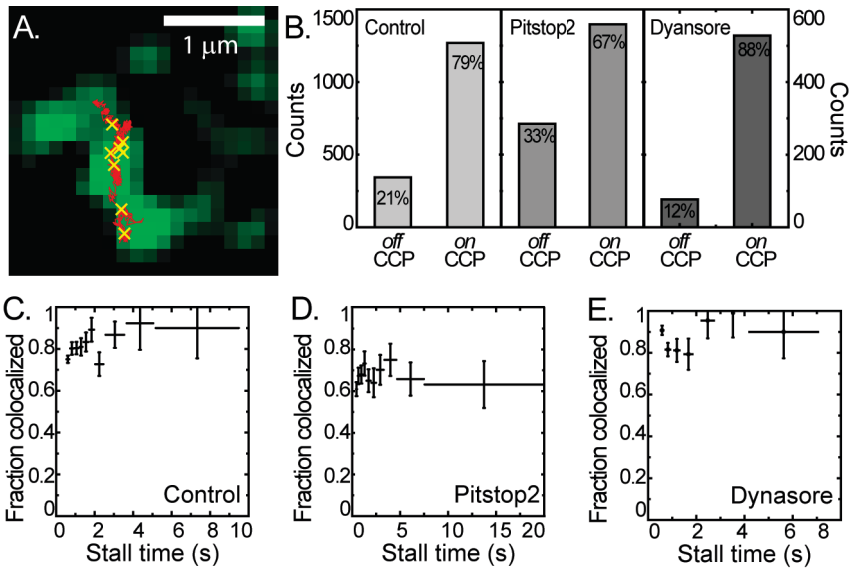


Figure 6.5: *Kv2.1 stalls on CCPs* (A) GFP-CLC was coexpressed with non-fluorescent Kv2.1 channels that were labeled with 655QDs. The red trajectory is the path of an individual QD-Kv2.1 channel. Yellow x's indicate where the channel stalled for more than 3 s within a circle of area, $R^2_{TH} = 500$ nm². (B) Percentage of QD-Kv2.1 stalls colocalizing to GFP labeled CCPs in control cells and cells treated with a clathrin-mediated endocytosis inhibitor Pitstop2 and Dynasore. (C), (D) and (E) Colocalization of QD-Kv2.1 stalls on CCPs according to stall time for control cells (C) and cells treated with Pitstop2 (D) and Dynasore (E). Error bars are $1/\sqrt{n}$ where $n$ is the number of stalls.

endocytosed via CME also decreased by 6% in Pitstop2 treated cells with 73 ± 5% (n = 65, mean ± s.d.) shown in Fig. 6.4A. Next 80 μM Dynasore was used to inhibit CME[264, 265]. Out of 421

| Model | $p$ | $BIC$ |
|---|---|---|
| 1-exp | 1 | -7967 |
| 2-exp | 3 | -9800 |
| 3-exp | 5 | -10406 |
| 4-exp | 7 | -10392 |
| 1-exp + 1-ray | 3 | -7192 |
| 2-exp + 1-ray * | 5 | -11468 |
| 1-exp + 2-ray | 5 | -10411 |

Table 6.1: *Minimization of the BIC* The corrected lifetime CDF, Eqs. 6.1 and 6.2 was fit to four different exponential distributions and the combinations of exponential and Rayleigh distributions. The model that minimized the $BIC$ was the Rayleigh distribution plus two exponentials.

trajectories in 6 different cells only one endocytic event was observed within a ~ 10 minute time frame, 0.2 ± 0.2% (n = 421, mean ± s.d.) and it coincided with the disappearance of clathrin.

### 6.3.2 *Kv2.1 stalls on clathrin-coated pits*

In Chapter 4 and 4 we show that Kv2.1 diffusion can be modeled by the combination of a stationary and non-stationary processes, namely a CTRW on a percolation cluster [49, 50]. We hypothesized that the transient binding events, modeled by a CTRW, may be involved in maintaining the channel at endocytic sites to allow interactions between the channel and adaptor proteins. QD labeled Kv2.1 channels were tracked using a modified version of the Danuser lab u-track algorithm, to account for QD blinking. The distribution of stall times of channels was constructed as in Chapter 4 [49] with $R_{TH}^2 = 500$ nm² and the time and location of stalls longer than 0.5 s recorded. As summarized in Fig. 6.5 Kv2.1 stalls highly colocalize to CCPs. Fig. 6.5A shows a representative QD-Kv2.1 trajectory superimposed onto a GFP-CLC image. The yellow x's indicate stalls that were greater than 3 s. Note that the stalls localize with clathrin. Overall 79 ± 2% (n = 1613, mean ± s.d.) of all Kv2.1 stalls longer than 0.5 s colocalized to CCPs. When endocytosis was inhibited with Pitstop2 the percentage of stalls on clathrin decreased. Fig. 6.5. We next analyzed the colocalization of Kv2.1 stalls according to the length of stalls. Fig. 6.5C shows that as the stall time increases the localization on clathrin also increases. However in cells treated with Pitstop2 the colocalization of stalls remains constant for all lengths of stall times with 67 ± 4 % (n = 844, mean ± s.d.), Fig. 6.5D.

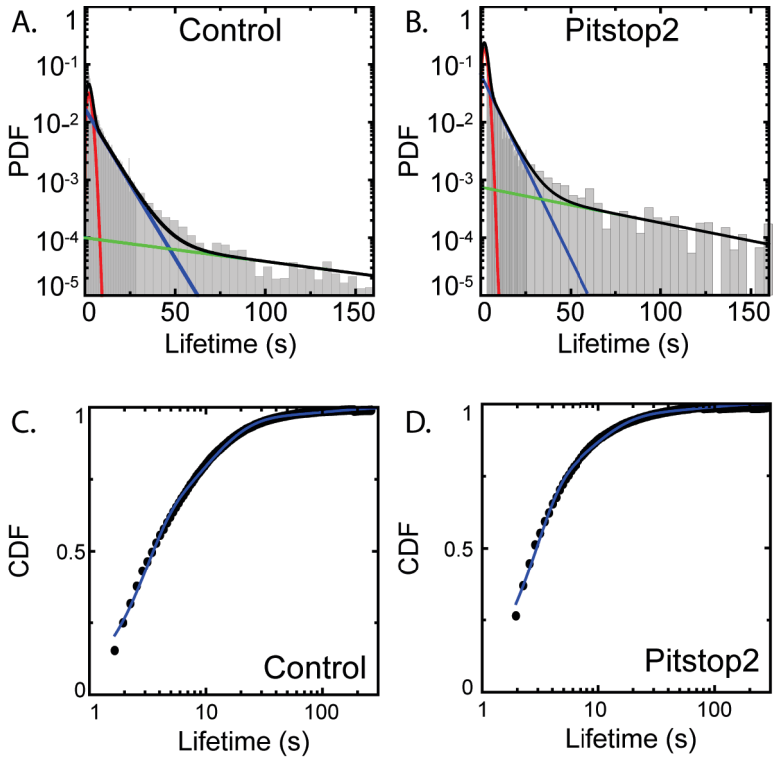


Figure 6.6: *CCP lifetimes* Lifetime distribution of CCPs for control cells (A) and cells treated with Pitstop2 (B). Line shown in (A) and (B) is the 1-Rayleigh plus 2-exponential distribution using the parameters from the fit to the CDF, (C) and (D).

In summary these results show that Kv2.1 is indeed endocytosed through CME. Additionally, immobilization of Kv2.1 occurs on CCPs suggesting CCPs might be responsible for the broad distribution of waiting times observed in Kv2.1 dynamics.

### 6.3.3 *Clathrin-coated pit lifetimes*

The distribution of CCP lifetimes is needed as an input for our model simulations. The length of the CCP trajectory, time between appearance and disappearance, corresponds to the lifetime of that CCP[2]. Minimization of the bayesian information criterion (BIC) for the fit of the lifetime CDF was used to distinguish the appropriate model for the lifetime of CCPs. We find that a combination of two exponentials and a Rayleigh distribution, Eq. 6.5 minimizes the *BIC*, Table 6.6. Fig. 6.6 shows the CCP lifetime distribution for control cells (A), $n = 31{,}492$ CCPs, and cells

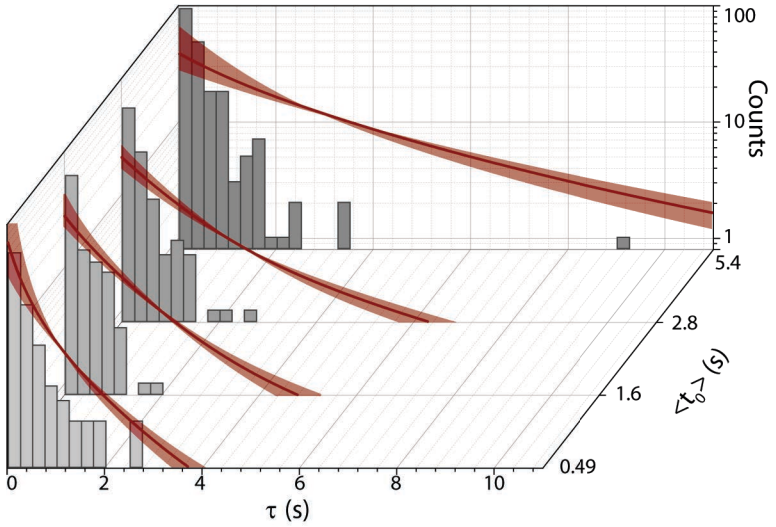


Figure 6.7: *ψ(t | to) in Control Cells* Histogram plots of stalling times,$\tau$ given a region of capture time, $t_0$. Model predications, Eq. 6.16, are shown in red with the shaded area using the minimum and maximum $t_0$ and darkened line the mean $t_0$ for the corresponding stalls.

treated with Pitstop2 (B), $n = 14{,}018$ CCPs, and the corresponding fits to the CDFs used for *BIC* model selection.

### 6.3.4 *Non-Markovian endocytosis causes weak ergodicity breaking*

We predict that not only does immobilization occur on CCPs, but binding of Kv2.1 to adaptor proteins in CCPs is responsible for the power law distribution of stalling events. To test this hypothesis we investigated the binding strength of Kv2.1 within a pit as a function of the age of a pit. Using the model derived in Section 6.2.5 and only the lifetime distribution of CCPs as an input parameter the trapping of Kv2.1 channels into CCPs was simulated.

Fig. 6.7 shows the comparison of our data with the simulations for the conditional probability density function of Kv2.1 binding times given the channel binds at time $t_0$, Eq. 6.16, in control cells. A histogram plot of binding times, $\tau$ was constructed for a range of $t_0$. The shaded region of the model is the minimum and maximum $t_0$ and the red line the average. The same analysis was also done for cells treated with Pitstop2, Fig. 6.8.

The distribution of times at which the channel was captured in the pit was modeled and compared to our data, shown in Fig. 6.9A, for both control cells and cells treated with 30 μM Pitstop2. Both treatments (control and Pitstop2) show very strong agreement with the model.

2 For the case of trajectories that are cut either by the end or the end of the movie the histogram count of lifetimes needs to be corrected. This is explained in Loerke *et al* [253] and in the Methods section.

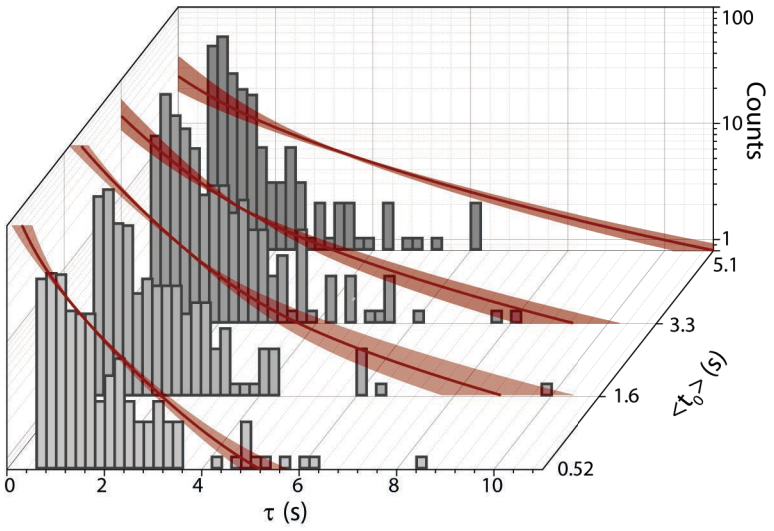


Figure 6.8: *ψ(t | to) in Pitstop2 Cells* Histogram plots of stalling times,$\tau$ given a region of capture time, $t_0$. Model predictions, Eq. 6.16, are shown in red with the shaded area using the minimum and maximum $t_0$ and darkened line the mean $t_0$ for the corresponding stalls. Cells were treated with 30 μM Pitstop2.

Note that the only input into this model is the measured lifetime distribution of CCPs, there was no fitting to the data.

Lastly the distribution of Kv2.1 stall times was modeled for control cells and Pitstop2 treated cells, Fig. 6.9. The agreement between the distribution of Kv2.1 stalls, $\tau$ measured experimentally and the simulated model is very strong.

We are able to model the capture of Kv2.1 channels within CCPs. The success of this model agrees with our hypothesis that the binding of Kv2.1 channels to adaptor proteins within a maturing pit is responsible for the weak ergodicity breaking behavior of Kv2.1 channels.

### 6.3.5 *Kv2.1 C-terminus is responsible for weak ergodicity breaking*

We speculated that sites within the C-terminus were binding to adaptor proteins within the CCP. In order to test this idea the last 318 amino acids of the C-terminus was removed, ΔC-Kv2.1[117]. Simultaneous imaging of GFP-CLC and QD-ΔC-Kv2.1 was done. With the deletion of the C-terminus stalls longer than 1.2 s ceased, Fig. 6.10A.The rate of endocytosis was also dramatically reduced with the mutant Kv2.1 channel lacking the C-terminus. Of the 537 trajectories analyzed in three different cells, only 7 channels were internalized within a ~ 10 minute time period. This is in sharp contrast to controls cells where the percentage of internalized channels within the same time frame drops from 13 ± 4% to 1 ± 4%.

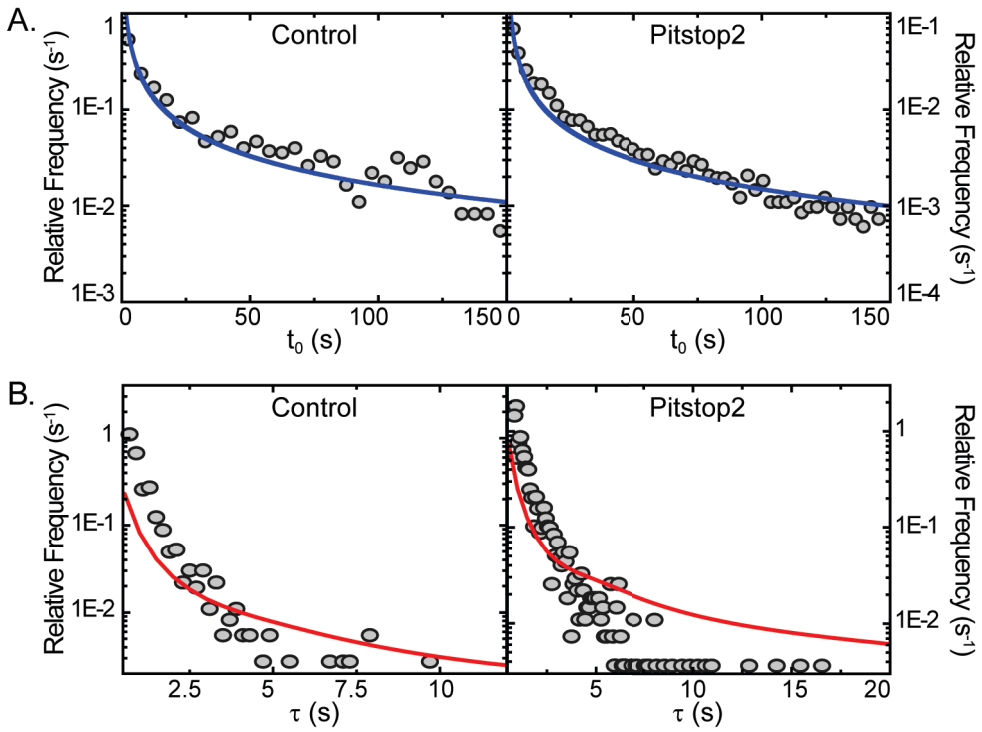


Figure 6.9: *$P(t_0 \mid bind)$ and $P(\tau)$* (A) Histogram plots of $t_0$ for control cells and cells treated with 30 μM Pitstop2. The model prediction (Eq. 6.19) is shown in blue. (B) Histogram plots of $\tau$ for control cells and cells treated with 30 μM Pitstop2. The model prediction (Eq. 6.20) is shown in red.

In an attempt to target the adaptor protein binding to the C-terminus of Kv2.1 we investigated possible binding motifs of AP2. The most commonly found internalization signals are tyrosine hydrophobic motifs YxxΦ (where Φ is a bulky hydrophobic residue F, I, L, M, or V) and acidic dileucine motifs (D/E)xxxL(L/I). Both of these signals are recognized by the major endocytic clathrin adaptor AP2 [272]. We found that there are three binding motifs for AP2 in the cytoplasmic domains of Kv2.1, D675 [DPTPLL], E704 [ECASLL], and D757 [DEGQLL]. We used a single point mutation LL761\2AA to alter the dileucine binding site in the furthest motif from the transmembrane domain. ΔAP2-Kv2.1-GFP.

The expressed mutant channel localizes to surface clusters, Fig. 6.10B. Interestingly a sharp decrease in the internalization rate was observed for this construct as compared to wild type Kv2.1, Fig. 6.10C, from 13 ± 4% to 4 ± 3%.

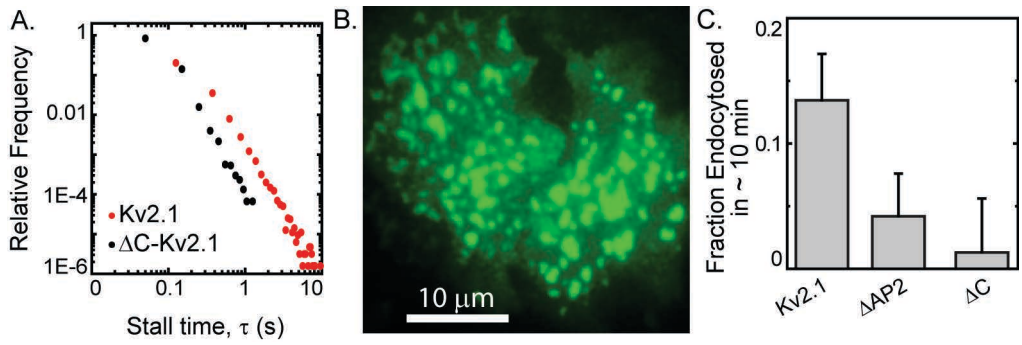


Figure 6.10: *ΔC-Kv2.1 Stalling Times and ΔAP2-Kv2.1* (A) The stalling times of Kv2.1 (black) and ΔC-Kv2.1 (red) were measured as described in the text and previously [49]. It is strikingly clear that upon the deletion of the C-terminus the channel no longer stalls for times greater than 1.2 s. (B) ΔAP2-Kv2.1-GFP expressed in HEK 293 cells. The AP2-mutant channel localizes to cell surface clusters. (C) In a 10 minute time frame 4 ± 3 % of ΔAP2-Kv2.1 channels were endocytosed (n = 860, mean ± s.d.) and 1 ± 4 % of ΔC-Kv2.1 (n = 537, mean ± s.d.). There is a drastic reduction of endocytic events with the AP2-mutant channel, ΔAP2-Kv2.1 and even more so with ΔC-Kv2.1.

## 6.4 DISCUSSION AND CONCLUSIONS

We found that Kv2.1 channels are endocytosed through clathrin mediated pathways and that stalling events predominately occur within a CCP. With the application of endocytic inhibitors, Pitstop2 and Dynasore, the rate of channel recycling is reduced and the colocalization of stalls with CCPs altered. The effect these two inhibitors have on endocytic dynamics is different. Pitstop2 is a small molecule inhibitor that blocks endocytic ligand, amphiphysin, association with clathrin terminal domain. Work presented by von Kleist *et al* [268] show that this drug effects endocytosis at all stages of pit formation. Dynasore is also a small molecule inhibitor. It selectively interferes with the GTPase dynamin[265]. Studies show that application of dynasore results in two populations of pits: U-shaped, half-formed pits and O-shaped, fully formed pits [265]. Because these two inhibitors block the interactions of different molecules within a growing CCP, the resulting dynamics of the pits are also different. We see that dynasore appears to block Kv2.1 endocytosis with more severity than Pitstop2, Fig. 6.4B.

We derived a kinetic model that accurately predicts the nonstationary and nonergodic traits of Kv2.1 dynamics. Here we are able to successfully and accurately model the capture of Kv2.1 channels within CCPs.

Deletion of the C-terminus of the channel causes the channel to be retained on the cell surface longer. Also, the ΔC-Kv2.1 channel no longer exhibits the same distribution of waiting times, with no stalls longer than 1.2 s being observed. These results indicate that the binding of the

C-terminus of Kv2.1 channels to adaptor proteins within a CCP leads to the broad distribution of observed stalling times and thereby the nonergodic, nonstationary processes indicative of Kv2.1 channel dynamics.

AP2 is one of the major endocytic clathrin adaptor. We found three binding motifs for AP2 on the C-terminal of Kv2.1 and mutated the motif furthest from the transmembrane domain. Results indicate that this mutation does have an effect of Kv2.1 internalization. The dynamics of the ΔAP2-Kv2.1 do not appear to change however (data not shown). This could be due to the two remaining AP2 binding sites. Further investigations with all three binding motifs altered should provide evidence for the role AP2 has in the non-ergodic behavior of Kv2.1.

## 6.5 ACKNOWLEDGEMENTS AND CONTRIBUTIONS

Michael M. Tamkun, Diego Krapf and Aubrey Weigel designed the research. Aubrey Weigel and Diego Krapf contributed analytical tools. Aubrey Weigel performed the research and together Aubrey Weigel and Diego Krapf analysed the data.

# CONCLUSION

This dissertation describes experimental studies of the dynamics of the voltage-gated potassium channel, Kv2.1. Kv2.1 uniquely localizes to stable, micro-domains on the cell surface [211, 239, 240] where it plays a non-conducting role [120]. There is clear physiological importance of Kv2.1 channels and exposed location dependence of channel function [115, 120]. However the underlining mechanisms of cluster formation and maintenance are still largely unknown. This work is centered around characterizing the diffusion pattern of Kv2.1 and determining alternate functional roles of surface clusters by exploring recycling pathways using single particle tracking in live cells.

Kv2.1 channels were intracellularly labeled with GFP on the N-terminus to provide an ensemble image of all expressed channels [134]. For single particle tracking the channels were then extracellularly tagged with a QD through a biotin streptavidin biochemistry. An extracellular biotin accepting domain (BAD) loop between S1 and S2 allows the channel to be biotinylated when the cell is cotransfected with biotin ligase [133]. This results in Kv2.1 channels with both an intracellular GFP and an extracellular biotin tag. By incubating the cells in a low concentration solution of streptavidin conjugated QDs the channels labeled with an ideal probe for single particle tracking.

Nearly all of the chapters presented in this thesis use single particle tracking of Kv2.1 channels using QDs. Controls were performed between QD labeled Kv2.1 and GFP tagged Kv2.1 to ensure thatt he extracellular QD label was not inducing artifactual dynamics. To increase the signal to noise ratio and thereby improve the localization accuracy it is importantt o reduce background fluorescence while imaging. Therefore TIRF microscopy was used in these studies.

The movement of Kv2.1 on the cell surface was first characterized. Analysis ofb oth the time and ensemble averages of trajectories revealed that Kv2.1 channel dynamics display both ergodic and nonergodic processes on the plasma membrane, or rather the time and ensemble averages do not coincide. We show thatt hese dynamics are accurately modeled by a CTRW on a percolation cluster [49]. We described a method for the analysis of the distribution of displacements, the propagators, of single-particle tracking measurements for the case of obstructed subdiffusion in two-dimensional membranes. We compared various propagators for differentt ypes of motion against Monte Carlo simulations and showed thatt hese models are effective in the analysis of

Kv2.1 channel diffusive measurements in the membrane of living mammalian cells. We see that the discrimination between percolation and FBM is complex, even with the use of advanced statistical tests such as the p-variation method. While the propagators of the two models are definitively different, a non-Gaussian propagator is not enough evidence to disclude the combination of both FBM and obstructed diffusion [50].

We have also studied the trafficking locations of Kv2.1 channels to and from the cell surface by imaging both the Kv2.1 cell surface clusters and individual channels using multi-color TIRF microscopy. We found that these clusters are in fact platforms involved in ion channel trafficking. By imaging individual QD labeled Kv2.1 channels we revealed that Kv2.1 containing vesicles deliver and retrieve cargo at the perimeter of Kv2.1 surface clusters. Very interestingly, further investigation with Kv1.4 channels showed that this non-clustering potassium channel is also delivered to Kv2.1 clusters. These results suggest that one of the non-conducting functions of the Kv2.1 channel is to form micro-domains involved in membrane protein trafficking [241].

To paint a more complete picture of trafficking to and from Kv2.1 clusters we measured the distribution of Kv2.1 domain sizes and studied the kinetics of their growth using a Fokker-Planck formalism. We found that there is no evidence for a feedback mechanism present and that the size of Kv2.1 clusters is in fact established by fluctuations in the endocytic and exocytic machinery. These results were confirmed by using likelihood and Akaike weights to identify the best model for the kinetics of domain growth [271].

Investigations using TIRF-based single-particle tracking demonstrate that Kv2.1 displays a confined subdiffusion type of motion on the cell surface and it undergoes frequent stalls. Multicolor imaging indicates that stable clathrin-coated pits actually capture Kv2.1 channels, and are responsible for causing these stalls. By monitoring the residence time of Kv2.1 within a clathrin-coated pit, we have been able to study the binding strength as a function of the age of a pit, e.g., the time since coat initiation. We derived a kinetic model that takes into account the coat assembly via the recruitment of adaptor proteins. This leads to non-stationary and nonergodic Kv2.1 dynamics. We find that this model very accurately predicts the statistics of transient binding between the pit and cargo revealing clathrin-coated pit capture of the Kv2.1 channel is responsible for the channel's nonergodic behavior.

Finally a closer examination of the relationship between Kv2.1 clusters and clathrin-coated pit maturation is currently being studied. We find that Kv2.1, specifically the C-terminal tail, has a direct effect on clathrin-coated pit lifetimes and stability. Cells expressing clustering Kv2.1 exhibit more rapidly maturing pits as seen by the rate of Kv2.1 internalization. In cells with a mutant, non-clustering Kv2.1 the pit lifetime is increased. Complete loss of Kv2.1 results in even longer clathrin-coated pit lifetimes, i.e. slower maturation. The movement of these pits also changes upon the addition of Kv2.1, where pits in cells without Kv2.1 move much more than pits in cells co-expressing Kv2.1. These results indicate that Kv2.1 cluster formation has a direct effect on clathrin mediated endocytosis and clathrin-coated pit dynamics.

# BIBLIOGRAPHY


[1] Bruce Alberts, Alexander Johnson, Julian Lewis, Martin Raff, Keith Roberts, and Peter Walter. Molecular biology of the cell. Garland Science, 2008. (Cited on page 1.)

[2] S J Singer and Garth L Nicolson. The Fluid Mosaic Model of the Structure of Cell Membranes. Science, 1972. (Cited on page 1.)

[3] Donald M. Engelman. Membranes are more mosaic than fluid. Nature, 2005. (Cited on pages 1 and 52.)

[4] Karl D Bellve, Deborah Leonard, Clive Standley, Lawrence M Lifshitz, Richard A Tuft, Akira Hayakawa, Silvia Corvera, and Kevin E Fogarty. Plasma Membrane Domains Specialized for Clathrin-mediated Endocytosis in Primary Cells. The Journal of Biological Chemistry . (Cited on pages 1 and 98.)

[5] Charles A Day and Anne K Kenworthy. Tracking microdomain dynamics in cell membranes. BBA - Biomembranes, 2009. (Cited on page 1.)

[6] Akihiro Kusumi and Mutsuya Yamamoto. Confined Lateral Diffusion of Membrane Receptors. Biophysical Journal, 1993. (Cited on pages 1 and 48.)

[7] D Lingwood and K Simons. Lipid Rafts As a Membrane-Organizing Principle. Science, 2009. (Cited on page 1.)

[8] Natasza E Ziółkowska, Romain Christiano, and Tobias C Walther. Organized living: formation mechanisms and functions of plasma membrane domains in yeast. Trends in Cell Biology, 2012. (Cited on page 1.)

[9] Ken Ritchie, Ryota Iino, Takahiro Fujiwara, Kotono Murase, and Akihiro Kusumi. The fence and picket structure of the plasma membrane ofl ive cells as revealed by single molecule techniques (Review). Molecular Membrane Biology, 2003. (Cited on pages 1 and 69.)

[10] Min Wu, David Holowka, Harold G Craighead, and Barbara Baird. Visualization of plasma membrane compartmentalization with patterned lipid bilayers. PNAS, 2004. (Cited on pages 1 and 2.)

[11] Akihiro Kusumi, Takahiro K Fujiwara, Nobuhiro Morone, Kenta J Yoshida, Rahul Chadda, Min Xie, Rinshi S Kasai, and Kenichi G N Suzuki. Membrane mechanisms for signal transduction: The coupling of the meso-scale raft domains to membrane-skeleton-induced compartments and dynamic protein complexes. Seminars in Cell and Developmental Bio , 2012. (Cited on page 1.)

[12] Thomas Harder and Dhaval Sangani. Plasma membrane rafts engaged in T cell signalling: new developments in an old concept. Cell Communication and Signaling, 2009. (Cited on page 2.)

[13] L Gagnoux-Palacios. Compartmentalization ofi ntegrin 6 4 signaling in lipid rafts. The Journal of Cell Biology, 2003. (Cited on page 2.)

[14] Yong Yang, Tie Xia, Wei Zhang, and XiaoHong Fang. Single-molecule fluorescence imaging of membrane-bound proteins for studies of cell signal transduction. *Chinese Science Bulletin*, 2011. (Cited on page 2.)

[15] Hernán E Grecco, Malte Schmick, and Philippe I H Bastiaens. Signaling from the Living Plasma Membrane. *Cell*, 2011. (Cited on page 2.)

[16] Elias T Spiliotis and W James Nelson. Spatial control of exocytosis. *Current Opinion in Cell Biology*, 2003. (Cited on pages 2, 97, and 98.)

[17] Levi A Gheber and Michael A Edidin. A Model for Membrane Patchiness: Lateral Diffusion in the Presence of Barriers and Vesicle Traffic. *Biophsical Journal*, 1999. (Cited on pages 2 and 54.)

[18] Ana J García-Sáez and Petra Schwille. Single molecule techniques for the study of membrane proteins. *Applied Microbiology and Biotechnology*, 2007. (Cited on page 2.)

[19] I V Perevoshchikova, E A Kotova, and Y N Antonenko. Fluorescence correlation spectroscopy in biology, chemistry, and medicine. *Biochemistry (Moscow)*, 2011. (Cited on page 2.)

[20] Søren Preus and L Marcus Wilhelmsson. Advances in Quantitative FRET-Based Methods for Studying Nucleic Acids. *ChemBioChem*, 2012. (Cited on page 2.)

[21] Víctor Fernández-Dueñas, Javier Llorente, Jorge Gandía, Dasiel O Borroto-Escuela, Luigi F Agnati, Carla I Tasca, Kjell Fuxe, and Francisco Ciruela. Fluorescence resonance energy transfer-based technologies in the study of protein–protein interactions at the cell surface. *Methods*, 2012. (Cited on page 2.)

[22] Daniel Axelrod, D E Koppel, J Schlessinger, E Elson, and W W Webb. Mobility measurement by analysis of fluorescence photobleaching recovery kinetics. *Biophsical Journal*, 1976. (Cited on pages 2 and 52.)

[23] Ahmet Yildiz and Paul R. Selvin. Fluorescence Imaging with One-Nanometer Accuracy (FIONA). *Accounts of Chemical Research*, 2005. (Cited on pages 2, 35, 36, and 188.)

[24] Douglas Magde, Elliot L Elson, and Watt W. Webb. Thermodynamic fluctuations in a reacting system - measurement by fluorescence correlation spectroscopy. *Physical Review Letters*, 1972. (Cited on page 3.)

[25] Miguel Ángel Medina and Petra Schwille. Fluorescence correlation spectroscopy for the detection and study of single molecules in biology. *BioEssays*, 2002. (Cited on page 3.)

[26] Russell E Thompson, Daniel R Larson, and Watt W. Webb. Precise Nanometer Localization Analysis for Individual Fluorescent Probes. *Biophysical Journal*, 2002. (Cited on page 3.)

[27] H Andersson, T Baechi, M Hoechl, and C Richter. Autofluorescence of living cells. *Journal of Microscopy*, 1998. (Cited on page 4.)

[28] Daniel Axelrod. Total Internal Reflection Fluroescence Microscopy in Cell Biology. *Traffic*, 2001. (Cited on page 4.)

[29] Joseph R Lakowicz. *Principles of fluorescence spectroscopy*. Springer, 2006. (Cited on page 6.)

[30] Marc Zimmer. *Glowing genes: A revolution in biotechnology*. Prometheus Books, 2005. (Cited on page 7.)

[31] Robert D Goldman, Jason R Swedlow, and David L Spector. *Live cell imaging*. Cold Spring Harbor Laboratory Press, 2010. (Cited on page 7.)

[32] X Michalet, Fabien Pinaud, L A Bentolila, J M Tsay, S Doose, J J Li, G Sundaresan, A M Wu, S S Gambhir, and S Weiss. Quantum Dots for Live Cells, in Vivo Imaging, and Diagnostics. *Science*, 2005. (Cited on page 7.)

[33] Titus Lucretius Carus. *De rerum natura* . Penguin Classics, 2007. (Cited on page 8.)

[34] Robert Brown and John Joseph Bennett. *The miscellaneous botanical works of Robert Brown*. Robert Hardwicke, 1866. (Cited on page 8.)

[35] Joseph Klafter and Igor Sokolov. *First steps in random walks*. Oxford, 2011. (Cited on pages 8 and 14.)

[36] Philip Nelson. *Biological Physics*. W H Freeman and Company, 2008. (Cited on page 8.)

[37] P W M Blom and M C J M Vissenberg. Dispersive hole transport in poly(p-phenylene vinylene). *Physical Review Letters*, 1998. (Cited on page 14.)

[38] Qing Gu, E A Schiff, S Grebner, F Wang, and R Schwarz. Non-gaussian transport measurements and the einstein relation in amorphous silicon. *Physical Review Letters*, 1996. (Cited on page 14.)

[39] G Pfister and C H Griffiths. Temperature dependece of transiet hole hopping transport in disordered organic solids: carbazole polymers. *Physical Review Letters*, 1978. (Cited on page 14.)

[40] G Pfister and Harvey Scher. Time-dependent electrical transport in amorphous solids: As2Se3. *Physical Review B*, 1977. (Cited on page 14.)

[41] Harvey Scher and M Lax. Stochastic transport in a disordered solid. II. Impurity conduction. *Physical Review B*, 1973. (Cited on page 14.)

[42] Harvey Scher and Elliott W Montroll. Anomalous transit-time dispersion in amorphous solids. *Physical Review B*, 1975. (Cited on pages 14, 18, 53, and 121.)

[43] G Zumofen, A Blumen, and Joseph Klafter. Current flow under anomalous-diffusion conditions: Lévy walks. *Physical Review A*, 1990. (Cited on page 14.)

[44] Jerzy Bodurka, R O Seitter, R Kimmich, and A Gutsze. Field-cycling nuclear magnetic resonance relaxometry of molecular dynamics at biological interfaces in eye lenses: The Lévy walk mechanism. *The Journal of Chemical Physics*, 1997. (Cited on page 14.)

[45] Jean-Philippe Bouchaud and Antoine Georges. Anomalous Diffusion in Disordered Media: Statistical Mechanisms, Models and Physical Applications. *Physics Reports*, 1990. (Cited on page 14.)

[46] S Stapf, R Kimmich, and R O Seitter. Proton and Deuteron Field-Cycling NMR Relaxometry of Liquids in Porous Glasses: Evidence for Lévy-Walk Statistics. *Physical Review Letters*, 1995. (Cited on page 14.)

[47] W Sung and P J Park. Polymer translocation through a pore in a membrane. *Physical Review Letters*, 1996. (Cited on page 14.)

[48] David K Lubensky and David R Nelson. Driven Polymer Translocation Through a Narrow Pore. *Biophysical Journal*, 1999. (Cited on page 14.)

[49] Aubrey Weigel, Blair Simon, Michael M. Tamkun, and Diego Krapf. Ergodic and nonergodic processes coexist in the plasma membrane as observed by single-molecule tracking. *PNAS*, 2011. (Cited on pages 14, 18, 22, 25, 53, 55, 56, 57, 66, 79, 84, 87, 91, 100, 102, 116, 121, 122, 123, 124, 133, 138, 140, 188, and 189.)

[50] Aubrey Weigel, Shankarachary Ragi, Michael Reid, Edwin K Chong, Michael Tamkun, and Diego Krapf. Obstructed diffusion propagator analysis for single-particle tracking. *Physical Review E*, 2012. (Cited on pages 14, 25, 133, 141, and 188.)

[51] Maxime Dahan, Sabine Levi, Camilla Luccardini, Beatrice Rostaing, and Antoine Triller. Diffusion Dynamics of Glycine Receptors Revealed by Single-Quantum Dot Tracking. *Science*, 2003. (Cited on page 14.)

[52] Luis A Veliz, Carlos A Toro, Juan P Vivar, Luis A Arias, Jenifer Villegas, Maite A Castro, and Sebastian Brauchi. Near-Membrane Dynamics and Capture of TRPM8 Channels within Transient Confinement Domains. *PLoS ONE*, 2010. (Cited on page 14.)

[53] James A Dix and A. S. Verkman. Crowding Effects on Diffusion in Solutions and Cells. *Annual Review of Biophysics*, 2008. (Cited on pages 14 and 52.)

[54] Melpomeni Platani, Ilya Goldberg, Angus I Lamond, and Jason R Swedlow. Cajal Body dynamics and association with chromatin are ATP-dependent. *Nature Cell Biology*, 2002. (Cited on page 14.)

[55] Elliott W Montroll and George H Weiss. Random Walks on Lattices. II. *Journal of Mathematical Physics*, 1965. (Cited on page 14.)

[56] Daniel ben Avraham and Shlomo Havlin. Diffusion and Reactions in Fractals and Disordered Systems. *Cambridge University Press*, 2000. (Cited on pages 14, 18, 19, 31, 34, 48, 55, 60, and 64.)

[57] I Bronstein, Y Israel, E Kepten, S Mai, Y Shav-Tal, E. Barkai, and Y Garini. Transient Anomalous Diffusion of Telomeres in the Nucleus of Mammalian Cells. *Physical Review Letters*, 2009. (Cited on pages 18, 24, and 50.)

[58] H G Duan and X T Liang. Ergodic properties of fractional Langevin motion with spatial correlated noise. *The European Physical Journal B*, 2012. (Cited on pages 18 and 197.)

[59] Benoit B Mandelbrot. *The fractal geometry of nature*. W H Freeman and Company, 1982. (Cited on page 18.)

[60] Michael J. Saxton. Anomalous Subdiffusion in Fluorescence Photobleaching Recovery:A Monte Carlo Study. *Biophsical Journal*, 2001. (Cited on pages 20 and 52.)

[61] Ido Golding and Edward Cox. Physical Nature of Bacterial Cytoplasm. *Physical Review Letters*, 2006. (Cited on pages 20, 24, and 50.)

[62] Benoit B Mandelbrot and John W Van Ness. Fractional Brownian Motions Fractional Noises and Applications. *SIAM Review*, 1968. (Cited on pages 20, 21, 31, and 52.)

[63] Gennady Samorodnitsky and Murad S Taqqu. *Stable non-gaussian random processes: stochastic models with infinite variance*. Chapman and Hall, 1994. (Cited on page 21.)

[64] Marcin Magdziarz, Aleksander Weron, and Krzysztof Burnecki. Fractional Brownian Motion Versus the Continuous-Time Random Walk: A Simple Test for Subdiffusive Dynamics. *Physical Review Letters*, 2009. (Cited on pages 21, 56, 60, 61, and 62.)

[65] Jens Feder. *Fractals: physics of solids and liquids*. Springer, 1988. (Cited on page 21.)

[66] Benjamin H Blehm, Trina A Schroer, Kathleen M Trybus, Yann R Chemla, and Paul R. Selvin. In vivo optical trapping indicates kinesin's stall force is reduced by dynein during intracellular transport. *PNAS*, 2013. (Cited on page 22.)

[67] Deepak Bhat and Manoj Gopalakrishnan. Effectiveness of dynein team in tug-of-war helped by reduced load-sensitivity of detachment: evidence from study of bidirectional endosome transport in D. discoideum. *Physical Biology*, 2012. (Cited on page 22.)

[68] Adam G Hendricks, Eran Perlson, Jennifer L Ross, Harry W Schroeder, III, Mariko Tokito, and Erika L F Holzbaur. Motor Coordination via a Tug-of-War Mechanism Drives Bidirectional Vesicle Transport. *Current Biology*, 2010. (Cited on page 22.)

[69] Izaak Neri, Norbert Kern, and Andrea Parmeggiani. Modeling Cytoskeletal Traffic: An Interplay between Passive Diffusion and Active Transport. *Physical Review Letters*, 2013. (Cited on page 22.)

[70] Avi Caspi, Rony Granek, and Michael Elbaum. Enhanced Diffusion in Active Intracellular Transport. *Physical Review Letters*, 2000. (Cited on page 22.)

[71] Delphine Arcizet, Börn Meier, Erich Sackmann, Joachim Rädler, and Doris Heinrich. Temporal Analysis of Active and Passive Transport in Living Cells. *Physical Review Letters*, 2008. (Cited on page 22.)

[72] Kinneret Keren, Patricia T Yam, Anika Kinkhabwala, Alex Mogilner, and Julie A Theriot. Intracellular fluid flow in rapidly moving cells. *Nature Cell Biology*, 2009. (Cited on page 22.)

[73] Marcus Otten, Amitabha Nandi, Delphine Arcizet, Mari Gorelashvili, Benjamin Lindner, and Doris Heinrich. Local Motion Analysis Reveals Impact of the Dynamic Cytoskeleton on Intracellular Subdiffusion. *Biophsical Journal*, 2012. (Cited on page 22.)

[74] Tom Misteli. Protein Dynamics: Implications for Nuclear Architecture and Gene Expression. *Science*, 2001. (Cited on page 22.)

[75] Makoto Adachi, Makoto Fukuda, and Eisuke Nishida. Two co-existing mechanisms for nuclear import of MAP kinase: passive diffusion of a monomer and active transport of a dimer. *EMBO*, 1999. (Cited on page 22.)

[76] Frederick Dahlquist. Slip sliding away: new insights into DNA-protein recognition. 2006. (Cited on page 22.)

[77] C Loverdo, Olivier Benichou, Raphael Voituriez, A Biebricher, I Bonnet, and P Desbiolles. Quantifying Hopping and Jumping in Facilitated Diffusion of DNA-Binding Proteins. *Physical Review Letters*, 2009. (Cited on page 22.)

[78] Paul C Blainey, Antoine van Oijen, Anirban Banerjee, Gergory L Verdine, and X Sunney Xie. A base-excision DNA-repair protein finds intrahelical lesion bases by fast sliding in contact with DNA. *PNAS*, 2006. (Cited on page 22.)

[79] Stephen E Halford and John F Marko. How do site-specific DNA-binding proteins find their targets? *Nucleic Acids Research*, 2004. (Cited on page 22.)

[80] Michael J. Saxton. A Biological Interpretation of Transient Anomalous Subdiffusion. I. Qualitative Model. *Biophysical Journal*, 2007. (Cited on page 23.)

[81] Michael J. Saxton. Lateral Diffusion in an Archipelago: Single Particle Diffusion. *Biophysical Journal*, 1993. (Cited on pages 23 and 46.)

[82] E Lenzi, R Mendes, and C Tsallis. Crossover in diffusion equation: Anomalous and normal behaviors. *Physical Review E*, 2003. (Cited on page 23.)

[83] Igor M. Sokolov. Models of anomalous diffusion in crowded environments. *Soft Matter*, 2012. (Cited on page 23.)

[84] Akihiro Kusumi, Chieko Nakada, Ken Ritchie, Kotono Murase, Kenichi Suzuki, Hideji Murakoshi, Rinshi S Kasai, Junko Kondo, and Takahiro Fujiwara. Paradigm Shift of the Plasma Membrane Concept from the Two-Dimensional Continuum. *Annual Review of Biophysical and Molecular Structures*, 2005. (Cited on pages 23 and 25.)

[85] Karla de Bruin, Nadia Ruthardt, Katharina von Gersdorff, Ralf Bausinger, Ernst Wagner, Manfred Ogris, and Christoph Bräuchle. Cellular Dynamics of EGF Receptor–Targeted Synthetic Viruses. *Molecular Therapy*, 2007. (Cited on page 23.)

[86] Nadia Ruthardt, Don C Lamb, and Christoph Bräuchle. Single-particle Tracking as a Quantitative Microscopy-based Approach to Unravel Cell Entry Mechanisms of Viruses and Pharmaceutical Nanoparticles. *Molecular Therapy*, 2011. (Cited on page 23.)

[87] Iva Tolić-Nørrelykke, Emilia-Laura Munteanu, Genevieve Thon, Lene Oddershede, and Kirstine Berg-Sørensen. Anomalous Diffusion in Living Yeast Cells. *Physical Review Letters*, 2004. (Cited on page 23.)

[88] Christine Selhuber-Unkel, Pernille Yde, Kirstine Berg-Sørensen, and Lene B Oddershede. Variety in intracellular diffusion during the cell cycle. *Physical Biology*, 2009. (Cited on page 23.)

[89] Vincent Tejedor, Olivier Benichou, Raphael Voituriez, Ralf Jungmann, Friedrich Simmel, Christine Selhuber-Unkel, Lene B Oddershede, and Ralf Metzler. Quantitative Analysis of Single Particle Trajectories: Mean Maximal Excursion Method. *Biophysical Journal*, 2010. (Cited on pages 23 and 31.)

[90] Jae-Hyung Jeon, Vincent Tejedor, Stas Burov, Eli Barkai, Christine Selhuber-Unkel, Kirstine Berg-Sørensen, Lene Oddershede, and Ralf Metzler. In Vivo Anomalous Diffusion and Weak Ergodicity Breaking of Lipid Granules. *Physical Review Letters*, 2011. (Cited on pages 23, 51, and 53.)

[91] Stephanie C Weber, Andrew J Spakowitz, and Julie A Theriot. Bacterial Chromosomal Loci Move Subdiffusively through a Viscoelastic Cytoplasm. *Physical Review Letters*, 2010. (Cited on page 24.)

[92] E Kepten, I Bronshtein, and Y Garini. Ergodicity convergence test suggests telomere motion obeys fractional dynamics. *Physical Review E*, 2011. (Cited on pages 24, 61, 62, and 69.)

[93] Felix Höfling and Thomas Franosch. Anomalous transport in the crowded world of biological cells. *Reports on Progress in Physics*, 2013. (Cited on page 25.)

[94] Marija Vrljic, Stefanie Y Nishimura, Sophie Brasselet, W. E. Moerner, and Harden M McConnell. Translational Diffusion of Individual Class II MHC Membrane Proteinsin Cells. *Biophsical Journal*, 2002. (Cited on pages 25, 37, and 55.)

[95] Toni J. Feder, Ingrid Brust-Mascher, James P. Slattery, Barbara Baird, and Watt W. Webb. Constrained Diffusion or Immobile Fraction on Cell Surfaces: A New Interpretation. *Biophysical Journal*, 1996. (Cited on pages 25, 53, and 121.)

[96] Richik N Ghosh and Watt W. Webb. Automated Detection and Tracking of Individual and Clustered Cell Surface Low Diensity Lipoprotein Receptor Molecules. *Biophysical Journal*, 1994. (Cited on pages 25, 52, 54, and 188.)

[97] Petra Schwille, Jonas Korlach, and Watt W. Webb. Fluorescence Correlation Spectroscopy with Single-Molecule Sensitivity on Cell and Model Membranes. *Cytometry*, 1999. (Cited on pages 25 and 43.)

[98] Petra Schwille. TIR-FCS: Staying on the Surface Can Sometimes Be Better. *Biophysical Journal*, 2003. (Cited on page 25.)

[99] Matthias Weiss, Hitoshi Hashimoto, and Tommy Nilsson. Anomalous Protein Diffusion in Living Cells as Seen by Fluorescence Correlation Spectroscopy. *Biophysical Journal*, 2003. (Cited on page 25.)

[100] Pierre-Francois Lenne, Laure Wawrezinieck, Fabien Conchonaud, Olivier Wurtz, Annie Boned, Xiao-Jun Guo, Herve Rigneault, Hai-Tao He, and Didier Marguet. Dynamic molecular confinement in the plasma membrane by microdomains and the cytoskeleton meshwork. *EMBO*, 2006. (Cited on page 25.)

[101] Margaret R Horton, Felix Holfling, Joachim O Radler, and Thomas Franosch. Development of anomalous diffusion among crowding proteins. *Soft Matter*, 2010. (Cited on pages 25, 30, and 52.)

[102] Flor A Espinoza, Michael J Wester, Janet M. Oliver, Bridget S. Wilson, Nicholas L Andrews, Diane S. Lidke, and Stanly L Steinberg. Insights into Cell Membrane Microdomain Organization from Live Cell Single Particle Tracking of the IgE High Affinity Receptor FcERI of Mast Cells. *Bulletin of Mathematical Biology*, 2012. (Cited on page 25.)

[103] Jonathan M Crane and A. S. Verkman. Long-Range Nonanomalous Diffusion of Quantum Dot-Labeled Aquaporin-1 Water Channels in the Cell Plasma Membrane. *Biophsical Journal*, 2008. (Cited on pages 25 and 55.)

[104] S A Kodirov. Attenuation of IK,slow1 and IK,slow2 in Kv1/Kv2DN mice prolongs APD and QT intervals but does not suppress spontaneous or inducible arrhythmias. *AJP: Heart and Circulatory Physiology*, 2003. (Cited on page 26.)

[105] Jeanne M Nerbonne. Molecular basis of functional votage-gated K+ channel diversity in the mammalian myocardium. *Journal of Physiology*, 2000. (Cited on page 26.)

[106] Haodong Xu, Dianne M Barry, Hulin Li, Sylvain Brunet, Weinong Guo, and Jeanne M Nerbonne. Attenuation of the slow component of delayed rectification, action potential polongation, and triggered activity in mice expressing a dominant-negative Kv2 alpha subunit. *Circ Res*, 1999. (Cited on page 26.)

[107] David A Jacobson, Andrey Kuznetsov, James P Lopez, Shera Kash, Carina E Ämmälä, and Louis H Philipson. Kv2.1 Ablation Alters Glucose-Induced Islet Electrical Activity, Enhancing Insulin Secretion. *Cell Metabolism*, 2007. (Cited on page 26.)

[108] Dafna Singer-Lahat, Anton Sheinin, Dodo Chikvashvili, Sharon Tsuk, Dafna Greitzer, Reut Friedrich, Lori Feinshreiber, Uri Ashery, Morris Benveniste, Edwin S. Levitan, and Ilana Lotan. K+ channel faciliatation of exocytosis by dynamic interaction with syntaxin. *The Journal of Neuroscience*, 2007. (Cited on page 26.)

[109] S K Pal, K Takimoto, E Aizenman, and Edwin S. Levitan. Apoptotic surface delivery of K+ channels. *Cell Death and Differentiation*, 2005. (Cited on page 26.)

[110] Sumon Pal, Karen A Hartnett, Jeanne M Nerbonne, Edwin S. Levitan, and Elias Aizenman. Mediation of Neuronal Apoptosis by Kv2.1-Encoded Potassium Channels. *The Journal of Neuroscience*, 2003. (Cited on page 26.)

[111] Jing Du, Laurel L Haak, Emily Phillips-Tansey, James T Russell, and Chris J McBain. Frequency-dependent regulation of rat hippocampal somato-dendritic excitability by the K+ channel subunit Kv2.1. *Journal of Physiology*, 2000. (Cited on page 26.)

[112] Elizabeth A Coppock, Jeffrey R. Martens, and Michael M. Tamkun. Molecular Basis of Hypoxia-Induced Pulmonary Vasoconstriction - Role of Voltage-Gated K(+) Channels. *American Journal of Physiology - Lung Cellular and Molecular Physiology*, 2001. (Cited on page 26.)

[113] Elizabeth A Coppock and Michael M. Tamkun. Differential Expression of K(V) Channel Alpha- and Beta -Subunits in the Bovine Pulmonary Arterial Circulation. *American Journal of Physiology - Lung Cellular Molecular Physiology*, 2001. (Cited on page 26.)

[114] J T Hulme, E A Coppock, A Felipe, J R Martens, and M M Tamkun. Oxygen Sensitivity of Cloned Voltage-Gated K+ Channels Expressed in the Pulmonary Vasculature. *Circulation Research*, 1999. (Cited on page 26.)

[115] Hiroaki Misonou, Durga P. Mohapatra, Eunice W Park, Victor Leung, Dongkai Zhen, Kaori Misonou, Anne E Anderson, and James S. Trimmer. Regulation of ion channel localization and phosphorylation by neuronal activity. *Nature Neuroscience*, 2004. (Cited on pages 26, 27, 92, 99, and 140.)

[116] Kang-Sik Park, Durga P. Mohapatra, Hiroaki Misonou, and James S. Trimmer. Graded Regulation of the Kv2.1 Potassium Channel by Variable Phosphorylation. *Science*, 2006. (Cited on page 26.)

[117] K M S O'Connell. Kv2.1 Potassium Channels Are Retained within Dynamic Cell Surface Microdomains That Are Defined by a Perimeter Fence. *Journal of Neuroscience*, 2006. (Cited on pages 27, 32, 72, 79, 83, 84, 103, and 136.)

[118] Hiroaki Misonou, Durga P. Mohapatra, and James S. Trimmer. Kv2.1: A Voltage-Gated K+ Channel Critical to Dynamic Control of Neuronal Excitability. *NeuroToxicology*, 2005. (Cited on page 27.)

[119] Hiroaki Misonou, Durga P. Mohapatra, Milena Menegola, and James S. Trimmer. Calcium- and Metabolic State-Dependent Modulation of the Voltage-Dependent Kv2.1 Channel Regulates Neuronal Excitability in Response to Ischemia. *The Journal of Neuroscience*, 2005. (Cited on pages 27, 79, 92, 99, and 100.)

[120] Kristen M. S. O'Connell, Robert Loftus, and Michael M. Tamkun. Localization-dependent activity of the Kv2.1 delayed-rectifier K+ channel. *PNAS*, 2010. (Cited on pages 27, 71, 79, 80, 97, 99, and 140.)

[121] C Schulzky, C Essex, M Davison, A Franz, and K H Hoffman. The similarity group and anomalous diffusion equations. *Journal of Physics A: Mathematical and General*, 2000. (Cited on pages 30 and 43.)

[122] Michael J. Saxton. Anomalous diffusion due to obstacles: a Monte Carlo study. *Biophysical Journal*, 1994. (Cited on pages 30, 52, 55, 60, 64, 65, and 121.)

[123] Steven B Zimmerman and Allen P Minton. Macromolecular crowding: Biochemical, Biophysical, and Physiological Consequences. *Annual Review of Biophysics and Biomolecular Structure*, 1993. (Cited on page 30.)

[124] Ralf Metzler and Joseph Klafter. The random walk's guide to anomalous diffusion - a fractional dynamics approach. *Physics Reports*, 2000. (Cited on pages 31, 34, 43, 47, 55, 117, and 121.)

[125] Joseph Klafter, A Blumen, and M F Shlesinger. Stochastic pathway to anomalous diffusion. *Physical Review A*, 1987. (Cited on page 31.)

[126] G Bel and E. Barkai. Weak ergodicity breaking in the continuous time random walk. *Physical Review Letters*, 2005. (Cited on pages 31 and 34.)

[127] Ariel Lubelski, Igor M. Sokolov, and Joseph Klafter. Nonergodicity mimics inhomogeneity in single particle tracking. *Physical Review Letters*, 2008. (Cited on pages 31, 34, and 47.)

[128] Y. He, S. Burov, Ralf Metzler, and E. Barkai. Random Time-Scale Invariant Diffusion and Transport Coefficients. *Physical Review Letters*, 2008. (Cited on pages 31, 34, and 47.)

[129] Jedrzej Szymanski and Matthias Weiss. Elucidating the Origin of Anomalous Diffusion in Crowded Fluids. *Physical Review Letters*, 2009. (Cited on pages 31, 52, and 69.)

[130] Marcin Magdziarz and Joseph Klafter. Detecing origins of subdiffusion: P-variation test for confined systems. *Physical Review E*, 2010. (Cited on pages 31, 61, and 62.)

[131] G. J. Schutz, H. Schindler, and Thomas Schmidt. Single-Molecule Microscopy on Model Membranes Reveals Anomalous Diffusion. *Biophysical Journal*, 1997. (Cited on pages 31, 32, 37, 48, 54, and 55.)

[132] M. A. Deverall, E. Gindl, E.-K. Sinner, H. Besir, J. Ruehe, Michael J. Saxton, and C. A. Naumann. Membrane lateral mobility obstructed by polymer-tethered lipids studied at the single molecule level. *Biophysical Journal*, 2005. (Cited on pages 31, 34, 43, 52, 55, and 59.)

[133] Michael M. Tamkun, Kristen M. S. O'Connell, and Annah S Rolig. A cytoskeletal-based perimeter fence selectively corrals a sub-population of cell surface Kv2.1 channels. *Journal of Cell Science*, 2007. (Cited on pages 32, 33, 37, 79, 84, 87, 89, 91, 100, 102, 118, 122, and 140.)

[134] Kristen M. S. O'Connell and Michael M. Tamkun. Targeting of Voltage-Gated Potassium Channel Isoforms to Distinct Cell Surface Microdomains. *Journal of Cell Science*, 2005. (Cited on pages 32, 100, 102, 122, and 140.)

[135] S. Condamin, Vincent Tejedor, Raphael Voituriez, Olivier Benichou, and Joseph Klafter. Probing microscopic origins of confined subdiffusion by first-passage observalbes. *PNAS*, 2008. (Cited on pages 34, 47, and 121.)

[136] J P Bouchaud. Weak ergodicity breaking and aging in disordered systems. *Journal de Physique I*, 1992. (Cited on page 34.)

[137] I. Y. Wong, M. L. Gardel, D. R. Reichman, Eric R. Weeks, M. T. Valentine, A. R. Bausch, and D. A. Weitz. Anomalous diffusion probes microstructure dynamics of entangled f-actin networks. *Physical Review Letters*, 2004. (Cited on page 34.)

[138] Harvey Scher. The dynamical foundation of fractal stream chemistry: The origin of extremely long retention times. *Geophysical Research Letters*, 2002. (Cited on page 34.)

[139] T H Solomon, Eric R. Weeks, and Harry L Swinney. Observation of Anomalous Diffusion and Levy Flights in a Two-Dimensional Rotating Flow. *Physical Review Letters*, 1993. (Cited on page 34.)

[140] Ludovico Silvestri, Leone Fronzoni, Paolo Grigolini, and Paolo Allegrini. Event-Driven Power-Law Relaxation in Weak Turbulence. *Physical Review Letters*, 2009. (Cited on page 34.)

[141] Eli Barkai. Aging in Subdiffusion Generated by a Deterministic Dynamical System. *Physical Review Letters*, 2003. (Cited on page 34.)

[142] Shlomo Havlin and Daniel ben Avraham. Diffusion in disordered media. *Advances in Physics*, 2002. (Cited on pages 34 and 43.)

[143] Bong June Sung and Arun Yethiraj. Lateral Diffusion of Proteins in the Plasma Membrane: Spatial Tessellation and Percolation Theory. *The Journal of Physical Chemistry B*, 2008. (Cited on pages 34, 67, and 121.)

[144] Ben O'Shaughnessy and Itamar Procaccia. Analytical Solutions for Diffusion on Fractal Objects. *Physical Review Letters*, 1985. (Cited on pages 34 and 59.)

[145] Michael K. Cheezum, William F. Walker, and William H. Guilford. Quantitative Comparison of Algorithms for Tracking Single Fluorescent Particles. *Biophysical Journal*, 2001. (Cited on pages 35, 57, 111, 188, and 189.)

[146] Michael J. Saxton. Single Particle Tracking - The Distribution of Diffusion Coefficients. *Biophysical Journal*, 1997. (Cited on page 36.)

[147] Maximilian H Ulbrich and Ehud Y Isacoff. Subunit counting in membrane-bound proteins. *Nature Methods*, 2007. (Cited on pages 36 and 111.)

[148] Michael J. Saxton and Ken Jacobson. Single Particle Tracking - Application to Membrane Dynamics. *Annual Review of Biophysical and Molecular Structures*, 1997. (Cited on pages 40, 52, and 54.)

[149] Thomas Neusius, Igor M. Sokolov, and Jeremy C. Smith. Subdiffuion in time-averaged, confined random walks. *Physical Review E*, 2009. (Cited on pages 41 and 197.)

[150] A Blumen, Joseph Klafter, B. S. White, and G Zumofen. Continuous-time random walks on fractals. *Physical Review Letters*, 1984. (Cited on page 47.)

[151] Yasmine Meroz, Igor M. Sokolov, and Joseph Klafter. Subdiffusion of mixed origins - when ergodicity and nonergodicity coexist. *Physical Review E*, 2010. (Cited on page 47.)

[152] Erin D Sheets, Greta M Lee, Rudolf Simson, and Ken Jacobson. Transient Confinement of a Glycosylphosphatidylinositol-Anchored Protein in the Plasma Membrane. *Biochemistry*, 1997. (Cited on page 48.)

[153] Gerhard J Schütz, Gerald Kada, Vassili Ph Pastushenko, and Hansgeorg Schindler. Properties of lipid microdomains in a muscle cell membrane visualized by single molecule microscopy. *EMBO*, 2000. (Cited on page 48.)

[154] A Pralle, P Keller, Ernst-Ludwig Florin, Kai Simons, and J K Heinrich Hörber. Sphingolipid–Cholesterol Rafts Diffuse as Small Entities in the PlasmaMembrane of Mammalian Cells. *The Journal of Cell Biology*, 2000. (Cited on page 48.)

[155] Christian Eggeling, Christian Ringemann, Rebecca Medda, Günter Schwarzmann, Konrad Sandhoff, Svetlana Polyakova, Vladimir N Belov, Birka Hein, Claas von Middendorff, Andreas Schönle, and Stefan W. Hell. Direct observation of the nanoscale dynamics of membrane lipids in a living cell. *Nature*, 2009. (Cited on page 48.)

[156] Jeffrey R. Martens, Naoya Sakamoto, Shelley A Sullivan, Tammy D Grobaski, and Michael M. Tamkun. Isoform-specific Localization of Voltage-gated K+ Channels to Distinct Lipid Raft Populations. . *Journal of Biological Chemistry*, 2001. (Cited on page 48.)

[157] Michael R. Bubb, Ilan Spectori, Alexander D. Bershadsky, and Edward D. Korn. Swinholide A is a microfilament disrupting marine toxin that stabilizes actin dimers and severs actin filaments. *The Journal of Biological Chemistry*, 1995. (Cited on page 48.)

[158] JoAnn Trejo. Internal PDZ Ligands: Novel Endocytic Recycling Motifs for G Protein-Coupled Receptors. *Molecular Pharmacology*, 2005. (Cited on page 50.)

[159] David J Owen, Brett M Collins, and Philip R Evans. ADAPTORS FOR CLATHRIN COATS: Structure and Function. *Annu. Rev. Cell Dev. Biol.*, 2004. (Cited on page 50.)

[160] Gary J Doherty and Harvey T McMahon. Mechanisms of Endocytosis. *Annual Review of Biochemistry*, 2009. (Cited on page 51.)

[161] M Mettlen, D Loerke, D Yarar, Gaudenz Danuser, and S L Schmid. Cargo- and adaptor-specific mechanisms regulate clathrin-mediated endocytosis. *The Journal of Cell Biology*, 2010. (Cited on page 51.)

[162] Sudipta Maiti, Ulrich Haupts, and Watt W. Webb. PerspectiveFluorescence correlation spectroscopy: Diagnostics for sparse molecules. *PNAS*, 1997. (Cited on page 52.)

[163] Elke Haustein and Petra Schwille. Ultrasensitive Investigations of Biological Systems by Fluorescence Correlation Spectroscopy. *Methods*, 2003. (Cited on page 52.)

[164] Oleg Krichevsky and Grégoire Bonnet. Fluorescence correlation spectroscopy: the technique and its applications. *Reports on Progress in Physics*, 2002. (Cited on page 52.)

[165] Hiroko Bannai, Sabine Levi, Claude Schweizer, Maxime Dahan, and Antoine Triller. Imaging the lateral diffusion of membrane molecules with quantum dots. *Nature Protocols*, 2007. (Cited on page 52.)

[166] Michael A Edidin, Martha C Zúñiga, and Michael P Sheetz. Truncation mutants define and locate cytoplasmic barriers to lateral mobility of membrane glycoproteins. *PNAS*, 1994. (Cited on pages 52 and 53.)

[167] Takahiro Fujiwara, Ken Ritchie, Hideji Murakoshi, Ken Jacobson, and Akihiro Kusumi. Phospholipids Undergo Hop Diffusion in Compartmentalized Cell Membrane. *The Journal of Cell Biology*, 2002. (Cited on pages 52, 53, and 54.)

[168] Kotono Murase, Takahiro Fujiwara, Yasuhiro Umemura, Kenichi Suzuki, Ryota Iino, Hidetoshi Yamashita, Mihoko Saito, Hideji Murakoshi, Ken Ritchie, and Akihiro Kusumi. Ultrafine Membrane Compartments for Molecular Diffusion as Revealed by Single Molecule Techniques. *Biophsical Journal*, 2004. (Cited on pages 52, 54, and 55.)

[169] Piet H M Lommerse, Gerhard A Blab, Laurent Cognet, Gregory S Harms, B Ewa Snaar-Jagalska, Herman P Spaink, and Thomas Schmidt. Single-Molecule Imaging of the H-Ras Membrane-Anchor Reveals Domains in the Cytoplasmic Leaflet of the Cell Membrane. *Biophsical Journal*, 2004. (Cited on page 52.)

[170] Bong Sung and Arun Yethiraj. Lateral Diffusion and Percolation in Membranes. *Physical Review Letters*, 2006. (Cited on pages 52 and 121.)

[171] Daniel S Banks and Cécile Fradin. Anomalous Diffusion of Proteins Due to Molecular Crowding. *Biophsical Journal*, 2005. (Cited on pages 52 and 69.)

[172] Matthias Weiss, Markus Eisner, Fredrik Kartberg, and Tommy Nilsson. Anomalous Subdiffusion Is a Measure for Cytoplasmic Crowding in Living Cells. *Biophysical Journal*, 2004. (Cited on page 52.)

[173] Weichun Pan, Luis Filobelo, Ngoc Pham, Oleg Galkin, Veselina Uzunova, and Peter Vekilov. Viscoelasticity in Homogeneous Protein Solutions. *Physical Review Letters*, 2009. (Cited on page 52.)

[174] Michael J. Saxton. Anomalous diffusion due to binding: A Monte Carlo study. *Biophysical Journal*, 1996. (Cited on page 53.)

[175] S J Sahl, M Leutenegger, M Hilbert, S W Hell, and Christian Eggeling. Fast molecular tracking maps nanoscale dynamics of plasma membrane lipids. *PNAS*, 2010. (Cited on pages 53 and 55.)

[176] Chieko Nakada, Ken Ritchie, Yuichi Oba, Mitsuhiro Nakamura, Yoko Hotta, Ryota Iino, Rinshi S Kasai, Kazuhiko Yamaguchi, Takahiro Fujiwara, and Akihiro Kusumi. Accumulation of anchored proteins forms membrane diffusion barriers during neuronal polarization. *Nature Cell Biology*, 2003. (Cited on page 53.)

[177] Casey C Cunningham. Actin Polymerization and Intracellular Solvent Flow in Cell Surface Blebbing. *JCB*, 1995. (Cited on page 53.)

[178] Yasuhiro M Umemura, Marija Vrljic, Stefanie Y Nishimura, Takahiro K Fujiwara, Kenichi G N Suzuki, and Akihiro Kusumi. Both MHC Class II and its GPI-Anchored Form Undergo Hop Diffusion as Observed by Single-Molecule Tracking. *Biophysical Journal*, 2008. (Cited on page 53.)

[179] Fen Zhang, Greta M Lee, and Ken Jacobson. Protein lateral mobility as a reflection of membrane microstructure. *BioEssays*, 1993. (Cited on page 53.)

[180] Nicholas L Andrews, Keith A. Lidke, Janet R. Pfeiffer, Alan R. Burns, Bridget S. Wilson, Janet M. Oliver, and Diane S. Lidke. Actin restricts FcERI diffusion and facilitates atigen-induced receptor immobilization. *Nature Cell Biology*, 2008. (Cited on pages 53 and 100.)

[181] Yael Lavi, Michael A Edidin, and Levi A Gheber. Dynamic Patches of Membrane Proteins. *Biophysical Journal*, 2007. (Cited on pages 54 and 100.)

[182] Michael A Edidin and Iwona Stroynowski. Differences betweent he lateral organization of conventional and inositol phospholipid-anchored membrane proteins. A further definiton of micrometer scale membrane domains. *JCB*, 1991. (Cited on page 54.)

[183] Yasushi Sako and Akihiro Kusumi. Barriers for lateral diffusion of transferrin receptor in the plasma membrane as characterized by receptor dragging by laser tweezers: fence versus tether. *JCB*, 1995. (Cited on pages 54 and 100.)

[184] Kenichi Suzuki, Ronald E Sterba, and Michael P Sheetz. Outer Membrane Monolayer Domains from Two-Dimensional Surface Scanning Resistance Measurements. *Biophsical Journal*, 2000. (Cited on page 54.)

[185] Rudolf Simson, Bing Yang, Stephen E Moore, Patrick Doherty, Frank S Walsh, and Ken A Jacobson. Structural Mosaicism on the Submicron Scale in the Plasma Membrane. *Biophsical Journal*, 1998. (Cited on page 54.)

[186] Marcel J M Schaaf, Wiepke J A Koopmans, Tobias Meckel, John van Noort, B Ewa Snaar-Jagalska, Thomas S Schmidt, and Herman P Spaink. Single-Molecule Microscopy Reveals Membrane Microdomain Organization of Cells in a Living Vertebrate. *Biophsical Journal*, 2009. (Cited on page 55.)

[187] Stefan Wieser and Gerhard J Schütz. Tracking single molecules in the live cell plasma membrane—Do's and Don't's. *Methods*, 2008. (Cited on page 55.)

[188] W R Schneider and W Wyss. Fractional diffusion and wave equations. *Journal of Mathematical Physics*, 1989. (Cited on page 55.)

[189] Sharon Khan, Andy Reynolds, Ian Morrison, and Richard J Cherry. Stochastic modeling of protein motions within cell membranes. *Physical Review E*, 2005. (Cited on page 55.)

[190] A M Reynolds. On the anomalous diffusion characteristics of membrane-bound proteins. *Physics Letters A*, 2005. (Cited on page 55.)

[191] Ralf Metzler and Joseph Klafter. The restaurant at the end of the random walk - recent developments in the description of anomalous transport by fractional dynamics. *Journal of Physics A: Mathematical and General*, 2004. (Cited on page 55.)

[192] Shlomo Havlin, David Movshovitz, Benes Trus, and George H Weiss. Probability densities for the displacement of random walks on percolation clusters. *Journal of Physics A: Mathematical and General*, 1985. (Cited on pages 55 and 57.)

[193] Michael J. Saxton. Lateral Diffusion in an Archipelago: The Effect of Mobile Obstacles. *Biophysical Journal*, 1987. (Cited on page 55.)

[194] Makoto Matsumoto and Takuji Nishimura. Mersenne Twister: A 623-Dimensionally Equidistributed Uniform Pseudo-Random Number Generator. *ACM Transactions on Modeling and Computer Simulation*, 1998. (Cited on page 56.)

[195] Anatolii Platonovich Prudnikov, Yuri A Brychkov, and Oleg Igorevich Marichev. *Integrals and Series*. Gordon and Breach Science, 1986. (Cited on page 57.)

[196] Robert M Ziff and B Sapoval. The efficient determination of the percolation threshold. *Journal of Physics A: Mathematical and General*, 2001. (Cited on page 58.)

[197] A Weron and M Magdziarz. Anomalous diffusion and semimartingales. *EPL (Europhysics Letters)*, 2009. (Cited on page 62.)

[198] K L Sebastian. Path integral representationfor fractional Brownian motion. *Journal of Physics A: Mathematical and General*, 1995. (Cited on page 63.)

[199] John R Taylor. *An Introduction to Error Analysis: The Study of Uncertainties in Physical Measurements*. University Science Books, 1996. (Cited on page 64.)

[200] T W Anderson. On the Distribution of the Two-Sample Cramer-von Mises Criterion. *Annals of Mathematical Statistics*, 1962. (Cited on page 64.)

[201] Tsutomu Tanabe, Kurt G Beam, Jeanne A Powell, and Shosaku Numa. Restoration of excitation - contraction coupling and slow calcium current in dysgenic muscle by dihydropyridine receptor complementary DNA. *Nature*, 1988. (Cited on page 71.)

[202] Lori Feinshreiber, Dafna Singer-Lahat, Uri Ashery, and Ilana Lotan. Voltage-gated potassium channel as a facilitator of exocytosis. *Mechanisms of Exocytosis: Annual New York Academy of Sciences*, 2009. (Cited on pages 71 and 98.)

[203] Yuk M Leung, Youhou Kang, Xiaodong Gao, Fuzhen Xia, Huanli Xie, Laura Sheu, Sharon Tsuk, Ilana Lotan, Robert G. Tsushima, and Herbert Y. Gaisano. Syntaxin 1A binds to the cytoplasmic C Terminus of Kv2.1 to regulate channel gating and trafficking. *The Journal of Biological Chemistry*, 2003. (Cited on page 71.)

[204] Sharon Tsuk, Anatoli Lvov, Izhak Michaelevski, Dodo Chikvashvili, and Ilana Lotan. Formation of the full SNARE complex eliminates interactions of it individual protein components with the Kv2.1 channel. *Biochemistry*, 2008. (Cited on page 71.)

[205] D P McEwen, Q Li, S Jackson, P M Jenkins, and J R Martens. Caveolin Regulates Kv1.5 Trafficking to Cholesterol-Rich Membrane Microdomains. *Molecular Pharmacology*, 2007. (Cited on page 72.)

[206] Mark Howarth, Daniel J-F Chinnapen, Kimberly Gerrow, Pieter C Dorrestein, Melanie R Grandy, Neil L Kelleher, Alaa El-Husseini, and Alice Y Ting. A monovalent streptavidin with a single femtomolar biotin binding site. *Nature Methods*, 2006. (Cited on page 76.)

[207] Claire E Chivers, Estelle Crozat, Calvin Chu, Vincent T Moy, David J Sherratt, and Mark Howarth. A streptavidin variant with slower biotin dissociation and increased mechanostability. *Nature Methods*, 2010. (Cited on page 76.)

[208] Jie Yao, Daniel R Larson, Harshad D Vishwasrao, Warren R Zipfel, and Watt W. Webb. Blinking and nonradiant dark fraction of water-soluble quantum dots in aqueous solution. *PNAS*, 2005. (Cited on pages 76 and 88.)

[209] Arnauld Sergé, Nicolas Bertaux, Herve Rigneault, and Didier Marguet. Dynamic multiple-target tracing to probe spatiotemporal cartography of cell membranes. *Nature Methods*, 2008. (Cited on pages 77, 89, and 189.)

[210] Arnauld Sergé, Nicolas Bertaux, Herve Rigneault, and Didier Marguet. Multiple-target tracing (MTT) algorithm probes molecular dynamics at cellsurface. *Protocol Exchange*, 2008. (Cited on pages 77, 89, and 189.)

[211] Patrick D Sarmiere, Cecile M Weigle, and Michael M. Tamkun. The Kv2.1 K+ channel targets to the axon initial segment of hippocampal and cortical neurons in culture and in situ. *BMC Neuroscience*, 2008. (Cited on pages 78, 93, 100, and 140.)

[212] H Misonou, S M Thompson, and X Cai. Dynamic Regulation of the Kv2.1 Voltage-Gated Potassium Channel during Brain Ischemia through Neuroglial Interaction. *Journal of Neuroscience*, 2008. (Cited on pages 79, 92, 97, and 99.)

[213] P J Mulholland, E P Carpenter-Hyland, M C Hearing, H C Becker, J J Woodward, and L J Chandler. Glutamate Transporters Regulate Extrasynaptic NMDA Receptor Modulation of Kv2.1 Potassium Channels. *Journal of Neuroscience*, 2008. (Cited on pages 79 and 97.)

[214] D P Mohapatra. The Kv2.1 C Terminus Can Autonomously Transfer Kv2.1-Like Phosphorylation-Dependent Localization, Voltage-Dependent Gating, and Muscarinic Modulation to Diverse Kv Channels. *The Journal of Neuroscience*, 2006. (Cited on pages 79, 92, and 100.)

[215] H Vacher, D P Mohapatra, H Misonou, and J S Trimmer. Regulation of Kv1 channel trafficking by the mamba snake neurotoxin dendrotoxin K. *The FASEB Journal*, 2007. (Cited on page 80.)

[216] Rubén Vicente, Núria Villalonga, Maria Calvo, Artur Escalada, Carles Solsona, Concepció Soler, Michael M. Tamkun, and Antonio Felipe. Kv1.5 Association Modifies Kv1.3 Traffic andMembrane Localization. *Journal of Biological Chemistry*, 2008. (Cited on page 80.)

[217] P M Jenkins, J C McIntyre, L Zhang, A Anantharam, E D Vesely, K L Arendt, C J L Carruthers, T K Kerppola, J A Iniguez-LluhI, R W Holz, M A Sutton, and J R Martens. Subunit-Dependent Axonal Trafficking of Distinct Heteromeric Potassium Channel Complexes. *Journal of Neuroscience*, 2011. (Cited on page 80.)

[218] Enrica Maria Petrini, Jiuyi Lu, Laurent Cognet, Brahim Lounis, Michael D Ehlers, and Daniel Choquet. Endocytic Trafficking and Recycling Maintain a Pool of Mobile Surface AMPA Receptors Required for Synaptic Potentiation. *Neuron*, 2009. (Cited on page 88.)

[219] Qi Zhang, Yu-Qing Cao, and Richard W Tsien. Quantum dots provide an optical signal specific to full collapse fusion of synaptic vesicles. *PNAS*, 2007. (Cited on page 88.)

[220] Linda J Stitka, Kathleen L Mosier, and Mark Burdick. Does automation bias decision-making? *The International Journal of Human-Computer Studies*, 1999. (Cited on page 89.)

[221] Martin Oheim and Walter Stühmer. Tracking chromaffin granules on their way through the actin cortex. *European Biophysical Journal*, 2000. (Cited on page 90.)

[222] J M Trifaró, S Gasman, and L M Gutiérrez. Cytoskeletal control of vesicle transport and exocytosis in chromaffin cells. *Acta Physiologica*, 2007. (Cited on page 90.)

[223] Stéphane Ory and Stéphane Gasman. Rho GTPases and exocytosis: What are the molecular links? *Seminars in Cell and Developmental Biology*, 2011. (Cited on page 90.)

[224] H Vacher, D P Mohapatra, and J S Trimmer. Localization and Targeting of Voltage-Dependent Ion Channels in Mammalian Central Neurons. *Physiological Reviews*, 2008. (Cited on page 95.)

[225] James S. Trimmer and Kenneth J Rhodes. Localization of Voltage-Gated Ion Channels IN Mammalian Brain. *Annual Review of Physiology*, 2004. (Cited on page 95.)

[226] E A L Muennich. Focal aggregation of voltage-gated, Kv2.1 subunit-containing, potassium channels at synaptic sites in rat spinal motoneurones. *Journal of Physiology*, 2003. (Cited on pages 97, 99, and 100.)

[227] Marjaana A Peltola, Juha Kuja-Panula, Sari E Lauri, Tomi Taira, and Heikki Rauvala. AMIGO is an auxiliary subunit of the Kv2.1 potassium channel. *EMBO*, 2011. (Cited on page 97.)

[228] Iain M Robinson, Jennifer M Finnegan, Jonathan Monck, R Mark Wightman, and Julio M Fernandez. Colocalization of calcium entry and exocytotic release sites in adrenal chromaffin cells. *PNAS*, 1995. (Cited on page 97.)

[229] Iain M Robinson, Mitsuhiko Yamada, Mariano Carrion-Vazquez, Vanda A Lennon, and Julio M Fernandez. Specialized release zones in chromaffin cells examined with pulsed-laser imaging. *Cell Calcium*, 1996. (Cited on page 97.)

[230] Timothy J Schroeder, Jeffrey A Jankowski, Jan Senyshyn, Ronald W Holz, and R Mark Wightman. Zones of Exocytotic Release on Bovine Adrenal Medullary Cells in Culture*. *The Journal of Biological Chemistry*, 1994. (Cited on page 97.)

[231] Karin G Stenkula, Vladimir A Lizunov, Samuel W Cushman, and Joshua Zimmerberg. Insulin Controls the Spatial Distribution of GLUT4 on the Cell Surface through Regulation of Its Postfusion Dispersal. *Cell Metabolism*, 2010. (Cited on page 98.)

[232] Marcelo Ehrlich, Werner Boll, Antoine van Oijen, Ramesh Hariharan, Kartik Chandran, Max L. Nibert, and Tomas Kirchhausen. Endocytosis by Random Initiation and Stabilization of Clathrin-Coated Pits. *Cell*, 2004. (Cited on pages 98 and 121.)

[233] Mark A McNiven. Big gulps: specialized membrane domains for rapid receptor-mediated endocytosis. *Trends in Cell Biology*, 2006. (Cited on page 98.)

[234] Hong Cao, Eugene W Krueger, and Mark A McNiven. Hepatocytes internalize trophic receptors at large endocytic "Hot Spots". *Hepatology*, 2011. (Cited on page 98.)

[235] A Hayer, M Stoeber, D Ritz, S Engel, H H Meyer, and A Helenius. Caveolin-1 is ubiquitinated and targeted to intralumenal vesicles in endolysosomes for degradation. *The Journal of Cell Biology*, 2010. (Cited on page 99.)

[236] Yael Lavi, Nir Gov, Michael A Edidin, and Levi A Gheber. Lifetime of Major Histocompatibility Complex Class-I Membrane Clusters Is Controlled by the Actin Cytoskeleton. *Biophsical Journal*, 2012. (Cited on page 100.)

[237] Akihiro Kusumi, Kenichi Suzuki, and Kotaro Koyasako. Mobility and cytoskeletal interactions of cell adhesion receptorsAkihiro Kusumi. *Current Opinion in Cell Biology*, 1999. (Cited on page 100.)

[238] Samuel T Hess, Travis J Gould, Manasa V Gudheti, Sarah A Maas, Kevin D Mills, and Joshua Zimmerberg. Dynamic clustered distribution of hemagglutininresolved at 40 nm in living cell membranesdiscriminates between raft theories. *PNAS*, 2007. (Cited on page 100.)

[239] Y Kihira, T O Hermanstyne, and H Misonou. Formation of Heteromeric Kv2 Channels in Mammalian Brain Neurons. *Journal of Biological Chemistry*, 2010. (Cited on pages 100 and 140.)

[240] D Guan, L R Horton, W E Armstrong, and R C Foehring. Postnatal development of A-type and Kv1- and Kv2-mediated potassium channel currents in neocortical pyramidal neurons. *Journal of Neurophysiology*, 2011. (Cited on pages 100 and 140.)

[241] Emily Deutsch, Aubrey V Wiegel, Elizabeth J Akin, Phil Fox, Gentry Hansen, Christopher Haberkorn, Rob Loftus, Diego Krapf, and Michael M. Tamkun. Kv2.1 cell surface clusters are insertion platforms for ion channel delivery to the plasma membrane . *Molecular Biology of the Cell*, 2012. (Cited on pages 101, 112, 116, 131, 141, and 189.)

[242] Nir S Gov. Modeling the Size Distribution of Focal Adhesions. *Biophsical Journal*, 2006. (Cited on pages 101, 104, and 108.)

[243] D Jesson, T Munt, V Shchukin, and D Bimberg. Tunable Metastability of Surface Nanostructure Arrays. *Physical Review Letters*, 2004. (Cited on page 101.)

[244] Hannes Risken. *The Fokker-Planck Equation: Methods of Solutions and Applications.* Springer, 1989. (Cited on page 102.)

[245] Didier Sornette and Rama Cont. Convergenet Multiplicative Processes Repelled from Zero: Power Laws and Truncated Power Laws. *Journal de Physique I*, 2007. (Cited on page 104.)

[246] N S Gov. Physical model for the width distribution of axons. *The European Physical Journal E*, 2009. (Cited on page 104.)

[247] Jerald B Johnson and Kristian S Omland. Model selection in ecology and evolution. *Trends in Ecology & Evolution*, 2004. (Cited on page 114.)

[248] Andrew M Edwards, Richard A Phillips, Nicholas W Watkins, Mervyn P Freeman, Eugene J Murphy, Vsevolod Afanasyev, Sergey V Buldyrev, M G E da Luz, E P Raposo, H Eugene Stanley, and Gandhimohan M Viswanathan. Revisiting Lévy flight search patterns of wandering albatrosses, bumblebees and deer. *Nature*, 2007. (Cited on page 114.)

[249] Kenneth P Burnham and David Anderson. *Model Selection and Multi-Model Inference*. Springer, 2002. (Cited on page 114.)

[250] Martine Coue, Stephen L Brenner, Ilan Spector, and Edward D. Korn. Inhibition of actin polymerization by latrunculin A. *FEBS Letters*, 1987. (Cited on page 116.)

[251] Melissa A Edeling, Corinne Smith, and David Owen. Life of a clathrin coat: insights from clathrin and AP structures. *Nature Reviews Molecular Cell Biology*, 2006. (Cited on page 120.)

[252] Tom Kirchhausen. Imaging endocytic clathrin structures in living cells. *Trends in Cell Biology*, 2009. (Cited on pages 120 and 121.)

[253] Dinah Loerke, Marcel Mettlen, Khuloud Jaqaman, Henry Jaqaman, Gaudenz Danuser, and Sandra L. Schmid. Cargo and Dynamin Regulate Clathrin-Coated Pit Maturation. *Plos Biology*, 2009. (Cited on pages 120, 121, 123, 124, and 135.)

[254] Frederick Maxfield and Timothy McGraw. Endocytic Recycling. *Nature Reviews Molecular Cell Biology*, 2004. (Cited on page 120.)

[255] Jennifer Hirst and Margaret S Robinson. Clathrin and adaptors. *Biochimica et Biophysica Acta*, 1998. (Cited on page 120.)

[256] Tomas Kirchhausen. THREE WAYS TO MAKE A VESICLE. *Nature Reviews Molecular Cell Biology*, 2000. (Cited on page 120.)

[257] Tomas Kirchhausen. Clathrin. *Annual Review of Biochemistry*, 2000. (Cited on page 120.)

[258] M Marsh. The Structural Era of Endocytosis. *Science*, 1999. (Cited on page 120.)

[259] Peter A Keyel, Simon C Watkins, and Linton M Traub. Endocytic Adaptor Molecules Reveal an Endosomal Population of Clathrin by Total Internal Reflection Fluorescence Microscopy. *Journal of Biological Chemistry*, 2004. (Cited on page 121.)

[260] Christien J Merrifield, David Perrais, and David Zenisek. Coupling between Clathrin-Coated-Pit Invagination, Cortactin Recruitment, and Membrane Scission Observed in Live Cells. *Cell*, 2005. (Cited on page 121.)

[261] Christien J Merrifield, Morris E Feldman, Lei Wan, and Wolfhard Almers. Imaging actin and dynamin recruitment during invagination of single clathrin-coated pits. *Nature Cell Biology*, 2002. (Cited on page 121.)

[262] Saveez Saffarian and Tomas Kirchhausen. Differential Evanescence Nanometry: Live-Cell Fluorescence Measurements with 10-nm Axial Resolution on the Plasma Membrane. *Biophysical Journal*, 2008. (Cited on page 121.)

[263] Michael J. Saxton. The membrane skeleton of erythrocytes: A percolation model. *Biophysical Journal*, 1990. (Cited on page 121.)

[264] Tom Kirchhausen, Eric Macia, and Henry E Pelish. *Methods in Enzymology*. Elsevier, 2008. (Cited on pages 123 and 132.)

[265] Eric Macia, Marcelo Ehrlich, Ramiro Massol, Emmanuel Boucrot, Christian Brunner, and Tomas Kirchhausen. Dynasore, a Cell-Permeable Inhibitor of Dynamin. *Developmental Cell*, 2006. (Cited on pages 123, 132, and 138.)

[266] Sanja Sever, Hanna Damke, and Sandra L. Schmid. Dynamin: GTP controls the formation of constricted coated pits, the rate limiting step in clathrin-mediated endocytosis. *The Journal of Cell Biology*, 2000. (Cited on page 123.)

[267] Radhakrishnan Narayanan, Marilyn Leonard, Byeong Doo Song, Sandra L. Schmid, and Mani Ramaswami. An internal GAP domain negatively regulates presynaptic dynamin in vivo: a two-step model for dynamin function. *The Journal of Cell Biology*, 2005. (Cited on page 123.)

[268] Lisa von Kleist, Wiebke Stahlschmidt, Haydar Bulut, Kira Gromova, Dmytro Puchkov, Mark J Robertson, Kylie A MacGregor, Nikolay Tomilin, Arndt Pechstein, Ngoc Chau,

Megan Chircop, Jennette Sakoff, Jens Peter von Kries, Wolfram Saenger, Hans-Georg Kräusslich, Oleg Shupliakov, Phillip J Robinson, Adam McCluskey, and Volker Haucke. Role of the Clathrin Terminal Domain in Regulating Coated Pit Dynamics Revealed by Small Molecule Inhibition. *Cell*, 2011. (Cited on pages 123, 131, and 138.)

[269] Khuloud Jaqaman, Dinah Loerke, Marcel Mettlen, Hirotaka Kuwata, Sergio Grinstein, Sandra L. Schmid, and Gaudenz Danuser. Robust single-particle tracking in live-cell time-lapse sequences. *Nature Methods*, 2008. (Cited on pages 124 and 191.)

[270] Rainer E Barkard and Eranda Çela. Linear Assignment Problems and Extensions. In *Handbook of combinatorial optimization*. 1999. (Cited on page 126.)

[271] Aubrey Weigel, Philip D Fox, Elizabeth J Akin, Kari H Ecklund, Michael M. Tamkun, and Diego Krapf. Size of Cell-Surface Kv2.1 Domains is Governed by Growth Fluctuations. *Biophsical Journal*, 2012. (Cited on pages 131, 141, and 189.)

[272] Bernard T Kelly and David J Owen. Endocytic sorting of transmembrane protein cargo. *Current Opinion in Cell Biology*, 2011. (Cited on page 137.)

[273] Greta M Lee, Akira Ishihara, and Ken A Jacobson. Direct observation of Brownian motion of lipids in a membrane. *PNAS*, 1991. (Cited on page 188.)

[274] Ralf Metzler, Vincent Tejedor, J.-H Jeon, Y. He, W. H. Deng, S. Burov, and E. Barkai. Analysis of single particle trajectories - from normal to anomalous diffusion. *Acta Physica Polonica B*, 2009. (Cited on page 197.)

# APPENDIX - PROTOCOLS

This appendix provides generalized protocols used for the experiments presented in this thesis, along with other useful protocols used in the Krapf Research Lab. Among these protocols are instructions for aligning the TIRF microscope, transfecting and preparing HEK293 cells for imaging. Also included are protocols for preparing imaging saline, cell medium and matrigel solutions and instructions for general cell culture and aseptic technique. Lastly information on labeling dishes with polystyrene beads used for co-aligning channels when multi-color TIRF is being done and cleaning imaging dishes is provided.

## 8.1 ALIGNING THE MICROSCOPE (TIRF)

This protocol begins with the assumption that the telescope (see Fig. 8.1) is already aligned. This should be checked before each imaging session and before starting this protocol. If more than one beam is being used for illumination further care will need to be taken to ensure that the beams are not only aligned for TIRF imaging, but also co-aligned to each other.

### 8.1.1 *Materials*

- SM1 tubes (total length of connected tubes needs to exceed at minimum 30 cm)
- Apertures (4x)
- Adaptor with external RMS threads and internal SM1 threads
- Crosshair (usually drawn on a sheet of paper)

### 8.1.2 *Protocol*

1. Remove focusing lens from path[1].
2. Place an aperture on the second lens of the telescope and close it so that the beam is small as it enters the microscope. Use the steering mirrors S1 and S2 and align with the SM1 tube. The beam should have an aperture before the two steering mirrors and be aligned such that it goes through the bottom and top iris of the tube and onto the ceiling. Use S1 to center the beam with the bottom aperture closed and S2 to center the beam through the top aperture.
3. Center the crosshair on the ceiling to the aligned beam as a marker for later steps. *Do not* touch the steering mirrors until after the focusing lens is in place.

1 The logic in this method is to first align the beam with the SM1 tubes so that it is entering the microscope parallel to the table and exiting the microscope perpendicularly. The crosshair on the ceiling marks this. Between steps 3 and 6 the biggest change made to the system is adding the focusing lens. Thus, to ensure alignment the beam needs to be adjusted so that it is aligned back to the crosshair using *only* focusing lens. After this only small adjustments are made with the mirrors to perfect the alignment.

4. Replace the tube with the objective. If using the objective heater you can put this on the objective now as well (and turn on the objective heater power supply).

5. Put the focusing lens back into the micrometer holder.

6. Adjust the lens so that the beam passes through the center. Use an aperture on the focusing lens and telescope (to reduce the size of the beam) to help find center more easily.

7. Make sure that the reflection of the beam off the focusing lens aligns to the original beam on mirror S2.

8. Once aligned tighten the focusing lens in place.

9. Using *only* the micrometer (do not use the steering mirrors at this point!) adjust the focusing lens so that beam on the ceiling is going through the crosshair. This will move the beam off center from the lens. This will be adjusted next.

10. Using S1 re-center the beam onto the focusing lens (close both the aperture on the telescope lens and the focusing lens to do this)

11. Open the apertures and re-center the spot on the ceiling using S2.

12. Repeat steps 10 and 11 until the beam is going through the center of the focusing lens *and* aligned to the crosshair on the ceiling.

13. Once aligned, remove all apertures (so as not to clip the beam) and if using the heated stage place this on the microscope as well[2] but do *not* turn on until a dish is in place. The system is reading for imaging.

2 The objective heater may be turned on immediumtely. It take time to warm up the objective so it is better to give the heater 30 minutes or more. The stage heater however provides instantaneous heat. The stage heater should *never* be turned on without a dish in place.

This protocol explains the method used to clean already-used imaging dishes. This ensures that the dishes are both sterile for the cells *and* the glass is clean so as not to add any background fluorescence while imaging.

### 8.2.1 *Materials*

- $ddH_2O$
- Soft bristle tooth brush
- 10% Bleach + 10% Alconox solution (made with $ddH_20$)
- Isopropyl Alcohol
- Compressed $N_2$

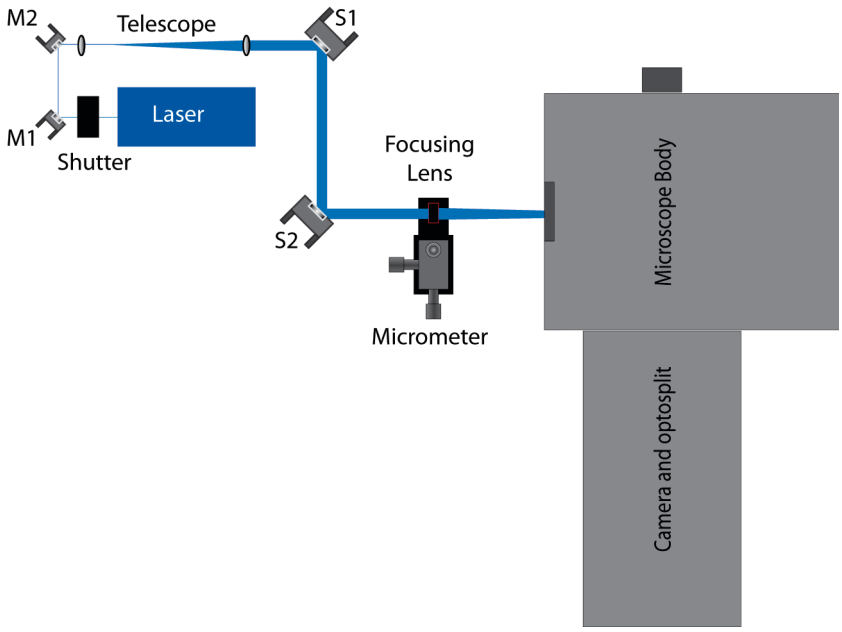


Figure 8.1: *TIRF Microscope* General schematic of TIRF microscope. Mirrors M1 and M2 are used for steering the beam into the telescope. The telescope expands the beam so that it overfills the back aperture of the objective. Mirrors S1 and S2 steer the beam into the focusing lens and then into the microscope. The focusing lens is on a micrometer for fine tune adjusting.

### 8.2.2 *Protocol*

1. Use a 10% Bleach + 10% Alconox with $ddH_2O$ solution to clean dishes with a soft bristle tooth brush.

    a) Be sure that there is no residue left in bottom 'rim' of dishes.

2. Rinse thoroughly with $ddH_2O$.

3. Wash last amount of $ddH_2O$ away with Isopropyl Alcohol and dry with compressed $N_2$.

    a) Be sure not to leave any water spots on glass surface.

    b) If there are oil smudges still present on glass bottom after drying with $N_2$use a cotton swab and Isopropyl Alcohol to scrub the bottom of the dish. Then repeat step 3.

4. If dishes are being used immediumtely for transfecting/imaging place in biosafety cabinet and UV for ~ 5 min.

## 8.3 HEK 293 CELL TRANSFECTION

This protocol describes the method used to transfect HEK293 cells with plasmid DNA of choice[3]. All solutions, except for Matrigel and plasmids, should be pre-warmed in 37˚C water bath before beginning protocol. Matrigel can be used directly from the fridge. Plasmid DNA should only be thawed, no need to warm in water bath. All work is done in the biosafety cabinet to prevent contamination of cells *or* any solutions being used.

### 8.3.1 *Materials*

- Confluent dish of HEK293 cells, p ~ 44 - 48 [4]
- Clean imaging dishes (See Protocol 8.2 for instructions on how to clean the dishes)
- DMEM + 10% FBS, without phenol red, with 10x antibiotic (usually streptomycin)
- Matrigel
- Optimem
- Trypsin
- Plasmid DNA
- Serological pipettes
- 0.5 mL microcentifuge tubes
- Electroporation cuvettes
- 15 mL conicals

3 Always be self minded of work being done with cells and solutions. It is *extremely* important to keep everything sterile!
4 If doing more than one type of transfection more than one dish of confluent cells is advised. Also, it is important to used p ~ 44 - 48 cells if imaging Kv2.1 channels. Cells younger/older than this tend to have abnormal Kv2.1 clusters.

### 8.3.2 *Protocol*

1. Add approximately 1mL (just enough to coat the bottom of the dish) of Matrigel to dishes that have been cleaned and UV'ed.
2. Prepare plasmid DNA:
    a) In sterile micro-centrifuge tube add
        i. Optimem: 200 μL
        ii. Plasmid DNA (example transfection given for reference below)
            A. GFP Loop BAD Plasmid: for 3 μg (1 μg/μL concentration) use 3 μL
            B. BirA Plasmid: for 1μg (1.5 μg/μL) use 0.66 μL
            C. CLC-GFP Plasmid: for 200 ng (100 ng/μL) use 2 μL
    b) Pipette optimem-plasmid solution up and down a couple times to mix.
    c) Place in water bath.
3. Place the dishes in the incubator.
    a) Total time of matrigel coating should surpass 5 minutes but not exceed 30 minutes.
4. Add 4mL of Trypsin to 100 mL dish of stock cells and place the cells back in incubator.
    a) Check on the cells intermittently.

b) Once the cells just start to lift from the bottom of the dish when gently 'swirled' take the dish out of the incubator.

c) Do not allow the Trypsin to completely lift the cells off the bottom of the dish.

5. Dilute the dish of 4 mL Trypsin and unbound cells with 10 mL medium (DMEM + 10% FBS)

a) Pipette up and down once or twice to wash off any remaining cells stuck to the dish.

b) Place 14 mL mixture of cells, Trypsin and medium into a 15 mL conical.

6. Centrifuge at 1.5 rpm for 3min

7. While cells are being centrifuged remove matrigel coated dishes from the incubator.

a) Aspirate Matrigel from dishes.

b) Replace with 1 mL of DMEM + 10% FBS (no phenol red, with antibiotic).

8. Bring optimem-plasmid solution prepared in step 2 into the biosafety cabinet.

9. Aspirate medium/Trypsin from 15mL conical tube with cell pellet, take care not to disturb the pellet of cells.

a) Re-suspend the cells with the Optimem-plasmid solution and pipette up and down once or twice using shear force to break up any clumps of cells.

b) Place suspended cells into electroporator cuvette.

10. Electroporate

a) For HEK293 cells from *HOME* screen on BioRad electroporator:

i. (4) Pre-set protocols

ii. (3) Mammalian cells

iii. (4) HEK293 cells

iv. Pulse

11. Transfer cells from cuvettes to micro-centrifuge tube

12. Place ~ 10 - 20 μL of transfected cells into the center of the imaging dishes. Use pipette tip to gently swirl the cells in the dish so that they are evenly dispersed throughout the dish[5].

a) This varies depending on how long the cells have to grow until imaging and how confluent the dish of cells was to start with.

b) i.e. the more cells to start with the less needed in each dish - or - the longer they have to grow the less cells in each dish.

13. Place cells back in the incubator.

5 If imaging with clathrin place transfected cells into a culture dish instead of directly into imaging dishes. One hour before imaging (allow ~ 2 - 3 hours for transfection) cells can be trypsinized and transferred to imaging dishes. This will help to alleviate clathrin plaque artifacts due to being plated for too long.

## 8.4 LABELING IMAGING DISH WITH POLYSTYRENE BEADS

This protocol is to be used when imaging with multi-color TIRF. The beads serve as a reference so that the two color channels can be cropped and overlaid post imaging.

### 8.4.1 *Materials*

- Clean imaging dish
- Imaging Saline
- BSA
- Polystyrene beads

### 8.4.2 *Protocol*

1. Coat imaging dish with Matrigel for ~10 min (usually this is done with the dishes being used for transfection in Protocol 8.3 the night before imaging)
2. Aspirate off Matrigel and replace with ~200-300 μL of bead solution:

    a) 1 mL Imaging Saline

    b) 10 mg BSA

    c) 200 μL polystyrene beads

    d) Let the dishes rest in the incubator with bead solution for a few hours (usually overnight)

3. Prior to imaging, aspirate bead solution from dishes and replace with 1mL imaging saline. Dish is now ready for imaging.

## 8.5 LIVE CELL IMAGING PREPARATION

This protocol explains how to prepare transfected cells plated in imaging dishes for imaging. All work should be done in the biosafety cabinet.

### 8.5.1 *Materials*

- Imaging Saline
- If labeling with QDs:
  - QDs
  - BSA
  - 1.5 mL micro-centrifuge tubes

### 8.5.2 *Protocol*

1. Heat Imaging Saline in water bath, 37˚C.
2. If labeling with QDs prepare QD solution: 1:10000 QD in 1% BSA in Imaging Saline
   a) 1% (by volume) BSA and Imaging Saline
      i. Measure out ~ 10 mg BSA
      ii. Place BSA and Imaging Saline into micro-centrifuge tube.
      iii. Vortex until BSA is completely dissolved.
   b) 1:10000 QD in 1% BSA

i. 5 μL of 1:100 QD in 1% BSA in Imaging Saline

A. 1 μL QD

B. 100 μL Imaging Saline

C. Vortex

ii. 500 μL of Imaging Saline

iii. Vortex

c) Place QD solution in water bath.

3. Aspirate medium from dish of cells and rinse 6x with Imaging Saline to remove medium.

a) Be careful not to suck all the medium off the dish, leaving the cells dry.

b) Do not suck off medium from middle, suck from the sides where there are no cells.

c) When rinsing do not add Imaging Saline too quickly or with too much force or directly the middle of the dish. These actions can wash away the cells.

d) On last rinse remove *ALL* Imaging Saline.

4. *QUICKLY* place 500 μL of the QD solution into the dish of cells and place in the incubator for 5 minutes.

5. Remove the QD solution then rinse 3x with Imaging Saline to remove any unbound QDs.

6. On the final rinse leave 1 mL of Imaging Saline in the dish for imaging.

a) If not labeling with QDs simply rinse 3-6x with Imaging Saline and leave 1 mL of Imaging Saline on final rinse in dish for imaging.

## 8.6 HEK293 IMAGING SALINE

HEK293 Imaging Saline is a buffer that keeps the pH stable for the cells. This way while imaging (without $CO_2$) the cells remain healthy.

### 8.6.1 *Materials*

- $ddH_2O$
- NaOH
- KOH
- 1 L bottle top filter
- 1 L sterile glass bottle
- Stir plate
- pH meter
- Osmolarity meter

Table 8.1: *HEK293 Imaging Saline* List of substances and amounts used to make Imaging Saline.

| Molar Concentration (mM) | Substance | Amount (g) |
|---|---|---|
| 146 | NaCl | 8.53 |
| 4.7 | KCl | 0.35 |
| 2.5 | $CaCl_2 2H_20$ | 0.36 |
| 0.6 | $MgSO_4$ | 0.072 |
| 0.15 | $NaH_2PO_4$ | 0.02 |
| 0.1 | Ascorbic Acid | 0.0176 |
| 8 | Glucose | 1.44 |
| 20 | HEPES | 4.76 |

### 8.6.2 *Protocol*

1. Begin by measuring out ~ 800 - 900 mL of $ddH_2O$.

    a) The final volume will be approximately 1 L. It is easier to adjust osmolarity later by adding water, so it is best to start with less than 1 L of water.

2. Add substances in Table 8.1 to water.

    a) It is easiest to use a stir plate to keep the solution constantly mixing.

3. Once everything is check osmolarity of solution.

    a) Add $ddH_2O$ until solution reaches 346 mOs.

4. Next check the pH of the solution.

    a) Adjust pH to 7.4

        i. If pH is high KOH for the adjustment.

        ii. If pH is low add NaOH.

        iii. Be sure to wait 20-30 seconds between adding drops of KOH or NaOH so that the pH meter can get an accurate reading.

5. Once the pH and osmolarity are correct pass the Imaging Saline through a bottle top filter into a 1 L glass bottle. This will sterilize the saline.

6. Store in fridge.

## 8.7 CELL CULTURE - SPLITTING CELLS

Here the general cell care is described, specifically splitting cells. All work should be done in the biosafety cabinet. Always take *extreme* care to be as clean and sterile as possible[6]. It is pertinent to be overcautious when working with cells or sterile solutions so as not to introduce any contaminations. Always make sure to warm all solutions in water bath at 37˚C before beginning the procedure.

### 8.7.1 *Material*

- DMEM + 10% FBS (with phenol red)
- Trypsin
- Serological pipettes
- 100 mL cell culture dishes

### 8.7.2 *Protocol*

1. Label dishes with:
    a) Your name/initials
    b) Date
    c) Cell type
    d) Passage number
    e) Amount of cells

6 See Protocol 8.10 for general aseptic technique.

i. 0.25 - 4 mL

2. UV new sterile culture dishes that cells will be split into.
3. Add10 mL DMSO + 10% FBS (with phenol red) medium into each dish.
4. Place dishes in incubator until ready to start step 4.
5. Aspirate medium from dish of confluent cells.
6. Pipette 4mL of Trypsin EDTA into dish.
7. Once cells have lifted from bottom of dish split into new sterile cell culture dishes dishes.

a) 0.25 - 4 mL

## 8.8 PREPARING CELL MEDIUM

This protocol describes the methods for preparing medium for cell culture and transfection. As with all cell culture related protocols all work should be performed inside the biosafety cabinet and proper aseptic technique practiced.

### 8.8.1 *Materials*

- 50 mL aliquot of FBS
- For transfection medium:
  - 500 mL DMEM (no phenol red)
  - 5 mL 100x Antibiotic (usually streptomycin)
- For cell culture medium:
  - 500 mL DMEM (with phenol red)
- Sterile 500 mL glass bottle
- Bottle top filter

### 8.8.2 *Protocol*

1. Heat shock aliquot of FBS
   a) Let FBS sit in water bath at 37˚C for ~ 1 hour after being thawed (also in water bath).

2. Thaw antibiotic if making transfection medium.

    a) Do not let thawed antibiotic remain unfrozen for an extended amount of time.

3. Once FBS is thawed and heat shocked add to DMEM.

    a) If preparing medium for cell culture use DMEM + phenol red.

    b) For transfection medium use DMEM *no* phenol red.

4. If preparing transfection medium:

    a) Add 5 mL 100x antibiotic to DMEM (no phenol) + 10% FBS solution.

5. Pass DMEM + 10% FBS solution through a bottle top filter into a sterile glass bottle.

6. Label bottle with description, initials and date.

7. Store medium in fridge.

## 8.9 PREPARING MATRIGEL

The protocol for preparing Matrigel solution to coat the bottom of imaging dishes is described here.

### 8.9.1 *Materials*

- Matrigel
- Optimem
- 15 - 50 mL conical

### 8.9.2 *Protocol*

1. Thaw Matrigel in 37˚C water bath *just* long enough for the solution to become gelatinous.

    a) Do not leave the Matrigel in the water bath for too long, it can denature the proteins and ruin the solution.

2. Add 1 part Matrigel to 300 parts optimem.

    a) Matrigel will be very thick so it is best to use a 1 mL pipette.

3. Vortex mixture.
4. Label conical with description, initials and date.
5. Store Matrigel in fridge.

## 8.10 GENERAL ASEPTIC TECHNIQUE

General aseptic technique and practice is described here. It is important to take great care while dealing with live cells and sterile solutions so as not to introduce any contamination.

### 8.10.1 *General cell handling principles*

- *Sterility* is essential.
  - All reagents and supplies must be sterile.
  - Always wash hands before handling cells or reagents.
- Inspect cell cultures daily for any signs of contamination.
  - In the case where contamination is spotted, remove all affected cell cultures from incubator, rinse dish with bleach and discard.

### 8.10.2 *General sterile reagent handling and principles*

- Aliquot stock sterile solutions whenever possible. This will not only make handling easier but also prevent accidental contamination.
- If possible avoid sharing reagents with other lab mates. This will prevent potential cross contaminations and accountability issues.
- Never re-use any pipettes. Do not insert a pipette back into a bottle of reagent.
- Take care not to insert the disposable/non-sterile portion of pipetters into the reagent bottle.
- Do not allow any liquid to touch the top of the bottle and/or bottle cap.

  - This includes tipping the closed bottle on its side when the bottle is closed.
  - Allowing liquids to reach this part of the bottle allows a bridge between the outside of the bottle and inside of the bottle thereby inducing contaminations.

- Close bottle whenever not in use.
- Keep bottle and cap off to the side of the work area (within the biosafety cabinet).

  - This is to avoid potential spills and sloughing off any dirt/skin, that would occur when passing arms over the bottle, into bottle while working.

### 8.10.3 *General biosafety cabinet principles*

- Before entering hood the sash should be opened and the fan allowed to run. By opening the sash the environment inside the hood is changed and thus the hood needs some time to re-establish laminar flow.[7]
- Wipe down reagent bottles and other supplies being brought into the cabinet with 70% isopropyl alcohol before bringing them into the biosafety cabinet.
- Make sure you are wearing gloves and a lab coat (used *only* for biosafety cabinet use) or long sleeves.

  - Flakes of skin that can slough off into the hood are full of bacteria.
  - If you have long hair, you should pull it back before starting any process in the hood as well.

7 There is nothing *magical* about isopropyl alcohol. It is not the mere application of this solution that cleans a surface. Rather, it is the *drying* of isopropyl alcohol that dehydrates cells and thereby kills them - ensuring a cleanly surface.

- Wipe down hands with 70% isopropyl alcohol and allow to dry inside the biosafety cabinet.
- Try to limit the number of people around the cabinet when working inside. Disturbances of people walking by disrupt the laminar flow within the hood. Also, distractions can lead to accidents causing potential contaminations.
- Keep your work area within the cabinet clean and organized.
    - It is best to work from one side of the hood to the other. For instance if transferring liquid keep sterile solutions on the right, vessels to be transferred into in the middle, and things to be disposed of on the left.
- It is also important to not clutter the inside of the cabinet. Disrupting the laminar flow defaults the insured cleanliness of the hood.

# APPENDIX - SOFTWARE

A list and description of the algorithms used for the work presented in this thesis is provided in thesis appendix. The order of presentation is the general order of analysis events.

## 9.1 acquiring data

The typical format of raw data is in the form ofi mages acquired while imaging. It is important to keep careful book-keeping of all of the parameters used while imaging. i.e.:

- Cell type, passage number, and transfection time
- Plasmid type and amountt ransfected into cells
- Emission filters used
- Alignment image name and location
- White light image name and location
- Dish number and cell number being imaged and recorded
- Dimensions and coordinates of ROI being imaged
- Exposure time
- EM Gain
- Number off rames
- Total movie time (needed to calculate accurate average frame rate)
- ND filters being used
- If a drug is being applied:
  - The concentration and time it was applied

This list is not exhaustive and it has degrees of variability dependent on the experiment being performed. The items listed here serve as general guidances and suggestions.

## 9.2 IMAGE PROCESSING

Image processing of acquired movies is usually performed in Labview or ImageJ. If the movies are going to be ran through a tracking algorithm (i.e. u-track) the following set of processes are done to enhance tracking of single particles.

### 9.2.1 *Image overlay*

If more than one fluorophore is simultaneously being imaged the tiffs will need to be split. This is done using the Cairn Image Splitter Analyzer plugin available in ImageJ. First, a white light image is used (typically an image of polystyrene beads on glass) to determine where the two channels need to be cropped and the coordinates of the overlay. Following the instructions of the plugin the first and second channel are selected, the alignment saved and the image split into the two corresponding channels (where each channel is one emission color). Once the parameters have been set the stack of tiffs collected can be processed using the *previous alignment* setting in the plugin. Each channel is saved separately as single image tiff files for further processing.

### 9.2.2 *Frame averaging*

When a quick frame rate is used (20 Hz or more) it is advantageous to frame average. Not only does this improve the signal to noise ratio of the movie but it also cuts the number of frames in half thereby allowing for quicker tracking. Frame averaging is done in Labview.

LOCATION: \Labview\Image Processing\average frames.vi

The program averages the intensity of each pixel between the number of frames specified and outputs a single averaged image. Typically only two frames are averaged. The program requires inputs of the location of the folder of tiffs to be averaged, the saving location of averaged tiffs,

the file pattern of the tiffs to be processed, and the number of frames to be averaged. The images are automatically named using the original tiff name.

### 9.2.3 *Gaussian filter*

Once the tiffs have been split and frame averaged a Gaussian blur filter is applied in ImageJ. Applying a Gaussian blur smooths the image, which reduces the noise. Essentially it behaves as a low pass filter. The filter is preset in ImageJ and a radius of 1 pixel is used. If the radius of the Gaussian is too large the individual fluorophores in the image will be spread too much and tracking will become problematic. Because the PSF width is slightly larger than 1 pixel a Gaussian kernel with a radius of 1 pixel will not result in too much blurring of the particles of interest[1].

## 9.3 TRACKING

There are a few different methods that can be used to track single particles, including fitting the PSF of the particle to a 2D Gaussian function[23], center-of-mass tracking[96], and cross correlation[273]. In general each of these methods can be separated into two distinct parts, particle detection and particle tracking, or rather 'connecting the dots'. As published by Cheezum et al the best method for tracking individual fluorophores is using the 2D Gaussian fitting method[145]. However, for conglomerates of fluorophores that might be elliptical instead of circular center-of-mass tracking is encouraged.

### 9.3.1 *Labview*

In Chapters 4 [49] and 4 [50] a custom written algorithm in Labview was used to track QD-labeled Kv2.1 channels.

LOCATION \Labview\Tracking\Moving multiple ROI Gauss efficient w R_intensity.vi

1 The width of the PSF is unique to each imaging system and so this setting can be variable depending on the microscope and imaging conditions.

This program is advantageous for low density labeling of particles either with fluorescent proteins or QDs. Artifacts due to collisions will be occur if the labeling density is too high. The algorithm requires the location of the folder of tiffs to be tracked, the file pattern of these tiffs, the frame to start tracking, the frame to end tracking, the exposure time of the movie, and the size of the ROI to be used for following the particle being tracked. The code analyzes each frame and the ROI surrounding each particle is adjusted to follow the particle. The optimal ROI size is 10 pixels[49].

As mentioned above for aggregates of fluorophores it can be advantageous to use center-of-mass tracking, especially when the object of interest is elliptical rather than circular in shape. This method was used for tracking GFP-Kv2.1 clusters in Chapter 05[271].

LOCATION \Labview\Tracking\Moving multiple ROI XY centers - Threshold.vi

The COM algorithm uses the same input arguments as the Gaussian tracker with the addition of thresholding. Thresholding is key for COM tracking[145]. In order to determine the optimal threshold an image viewer is used to view when the background is reduced the greatest while not extinguishing the signal of the objects of interest.

LOCATION \Labview\Image Viewers\Image viewer - THRLSD.vi

### 9.3.2 *MTT Algorithm*

The Labview tracking algorithm works efficiently for tracking a low density of particles. This requires many movies to accumulate enough data for statistical analysis, which is very time and energy consuming. It is easier to acquire fewer movies with more particles than more movies with few particles. To be able to track these higher particle density movies a multiple-target tracing algorithm[209, 210] was employed. Furthermore, because particles are not manually detected as an initial step (as is the case for the Labview algorithm) newly arriving particles can be determined more easily. This algorithm was used for the work presented in Chapter 04[241].

The input parameters are set in:

LOCATION \Matlab\MTT\detect_part_v2\MTT_param.m

An example of input parameters for tracking QD-labeled Kv2.1 channels is given below. The algorithm requires the images be saved as a *.stk file as well. This may be done using ImageJ.

| Detection Parameter | |
|---|---|
| *Pre-detection threshold* | seuil_preiere_detec = 90; |
| *Final detection threshold* | seuil_detec_1vue = 95; |
| *ROI size in pixels* | wn = 9; |
| *Gaussian radius in pixels* | ro = 1.8; |
| **Reconnection Parameters** | |
| *Temporal sliding window* | T = 50; |
| *Number of deflation loop* | nb_defl = 50; |
| *Disappearance / probability of blinking* | T_off = -500; |
| *Maximum diffusion coefficient in pixel* | sig_free = 2; |
| *Reference diameter* | Boule_free = 3.5; |
| *Limitation of combinations* | Nb_combi = 4; |
| *Validation of pre-detected particles* | seuil_alpha = 1500; |
| *Likelihood between uniform and Gaussian law* | Poids_melange_alpha = 0.99; |
| *Likelihood between maximum and local diffusion* | Poids_melange_diff = 0.99; |

Once the parameters have been set the detection and tracking program may be ran using:

LOCATION \Matlab\MTT\detect_part_v2\detect_reconnex_22.m

Use trace_particle.m to convert output of MTT_algorithm to XYI.txt file.

LOCATION \Matlab\trace_particle.m

### 9.3.3 *U-track*

The particle tracking used in Chapter 05 to the present was tracked using an algorithm from the Danuser lab: u-track[269]. This code is also ran in Matlab, however it is slightly more computationally friendly than the MTT algorithm. It also provides better tracks with our imaging system. U-track is designed for tracking dense particle fields, closing gaps in trajectories as a result of detection failure thereby enabling the capture of splitting and merging events. The basis of the algorithm formulates correspondence problems as linear assignment problems and searching for a globally optimal solution. The algorithm is written for tracking tracer particles labeled with fluorophores that bleach. Because of this, when tracking QDs (which do not bleach) alterations must be made.

For tracking photobleaching fluorophores the algorithm may be used directly from the Danuser lab website:

LOCATION http://lccb.hms.harvard.edu/software.html

1. Before beginning be sure to add the *u-track* folder to the Matlab directory
2. Detect Particles:

    a) \Matlab\Jaqaman Code\U-track\scriptDetectGeneral.m

| Detection Parameters | |
|---|---|
| *Camera bit-depth detection* | Param.bitDepth = 16; |
| *St. dev. of the PSF* | detectionParam.psfSigma = 1.5; |
| *Time averaging* | Param.integWindow = 0; |
| *Alpha-value for detection of local maxima* | Param.alphaLocMax = 0.0001; |
| *Maximum iterations for PSF estimation* | detectionParam.numSigmaIter = 10; |
| *Mixture model fitting* | detectionParam.doMMF = 0; |
| *Alpha-values for mixture-model fitting step.* | detectionParam.testAlpha = struct('alphaR', 0.001,'alphaA', 0.001,'alphaD', 0.001,'alphaF', 0); |

3.

4. Once particles have been detected they need to be connected to create trajectories.

   a) \Matlab\Jaqaman Code\U-track\scriptTrackGeneral.m

5.

| Tracking Parameters | |
|---|---|
| Gap closing time window | gapCloseParam.timeWindow = 3; |
| Flag for merging and splitting | gapCloseParam.mergeSplit = 1; |
| Minimum track segment length | gapCloseParam.minTrackLen = 15; |
| Flag for linear motion | parameters.linearMotion = 2; |
| Search radius lower limit | parameters.minSearchRadius = 2; |
| Search radius upper limit | parameters.maxSearchRadius = 5; |
| Standard deviation multiplication factor | parameters.brownStdMult = 3; |
| Scaling the Brownian search radius | parameters.brownScaling = [0.5 0.01]; |
| Power for scaling the Brownian search radius | parameters.timeReachConfB = 4; |
| Amplitude ratio lower and upper limits | parameters.ampRatioLimit = [0.7 4]; |
| Formula for scaling the linear search radius | parameters.linScaling = [0.5 0.01]; |
| Max angle between the directions of motion | parameters.maxAngleVV = 30; |
| Gap length penalty | parameters.gapPenalty = 1; |

6. Next convertt he tracking output into the typical XYI.txt file used for further analysis.

   a) [trackedFeatureInfo, trackedFeatureIndx, trackStartRow, numSegments] =

   b) Save trackedFeatureInfo as a *_pixel*.mat file

   c) Use that *_pixel*.mat file in write_trajectories_utrack.m to save a XYI *_pixel*.txt file

location \Matlab\write_trajectories_utrack.m

When tracking QD-labeled particles modified cost functions must be used. Tracking then goes as follows:

1. Add the u-track folder and the CollectedTrackingFunctions folder to the Matlab directory.

a) Remove the *detection* folder within *CollectedTrackingFunctions* from the path.

2. Detect Particles as before.

   a) \Matlab\Jaqaman Code\U-track\scriptDetectGeneral.m

3. Connect detected particles:

   a) Remove the *u-track* folder from the Matlab directory

   b) Open tracksettings.mat

      LOCATION Matlab\Jaqaman Code\exactFunctions\tracksettings.mat

   c) Run Track.m

      LOCATION Matlab\Track.m

4. Convert the tracking output into the typical XYI.txt file using the same method described above.

Before using XYI.txt file in further analysis a few clean-up steps need to be done.

1. First insert the exposure time into the first row of the XYI file. This is used in all later analysis codes.

location \Labview\Arrange Data Files and Arrays\Insertt lag into XYI file.vi

2. Next convertt he XYI file from pixel to nm

   location \Labview\Arrange Data Files and Arrays\Convert from pixel-nm or nm-pixel file.vi

3. If the XYI file is to be used for ergodicity analysis (i.e.. time / ensemble averaged MSD, ergodicity breaking parameter) the following steps should be followed:

   a) First remove the buffered zeros from the XYI file, so that all trajectories start in the first frame.

      location \Labview\Arrange Data Files and Arrays\Remove buffered zeros in array.vi

   b) Next replace all zeros with NaNs. The resulting file will have be in pixels, have all trajectories start in the first frame, and have no zeros.

      location \Labview\Arrange Data Files and Arrays\Replace zeros with NaNs.vi

4. Sometimes it is also useful to analyze trajectories that are of at least a minimum length. do this a Labview program to find long trajectories is used.

   location \Labview\Arrange Data Files and Array\FindLongTrajectories.vi

## 9.4 useful labview analysis algorithms

This section lists Labview algorithms used for statistical analysis presented in this dissertation. The location of each code is given and explanation/description where needed.

### 9.4.1 Square displacement analysis

- Displacement squares

  location \Labview\Displacement Squared\displacement squared automatic with

- MSD

  - Time-averaged MSD

    location \Labview\MSD\MSD - automated dot number - no fitting_utrack.vi

  - Time-averaged MSD and Ensemble-averaged MSD distributions

    location \Labview\MSD\Means of rows and columns - disc short.vi

  - Alpha

    location \Labview\MSD\analyze linear MSDs no first row.vi

- CDF

location \Labview\CDF\Cumulative probability - automated dot number_new.vi

- Waiting times

  location \Labview\Waiting times\waiting times automated with location - no drift.vi

- Ergodicity breaking parameter

  – To calculate ergodicity breaking parameter for one tlag according to the total movie time[58, 149, 274]:

    location \Labview\MSD\Ergodicity Breaking Parameter.vi

  – To calculate ergodicity breaking parameter for each tlag for a given total movie time

    location \Labview\MSD\Ergodicity Breaking Parameter_vary tlag.vi

### 9.4.2 Lifetime analysis

- First extract intensities from multiple XYI trajectory file:

  location \Labview\Lifetimes\Extract array of Intensities from multiple XYI trajectory file_3.vi

- Next find lifetimes

location \Labview\Lifetimes\channel lifetimes and dark stats - automated v4_utrack.vi

### 9.4.3 CCP trapping and colocalization

The following list of Labview programs was used in Chapter 06 to match the location of QD stalls to CCPs.

- First outputt he time and location of QD stalls

  location \Labview\Waiting times\view trajectory and stops_automatic - output stops

  - This can be used to manually determine whether a QD stall occurs on a CCP andused to match up the stall with the lifetimes of CCPs

- Next match CCPs to QD stalls (connections file)

  location \Labview\Clathrin\Match clathrin track to QD stops_2.vi

- Last compile array of QD stalls with corresponding CCP lifetime and time at which QD stalls in CCP

  location \Labview\Clathrin\QD stops with corresponding clathrin lifetime.vi